Operando studies of the electrode/electrolyte interface using X-Ray absorption and X-Ray photoelectron spectroscopies

Benjamin Rotonnelli

UNIVERSITÉ DE STRASBOURG

ÉCOLE DOCTORALE SCIENCES CHIMIQUES

Institut de Chimie et Procédés pour l'Energie l'Environnement et la Santé

ICPEES, UMR 7515

THÈSE présentée par :

Benjamin Rotonnelli

soutenue le: **27 novembre 2023**

pour obtenir le grade de : **Docteur de l'université de Strasbourg**

Discipline/ Spécialité : Chimie / Chimie Physique

Études *operando* de l'interface électrode/électrolyte par les techniques de spectrométrie d'absorption des rayons-X et de photoélectronique-X

Operando studies of the electrode/electrolyte interface using X-Ray absorption and X-Ray photoelectron spectroscopies

THÈSE dirigée par :

Mme. SAVINOVA Elena	Professeur, Université de Strasbourg
M. GALLET Jean-Jacques	Maitre de Conférence, Sorbonne Université
M. ASSET Tristan	Chargé de recherche, CNRS

RAPPORTEURS :

Mme. ROTH Christina	Professeur, University of Bayreuth (DE)
Mme. ARRIGO Rosa	Maître de Conférence, University of Salford (UK)

AUTRES MEMBRES DU JURY :

M. MAILLARD Frederic	Directeur de recherche, CNRS
M. LASSALLE-KAISER Benedikt	Scientifique de ligne, Synchrotron Soleil
Mme. PROUST Anna	Professeur, Sorbonne Université

MEMBRE INVITÉ :

M. BOURNEL Fabrice	Maître de Conférence, Sorbonne Université

Table of Contents

Acknowledgements

First of all, I would like to acknowledge **the readers** that are brave enough to face this manuscript, pay interest into my work and who are ready to face the hard reality of *operando* synchrotron experiments. I thank warmly the reviewers and jury members who took a close look to my work and with whom I had interesting discussions following the defence of my Ph.D.: **Rosa Arrigo**, **Christina Roth**, **Frédéric Maillard**, **Fabrice Bournel**, **Benedikt Lassalle**, and **Anna Proust**.

The three and half years I worked on this project were particularly challenging to me. Apart from the technical difficulties of the Ph.D., I faced events that went in my way and slow down my work. To the Covid−19 that limited the access to the laboratory, to the Russo-Ukrainian war that created an energetic crisis and forced Soleil synchrotron to close just before my beam-time; and to my right arm that decided that falling from my bike was enough to go on strike for few months, two days before a synchrotron run; I am not grateful. However, those bad events can only highlight how my Ph.D. remains a great experience to me, especially thanks to all the support I received from all the persons below mentioned.

I was lucky to be supervised by humanly and scientifically wonderful persons who were always present to answer my questions, and guide me through that scientifical journey. **Elena**, who supervised me directly and followed my work regularly since my M2 internship and encouraged my scientifical stubbornness to work on stuff that interested me, despite they had low chances of success; **Jean-Jacques** who was the first to accept to work with me on this project and who taught me how to manage a synchrotron run; and **Tristan**, who I met first as a synchrotron colleague, then continue hanging out with as a friend, and finally became a very active supervisor for me. To all three of you I am indebted for the efforts and support I received from you during this Ph.D., but also from your advises and support in the few personal trials I faced since we met.

I am also grateful to the close collaborators I worked with. Firstly, regarding the CoPOM project: **Anna,** for our numerous discussion and exchanges around the CoPOMs; **Séverine** who explained me the CoPOM synthesis during the beginnings of my M2 internship on this project, and accepted to provide more of this catalyst for my Ph.D.

Synchrotron runs would not have been as interesting as it was without the numerous help I received from local contact, colleagues, and collaborators. I thank warmly **Fabrice**, **Jean-Jacques**, **Andrey**, **Benedikt,** and **Antoine** for their huge help during the days, and **Iryna** and **Tristan** for their company and the sharing of our brain cells during the long nights. Synchrotron beamtimes are an experience, and thanks to all of you, each run I participated in was a good one.

On the everyday basis, the life in the lab was very pleasant thanks to all my co-Ph.D. students (already graduated for some of them). **Lisa**, **Taylan**, **Alejandra**, **Jules**, **Wafaa**, **Evgeniia**, **Viktoriia**, **Julie, Amandine,** and **Kirill,** exchanging with you around scientific discussions, a cup of coffee, some tarot cards or a chess board was always very pleasant, and I can only hope to find again such a good and friendly team in my professional future. I also thank the other group members who were always there to discuss and advise me scientifically, experimentally, and share their longer experience in the public research: **Alexandr**, **Gwenaëlle**, and **Sergey**.

From a more technical point of view, my scientifical work was greatly helped thanks to the regular help of the laboratory technicians, research engineers and administrators: **Michel**, **Alain**, **Vaso, Thierry**, **Sylviane**, **Julien** and **Kevin**.

I would like to thank all my friends that I met during my scholarship and kept contact with. **My-An**, **Auriane**, **Louis**, **Valentin**, **Cédric**, **Océane**, **Florent**, **Alexis** and **Guillaume**. Your listening hears when I had doubts about the success of my experiments, the Ph.D. life and career opportunities, and the relaxing time we spend together were very precious to me.

Finally I warmly thank my family : **my parents**, **grand-parents,** and my brother **Bastien** who always encouraged my curiosity and interest in science up to the point that it became hard for me to explain them clearly the topics of my work, but always tried to understand my problems to help me to find a direction. I also thank my **parents-in-law** and **Lola,** who always cared about my advances and supported me during this journey. And last but not least, I especially thank **Romane**, for sharing my life, her patience, her constant support in my personal and professional life, and for reminding me every day what really matters.

To all of you, I am deeply grateful, and I hope the following pages are a good reflection of your interest and support.

List of Abbreviations

AEM	Anion Exchange Membrane
AFM	Atomic Force Microscope
AEMWE	Anion Exchange Membrane Water Electrolyzer
CAPEX	Capital Expense
DEMS	Differential Electrochemical Mass Spectroscopy
D&P	Dip and pull
EDL	Electrochemical Double Layer
EELS	Electron Energy Loss Spectroscopy
EXAFS	Extended X-Ray Absorption Fine Structure
FT	Fourier Transform
GC(E)	Glassy Carbon (Electrode)
GCS	Gouy-Chapman-Stern
GDC	Gadolinium Doped Ceria
HER	Hydrogen Evolution Reaction
IHP	Inner Helmholtz Plane
IMFP	Inelastic Mean Free Path
IPE	Ideally Polarizable Electrode
IR	InfraRed
LMCT	Ligand to Metal Charge Transfer
NEXAFS	Near-Edge X-Ray Absorption Fine Structure
NMR	Nuclear Magnetic Resonance
OER	Oxygen Evolution Reaction
OHP	Outer Helmholtz Plane
PEM	Proton Exchange Membrane
PEMFC	Proton Exchange Membrane Fuel Cell
PEMWE	Proton Exchange Membrane Water Electrolyzer
PZC	Point of Zero Charge
PZFC	Point of Zero Free Charge
PZTC	Point of Zero Total Charge
RHE	Real Hydrogen Electrode
SEM	Scanning Electron Microscopy
SERS	Surface Enhanced Raman Spectroscopy
SOEC	Solid Oxide Electrochemical Cell
STM	Scanning Tunnelling Microscopy
TEM	Transmission Electron Microscopy
TERS	Tip Enhanced Raman Spectroscopy
UV-Vis	Ultraviolet-Visible
WOC	Water Oxidation Catalyst
XANES	X-Ray Absorption Near Edge Structure
XAS	X-Ray Absorption Spectroscopy
XMCD	X-ray Magnetic Circular Dichroism
XPS	X-Ray Photoelectron Spectroscopy
XRD	X-Ray Diffraction
YSZ	Yttrium Stabilised Zirconia

List of Figures

List of Equations

List of tables

General introduction

Given that the majority of global energy supply is currently derived from fossil fuels, which are major contributors to greenhouse gas emissions and thus climate change, it is imperative to reduce our dependence on these non-renewable energy sources. However, renewable energies such as solar or wind-power, are intermittent and cannot be used directly for transport applications. Developing efficient ways to store energy is therefore necessary, and hydrogen as an energy carrier provides a durable and convenient way to store and transport energy, as long as it is produced from water electrolysis. Low temperature water electrolysis technologies, notably anion and proton exchange membrane electrolyzers are the most promising from an industrial point of view as they are compact, have a high operational capacity, can work at higher pressures, and avoid efficiently the O_2 and H_2 crossover through the cell.

Anion exchange membrane water electrolyzers in particular are interesting as they avoid the utilization of expensive and scarce Pt-group metals as electrocatalyst, and reduce corrosion inside the cell. However, despite recent advances regarding this technology, the overpotentials for the hydrogen evolution reaction, and more importantly for the oxygen evolution reaction, are still high, which is responsible for a global energy efficiency decrease and a lack of competitivity compared to other non-renewable hydrogen production means. Consequently, it is necessary to develop new catalysts that are inexpensive and active towards the hydrogen evolution reaction (HER) and oxygen evolution reactions (OER).

Though, the lack of understanding of the active states in the anode and cathode catalyst during operation, hinders the comprehension of the relations existing between the catalyst structure and composition towards its activity and durability. In order to bridge this knowledge gap, the use of *operando* spectroscopic techniques has proven to be effective, as they are powerful tools to probe chemical changes occurring at the electrode-electrolyte interface.

In this thesis, we present how X-Ray absorption (XAS) and X-Ray photoelectron spectroscopies (XPS) can be used to provide decisive information regarding different electrochemical systems, while keeping a critical eyesight on the method and the limitations that burden the coupling of the X-Ray spectroscopy with *operando* methods.

In **Chapter 1** we begin with a general presentation of those spectroscopy methods, in order to highlight their fundamental strength and differences. Then, we present literature studies that involved X-Ray absorption or X-Ray photoelectron spectroscopies to understand different electrocatalytic systems, and to what extent they brought valuable information.

In **Chapter 2** we embrace the study of one of the most fundamental phenomena in electrochemistry which is present and influences any electrocatalytic system: the electrochemical double layer. Thanks to technical developments, the electrochemical double layer study under operando conditions with dip and pull (D&P) XPS appears to be possible. Through the study of three different systems, using polycrystalline Pt or glassy carbon electrodes, and CsOH 1 M or NaOH 0.1 M as electrolyte; **we illustrate a method for D&P *operando* studies, and discuss the relevance of this setup for the study of the electrochemical double layer in realistic conditions for the electrocatalysis**.

To explore the potential of X-ray absorption and X-Ray photoemission spectroscopy for the understanding of electrocatalysis of the OER, we present in **Chapter 3 the study of model molecular OER electrocatalyst: complexes of cobalt stabilised polyoxometalates.** Those species offer the strong advantage of presenting a clearly defined and unique chemical environment, which contrast with heterogeneous metal oxide-based OER catalysts which have a variety of different particles sizes, shapes, defects, and metallic−center coordinations. We therefore illustrate how X-Ray absorption and X-Ray photoemission spectroscopies can be used under *operando* and *in-situ* conditions to provide information on an electrochemical system under different oxidative environment.

In **Chapter 4**, we highlight how those spectroscopic methods can be used in a more realistic and industrially relevant system through **the study of core@shell nanoparticles composed of $CoFe_2O_4$@Fe_3O_4**. This stable, active, and still model-like electrocatalyst in terms of nanostructure system, is used as an example to illustrate how the joint use of electrochemistry study and *operando/in situ* characterizations can provide information regarding the relations between the system activity, its structure and the changes occurring under reaction conditions.

Finally, through the **General conclusions and outlook**, we present an overview of the opportunities and challenges of X-Ray absorption and X-Ray photoelectron spectroscopy techniques under *operando* and *in-situ* conditions, as well as the extent of preliminary information and system design one should pay attention to when it comes to the *operando* study of electrocatalytic systems for applications such as the OER.

Chapter 1 State of the Art

Section 1.5 is partially based on a published article in Current Opinion in Electrochemistry:

[2]: **Rotonnelli, B.**, Fernandes, M.-S. D., Bournel, F., Gallet, J.-J., & Lassalle-Kaiser, B. (2023). *In-situ/operando* X-ray absorption and photoelectron spectroscopies applied to water-splitting electrocatalysis. Current Opinion in Electrochemistry, 40, 101314.

1.1 Socio-Economic context

Most of the world energy is produced from fossil fuel (*i.e.* carbon based) sources, such as coal, natural gas and oil which were representing > 80% of the global energy supply in 2020.[3] This energetic mix is nowadays recognised as problematic due to resource depletion over time and CO_2 emissions related to the combustion of such fuels, being the main cause for global warming [4,5].

In order to limit CO_2 emissions related to energy and transport, the use of renewable energy sources such as solar-power or wind-power has long been one of the considered long term solution, but such energy sources are intermittent and not suitable for transport applications. Thus, ways to store and carry energy are therefore required to generalise the use of renewable energy.

Several ways to store energy exists, such as pumped hydro [6] or rechargeable batteries [7], but pumped hydro requires an adapted geological relief, which prevent a generalisation of such storage method and is not being suitable for transport applications, while rechargeable batteries are limited by their storage capacity, short lifetime, huge waste generation and key elements shortage.[8] Hydrogen as an energy carrier therefore appears as a competitive solution for energy storage and transport .

Equation 1.1 : $H_{2(g)} + \frac{1}{2} O_{2(g)} = H_2O_{(l)} + 286\ kJ.mol^{-1}$

Dihydrogen is a light molecule that has a high energy density and is particularly interesting as its oxidation only produces water (**Equation 1.1**). Its use either by direct combustion or in a fuel-cell to produce electricity, is a convenient way to use stored energy, especially for transport applications.[9] Since dihydrogen as a naturally occurring resource (**white** hydrogen) is quite uncommon, one needs to produce it from

molecules rich in hydrogen, such as water (H_2O) or methane (CH_4), defining dihydrogen as an energy carrier rather than a source. The carbon footprint of hydrogen use for transport or energy production will therefore depend essentially on the way it is produced. To differentiate its production method, and therefore the carbon emission related to hydrogen consumption, colours are associated to hydrogen (**Figure 1.1**).[10] **Grey hydrogen** is associated to steam methane reforming. It is the most commonly produced worldwide because of its low price (96% of global H_2 market [11]). However, its production consumes methane and emits carbon dioxide (see **Equation 1.2**), therefore it does not appear as an interesting replacement for fossil fuels. In order to limit CO_2 emissions, **blue hydrogen** [12] is proposed as a mid-term solution. Its production is still based on natural gas and bio sourced methane reforming, but the produced carbon dioxide is captured and stocked in depleted natural gas reservoir instead of being released into the atmosphere. However the long term effects of CO_2 storing underground are not yet known.

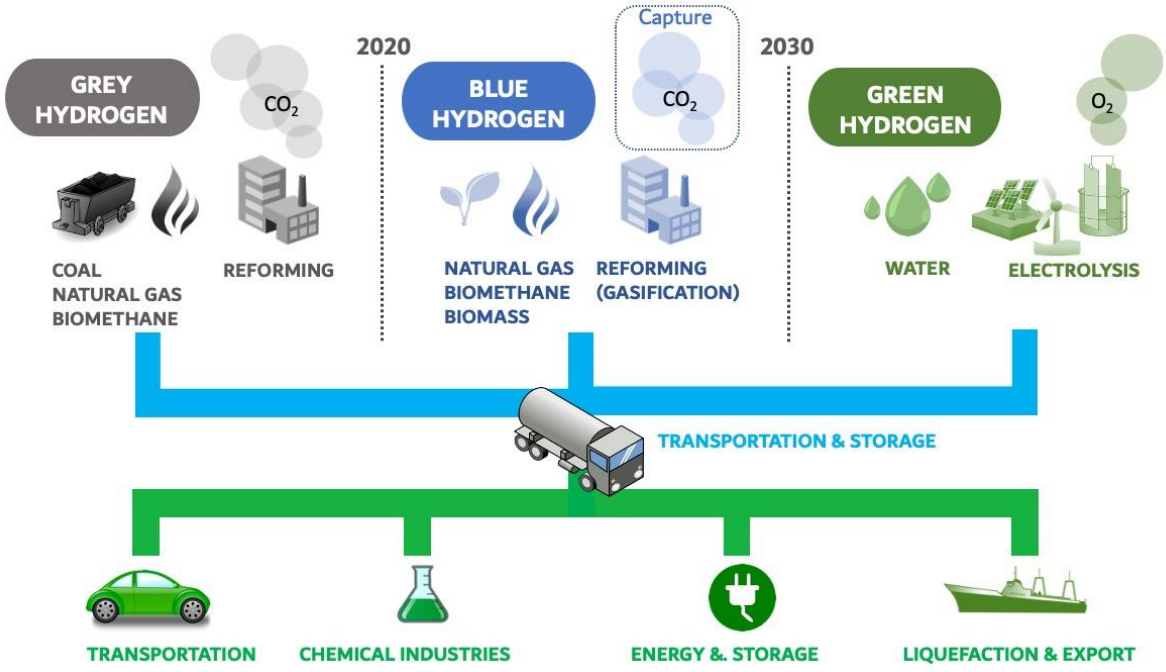

Figure 1.1: Scheme illustrating the different colours associated with hydrogen depending on its production, and different applications. Reproduced from Ref.[13].

Equation 1.2 : $CH_4 + 2H_2O + 165\,kJ.mol^{-1} = CO_2 + 4H_2$

Finally, **green hydrogen** is produced from water electrolysis, preferably using renewable energy sources and therefore does not produce greenhouse gas during its production or consumption. Additionally, water electrolysis presents several

advantages, such as the production of high hydrogen purity, and the use of abundant water sources.[14,15]. Other shades of hydrogen do exist (*e.g.,* yellow, purple, *etc*.) but shall not be discussed in this manuscript.

1.2 Water electrolyzers

At the core of a water electrolyzer, lies an electrochemical cell, that is composed of two electrodes and an electrolyte ensuring the ionic connection between the two. The hydrogen production in this cell is ensured by the water electrolysis, which occurs when a certain potential is applied between the two electrodes in presence of water. Electrolyzers technology can be divided in two groups, *i.e.,* (i) high temperature electrolyzers that use steam, and (ii) low temperature electrolyzers that use liquid water.

1.2.1 Solid Oxide Electrochemical Cells

High temperature water electrolyzers are usually based on Solid Oxide Electrochemical Cells (SOEC), which are composed of 3 main parts (see **Figure 1.2.A).**[16]

- the cathode (or hydrogen electrode) is the electrode in contact with steam and which performs the water reduction to produce hydrogen and O^{2-}, consuming 2 electrons in the process. Cathode state of the art electrocatalysts are ceramic-metal materials based on nickel and supported onto ionic conductive ceramics (Yttrium Stabilised Zirconia: YSZ, or Gadolinium Doped Ceria: GDC);
- the solid ceramic electrolyte, that ensure the O^{2-} ionic conductivity between the two electrodes and that consists as well of YSZ or GDC;
- finally, the anode (or oxygen electrode) performs the O^{2-} oxidation to O_2. Here, the state of the art electrocatalysts are mixed ionic and electronic conductor perovskite such as (La,Sr)(Co,Fe)O_3 and $La_{0.8}Sr_{0.2}MnO_{3-\delta}$ materials.

Those systems, which are operating under high temperature reaction conditions (700~800°C usually), benefit from a decrease of the absolute value of the Gibbs energy of the cell reaction (**Equation 1.1**) with temperature, hence a smaller equilibrium cell voltage and an ensuing decrease of electricity consumption. Coupling this method of hydrogen production with a cheap heat source is therefore interesting from an economic point of view. However, these high temperature conditions are also the main

limit of the system since they greatly accelerate the ageing kinetics of the core components of the system, notably under intermittent operation. Specifically, temperature facilitates chemical changes at the crystals grain boundaries as well as at the mechanical defects propagation (delamination, cracks). Those problems are particularly important at the electrolyte-anode interface, which is why an additional intermediate layer is often introduced there, that ensure a physical separation between the electrolyte and the air electrode, thus avoiding chemical interaction between the two materials.[17]

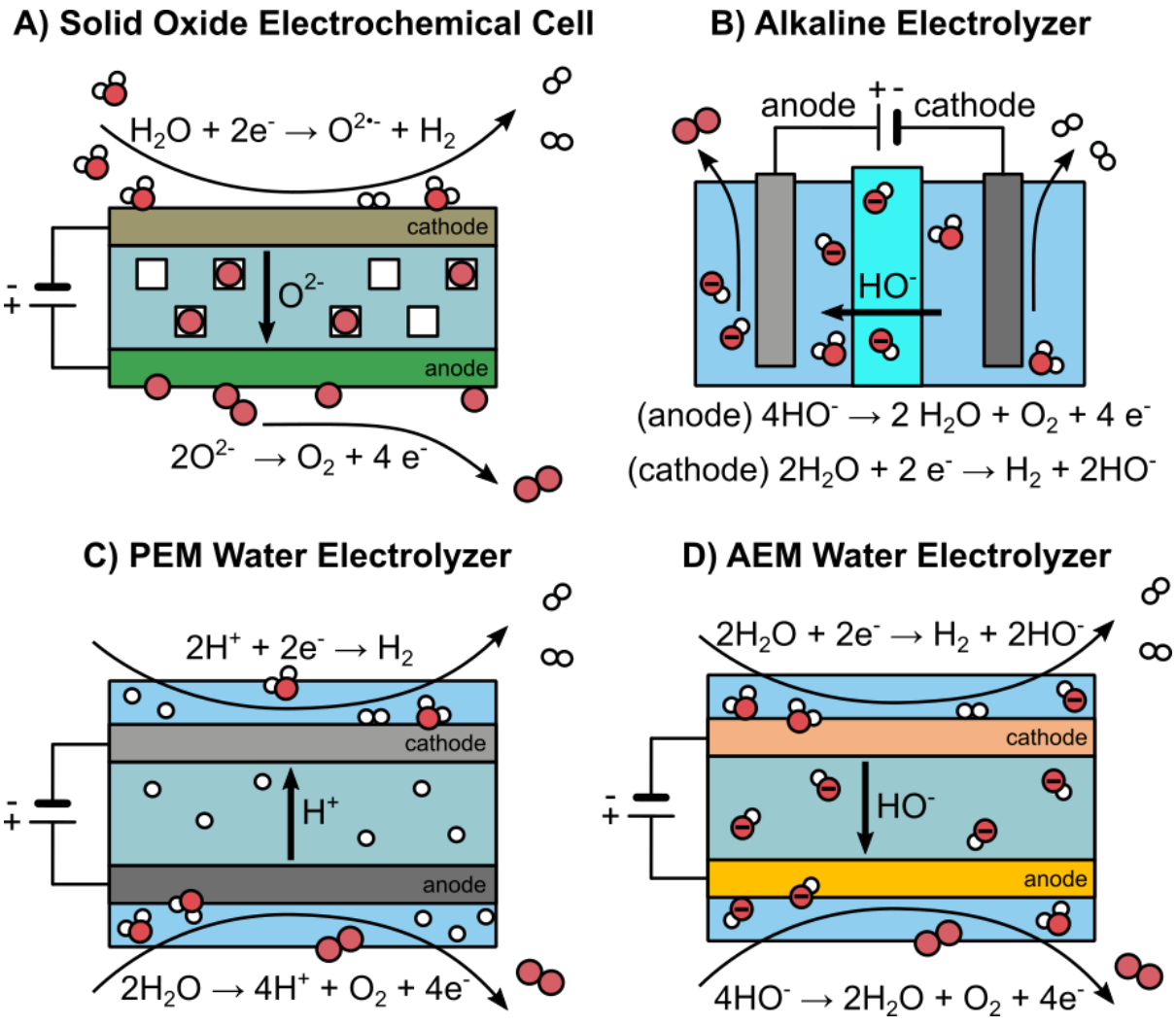

Figure 1.2 : Leading technologies for the water electrolysis: **(A)** solid oxide electrochemical cell, **(B)** alkaline water electrolyzer, **(C)** proton exchange membrane (PEM) and **(D)** anion exchange membrane (AEM) water electrolyzers.

Several technologies exist in terms of low temperatures electrolyzers: Alkaline, Proton Exchange Membrane (PEM) and Anion Exchange Membrane (AEM) water electrolyzers.

1.2.2 Alkaline Water Electrolyzer

The most mature technology is the alkaline electrolyzer, where the cathode and the anode are directly immersed in an alkaline media, separated by an electrolyte permeable membrane also called diaphragm (see **Figure 1.2.B**). The electrodes are usually cobalt and nickel based materials, while the electrolyte is a strongly alkaline aqueous media (*e.g.,* KOH = 20~40 wt.%) due to its high ionic conductivity, and the membrane is based on composite materials (polysulfone matrix and ZrO_2: Zirfon^{TM}).[18] Those cells usually operate in the 60°C-100°C range with a voltage between 1.8 and 2.4 V. Here the hydrogen is produced by reduction of water following the Hydrogen Evolution Reaction (HER, see **Equation 1.3**), while the counter electrode (the anode) oxidize water to form oxygen following the Oxygen Evolution Reaction (OER, see **Equation 1.4**). The separation of both electrodes by the diaphragm allows separation of the produced hydrogen and oxygen.

Equation 1.3 : $2\ H_2O + 2e^- = H_2 + 2HO^-$ $\qquad E° = 0\ V\ vs\ RHE\ at\ 298\ K$

Equation 1.4 : $4\ HO^- = 2H_2O + O_2 + 4\ e^-$ $\qquad E° = 1.229\ V\ vs\ RHE\ at\ 298\ K$

The main advantage of this technology is that it is noble-metal free, as the electrocatalysts can be made out of transition metals [19] rather than noble metals, while remaining competitive from an energetic standpoint. However several technical issues can impact the electrolyzer efficiency and performances, such as (i) the formation of carbonates in the electrolyte if exposed to carbon dioxide; (ii) gas diffusion through the separator which can impact both the efficiency and be a significant safety issue as H_2:O_2 mixture is explosive; and (iii) the corrosion of the catalysts and cell components.[19–21] Furthermore, alkaline electrolysis has a high capital expense (CAPEX, *i.e.* long term capital investments) and cannot deliver as high currents as proton exchange membrane electrolysis as discussed below.

To avoid gas crossover, electrochemical cells based on ion exchange membranes are developed. Two types of electrolyte membranes adapted for water electrolysis exist:

- proton exchange membranes, which rely on H^+ charge carriers and are usually polymers including perfluorosulfonic functions;
- anion exchange membranes, which rely on HO^- charge carriers and are usually polymers including quaternary ammonium or imidazolium groups.

On this type of architecture, the electrodes are directly in contact with the electrolyte membrane, the cells have a higher operational capacity, separate gas more efficiently, and allow better system compacity. These are key advantages from an industrial point of view.[22]

1.2.3 Proton Exchange Membrane Water Electrolyzers

Proton exchange membranes water electrolyzers (PEMWE, see **Figure 1.2.C**) are the most technologically advanced, as the membranes used in these cells are similar to proton exchange membranes fuel cells (PEMFC) and therefore they benefit from the knowledge established for those electrochemical systems. However, the strong acidic conditions lead to a notable corrosion of the metallic parts of the cell. To avoid that, expensive corrosion resistant materials such as titanium are required for the supports and electrolyte circulation plates. Additionally the state of the art electrocatalysts for the cathode and the anode in these systems are Pt and IrO_x respectively, which are both costly, critical materials and lead to an overall expensive system. Another point of notable importance is the membrane ageing, as the operating conditions (pressure up to ~100 bars, T = 60~100°C) are harsh and can lead to premature ageing of the membrane (thinning, metal poisoning) on the timescale of the industrial requirements.[17,23]

1.2.4 Alkaline Exchange Membrane Water Electrolyzers

Anion exchange membranes water electrolyzers (AEMWE) therefore appear to be a system combining both the advantages of the alkaline medium and of the PEMWE structure. Working in alkaline media limits the corrosion on current collectors and other metallic parts of the stack, allowing to work with cheaper components. The HER electrocatalyst (cathode) in those systems is typically based on platinum and platinum group metals due to the sluggish kinetic of the HER in alkaline media. Indeed, the HER activity on Pt is decreased 200-fold when increasing the pH from 1 to 13. However, this activity nevertheless remains far superior to the activity of non-precious metal based electrocatalysts.[24–27] However, the anode can be based on transition metal oxides as those materials appear to be good OER electrocatalysts in alkaline media, while being far cheaper and more abundant than iridium. This reduces drastically the fabrication price of those setups. However, the development of stable anion exchange membranes often appears as the main technological bottleneck for those systems, as

the anion exchange membranes degrades in strong alkaline media due to polymer-chain reaction with hydroxide ions, leading to an overall loss of the mechanical and ionic conduction properties of these membranes.[22,28,29] However, works throughout the past decade led to significant improvements of the membrane chemical stability through innovative molecular design and the addition of protective functionalities onto the hydrophilic section of the polymer.[30,31]

All previously exposed technologies are either commercially available or in development, but it is important to note that the feed water needs to be of high purity, with only the addition of the required salts to modify its pH toward the adequate operating region. Yet, the most suitable areas for renewable energy production (oceanic offshore for wind power, coastal desertic area for solar panels) are also hard to be supplied with water of such quality. Performing water electrolysis using seawater as a feed would therefore become necessary from a logistical point of view in those regions. Sea-water direct electrolysis is an issue due to the presence of many salts that can be oxidized or reduced alongside water (mostly chloride, that can be oxidized, the chlorine evolution reaction competing with OER), as well as the strong local pH modification which occurs at the anode (H^+ production or OH^- consumption) and the cathode (H^+ consumption or OH^- generation). The development of efficient and selective catalysts in (i) neutral media and/or (ii) in presence of chlorine and other salts would then be pivotal.[32,33] Another option (which could be easier to realise) is to combine water desalination unit with water electrolysis (see, *e.g.,* Ref.[34]).

To improve the efficiency and durability of any of the above mentioned systems, improving the OER and HER efficiency at electrodes is critical, as those reactions are directly tied to the energetic efficiency and kinetics of H_2 production in the electrolyzer. To achieve said improvement, the understanding of the properties of the reactive interface during the electrochemical reactions, and how those properties are tied to the reaction mechanism and kinetics is essential: such knowledge would feedback in the development of cheaper and more efficient electrocatalysts and would thus makes green hydrogen financially competitive. This requires a wide array of characterization methods and, to understand the chemical changes occurring during the reaction, the use of non-invasive, sensitive, and system compatible characterization methods is necessary. Spectroscopy methods, based on the interaction between light and matter,

therefore appears to be suitable tools to further understand, and develop, the water electrolysis technology.

1.3 X-Ray spectroscopy techniques

1.3.1 Photon-absorption spectroscopy overview

Light can be described as both an electromagnetic wave and a stream of corpuscular entities named photons. Photons obey the laws of quantum optics which define their energy *E* according to the Max-Plank equation (**Equation 1.5**), as function of the Plank constant (h) and the frequency of the associated electromagnetic wave (v).

Equation 1.5 : $E = hv$ $\quad\quad$ $h = 6.626 \times 10^{-34}\ \mathrm{J.s}$

As photons have a constant speed (c) in vacuum, their frequency and wavelength (λ) are related by the **Equation 1.6**, which is therefore inversely proportional to the photon energy.

Equation 1.6 : $v = c/\lambda$ $\quad\quad$ $c\ = \ 2.998 \times 108\ m/s$

Photons can interact with matter through two main phenomena, namely scattering (inelastic or elastic) and absorption. When a photon interacts with a molecule, an atom, or a crystal, taken in the ground state it provokes an energetic transition from this ground state ($S_{0,0}$ on **Figure 1.3.B**) to an excited state ($S_{n,m}$ with [n,m]≠[0,0]). The nature and the probability of this transition, *i.e.,* the intensity, depends both on the chemical nature of the absorbing entity and the photon energy. Spectroscopy is then defined as the science that correlates spectra resulting from photon-matter interaction to the absorbing sample nature. In **Figure 1.3.A** the different types of energy transitions induced by the absorption of electromagnetic radiation are represented according to their energy range. Since a wide energy range of electromagnetic radiations is used in spectroscopy, it is appropriate to adapt the energy unit to the technique considered.[35,36] The following subsections focus on a non-exhaustive list of commonly used spectroscopy techniques that result from the direct absorption of a photon and which information they can provide. **Finally X-Ray based spectroscopy techniques are introduced and furtherly developed.**

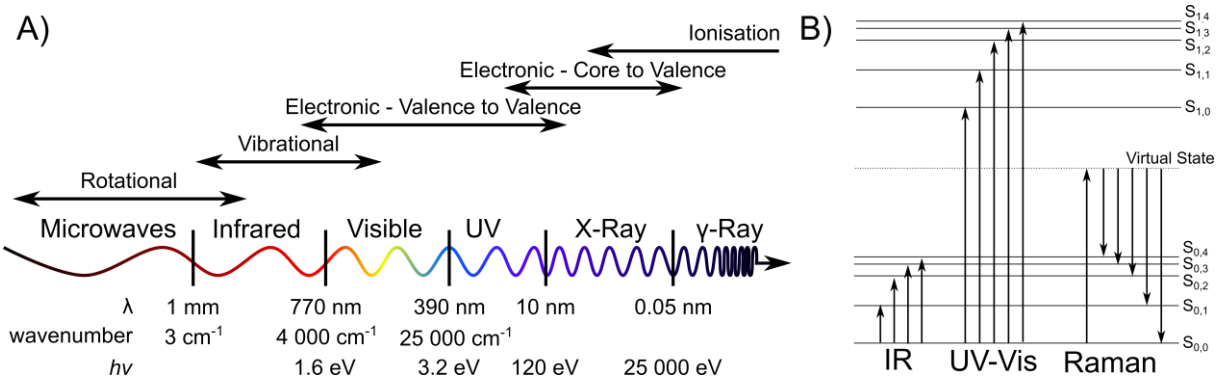

Figure 1.3: **(A)** names associated to the light depending on the photon energy and which type of energy transition can be triggered once absorbed by an atom, molecule or crystal. **(B)** Schematic representation of the first transitions observed in the different spectroscopies in the infrared-UV domain. Each state is given a name S(n,m), n representing the electronic states, m, the vibrational states of a molecule, 0 being the number associated to a fundamental level.

Infrared spectroscopy

Infrared (IR) light goes from 10 cm^{-1} (λ =1 mm) to 12 500 cm^{-1} (λ = 770 nm), the most commonly used unit in that range is the wavenumber [cm^{-1}] defined as the inverse of the wavelength. Infrared light induces low energetic transition corresponding to vibrational and rotational transitions in a molecule. This spectroscopy is particularly useful when it comes to the characterization of molecules, especially in organic chemistry. In the electrocatalysis field, it allows to characterize reactants, the reactive intermediates, and the products in their different geometry as well as their interaction with heterogeneous catalysts (*e.g.,* specific adsorption). It is important to note that the active vibration modes are those which induce a variation of the dipolar momentum.[37]

Inelastic scattering and Raman spectroscopy

Scattering interaction between photon and matter can also be exploited for sample characterization. Scattering effects are a one step process which can be described as the absorption of a photon which energy does not match the energy difference between the ground state and an excited state (see **Figure 1.3.B**), the species therefore reaches a *virtual excited state* that de-excites back to a lower energy state and reemits a photon. In most of the case, the final state is the same as the initial one, the emitted photon has the same energy as the incident one and the scattering is said elastic (Rayleigh scattering). But in a low probability (1 for 10^8 transitions), the final state is different than the initial one and reaches a lower (anti-Stokes transitions) or a higher

energetic state (Stokes transitions). The emitted photon has therefore an energy different than the initial one, and this difference is equal to the energy transition between the initial and final energy state (inelastic scattering or Raman scattering). Raman spectroscopy aims to use that inelastic scattering effect to probe the vibrational transition in a molecule or a crystal. It uses a laser of UV-Vis or near-IR energy range (*e.g.,* Nd:YAG laser for instance with 1064 nm wavelength), and record the spectra of the scattered light. The energetic states probed are vibrational ones, which is quite similar to IR spectroscopy and particularly useful for carbonaceous materials. The active modes in Raman are those which are sensitive to a change in the polarizability of the molecule induced by the electromagnetic field of the incident light. This spectroscopy is particularly well-adapted for graphene and graphene like material characterization (which cannot be studied by IR). However, the low probability that a photon triggers Raman scattering is the main limit of the technique, as the laser energy flux necessary to record a signal must be intense and thus can degrade the sample. One can note that several approaches exist to enhance Raman phenomena and rely on the plasmonic effects of metallic surfaces and nanoparticles (surface enhanced Raman spectroscopy SERS, tips enhanced Raman spectroscopy TERS) which can improve Raman signal intensity up to a 10^6 factor and provide a surface sensitivity to the technique, which show interesting applications for electrocatalysis studies.[36,38,39]

Ultra-violet - visible spectroscopy

Visible and ultra-violet (770 nm to 390 nm, and 390 nm to 10 nm respectively) light induces electronic transitions of low energies. The study of a sample absorption in that energy range refers to UV-Vis spectroscopy and is one of the most accessible spectroscopy methods due to the low prices of the equipment needed and its versatility. Even though this method lacks the chemical environment and structural sensitivity offered by other spectroscopy techniques, one is able to assess information regarding specific electronic transition such as the ligand to metal charge transfer (LMCT) in complexes or oxides that can provide basic electronic and structural information. Finally, during electrochemical reactions, as the reaction triggers electron transfer, the occupation of valence orbitals is modified, which can be observed by the change of UV-Vis fingerprint in the reactive molecule spectra.[40] Another interesting application of the UV-vis spectroscopy in electrocatalysis is the study of the properties

of the reactive interface using fluorescent molecular probes, which are sensitive to the environment conditions such as the local pH.[41]

X-Ray spectroscopy

X-Ray beam includes photons in the wavelength interval from 10 to 0.01 nm (energy from ~100 eV to 25 keV). Their energies are the typical energies of core orbitals in atoms, and their wavelength on the same order of magnitude as atomic distances in crystals. *The elastic scattering of X-Rays by atoms in an organised crystalline structure therefore results in the formation of a pattern which provide information regarding the atoms organisation, namely X-Ray Diffraction (XRD). This method is commonly used as a bulk characterization method for materials. Despite its usefulness in electrocatalysis in-situ and operando studies,*[42] *we will here restrain our discussion on X-Ray absorption techniques as they provide more information on the chemistry of the studied sample and are the core method of this manuscript.*

The absorption of X-Ray photon results either in the electron transition from the core to an unoccupied valence orbital or the ionisation of the atom or molecule. The energy levels of the core orbitals are predominantly determined by the atomic nuclear charge, and, to a lesser extent, by the chemical environment and oxidation state. Thus, the study of transitions involving those orbitals give an elemental information on the studied sample, as well as an information on the oxidation degree and the chemical environment of the probed element. These specificities give X-ray based spectroscopy the tools for the deconvolution and the analysis of complex environments such as the electrode-electrolyte interface. Depending on the X-ray energy, the core levels of different elements are probed. One generally distinguishes three ranges of X-rays: (i) soft X-rays (~100 eV to ~1500eV), (ii) tender X-rays (1500 eV to 5 keV) and (iii) hard X-rays (5 keV to 25 keV).

Two main families of methods relying on X-Ray absorption can be distinguished: (i) X-ray-absorption spectroscopy (XAS, **Figure 1.4.A**), based on the X-ray absorption as a function of the photon energy, and (ii) X-ray photoelectron spectroscopy (XPS, **Figure 1.4.B**), which record the photoelectron energy and flux resulting from a sample ionisation exposed to a monochromatic X-ray beam.

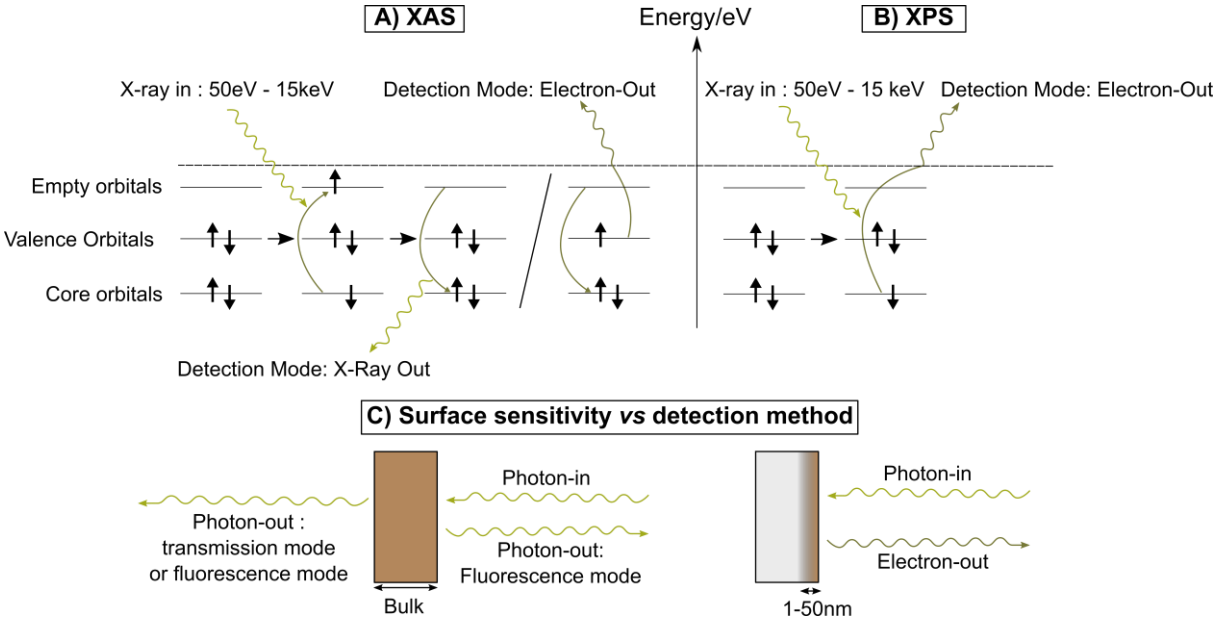

Figure 1.4: principle of **(A)** X-Ray Absorption and **(B)** X-Ray Photoelectron spectroscopies techniques (XAS and XPS respectively) followed by a schematical representation of the detection method on the analysis depth. Reproduced from Ref.[2].

1.3.2 XPS principle

XPS is based on the photoelectric effect that was first explained by Einstein in 1905 using the quantum mechanics. When an atom absorbs a photon which has a greater energy than a core electron, the energy can be transmitted to the electron which has enough energy to be ejected from the atom. The emitted electron is referred as photoelectron and, due to the energy conservation law, its kinetic energy KE is related to the absorbed photon energy ($h\nu$), the promoted electron binding energy (BE, *i.e.,* the orbital stabilisation energy, generally refers to the Fermi level), and the work function ϕ, which represents the electrical potential difference between the sample fermi level and the vacuum level, following **Equation 1.7** (see **Figure 1.5.A**).

Equation 1.7 : $h\nu = BE + KE + \phi$

Photoelectrons have a strong interaction with atoms, and one can define the inelastic mean free path (IMFP) of electrons as the average distance a photoelectron can travel before undergoing an inelastic scattering interaction with another atom in a given media. This characteristic length depends on the atomic characteristics (electron density mostly) of the travelled media, and on the kinetic energy of the considered photoelectron. A typical dependence of the photoelectron IMFP, noted λ_{IMFP} in gold is

given on **Figure 1.5.B**. The typical length of the IMFP is between 0.5 nm and 10 nm and the minimum IMFP length is observed for photoelectrons around 50 eV. This limited distance that photoelectrons can travel through a non-vacuum media has two main influences on XPS measurements: (i) the sample characterization is easier in vacuum as the photoelectron intensity would quickly decay due to inelastic scattering under atmosphere; (ii) it defines XPS as a surface sensitive technique. The signal intensity coming from a layer distant of *x* from the sample surface can be determined thanks to **Equation 1.8** (where I is the photoelectron intensity coming out of the sample, and I_0 is the photoelectron intensity emitted by the considered layer), which means 63% of the XPS signal comes from a distance inferior to λ_{IMFP} depth, and 95% from a depth less than three times the λ_{IMFP}. In addition, as the photoelectron IMFP depends on the kinetic energy, one can tune the depth sensitivity of the technique by changing the energy of the incident X-Ray beam, which is possible on a synchrotron source.

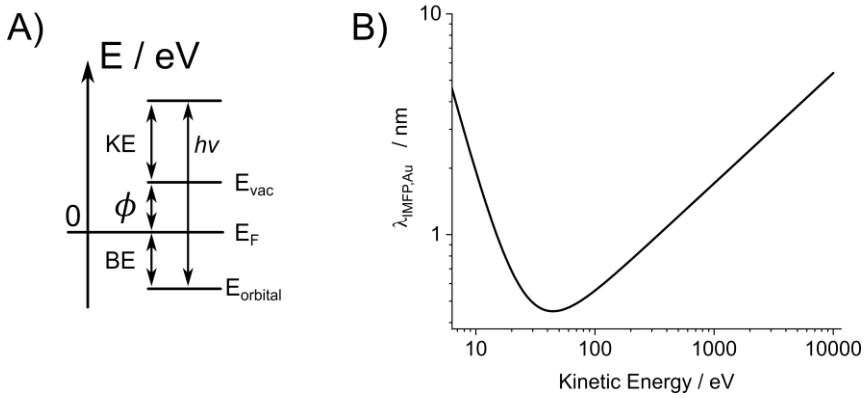

Figure 1.5: **(A)** scheme of the energetic relation in the photoelectric effect, where the absorbed photon energy is $h\nu$, the kinetic energy of the photoelectron is KE, the work function (*i.e.,* the electrical potential difference between the sample Fermi level EF and the vacuum electrical potential Evac) is ϕ, and the binding energy of the electron is BE. **(B)** Simulation of the photoelectron inelastic mean free path (λ_{IMFP}) depending on its kinetic energy in gold, according to equation (5) from Seah *et al.* [43].

Equation 1.8 : $I = \mathrm{I}_0 \times e^{-\left(\frac{x}{\lambda_{IMFP}}\right)}$

Finally, assuming a homogeneous and flat sample, the photoelectron intensity emission of an atom i can be evaluated thanks to **Equation 1.9**, where J is the X-ray flux that strikes the sample surface, c_i is the atomic ratio of photoelectron emitting

atom/ion within the sample volume probed, K_f is a factor that encapsulates instrument characteristics, and α_i is the atom cross section.[44]

Equation 1.9 : $I_i = J \times c_i \times \alpha_i \times K_f \times \lambda_{IMFP,i}$

Consideration of the definition of the atomic ratio and **Equation 1.9,** we can define **Equation 1.10**, that allows the quantification of the i element atomic fraction compared to the other photoelectrons emitting elements in the sample.

Equation 1.10 : $c_i = \frac{I_i}{\alpha_i \times \lambda_{IMFP,i}} / \Sigma_j (\frac{I_j}{\alpha_j \times \lambda_{IMFP,j}})$

XPS is therefore a powerful quantitative technique with errors from 30% down to <5%. Inaccuracies sources can be multiple, such as sample inhomogeneities, sample thickness lower than analysis depth ($3 \times \lambda_{IMFP}$) and inappropriate background fitting procedure. The fitting procedure to quantify the different contributions in XPS peaks is therefore essential to the quantification and sample analysis process. From the experimental raw data obtained (**Figure 1.6.A**) one must first define a proper background (**Figure 1.6.B**), and then define a set of peak-functions that will be used to fit the signal (**Figure 1.6.C**). Several functions exist to fit the background shape (linear, Shirley, Touggard, *etc*.), and the chosen function usually depends on the background shape. Regarding the sample XPS signal, one type of chemical environment/oxidation degree results in one peak, whose area is the actual total photoelectron intensity associated to the emitting specie in the given environment/oxidation degree (*I* in **Equation 1.9** and **10**).[43]

The most appropriate function to reproduce a XPS peak is a Voigt function, *i.e.* a convolution of a Gaussian and Lorentzian functions. The Lorentzian shape accounts for the broadening of the electron core-hole life while the Gaussian contribution accounts for the experimental dispersion due to the analysed material and instrumental broadening.[45] To propose a coherent fitting model, one should therefore (i) have a preconstructed idea of the sample composition and (ii) obtain reference spectra from literature, databases or experimental assessment of standard, well defined samples, to design a correct peak shape for each contribution and (iii) impose a maximum of physically meaningful constraints to the fitting model such as: the area ratio between two spin-orbit splitted orbitals (*e.g.,* $2p_{3/2}$ and $2p_{1/2}$ orbitals should have a 3/2 area ratio, induced by the orbitals degeneracy ratios), similar peak shapes between two

components of the same element in the same phase (mathematical function and full width half maximum of the peak) and relative peak positions. Finally, some transitions are impacted by inelastic phenomena (peak energy loss) that may combine electronic transition inside the emitting atom and the photoelectron transition leading to a *shake-up* or *shake-off* satellite signal, which should be taken into account for a proper fitting procedure.[46–48]

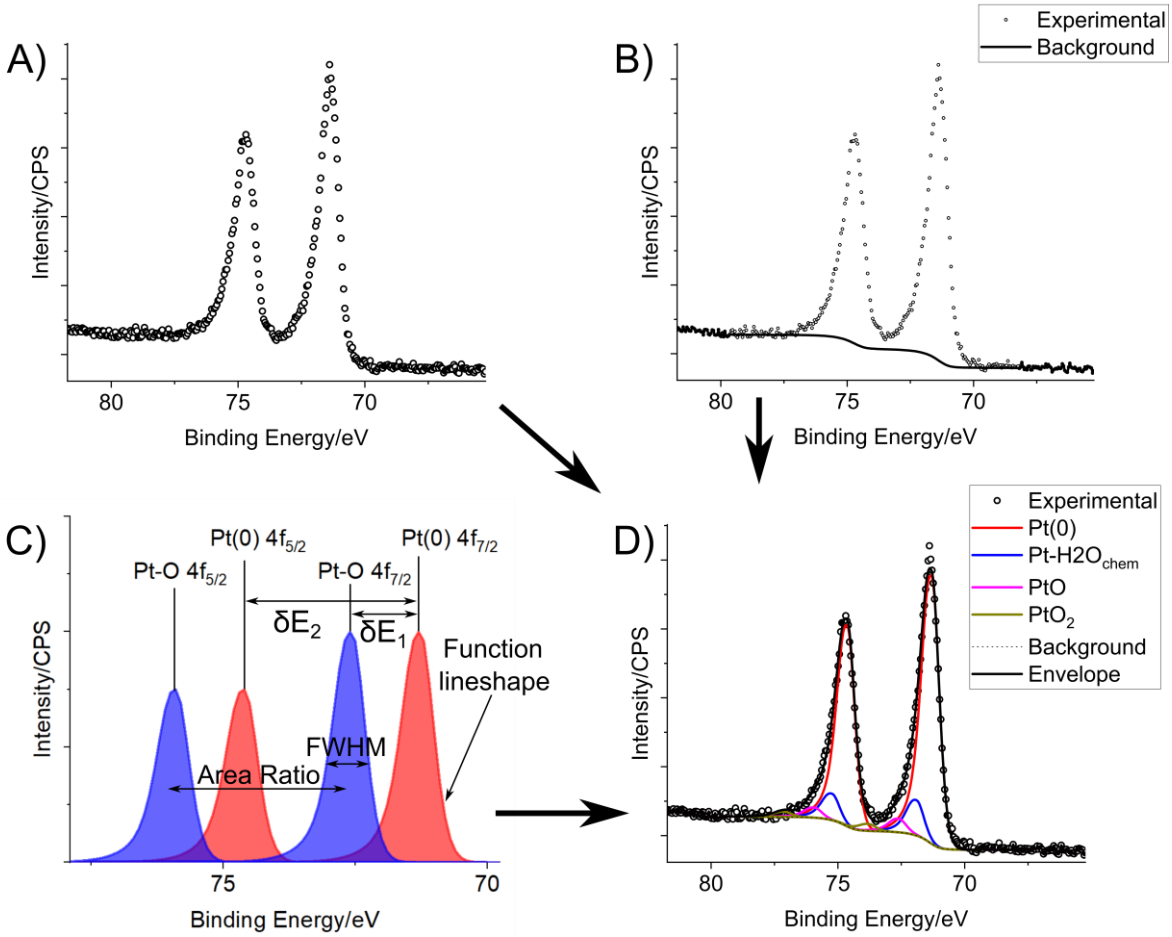

Figure 1.6: (A) Experimental Pt foil XPS spectrum; **(B)** typical background determination on XPS spectra. Different type of background function can be used, the Shirley function is shown here; **(C)** functions used to fit the XPS peak. As XPS is chemical environment and oxidation degree sensitive, the same element at two different oxidation degrees will emit an XPS peak at a different position. The peak function, full width half maximum (FWHM) and positions are the main parameters to control during the fitting process. Hence, correlations between these peaks parameters should be controlled for a good fitting; **(D)** XPS fitting result highlighting the different components and the main contributions in the peak.

In a nutshell, XPS technique is an excellent method for surface materials studies, especially when it comes to the study of electrochemical interfaces, as it presents

several advantages compared to other photon-detection technique, because it is (i) an elemental and chemical environment sensitive method, (ii) not limited by the electronic transitions rules, (iii) sensitive to the sample surface (5~50 nm depth) and (iv) which does not necessarily require a tuneable X-Ray sources.[49]

1.3.3 XAS principle

X-Ray Absorption Spectroscopy (XAS), also named X-Ray Absorption Fine Structure (XAFS) was firstly observed in 1913, and theoretically explained in 1970's [50], much later than XPS. The first reason behind this delay is the instrumental limitations. XAS requires a continuous variation of X-Ray source to determine the photon absorbance depending on its energy. This technique development therefore came along the development of synchrotrons that allows the continuous scanning of X-Ray energy.[51,52]

Equation 1.11 : $\mu(E) = \frac{I}{I_0}$

Similar to optical microscopy, X-ray absorption spectroscopy relies on the absorbance of X-Ray photons ($\mu(E)$) by **Equation 1.11,** where I_0 is the incident beam intensity, and I is the transmitted beam intensity. Generally $\mu(E)$ decreases as the energy increases (approximately $\propto 1/E^3$) but whenever a specific energy (characteristic of atoms constituting the sample) is reached, a sudden increase of the absorption is observed. This absorption increase is called an edge, and correspond to an electronic transition from a core level energy to an unoccupied valence orbital (**Figure 1.4.A**). XAS transitions satisfies the Laporte selection rules (Δl = ±1 for dipole selection rule, Δl = ±2 for quadrupole selection rule, where Δl is the difference in the quantum magnetic number between the final and initial orbitals). Depending on the energetic level of the promoted core-electron involved in the transition, a specific name is given to the transition (K, L_n, *etc*. see **Figure 1.7.B**). Regarding the K-edge, two main regions can be observed (**Figure 1.7.A**). The first region is associated to 1s → unoccupied valence state transitions and is named X-Ray Absorption Near-Edge Structure (XANES, also referred to Near Edge X-Ray Absorption Fine Structure, NEXAFS). The edge position and XANES shapes gives important information regarding the element oxidation degree (oxidation results in the edge shifting towards higher energies), and the specific shape can be used to identify a specie using its 'fingerprint'. First row transition metals XANES K-edge includes a lower energy transition named 'pre-edge'

associated to the 1s → 3d transition, and is a quadrupole authorised transition, which can provide information regarding the local site symmetry.[53] A quadrupole transition, however, is 'less authorised' than a dipole transition. Hence, the absorption intensity is lower.

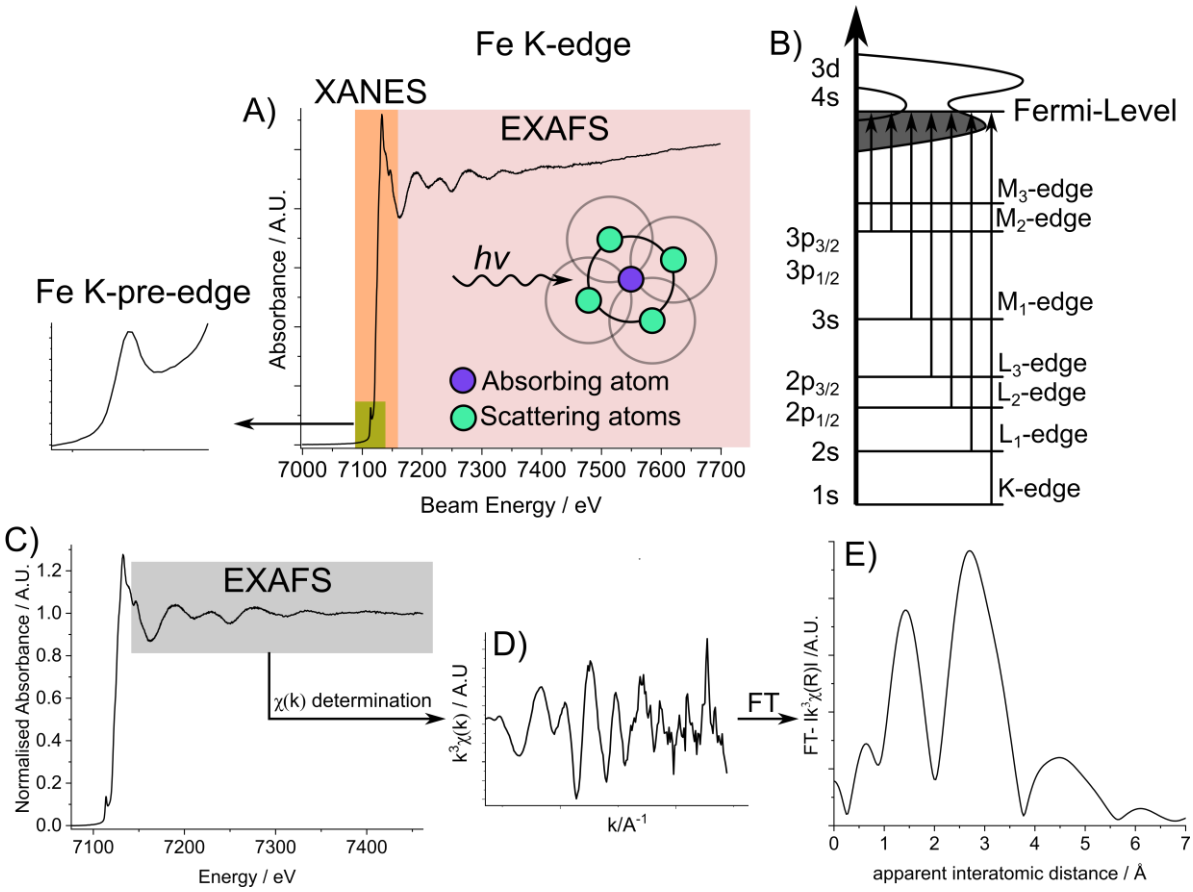

Figure 1.7: **(A)** non-normalised $CoFe_2O_4$ Fe K-edge spectra, with the different X-Ray Absorption Near Edge Structure (NEXAFS/XANES) and Extended X-Ray Absorption Fine Structure (EXAFS) regions highlighted. **(B)** edge transitions studied in X-Ray Absorption Spectroscopy (XAS), associated to the initial atomic orbital. **(C)** Normalised XAS signal associated to the different steps of EXAFS processing: **(D)** determination of the scattering factor 'χ' from neighbouring atoms, and **(E)** its Fourier-Transform (FT) to determine the neighbouring atoms positions and provide a detailed information of the absorbing atom chemical environment.

The first part of the XAS spectrum concerns electronic transitions and produces intense peaks called resonances or white lines, the second part presents oscillations which attenuate with increasing energy. This area corresponds to the Extended X-Ray Absorption Fine Structure (EXAFS). These oscillations result from quantum interferences of the elastically scattered photoelectrons by the neighbouring atoms,

and are quantified experimentally using the 'scattering factor' χ defined by **Equation 1.12**. This modification in the X-Ray absorption coefficient can be quantified theoretically using **Equation 1.13**.

Equation 1.12 : $\chi = \frac{\mu_{exp} - \mu_{bkg}}{\Delta\mu_{exp}}$

Equation 1.13 : $\chi(k) = -\sum_j \frac{N_j * F_j}{kR_j^2} \times e^{-\frac{2R_j}{\lambda_e(k)}} \times e^{-2k^2\sigma_j^2} \times \sin(2kR_j + 2\delta_1(k))$

Equation 1.14 : $k = \sqrt{2m(E - E_0)h^2}$

In this equation: N_j is the number of neighbouring scattering atoms, R_j is the distance between the scattering and the emitting atom. F_j describes the scattering properties of the neighbouring atoms j, k is photoelectron wavenumber and is defined by **Equation 1.14**, the $exp(-2R_j/\lambda_e(k)$ term is a damping factor that originates form the loss of coherence in the backscattered signal due to multielectron excitations ($\lambda_e(k)$ is the inelastic mean free path of the emitted photoelectron); $exp(-2k^2k^2\,\sigma_j^2)$ is another damping factor associated to the variation of position of the j[th] atoms (σ_j^2 is the mean square variation of the R_j atom); $\sin(2kR_j + 2\delta_1(k))$ term highlights the fact that χ is actually a sum of sinusoids which frequency depends on R_j ($\delta_1(k)$ is a phase shift term). A proper determination of χ (**Figure 1.7.D**) followed by the Fourier-Transform (FT) of the obtained spectra in the k space (**Figure 1.7.E**) therefore provides precise information of the absorbing atom chemical environment.

Several techniques can be used to measure the sample's absorption coefficient ($\mu(E)$). First, one can detect the X-ray absorption through *photon-out* techniques: the direct measurement of transmitted X-rays through the sample, or the fluorescence signal, that is produced from the de-excitation of a high energy level electron to the core-hole created by the X-ray absorption (**Figure 1.4.A** and **C**). It can also be detected using *electron-out* technique, which detects electron emitted by the X-Ray absorption, mainly originating from deexcitation. To be more selective we can detect the Auger-electron line from a particular atom. Similarly to XPS, due to limited electron IMFP in condensed matter, the electron-out method is surface sensitive, while photon-out method is rather bulk sensitive (this varies with X-Ray energy and sample's absorption coefficient) and can easily be used in gas or liquid media. This means that the technique surface sensitivity can be tuned with the detection method. XAS therefore appears to be

complementary technique to XPS, as it can be bulk-sensitive and shows more versatility to the pressure conditions in *photon-out* detection mode. Additionally, this technique can provide precise information on the chemical environment of the absorbing atom thanks to FT-EXAFS and on its oxidation degree using XANES edge shift, while, through XPS, an easy deconvolution and quantification of different elements that are found on the surface of a material and their chemistry can be achieved.[54]

1.4 Spectro-electrochemical operando setup development

The progress and the final state of chemical reactions strongly depend on the conditions in which they are carried out. It is therefore necessary to specify these experimental conditions and the way in which the measurements were taken in order to avoid misinterpretations. We propose underneath definitions of *ex-situ*, *in-situ* and *operando* conditions that we will stick to through this manuscript. *However, one should keep in mind that they may differ depending on the scientific field*. *Ex-situ* analysis relates to sample characterizations that are performed outside the reaction conditions, *in-situ* analysis is performed in conditions that mimic the system reaction conditions but without the reaction happening, while *operando* conditions aim to characterize the system while the reaction is happening, and finally *post-mortem analysis* refers to a system characterization, often *ex-situ*, after the reaction.[55]

While *post-mortem* analysis is easier to carry on, and can provide information regarding the system ageing and irreversible changes during the reaction, the understanding of the reactional mechanism requires *operando* characterization which can provide information on the reaction intermediates and the involved active species. XAS and XPS in particular are presented as the 'workhorses' of characterization techniques to follow electrocatalysis reactions as (i) they are sensitive to changes of the oxidation degree induced by the electron transfer in redox reactions, (ii) they are sensitive to changes in the chemical environment around metallic catalytic centres, and (iii) they can be surface sensitive techniques. However, adapting an electrochemical system to an X-ray based spectroscopic instrument, hence developing a so-called spectro-electrochemical cell, is a technically challenging issue.[56]

While *in-situ* and *operando* studies in heterogeneous electrocatalysis are performed for decades in the hard X-Ray spectroscopy region using XAS as a *photon-out*

technique,[57–59] the XPS, which is an *electron-out* technique, is limited to measurements in vacuum and low-pressure atmosphere due to strong interaction of photoelectron with the environment. The low electron mean free path is an issue for analysis in the electrocatalytic conditions which requires a liquid phase in the low temperature range (*e.g.* for applications in PEMWE, AEMWE, *etc*.). However, thanks to technical advances in the electron analysers and the use of intense synchrotrons sources, Ambient (or Near-Ambient) Pressure XPS (APXPS or NAP-XPS) has been developed in the 2000's. [60,61] To improve the photoelectron counting rate, it is nevertheless preferable to work at the lowest pressure possible. That is why the first XPS spectro-electrochemical cells developed separated as much as possible the electrolyte from the atmosphere, to avoid evaporation and an increasing pressure in the analysis chamber. **Several examples of such cell designs are discussed in the following paragraph.**

Figure 1.8.A shows a typical electrochemical-cell design for XANES measurement in fluorescence mode where the cell is separated from the atmosphere with an SiN_x window which X-rays pass through easily. In the design presented on **Figure 1.8.B** and **C** dedicated to XPS measurement, the liquid electrolyte phase is separated from the vacuum by (i) the working electrode and (ii) a series of solid layers acting as current collector (graphene), sometimes reinforced mechanically by holey SiN_x separator and/or ion exchange membrane.[62] These architectures limit the liquid phase evaporation while being transparent to electrons. However, as XPS is surface sensitive and as the electrochemical reaction occurs at the electrode-electrolyte interface, these setups are restricted to free-standing graphene working electrodes supporting low active materials loading [63–65] and porous working electrodes.[66–69] In case of low loading materials deposited on graphene, the combination of a low loading and supporting holey SiN_x in front of the sample diminish drastically the signal, while graphene layer is reported to be sensible to electrochemical oxidation and to radicals created by beam-induced water radiolysis.[70] On the other hand, porous working electrodes prepared from direct sputtering of NP suspension [71,72] or nanostructured materials [73] onto ion-exchange membrane (suitable for ion exchange membrane cells) allows electrolyte diffusion through the working electrode up to the analysed surface exhibit an increased signal compared to the first architecture, owing to a larger quantity of analyzed samples. Though, this last architecture is limited by ionic diffusion

through the WE (unless ion-conducting polymer, an ionomer, is mixed with catalytic particles), drying issues at the working electrode external surface (*i.e.* analysed part of the system), and ion-exchange membrane/ionomer beam damage sensitivity, *which altogether might lead to a difference between the electrochemical properties of the membrane/WE interface and the electrochemical properties of the analyzed region (i.e., far away from the membrane), thus leading to a loss of relevance of the obtained results.*

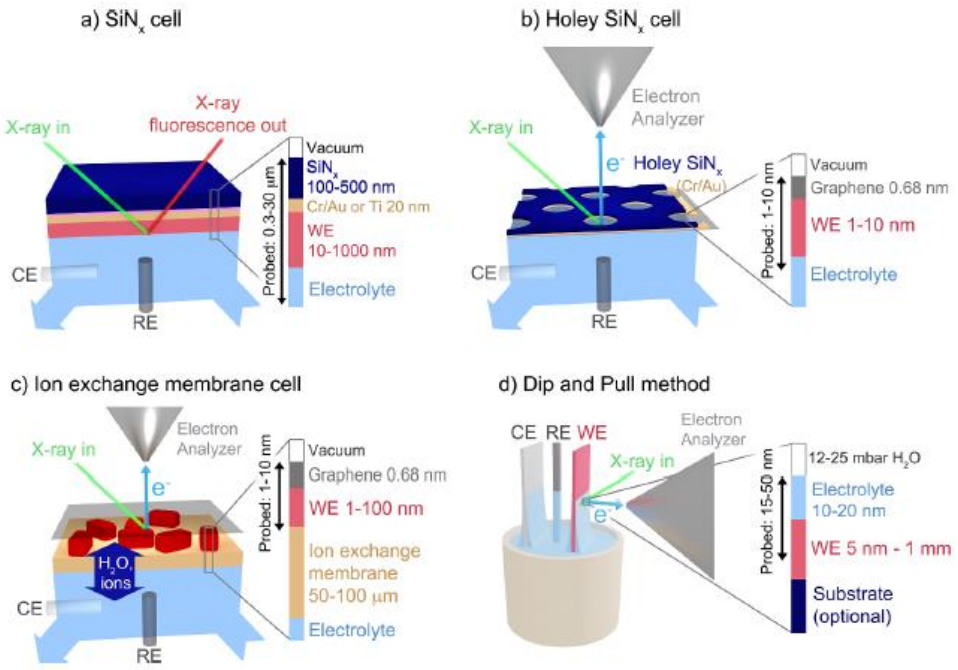

Figure 1.8: Different types of spectro-electrochemical cells used for operando XPS; **(A)** SiN_x flow cell for fluorescence yield X-Ray Absorption spectroscopy (XAS); **(B)** Holey SiN_x flow cell for X-ray Photoelectron Spectroscopy (XPS) and electron yield XAS. **(C)** Ion exchange membrane flow cell for XPS and electron yield XAS. **(D)** 'Dip and pull' setup for XPS and electron yield XAS. CE: Counter Electrode, RE: Reference Electrode, WE: Working Electrode. Reproduced from Ref.[62].

The development of end-stations working in the tender X-Ray range, and able to support pressures up to 150 mbar (above the water saturating vapor pressure at 25°C, ~30 mbar) recently allowed the development of the remarkable 'dip and pull' (D&P) spectro-electrochemical cell,[74] which allows water liquid electrolyte presence in the analysis chamber. The setup can be seen on **Figure 1.8.D** and is rather close to a conventional three electrode cell: working, counter and reference electrodes are all

three immersed in a liquid electrolyte reservoir (aqueous or organic) vertically, allowing the analysis of a model 2D electrode-electrolyte interface.

The development of such spectro-electrochemical cells that can closely mimic the reaction conditions performed in laboratory or in industrial systems is essential for the understanding of the electrocatalyst/electrolyte during the reactions and electrocatalysis mechanisms, and is illustrated in the following subsection.

1.5 XP and XA spectroscopic techniques for studies of the OER electrocatalysis

As discussed in **Section 1.2**, high efficiency of electrocatalysts for the OER and HER half-reactions is fundamental to the hydrogen implementation as an energy carrier. OER requires further attention as it is a sluggish and complex reaction that involves transfer of 4 electrons (**Equation 1.4**). The understanding of how an electrocatalytic surface or system behaves in the OER operating conditions, and how this behaviour impacts its activity and durability is therefore an important step to cross in the view to develop stable and efficient electrocatalyst.

Various classes of electrocatalysts have been investigated as anode materials for water electrolysis,[75,76] their choice being largely determined by the type of electrolyte used (acidic,[77,78] alkaline [79–82] or seawater [83]). **The objective of this section is to provide some examples of successful *operando* XPS and XAS investigations to illustrate types of spectro-electrochemical cells used, and kind of information, which can be extracted from such measurements.**

Under acidic conditions, metal oxides such as IrO_x and RuO_x are the most active catalysts for this reaction, due to their near-optimal energy for the M-O bond according to thermochemical theory and their high electronic conductivity. However, Ru oxides are prone to fast degradation, which Saveleva *et al.* [68] attributed to the transformation, under the reaction conditions, of RuO_2 with rutile structure into unstable ruthenium hydroxide and volatile forms of Ru with a high oxidation state. In the meantime, Ir catalysts (notably crystalline IrO_2 with rutile structure) are much more stable than Ru-based. As a consequence, and despite its very high price and small abundance, IrO_x is the reference (and commercially used) catalyst for OER in acidic media, showing low overpotential (from +0.2 V to +0.4 V corresponding to potentials of 1.4 V to 1.6 V *vs.* the Reverible Hydrogen Electrode, RHE) and hence a high activity. Several theories still coexist to explain the mechanism of OER on IrO_x, which are well

explained elsewhere.[84] The questions that currently remain to be solved revolve around the redox active site, which can either be the metal cation or the oxygen anion, and the role of lattice oxygen in the catalytic cycle.

XPS and XAS in-operando methods have been of paramount importance in advancing the understanding of the mechanism of OER over the years. Several studies [85,86] detected high oxidation states of Ir and proposed mechanisms involving Ir(+V) or Ir(+VI) intermediates. Those intermediates are now rather attributed to a mechanism involving lattice oxygen and high overpotential conditions (>1.6 V *vs.* RHE).[84,87] The most likely mechanism taking place in acidic media at low overpotentials instead seems to involve the formation of electrophilic O(–I) species, followed by a nucleophilic attack from (HO^-) or (H_2O). This mechanism was first proposed by Pfeifer *et al.* [88] in 2016 and then confirmed by Saveleva *et al.* in 2018 [89] by the influence of potential onto the specific signature of O(–I) in the O K-edge XA spectra (similar to **Figure 1.9.A**) in *operando* conditions (ion-exchange membrane design, electron-out detection mode, **Figure 1.8.C**). The binding mode of this electron-deficient O(–I) species, either coordinated to a single metallic center (μ_1), or bridging two surface centres (μ_2), or three lattice centres (μ_3), crystallizes discussions on the catalytic cycle and the parameters that positively influence the OER (**see Figure 1.9.B**).

In the absence of easily accessible XAS references, theoretical calculations are frequently used to complement and help the interpretation of XAS spectra. For instance, Mom *et al.* [90] used DFT calculations to determine the peak positions in the O K-edge XA spectra of the aforementioned μ_1−O(H), μ_2−O(H) and μ_3−O. Comparing the data obtained from IrO_x samples with different crystallinity in ion exchange membrane *operando* cell under different polarization (from 0.25 V to 1.65 V *vs.* RHE), they observed that μ−OH deprotonation happens when the oxide is positively polarized (+1.25 V *vs.* RHE). Interestingly, IrO_x samples with different crystallinity showed similar trends in μ-OH behaviour for the same applied potentials (*i.e.,* increasing μ_2−O component with higher potentials on **Figure 1.9**.**A**) independently of the deprotonation potential of the active sites. In parallel, the Ir4f XPS signal was followed as a function of the potential applied. When the potential reaches values at which the OER occurs, it was observed that the oxidation of Ir is concomitant to the deprotonation of the μ_2−OH, and, to a lesser extent, of the μ_1-OH, sites. However, the very small energy shift observed in the Ir4f-XP spectra under OER conditions points towards an oxidation

primarily located on the oxygen rather than on the metal, as suggested by other studies.[72,88,91]

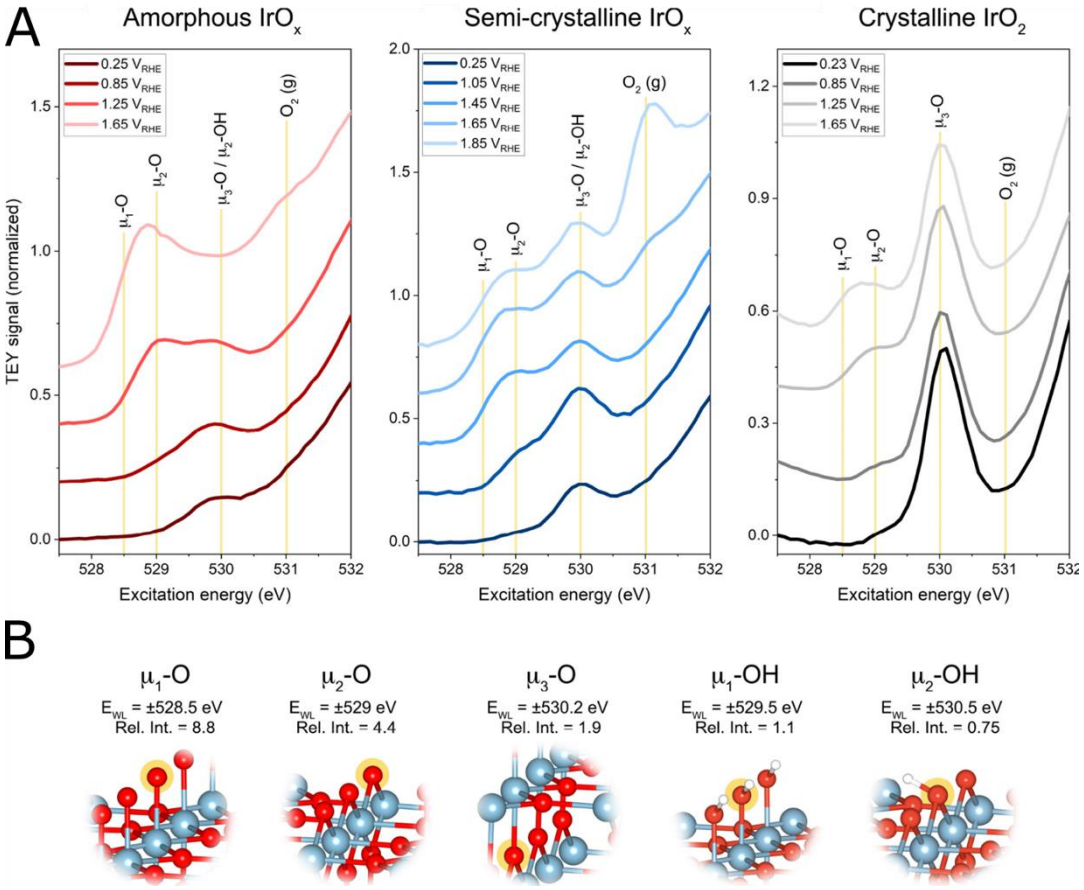

Figure 1.9: **(A)** O K-edge recorded under *operando* conditions on IrO_x-based OER catalysts with different crystallinity levels. The energy positions of several bridging oxygen species obtained from DFT calculations are displayed as vertical guides on the plots. The chemical structures of these species are shown on panel **(B)**. Adapted from [90].

Finally, a quantification study showed that more μ_1−OH and μ_2−OH sites are deprotonated than the number of sites available on the topmost surface, meaning that deprotonation must happen in subsurface sites as well. A higher OER activity was observed for lower crystallinity samples. As subsurface μ_1−OH and μ_2−OH moieties are more represented in low crystallinity samples, the increasing OER activity for those samples compared to crystalline one was then explained by the inductive effect resulting from subsurface deprotonation that makes surface μ-O sites more electrophilic and therefore more active. This explanation is consistent with the work of El Maalouf *et al.*, who used *Operando* XAS at the L_3-edge of iridium to determine the

oxidation state of $IrMoO_x$ hierarchically porous OER electrocatalysts under applied potential.[92] In this study, the presence of molybdenum in the oxide was used to decorrelate the temperatures at which the crystalline/amorphous transition occurs from the Ir(III)/Ir(IV) transition. The authors showed, with a combination of *ex-situ* XPS and XAS as well as *operando* XAS, that the crystallinity of the samples was directly correlated to the activity, while the oxidation state was not.

Drawing conclusions for the mechanism of water oxidation by iridium oxides in acidic media requires a precise understanding of crystallinity and metal oxidation state with a depth resolution. This profiling can be performed, although it is challenging, with a combination of XAS and XPS using a range of low to high X-ray energies (so called *depth-profiling*). Such experiments were already performed under *ex-situ* conditions for core-shell nanoparticles [72,93] and under operando conditions for RuO_2 and $Ir_{0.7}Ru_{0.3}O_2$ electrocatalyst [68] but remain to be applied to IrO_x on the light of the above presented results.

Transition metal based OER catalysts operating in alkaline medium have also been subject to in situ and operando investigations, notably with XAS and XPS (see Ref. [94] and references therein). For instance, Han *et al.* [95] used NAP-XPS in a D&P approach (**Figure 1.8.d**) to study transformations occurring at the surface of a cobalt metal foil electrode in alkaline media (0.1 M KOH) in a wide potential range up to the OER conditions, thus being able to determine the changes in the oxidation state of the electrode surface *operando*. These results were particularly interesting with regards to the oxidation behaviour of cobalt, as the sample was successfully reduced to Co(0) at low potential (−1.35 V *vs.* Ag/AgCl) while cobalt oxy-hydroxide was detected above 0.4 V *vs.* Ag/AgCl (+1.4V *vs.* RHE) (**Figure 1.10.a** and **b**) and associated to the OER active phase in those conditions, a result confirming other studies that are discussed in **Chapter 4.** Additionally, assuming a uniform oxide layer on top of the cobalt metal (and owing to the D&P ability to use flat, and not nanostructured, electrodes), the authors were able to estimate the thickness of the oxide layer formed (~7.5 nm). Similar observations were made on Co_3O_4/CoOOH electrocatalyst by Favaro *et al.,*[96] where the CoOOH phase was detected under oxidative *operando* condition and associated to the OER active phase using the D&P setup.

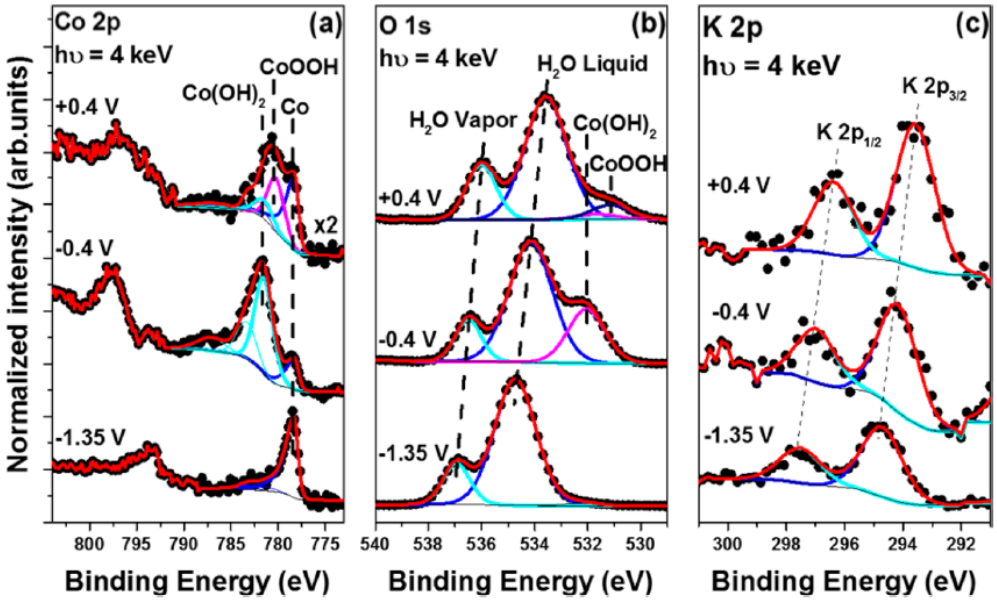

Figure 1.10: Co metal foil working electrode oxidation up to oxygen evolution reaction conditions, and reduction, in 0.1 M KOH using operando 'dip and pull' method. **(A)** Co2p, **(B)** O1s, and **(C)** K2p X-ray photoelectron spectra recorded at –1.35 V, –0.4 V and +0.4 V vs Ag/AgCl. Photon energy is 4 keV. Reproduced from Ref.[95].

Co(Fe) spinel oxides have also been investigated with operando EXAFS spectroscopy (see *e.g.,* Ref.[97] and **Figure 1.11**). As further discussed in **Chapter 4**, $Co_xFe_{3-x}O_4$ are very attractive since they demonstrate enhanced activities in the OER compared to either Co_3O_4 or Fe_3O_4. It is interesting to note that while CoO_x with rock salt-like structure was found to transform, at positive potentials, first into spinel and then CoOOH-like structure, for $Co_xFe_{3-x}O_4$ (notably Fe-rich) catalysts only subtle changes in the EXAFS spectra were observed evidencing a lack of transformation into a CoOOH phase (**Figure 1.11**). The authors combined time-resolved XANES and EXAFS with machine learning, namely, principal component analysis (PCA) to qualitatively interpret subtle changes in the spectra under the reaction conditions. They highlight an increase in the oxidation state of both Co and Fe species, and contraction of interatomic distances, and infer participation of both Co and Fe in the OER.

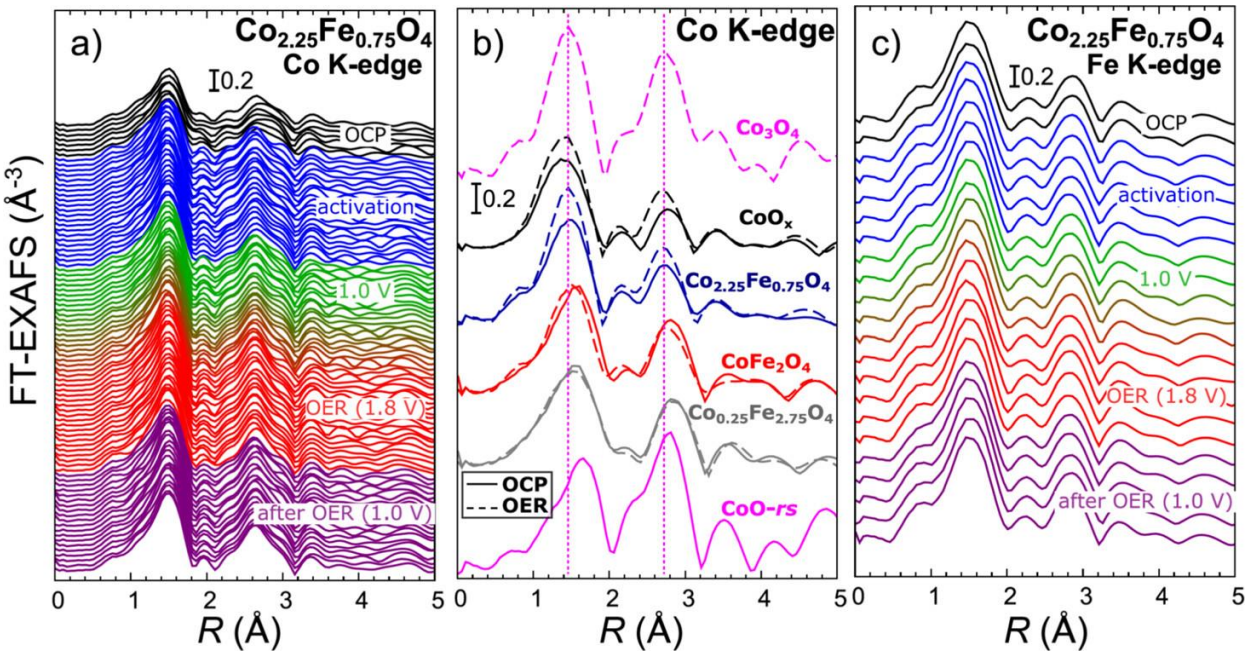

Figure 1.11: Evolution of Fourier transformed (FT) Co K-edge **(a,b)** and Fe K-edge **(c)** EXAFS spectra during the activation and under OER conditions for **(a,c)** $Co_{2.25}Fe_{0.75}O_4$ and CoO_x, $CoFe_2O_4$, and **(b)** $Co_{0.25}Fe_{2.75}O_4$ nanocatalysts. Spectra are shifted vertically for clarity. A comparison of Co K-edge FT-EXAFS spectra for all $Co_xFe_{3-x}O_4$ samples with different Co to Fe ratio is shown in **(b)**. The spectra collected for the as-prepared samples under OCP and for the samples under OER conditions are shown, as well as the spectra for reference oxides CoO (rocksalt structure) and Co_3O_4 (spinel structure). Reproduced from Ref.[97].

To sum up, XPS and XAS appear as powerful methods for *in situ* and *operando* monitoring of dynamic transformations that materials undergo under the reaction conditions. They may also allow one to detect active species provided that their concentration, which depends on the reaction kinetical steps, is strong enough. One should keep in mind however that electrocatalysis being interfacial phenomenon, it depends not only on the structure and composition of the electrode material but also on the structure and composition of the so-called 'electric double layer, EDL' (for more details see **Chapter 2**) formed at the electrode/electrolyte interface. The first mention of the EDL effects on the electrode kinetics dates back to seminal works of A. Frumkin,[98] but the interest to this topic has greatly increased in recent years when "unusual" pH and cation effects were documented for the OER, HER and carbon dioxide reduction reaction. Unfortunately, despite decades of research, the EDL remains the most 'mysterious' part of electrochemical systems (see *e.g.* Refs. [99–102]), which is an obstacle for the fundamental understanding of electrocatalysis.

However, recently, NAP-XPS in its D&P version was proposed as a new tool to study the EDL and will be also considered in the **Chapter 2** of this manuscript.

1.6 Conclusions and objectives of the PhD thesis

Implementation of green hydrogen production into the global energetic mix is still confronted to the low financial competitiveness of water electrolysis compared to non-renewable hydrogen production processes (grey and blue hydrogen). AEM and PEM technologies appear to be promising candidates for the development of new electrolyzers. However, the development of more active and noble-metal free electrocatalysts for the HER, and in particular for the OER, in alkaline media remain a bottleneck to decrease the production and overall technology costs. The complexity of this reaction, coupled with the dynamic changes that an electrocatalyst undergoes when exposed to the oxidation conditions, present major challenges. Understanding the mechanisms, as well as the structural and chemical changes occurring at the electrochemical interface (*i.e.,* at the interface between the electrode and electrolyte) is essential, as it would feedback into the development of the future generations of electrocatalysts.

To this end, the development of adapted characterization methods is necessary. X-Ray absorption spectroscopy and X-Ray photoelectron spectroscopy (XAS and XPS respectively), in particular, are promising as both are element-specific spectroscopy methods that allows to decorrelate contributions of each element in a complex system, while presenting complementary specificities.

- XPS is a surface sensitive technique which is not submitted to the electronic transition rules. It is quantitative and allows a straightforward deconvolution of samples presenting elements in different chemical environments. However, the limited inelastic mean free path of electrons at ambient pressure complicates the electrochemical reactions studies under *operando* conditions.
- XAS, on the other hand, is less handy when it comes to deconvolute an element signal in multiple phases. However, it is efficient in assessing oxidation degree changes in a material, and possesses an exceptional ability to precisely probe the chemical environment. Additionally, it can be either bulk or surface sensitive depending on the detection mode, which eases the spectro-electrochemical cells development using the bulk sensitive photon-out detection mode.

This chapter highlights how the XAS and XPS were successfully used in the literature to provide insights onto electrocatalytic processes and the electrode-electrolyte interface, with a specific focus on the OER in acidic and alkaline environment. In the following chapters of this manuscript, we are focusing on those two techniques to further explore their reach as tools to understand the properties of electrochemical systems of various complexities.

In **Chapter 2** we aim to tackle one of the key questions of electrochemistry on one of the most important features of an electrochemical system, through the study a model system in absence of faradaic reactions, *i.e.,* **is it possible to observe the electrochemical double layer (EDL) by spectroscopic methods in realistic conditions for electrocatalysis?** To this end, we are focusing onto the study of the electrode-electrolyte interface of polycrystalline platinum or glassy carbon with an alkaline electrolyte, using the XPS D&P method. Indeed, the D&P is especially suited to record the signal at the interface of planar electrodes, therefore allowing a tentative mapping of the cation distribution near the electrode surface. This chapter hence describe both the methodology of our analysis and the relevance of the D&P to study the EDL.

In **Chapter 3**, the complexity of the electrochemical system is increased through the introduction of the OER, whose key role in the hydrogen cycle has been highlighted in this chapter. However, conventional metal oxide-based heterogeneous OER catalysts (see **Chapter 1** and references therein) are constituted of particles of different sizes and shapes, may contain different types of defects, hence sites of different coordination (e.g. tetrahedral, octahedral) and chemical environment. This makes the deciphering of information collected during operando studies very challenging.

Thus, in **Chapter 3**, we choose to focus on a model molecular OER electrocatalyst, namely **complexes of cobalt-stabilised polyoxometalates** that offer a clearly defined, unique chemical environment. We use XP and XA spectroscopies under *operando* conditions to answer critical questions regarding their activity and stability under the OER conditions, and show how spectro-electrochemical tools can be used to study molecular catalysts in homogenous or heterogenous environments.

In **Chapter 4**, we move closer to industrially relevant electrocatalytic systems, through the study of a more realistic OER electrocatalyst: **$CoFe_2O_4$@Fe_3O_4 core@shell**

nanoparticles. Those nanostructures are used as a showcase of how complementary use of conventional electrochemistry, spectroscopic *operando* and *in-situ* studies can provide an insightful picture on the structural transformations occurring when a system is operating, and how these transformations are related to its electrochemical properties, here as a function of the shell thickness.

Finally, through its **General conclusions and outlook**, this manuscript provides an overview of the opportunities and challenges of synchrotron-based spectroscopic methods based on the utilization of X-rays, when applied to electrochemical systems, with a focus on the OER. The diversity of systems that are studied in the manuscript will be used to highlight the versatility and the wealth of information that spectroscopy techniques can provide, while providing methods and critical discussion regarding the relevance of data obtained.

Chapter 2: Assessing the Electrode-Electrolyte interface by X-Ray Photoelectron Spectroscopy using the 'dip and pull' approach

2.1 General introduction

Since the electron transfer between an electrode and a reactive species happens at the electrode/electrolyte interface, electrochemistry is defined as an interface science. When it comes to electrocatalysis or other application (battery, EDL capacitors, electrodeposition, *etc.*) this interface is especially important as it defines the system durability and its activity. It is then a strategic place to study when it comes to the understanding of electrochemical systems, either from a mechanistic or applied standpoint, to correlate the aforementioned activity and durability with the interfacial properties.

While it is easier to perform characterization of the system after the reaction (*post-mortem*), as the setup can simply be disassembled and analysed by spectroscopic, electronic and physico-chemical methods (*e.g.,* Transmission Electron Microscopy, Scanning Electron Microscopy, X-Ray Photoelectron Spectroscopy, Raman, X-Ray Diffraction, *etc.*), characterising the system during the reaction (*operando*) with said methods allows to complement information obtained from electrochemical measurements. This is especially true when it comes to species in the electrolyte, or whose existence is potential-, time- or atmosphere-controlled, and therefore could be altered/destroyed unless it is characterised during the operation of the system.

Specifically, the electrochemical double layer (EDL) is a part of the system which cannot be studied out of *operando* conditions, as the organization of the ionic charges occurs at the electrolyte side of the electrode/electrolyte interface, and depends on the potential applied. *This makes an experimental, direct, assessment of the EDL extremely challenging*. Hence, information on the EDL which was gathered until very recently, is limited to macroscopic electrochemical and physical measurements, and simulations, which makes the EDL one of the less understood parts of an electrochemical system.[102–105]

In this chapter, we briefly introduce the theoretical basis of the EDL and how it was studied in the past. Then a rather new spectro-electrochemical *operando* system will be introduced: the 'dip and pull' (D&P) setup, which allows study of a model planar electrode/electrolyte interface by XPS. We then discuss how it can be used to study the EDL, by (i) presenting a series of experimental data obtained using this setup and (ii) providing a critical discussion on the key parameters defining the relevance of the method in the frame of that application.

2.2 State of the art

2.2.1 Introduction into the electrochemical double layer

When a potential is applied to an electrode, electron transfer can occur depending on the nature of the electrode material and species that are present at the interface. In case of absence of electron transfer (redox reaction) upon polarization, an electrode can be assimilated to an ideally polarisable electrode (IPE). In those conditions, the charges cannot cross the electrode/electrolyte interface and the electrode then performs as a capacitor. Charges are then accumulated on top of the electrode surface (~0.1 Å for a metal), with its polarity (negative or positive) and capacity depending on the nature of the electrode, the potential, and the electrolyte constituents.[106,107] At all times, the charge excess at the electrode is counterbalanced by an equal charge excess from the electrolyte ions of opposite polarity, resulting in a heterogenous distribution of ionic charges (*vs.* the electrolyte bulk) and solvent dipoles in the electrode vicinity. The layer in which this charge distribution occurs is defined as the Electrical Double Layer (EDL).[104,105] The exact EDL structure is yet to be fully understood despite its importance, and models developed so far still fail to accurately

describe the EDL and its characteristic features.[102] In the following part we will briefly introduce a simplified description of the EDL to depict the overall interface organisation.

The EDL structure can be mentally divided in two layers (see **Figure 2.1.A**). Ions and molecules that are located in the closest proximity to the electrode surface (also called Stern or Helmholtz layer) are said to be *specifically adsorbed* (chemical interaction with electrode surface) and form the so-called *compact (or dense) layer*. Centres of those specifically adsorbed species are referred to the *Inner Helmholtz Plane (IHP)*. Ions that are attracted to or repulsed by the electrode charge excess due to long range coulombic interaction, and are still surrounded by solvent molecules are referred to *non-specifically adsorbed* ions. As solvent molecules prevent them from getting too close to the electrode surface, the closest position they can get to the electrode is then defined as the *Outer Helmholtz Plane* (OHP). Since solvated ions are subjected to thermal motion, non-specifically adsorbed ions forms the so-called *diffuse layer*, which is defined as the space between the OHP up to the bulk electrolyte. In addition to the coulombic forces, interactions of the electrode and ions with the solvent molecules also affect the structure and composition of the EDL. The latter has been subjected to several models throughout electrochemistry history.[108] One of the direct consequences of the EDL is that the electrical potential drop between the metal (ϕ_M) and the electrolyte bulk (ϕ_S) is distributed through the entire length of the EDL, as illustrated in **Figure 2.1.B**, rather than abruptly dropping at x = 0 nm. However, one should keep in mind that despite those theoretical descriptions, which are convenient to have a mental representation about phenomena occurring at the electrode/electrolyte interface, <u>*those notions are still questioned and have no physical basis*</u>.[102] Indeed, recently Wolfgang Schmickler wrote: "*Simple geometrical models based on concepts like the inner or outer Helmholtz plane, or the Stern layer have no scientific basis. They should be buried in the cemetery of discarded electrochemical concepts with the hydrogen in status nascendi*".[99]

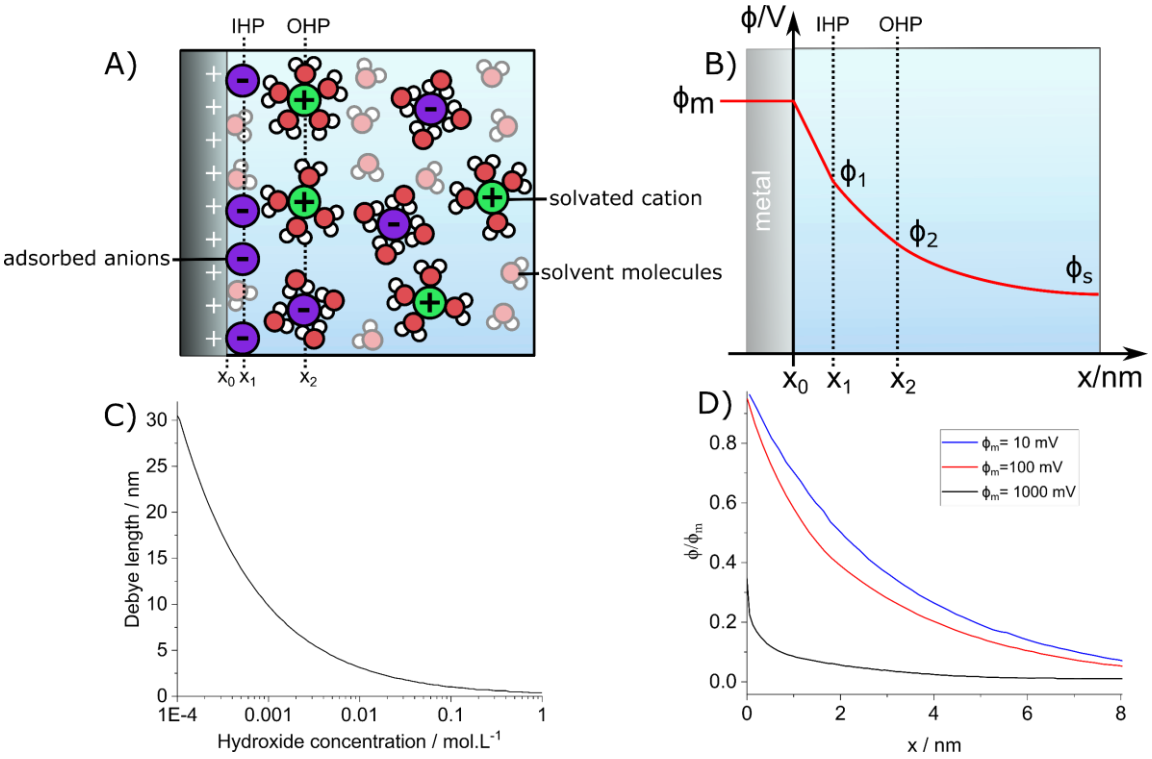

Figure 2.1: **(A)** electrochemical double layer structure, formed by the compact layer (0−x_2) and the diffuse layer (x_2−bulk). IHP: Inner Helmholtz Plane (*i.e.* plane of closest approach of specifically adsorbed ions), OHP: Outer Helmholtz Plane (plane of the closest approach of non-specifically adsorbed ions). **(B)** Electrical potential distribution in the electrochemical double layer. ϕ_m, ϕ_1, ϕ_2, and ϕ_s are electrical potentials in metal, IHP, OHP and in solution bulk, respectively. **(C)** Estimated Debye length in an alkaline solution (*e.g.,* KOH in the absence of other electrolyte) depending on the hydroxide concentration. Reproduced from Ref.[109]. **(D)** Electrical potential evolution depending on the electrode distance at different electrode potential (ϕ_m) according to Gouy-Chapman electrical double layer model. Reproduced from Ref.[104].

The EDL thickness and structure depend on the ion concentration and on the electrode potential. Its thickness can vary from few angstroms in electrolytes with a strong ionic strength (*e.g.,* 1 M) to dozens of nanometres for diluted electrolytes (*e.g.,* 10^{-4} M). An illustration of the EDL characteristic length (Debye length) depicting this phenomenon is shown in **Figure 2.1.C** for the specific case of alkaline solution. Similarly, the greater the electrode potential, the stronger the ionic overconcentration excess at the interface, and the shorter the Debye length (see **Figure 2.1.D**). Albeit it was little investigated, the use of highly concentrated electrolyte (>> 1 M) would result not only in further decreasing the thickness of the EDL, but also in its structural reorganization, through the change in the ions solvation shells, the diminishing number of water molecules not

involved in ions solvation shells *etc.* as recently observed by Li *et al.* with highly concentrated Li-salts [110] and Lee *et al.* with RbI and RbCl highly concentrated electrolytes.[111] The EDL influence on the electrochemical system behaviour cannot be overlooked, as EDL-induced phenomena (*e.g.,* interfacial charges distribution,[112,113] surface crowding effect [114], capacitance behaviour [115,116], *etc.*) have a key influence on the electrocatalyst activity.[117,118]

2.2.2 Historical EDL model development

Since the EDL influences the electrochemical properties of a given material, the EDL was originally studied through a range of electrochemical methods (discussed in more detail in **Section 2.2.3**). However, these experiments provided information regarding the global EDL behaviour depending on potential, electrolyte concentration, pH, *etc.* They could not provide 'mapping' of the ion arrangement at the interface, which led to a focus on the model development, and a comparison of the model predictions with electrochemical findings to assess their validity.[104] The evolution of these models through history is illustrated in **Figure 2.2**.

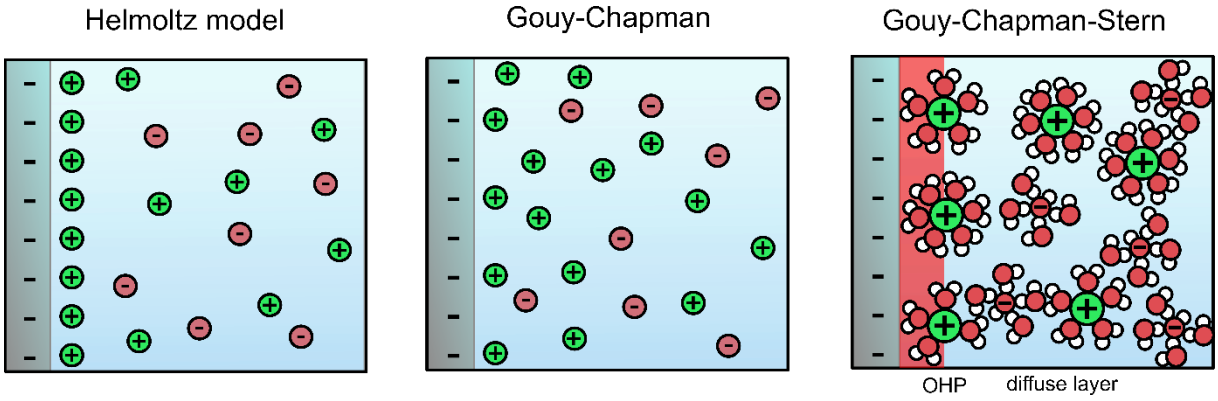

Figure 2.2: Historical EDL model illustrations. **(A)** Helmholtz model: the ions are arranged in a compact layer at the interface. **(B)** Gouy-Chapman model: ions are in a higher or lower concentration next to the surface compared to the bulk, and this difference diminishes with the distance (diffuse layer). **(C)** Stern modification: Same as Gouy-Chapman model, but we consider the existence of a minimum distance between ions and the electrode surface related to the solvation sphere around ions.

Helmholtz model

The first EDL model was elaborated in 1853 by Helmholtz.[119] As there is an excess of charge at the metal surface, it was then believed that the said charges were

compensated by the ions in solution. The formation of a layer of ions of opposing charge at the interface is therefore expected (see **Figure 2.2.A**). This results in the formation of the so-called *electrical double layer*, with a layer of charges residing within the electrode and a layer of charges within the electrolyte. Yet, this model quickly found its limits as it is similar to a parallel plate capacitor and results in a constant capacitance, while experiments evidenced in favour of capacitance depending on the electrolyte concentration and potential.

Gouy-Chapman model

Helmholtz model especially shows its limits in diluted electrolytes, where, as illustrated in **Figure 2.1.C**, as the EDL extends into the electrolyte bulk much beyond an ionic radius. As a consequence, Gouy (1910) [120,121] and Chapman (1913) [122] elaborated independently a second model, which considers two phenomena of opposite actions, (i) the tendency of electrode charge excess to repulse or attract ions in solution, (ii) and the thermal motion that randomizes their position. This model results in a diffuse layer (see **Figure 2.2.B**) in which the concentration of ions depends on the electrode charge excess and the electrolyte concentration in the solution. The ionic overconcentration being stronger in the electrode vicinity (where the electrode charge excess has more influence) while slowly getting back to the bulk values at further distance to the electrode interface. Incidentally, this model allowed the definition of the *point of zero charge* (PZC), *i.e.* the potential at which the ion charge excess at the interface is null. However, in specific cases (*e.g.,* PZC determination, capacitance at extreme potentials) and at high electrolyte concentrations, it still showed differences between the model prediction and the experimental findings.[104,123,124]

Gouy-Chapman-Stern model

The main limitation of the Gouy-Chapman model is the description of ions as point charges, allowing an infinite concentration of ions at the interface under extreme conditions (high electrolyte concentration and high electrode potential). To solve this problem, Stern added a plane of closest approach to the electrode for the solvated ions, limited by the ion size and their solvation shell, which corresponds to the aforementioned OHP (**Figure 2.2.C**).[125] The model was then refined by including the specifically adsorbed ions at the IHP, as well as the ion-solvent interactions. Those refinements aimed to describe more precisely the influence of the metal surface-ion

interaction which are considered purely coulombic in the Gouy-Chapman-Stern (GCS) model.[126–131]

2.2.3 Existing methods to study the EDL

Historically, EDL studies were first performed using a dropping mercury electrode.[127] The modification of the concentration of ions at the interface directly impacts the surface tension following Gibbs adsorption isotherm, and therefore the dropping frequency of the mercury (which is related to the surface tension). One can therefore determine the surface charge density and hence have an indirect information about the interfacial ion concentration as a function of the system parameters (electrolyte concentration, pH, potential, *etc*.) through the electrocapillary curves presented in **Figure 2.3.A,** where a maximal surface tension corresponds to the lowest charge density. Similarly, experimental assessment of the surface capacitance as a function of the potential and electrolyte concentration led to the observation of the PZC values (see **Figure 2.3.B,** 0.001 M and 0.01 M curves). PZC determination through electrochemical measurements is nevertheless limited to low electrolyte concentrations, where the EDL is diffuse, and its effective thickness is large. At high electrolyte concentrations the EDL is more compact and hence no minimum is observed on the differential capacitance curve (see **Figure 2.3.B,** 0.1 M and 1.0 M curves). Specific adsorption has significant impact on the EDL structure/composition. For instance on **Figure 2.3.A** one can observe a shift of PZC (curve maxima) depending on the electrolyte nature, which can be explained by the difference in ions specific adsorption depending on the system. If specific adsorption results in charge transfer across the interface (chemisorption of hydroxide or proton for instance), then a second PZC can be observed,[132,133] which result in the definition of the *point of zero free charge* corresponding to the PZC in absence of specifically adsorbed species involving charge transfer, and the *point of zero total charge* corresponding to the PZC in presence of specifically adsorbed species involving charge transfer. This notion is especially important in case of metal electrodes that can strongly interact with hydrogen (Ir, Pt, Rh, *etc*.). Today, the EDL at such interfaces is still poorly understood when it comes out of the GCS limits.[134–136]

Recently, the understanding of the EDL was strengthened by the use of computational methods. Such support started as early as the second half of the 20th century using Monte Carlo methods,[137] but owing to the calculating cost of modelling the complete

EDL, it only saw a drastic improvement in the 2000's. Density Functional Theory (DFT) calculations were firstly used to describe water molecules behaviour at the interface [138,139] and HER electrochemical reactions.[140] In parallel, the use of molecular dynamics allowed 2D and 3D mapping of various interfaces exposed to diverse potentials fields,[141–143] along with developing detailed models of the potential distribution at the electrode/electrolyte interface,[144,145] with recent years seeing notable developments in (i) the complexity of the interface (*e.g.,* from planar to porous), (ii) the parameterisation of the charges, molecules and their complexity,[116] (iii) the accuracy of the polarization and (iv) of the charge distribution throughout the electrode (*e.g.,* through the use of MetalWalls software [146,147]).

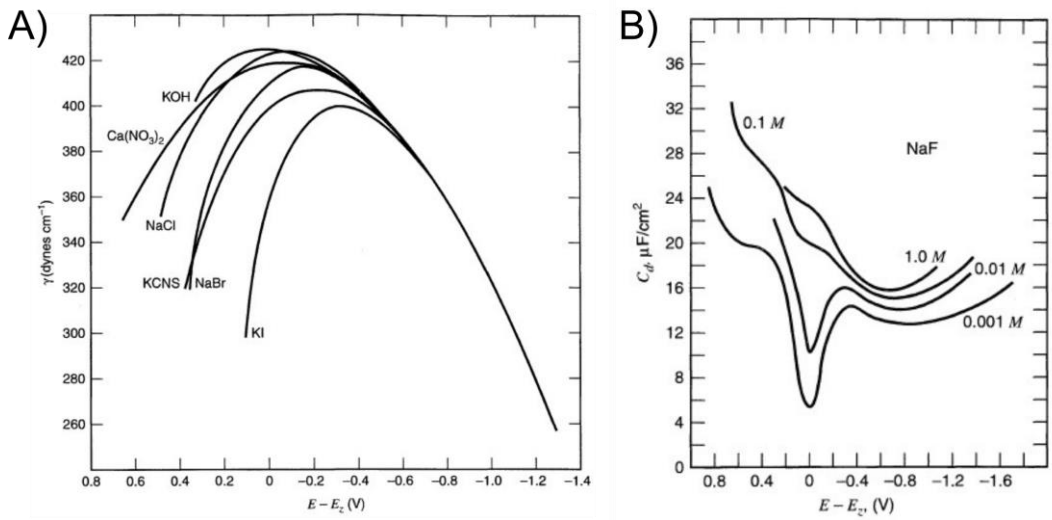

Figure 2.3: Example of **(A)** electrocapillary curves, representing the interfacial tension of mercury in contact with aqueous solutions of different electrolytes at 18°C. The potential E_z is the potential of zero charge for mercury in contact with NaF solution. The curve maxima (the highest surface tension) correspond to the lowest concentration of adsorbed ions at the interface. **(B)** Differential capacitance (charge derivative with potential) depending on the potential on a mercury electrode at different NaF electrolyte concentrations at 25°C. Minimal capacitance reflects lower ionic concentration excess at the interface. Reproduced from Ref.[127].

From a more experimental point of view, due to technical difficulties to study the electrode/electrolyte interface under *in-situ* or *operando* conditions, the EDL study only began in the 1990's with the development of Scanning Tunnelling Microscopes (STM).[164], [165] Other microscopic and spectroscopic techniques were later adapted to be used under electrochemical *operando* conditions, such as Transmission Electron

Microscopy (TEM), Scanning TEM Electron Energy Loss Spectroscopy (STEM EELS), Nuclear Magnetic Resonance (NMR), and XAS. Yet those techniques are limited to characterizations of the interface as a whole, and cannot provide either information or resolution for a precise ion distribution through the layer, which make them ill-adapted for the EDL assessment. Other techniques provide information limited to specifically adsorbed species in the Stern layer, such as (i) Surface Enhanced Raman Scattering (SERS) [150] that allows investigations onto the distribution of species at the electrode-electrolyte interface as a function of the potential [151] and onto the adsorbed water molecules orientation at the interface;[152] (ii) Atomic Force Microscopy (AFM) [153] and (iii) XPS, which saw its early development in interface characterization under *ex-situ* conditions with the emersion [154] and fast freezing techniques.[155–157] This last technique though relied on the strong assumption that part of the electrode/electrolyte interface remains unchanged when removed from the bulk solution. To the author's knowledge, until now very few spectroscopic techniques were able to bring more precise information regarding the ionic distribution in the whole double layer (Stern and diffuse layer) under *operando* conditions. Some of the most relevant examples being (i) X-Ray Reflectometry (XRR) coupled with simulation, which did provide information of the molecules distribution at the interface of non-aqueous Li-ion battery setup in a study by Steinbrück *et al.* in 2018;[174] and XPS in D&P setup, firstly used for that purpose by Favaro *et al.* in 2016 and Lichterman *et al.* in 2017.[109]

2.2.4 Dip and pull setup

The D&P setup for XPS measurements made its appearance with the development of synchrotron end-stations able to support pressures up to 150 mbar (above the water saturating vapor pressure at 25°C, ~30 mbar). It was firstly developed in 2015 by Axnanda *et al*. [74] at the Advanced Light Source (Berkeley) synchrotron, under the inspiration of the electrode emersion technique,[154] and was later adapted in other synchrotrons: Paul Scherrer Institute (Switzerland), Bessy II (Germany), and MAX IV (Sweden).[159] The setup can be seen on **Figure 2.4.A** and is close to a conventional three electrode cell: working, counter and reference electrodes are all three vertically immersed in a liquid electrolyte reservoir (aqueous or organic). The working electrode is then immersed (dip) in the electrolyte while analysing the emerged part of it with XPS. The working electrode is then slowly pulled out from the solution until the meniscus reaches the analysis spot (see **Figure 2.4.D$_1$-D$_4$**).

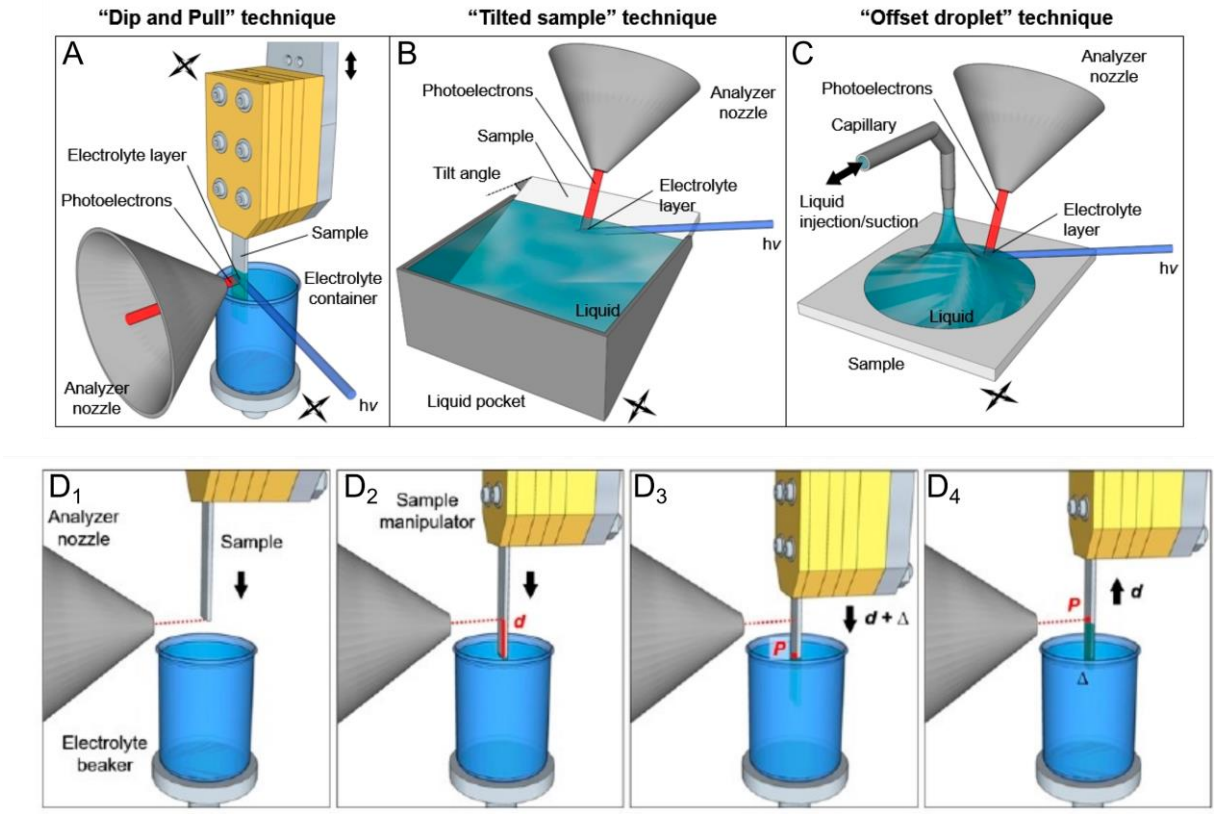

Figure 2.4: **(A)** 'Dip and pull' setup representation, **(B)** 'tilted sample' technique setup representation, **(C)** 'offset droplet' technique setup representation. **(D)** Dip and pull procedure: **(D_1)** and **(D_2)** prior to the measurement, the optical focus is made out of the electrolyte, **(D_3)** The electrode is then dipped into the electrolyte and **(D_4)** pulled carefully out of it, so that a thin meniscus film is formed on top of the electrode surface. Usually the working pressure for this setup is close to the solvent saturated vapor (~30 mbar for water at 298 K). Reproduced from [159].

At this point, if the electrolyte layer is thin enough, one is able to observe both the electrolyte and the working electrode surface signals. As the beam and the analyser are on the electrolyte side, the signal is much more sensitive to the working electrode surface in direct contact with the electrolyte, along with allowing the use of planar, non-porous, model electrodes. The main limitation in terms of sensitivity now arises from the electrolyte thickness, *i.e.,* as the photoelectron IMFP in liquid water can range from ~4 nm (at 1000 eV) to ~15 nm (at 5000 eV),[160,161] the electrolyte must reach a thickness as thin as 15 nm and up to 45 nm so that one can be able to assess the interface properly. *Obviously, the management of a vertical nanometric thin film in a low pressure atmosphere, while performing electrochemical experiments under an X-Ray beam irradiation, is challenging and constitutes the main barrier to obtaining*

reliable spectroscopic data. Finally, it is worth to highlight that other experimental approaches are developed to study the electrode from the 'electrolyte' side by XPS using a flat model working electrode, such as the 'tilted sample' [162] (**Figure 2.4.B**) and the 'offset droplet' [163] methods (**Figure 2.4.C**). Nevertheless the D&P setup presents major advantage of allowing the easy tuning of different parameters (such as electrolyte-beaker distance to the analysis spot, electrode dipping and pulling lengths) and the exposure of a new surface without changing the whole setup.

In addition to the aforementioned challenges such as the thickness of the electrolyte, other parameters can alter the quality of the interface assessment, both from an electrochemical and spectroscopic standpoint, *e.g.* (i) the ohmic losses in the meniscus, (ii) the electrolyte evaporation, and (iii) the variation of the meniscus thickness. Furthermore, whereas the main drawback of the methods analysing a nanostructured working electrode is the complexity of the interface, and the resulting limitations in terms of EDL assessment, the D&P might suffer from a strong contribution of the electrolyte at the interface between the meniscus and the low pressure chamber (*i.e.,* far away from the electrode/electrolyte interface) to the signal. Those challenges and eventual drawbacks, along with the methods to limit/overcome them, are extensively discussed within this chapter.

2.3 'Dip and pull' method for the studies of electrochemical interfaces

The D&P method seems especially suited for the study of the electrode surface properties (*e.g.,* oxidation degree, behaviour during electrocatalysis, *etc*.), the electrolyte (for homogenous redox reactions) and the electrode-electrolyte interface (*e.g.,* the EDL). Some examples of those works are presented in what follows.

2.3.1 Electrode surface study during electrocatalysis

As already presented in **Section 1.5**, Han *et al.* [95] used D&P setup with a cobalt metal foil working electrode in alkaline media (0.1 M KOH), and were able to determine the changes in the oxidation state of the electrode surface under *operando* conditions to assess the active phase under OER conditions. Analogously, Stoerzinger *et al.* [164] and Favaro *et al.* [165] used the same setup with a platinum foil working electrode to study the metal surface state under HER and OER conditions, in alkaline media.

Regarding the OER, the authors followed the Pt4f XPS signal at different potentials and observed the formation of Pt-$(OH)_{ads}$ in the OER potential range (+0.9 V vs Ag/AgCl, see **Figure 2.5.A**) over time (**Figure 2.5.B**), while PtO_2 and PtO components remained essentially unchanged. This led the authors to propose Pt-$(OH)_{ads}$ as the main active species for the OER on Pt. The increasing signal over time highlighted its formation in the materials depth, involving catalytic activity in subsurface active sites, and finally led to a revised OER mechanism for this system.

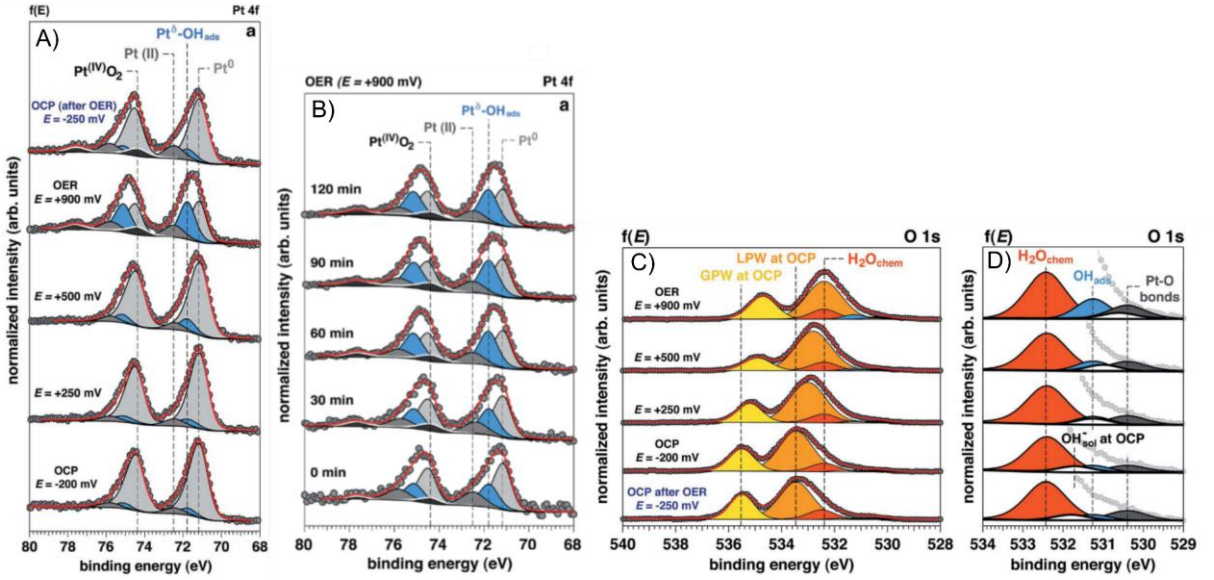

Figure 2.5: Pt4f XPS fitting at **(A)** −200 mV, +250 mV, +500 mV and +900 mV, **(B)** at +900 mV and different exposure times: 0 min, 30 min, 60 min, 90 min and 120 minutes. **(C)** O1s XPS fitting and its zoom **(D)** at the same potentials as in (A). The system is composed of a platinum metal electrode in a 'dip and pull' setup and 1 M KOH electrolyte. Potentials are indicated versus Ag/AgCl reference electrode. Images are reproduced from Ref.[165].

2.3.2 Electrode / electrolyte interface studies

On **Figure 1.10** and on **Figure 2.5,** one will note a binding energy (BE) shift in the XPS soluble species peaks with the applied potential (for instance species that are in liquid phase *e.g.*, $K^+_{(aq)}$, $OH^-_{(aq)}$, **Figure 2.5.C** and **D**), while this peak shift is absent for the peaks associated to the electrode material, or to species adsorbed on it (**Figure 2.5.A**). This BE shift is due to a combination of two effects. Firstly, the kinetic energy measured by the analyser depends on the incident photon energy, on the binding energy of the electron emitted but also on the work function ϕ (see **Equation 1.7**), the latter representing the electrical potential difference between the probed atom, and the

vacuum. Secondly, the electrical potential in the electrolyte layer is influenced by the electrical field induced by the application of a potential. As the working electrode is connected to the ground through the potentiostat, the work function of the electrode species does not depend on the potential difference applied between the working electrode and the reference electrode; and all species in electrical contact with the electrode will remain at the same binding energy position. On the other hand, the BEs of the species in the electrolyte shift according to the electrical potential difference between the electrode and the point of their localisation (see **Figure 2.1.B**). In absence of any external electrolyte-induced effects (*e.g.,* ohmic losses, *etc.*) and assuming the PZC at 0 V *vs.* the Standard Hydrogen Electrode (SHE), the application of a −1 V *vs* SHE potential on a working electrode will create a −1 V electrical potential difference between the working electrode and the electrolyte bulk, resulting in a +1 eV work function difference between the electrolyte bulk and the ground (**Figure 2.6.A**). This will decrease the measured electron kinetic energy and shift the apparent binding energy position in the XP spectrum to higher energy. The shift might be altered by the non-ideal properties of the system, *e.g.,* the electrical potential difference between the working electrode and the electrolyte bulk might be attenuated because of ohmic losses and the peak will only shift of –x eV, where x (< 1) is the actual electrode potential. This peak shifting is critical when it comes to studying the electrode-electrolyte interface using D&P XPS, as it allows to differentiate adsorbed species or soluble species and quantify the actual electrode potential. Furthermore, it can also be used to assess the ion distribution in the EDL. Indeed, considering the electrolyte as the superposition of several thin layers parallel to the electrode surface, all the electrolyte-related XPS peaks (for instance originating from non-specifically adsorbed cations) are the sum of each contribution from these different layers, the contribution from the electrolyte-air interface being stronger than contribution from the electrode-electrolyte interface due to strong electron scattering in condensed matter. In case of absence of electrical potential drop across the layer (*i.e.,* specific case of the PZC), the XPS peak remains unchanged as all contributions are superposed (**Figure 2.6.B**). But in case of electrical potential distribution from the electrode to the electrolyte bulk due to the EDL formation, the resulting XPS peak is asymmetrically broadened (**Figure 2.6.C**), which can be roughly followed using the Full Width at Half Maximum (FWHM) of the XPS peak, and which appears higher when potential is further from the PZC.

The signal can then be further deconvoluted to obtain a distribution profile of the ions within the EDL.

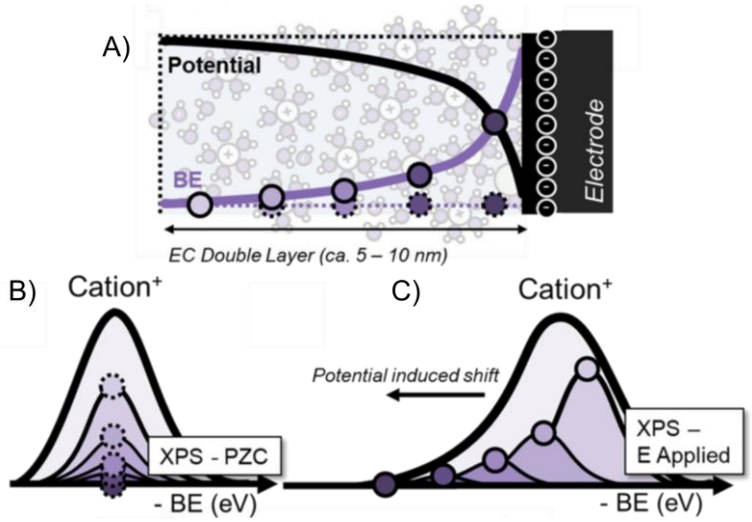

Figure 2.6: **(A)** Scheme of the electrode-electrolyte interface, highlighting the change of electrical potential with the distance to the electrode surface (black) and the resulting apparent shift in XPS peak binding energy (BE, in blue). **(B)** Cation XPS peak representation as the sum of the cations contributions from the different layers of electrolyte at the point of zero charge (PZC), corresponding to the absence of electrical potential (*i.e.* BE) change at the interface, resulting in a symmetrical peak. **(C)** Cation XPS peak representation as the sum of the cations from the different layers of electrolyte at potential below the PZC (*i.e.* negative charge of the electrode), resulting in a lower apparent binding energy for cations far from the electrode (*i.e.* closer to the electrolyte-air interface) and a broadened XPS peak.

The exploitation of that peak shifting and broadening for the EDL study is reported in two articles. The first one is from Favaro *et al.* in 2016,[103] who proposed using D&P setup for studying the EDL and provided the first proof of concept associated. Authors used a gold foil working electrode with low electrolyte concentration (from 0.1 mM to 80 mM KOH) to obtain an EDL thickness of the same magnitude as the electrolyte film thickness (~30 nm). This configuration is highly advantageous as the XPS peak broadening is more apparent if the shift of the peak is distributed in the whole meniscus thickness. However, since the cation concentration was rather low in the electrolyte, they followed the O1s broadening of the liquid phase water contribution (**Figure 2.7.B**) and used a neutral soluble probe (pyrazine) as a probe to add an additional XPS signal in the system and follow the N1s broadening from the liquid phase contribution of pyrazine (**Figure 2.7.A**). The evolution of the FWHM of O1s and N1s (from liquid phase water and pyrazine, respectively) depending on the applied potential is represented on

Figure 2.7.D and is compared to the system differential capacitance at the same potential. One may note that both graphs show minima at the same potential (~0.140 V *vs.* Ag/AgCl). The FWHM is supposed to be minimal at the PZC as illustrated by **Figure 2.6.B**, while the capacitance is minimal when the ion concentration excess at the interface is minimal (*i.e.* at the PZC as well), meaning that both methods led to the same results, which highlights that D&P can be used to study the EDL and identify PZC values.

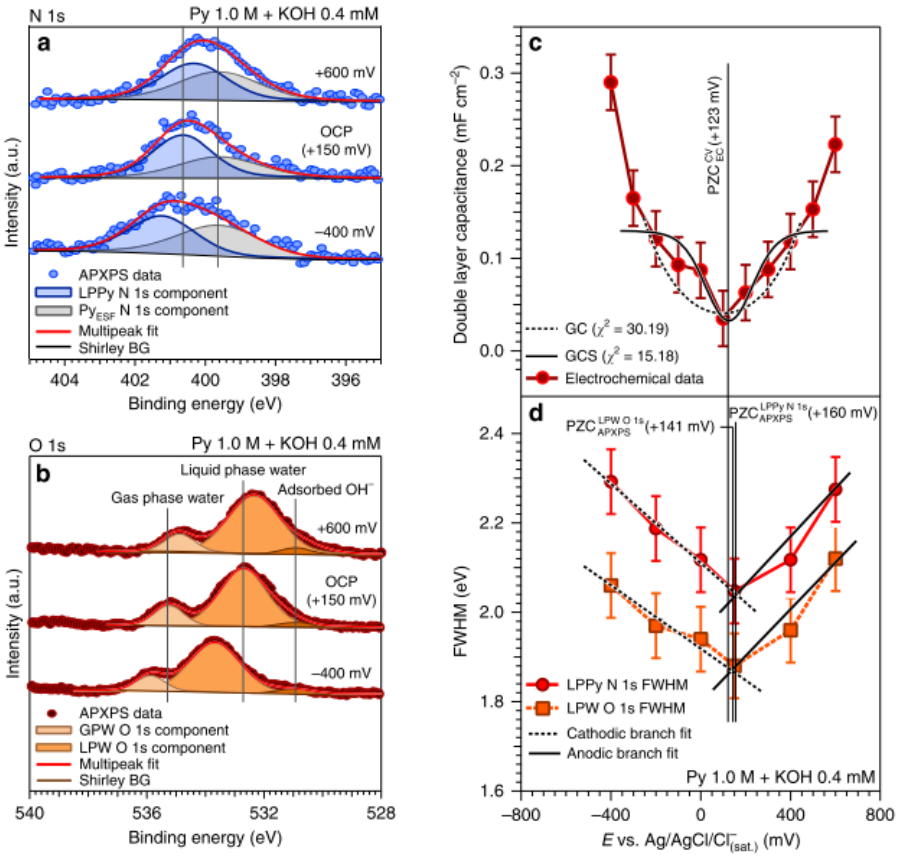

Figure 2.7: Electrochemical double layer probing from the spectral broadening of pyrazine (Py) and water core levels on a polycrystalline gold working electrode: **(A)** and **(B)** represent N1s and O1s XP spectra, respectively, in a KOH 0.4 mM aqueous solution (EDL thickness is estimated as 15.2 nm) containing 1.0 M Py. **(C)** Double layer capacitance (obtained from electrochemical method) as a function of the applied potential, fitted using Gouy-Chapman (GC), and Gouy-Chapman-Stern models (GCS). **(D)** Liquid Phase (LP) Pyrazine N1s signal and LP water (LPW) O1s full width at half maximum (FWHM) trends as a function of the applied potential within the EDL region. OCP, BG, GPW, Py_{ESF} stand for the 'open circuit potential', background, 'gas phase water' and 'pyrazine at the electrode surface' respectively. Photon energy is 4.0 keV. Reproduced from Ref.[103].

The second study, from Lichterman *et al.* in 2017,[109] used iridium foil working electrode in KOH electrolyte at different pH (11.5 to 14, corresponding to 3.2×10^{-3} M to 1 M KOH) and different electrolyte film thickness (18 nm to 42 nm), to verify calculations regarding the influence of these parameters onto the different characteristics of the D&P XP spectra, such as electrolyte peak shifts and its FWHM. They highlighted experimentally the influence of pH and electrolyte thickness on the shift of the apparent XPS binding energy peak (supposedly −1 eV/V in the bulk electrolyte, see **Figure 2.8.a**), and verified that in case of 'low' electrolyte concentration (pH 11.5, 3.2×10^{-3} M KOH) the EDL is larger than the actual electrolyte thickness, which is illustrated by the lowering of the O1s peak shifting with the electrolyte film thickness decrease (see **Figure 2.8.a.**, where the O1s peak shift is of ~0.4 eV/V at a meniscus thickness of ~20 nm, vs. 0.8 eV/V at a meniscus thickness of ~40 nm, at pH = 11.5). On the other hand, at stronger electrolyte concentration (pH 14) this trend is not observed due to a much shorter EDL. The authors followed as well the O1s XPS peak broadening depending on the pH and the electrolyte film thickness (**Figure 2.8.b-d**) but the strong uncertainty in the electrolyte thickness evaluation, mixed with strong noise on XP spectra prevented any clear correlation between the predicted trend and the experiment, highlighting the technical difficulties in the D&P method.

The D&P method was also used to assess the electrolyte properties of other electrochemical systems. In Li-ion batteries, Kallquist *et al.* [166,167] observed, through the trend in the C1s kinetic energy, that the presence of an interfacial charge transfer (*i.e.,* Li from the electrolyte to/from the electrode) would result in a deviation from the ideal 1 eV/V trend in the electrolyte-related BE shift. In biology, the Donnan potential (*i.e.,* the potential difference at a charged membrane/electrolyte interface) was also first assessed by the use of the D&P method.[168] Finally, Temperton *et al.* [169] recently published a proof-of-concept study in which they show that the XPS measurement of species dissolved in a homogeneous medium (an electrolyte film) is possible through the use of D&P. To do so, they recorded XPS reference spectra of the $Fe(CN)_6^{3-}$/ $Fe(CN)_6^{4-}$ redox couple in a liquid jet setup (XPS setup adapted for liquids and suspensions,[170]) and compared it with the *operando* redox transition in the D&P configuration, which allowed them to follow the oxidation changes of said species at a 0.4 M concentration, thus paving the way toward the operando study of homogeneous systems.

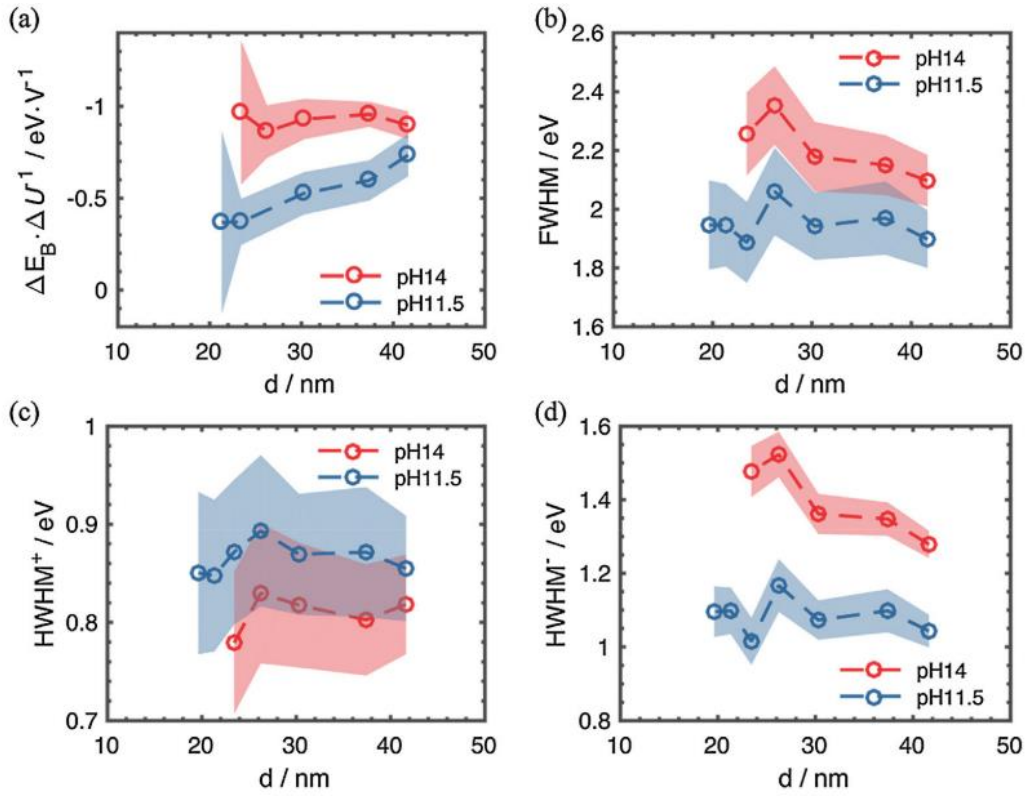

Figure 2.8: O1s peak X-Ray photoelectron spectra (XPS) values recorded at pH 11.5 (3.2×10^{-3} M) and pH 14 (1 M) in KOH solution, using the dip and pull method with Ir foil as working electrode. **(A)** O1s XPS peak shifting, **(B)** Full Width Half Maximum (FWHM), **(C)** Half Width Half Maximum on the positive binding energy side ($HWHM^+$), and **(D)** HWHM on the negative binding energy side ($HWHM^-$) depending on the estimated electrolyte film thickness that cover the working electrode. Reproduced from Ref.[109].

In a nutshell, despite its recent development, the D&P already covers a vast array of applications. Its ability to analyse both sides of the electrode-electrolyte interface, on model 2D-like electrodes, facilitates both the data analysis and the comparison with theoretical calculations and simulations. For instance, when applied to the electrode, D&P ease a careful assessment of the depth at which the chemical changes are occurring. Since it provides a clear view of the electrolyte properties through the meniscus, it may be considered as an ideal tool to follow redox changes of molecular species and study electrocatalysis involving soluble species. For the study of the electrode-electrolyte interface (*e.g.,* EDL), the XPS peaks shifting depending on the local electrical potential in the electrolyte is a fortunate phenomenon which allows to gather insights into the EDL, the PZC and, potentially, the ions profile distribution near the reactive interface. Yet, one of the XPS strengths, the surface sensitivity, is also one of its main limitations in electrochemical *operando* condition. The pressure close to the

solvent vapor saturated pressure and the electrolyte thickness are strongly limiting the signal intensity and only allow the study of species at high concentrations. Additionally, the mastering of D&P system remains difficult due to the necessity to control as much as possible the electrolyte thickness, which is a key parameter for the electrode-electrolyte interface sensitivity, and electrode polarization.

In the following section, we propose to further explore this method in the specific case of the EDL study of concentrated alkaline solutions (1 M CsOH and 0.1 NaOH) on Pt foil and glassy carbon electrode (GCE). The objective of this study is to evaluate the D&P approach ability to assess the cationic charges distribution within the thickness of the EDL. This could be made possible by deconvolving the XPS signal obtained for the Cs3d and Na1s signals as illustrated in **Figure 2.6**. Indeed, it has recently been observed that the nature of the cationic species in the electrolyte greatly impacts the electrochemical performance of a given system, caused either by cation size and screening effects, or by modification of the adsorption strength and dissociation properties of the reactive intermediates, or more generally by modification of the EDL structure owing to the nature of the cationic species, which further strengthen the need for such understanding. [171–174]

The choice of using two different electrode materials (Pt and glassy carbon) stems from their different properties in terms of known EDL behaviour, polarizability (GC electrode better fits the definition of the ideally polarizable electrode than Pt), but also ‘non-electrochemical’ parameters such as their wettability, that would control the shape of the meniscus. The choice of the concentration, albeit high (and therefore leading to small Debye length), is mandatory to obtain a cation-related signal of high enough intensity to perform its deconvolution. Hence, in the upcoming sections, we discuss which information can be obtained by D&P on such interfaces, what are the limitations that are unveiled through this study and how they can be overcome.

2.4 ‘Dip and pull’ experimental study

2.4.1 Pt / CsOH 1.0 M interface

Prior to its immersion in the electrolyte, the XPS signal of the platinum surface is recorded (**Figure 2.9.A**). The survey spectrum (not shown here) did not reveal any other element present on the surface than platinum and oxygen. According to literature, it is expected that the platinum surface is slightly oxidized due to prior

exposure to water and dioxygen from the atmosphere (note also that in order to remove organic contaminants, Pt was annealed in air at 950°C, see experimental procedure in **Section 2.7**).[175] This is confirmed by O1s signal that shows different oxygen contributions (**Figure 2.9.B**). One can observe traces of dioxygen (specific doublet around 542 eV [176]), which remained in the chamber since the pressure was around 15 mbar due to the liquid water presence and thus did not allow a full removal of air. A large peak of $H_2O_{(g)}$ around 538 eV, and two other peaks at 535.6 eV and 533.8 eV (δ = +1.8 eV) are observed. These two last peaks are associated with chemisorbed H_2O and HO^- as already reported in the literature.[60] It was additionally hypothesised that HO^- peak might also include an oxygen contribution from platinum oxides similarly to the observations of Stoerzinger *et al.*[164] Since platinum is slightly oxidized, the Pt4f spectra (see **Figure 2.9.A**) includes different components: Pt(0), Pt-$OH_{(chem)}$, PtO and PtO_2. The BE shifts from the Pt(0) photoemission line are taken from Favaro *et al.* study of platinum shown in **Figure 2.5**, *i.e.,* δ(Pt-OH)= +0.6 eV and δ(PtO)= +1.3 eV [165]. The PtO_2 position, *i.e.,* δ(PtO_2) = +2.5 eV, is taken from Saveleva *et al.* work, as it was offering a closer fit.[67] Finally, the peak fitting function was adjusted to match the signal ratio between peaks expected from a passivation monolayer (1 monolayer = 3 Å, which should represent 15~20% of the total platinum signal). It is nevertheless hard to rule out formation of islands (rather than a continuous film) of platinum oxide (which could be due to the Pt cleaning procedure, *cf.* **Section 2.7**) as their eventual contribution would be included in the Pt-Ox signals of the passivation layer. This procedure allowed a reasonable fit of the electrode-associated peaks using a Voigt function with an exponential tail function.[67] Detailed XPS peak fitting parameters for this figure, and the following ones are reported at the end of this chapter, in **Table 2.1**.

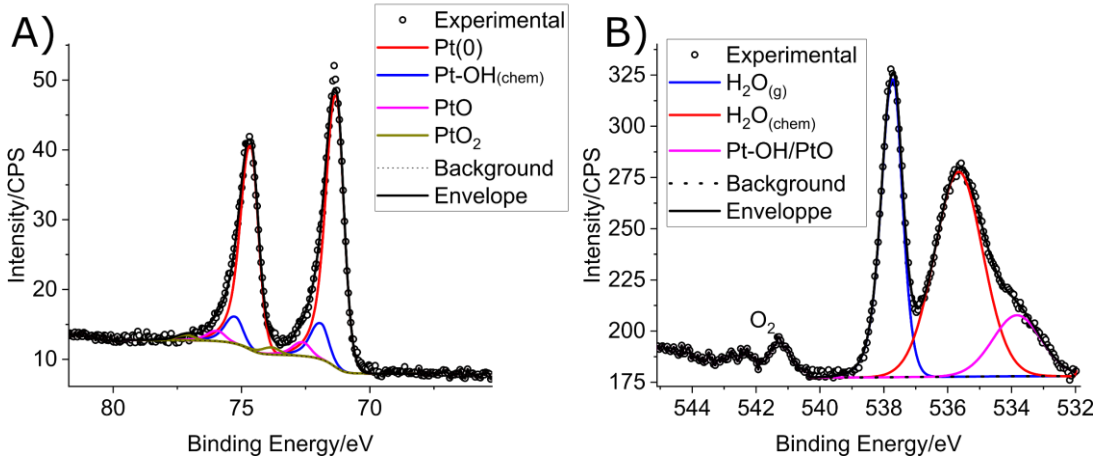

Figure 2.9: **(A)** Pt4f and **(B)** O1s XP spectra of the pristine working electrode (platinum foil) surface before dip and pull experiment. Beam energy = 1.6 keV. Peak fitting parameters are described in **Table 2.1**.

To obtain an accurate fitting for the electrolyte peaks with a minimized contribution of the electrode-electrolyte interface, the electrode is dipped and pulled out of the electrolyte until a > 30 nm thick electrolyte layer is obtained at the analysis spot (visible electrode related XPS peaks). The obtained XP spectra are shown on **Figure 2.10**. The almost invisible Pt4f peak which appears at the same energy window confirms the presence of a thick electrolyte layer on the electrode surface. Hence, it is believed that the majority of the signal comes from the 'electrolyte bulk', *i.e.,* the part of the electrolyte which is not impacted by the interface. Cs3d and Cs4d peak doublet relative positions and fitting function were then determined for our experimental setup and are detailed in **Table 2.1**. In the meantime O1s signal (**Figure 2.10.B**) shows two electrolyte-related contributions, attributed to $H_2O_{(l)}$ and $HO^-_{(aq)}$ as no other oxygen contributions are expected in this system. One notes the high contribution of the HO^- peak compared to the $H_2O_{(l)}$ peak (1:5 respective area ratio). As (i) XPS is quantitative, (ii) those peaks have almost the same energy and (iii) come from the same phase, one can roughly attribute this area ratio to the actual ratio of associated species. Assuming the electrolyte concentration is homogeneous in the whole electrolyte film, this means the actual $HO^-_{(aq)}$ concentration in the meniscus is **~10 M**, *i.e.,* much higher than the one in the electrolyte bulk (1 M). An approximate computation of the Cs^+ relative concentration using **Equation 1.10** was also performed and provide a similar estimation. This directly highlights one of the first limitations of the D&P approach when

the pressure conditions are lower than the saturating vapor pressure. Owing to its high surface exposed and the low chamber pressure (~15 mbar while the saturation water vapour pressure at 25°C is about 30 mbar), it is believed that a water evaporation in the meniscus took place during the measurements. Owing to the peculiarity of the diffusion in thin films (*e.g.,* in the meniscus) overall limited to the orthogonal direction to the electrode surface,[177] an equivalent concentration between the electrolyte bulk and the meniscus was not reached to compensate for that evaporation effect. Albeit this higher concentration is of interest in terms of data acquisition (*i.e.,* higher intensity of the signal), we believe it might be detrimental for the assessment of the EDL itself, as the Debye length shall be greatly decreased as a consequence of this increased concentration.

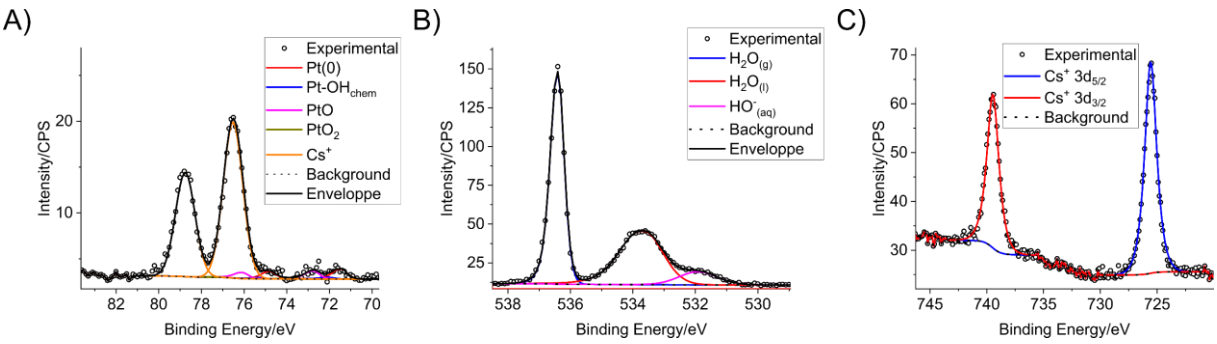

Figure 2.10: **(A)** Cs4d, **(B)** O1s and **(C)** Cs3d XP spectra obtained from a thick electrolyte layer for a Pt electrode in 1 M CsOH electrolyte. Photon energy is 1.8 keV.

The electrode was then dipped again in the electrolyte and a cyclic voltammogram was measured to determine the potential range one could work in the chamber to avoid bubbling resulting from either the OER or the HER, which could be detrimental to the detector. *Due to reference electrode (RE) calibration issues in such operando systems, the potentials indicated in the rest of this chapter is indicated* ***vs. Ag/AgCl*** *(RE) and may vary from a more classic laboratory experiment in a conventional three-electrode cell.* The obtained CV is shown on **Figure 2.11.C** and shows Pt features in alkaline media.[178] One recognises the hydrogen adsorption/desorption features within −1.0 V and −0.6 V, the Pt oxide formation on the anodic cycle above 0.05 V, and the platinum oxide reduction peak around −0.3 V on the cathodic cycle.

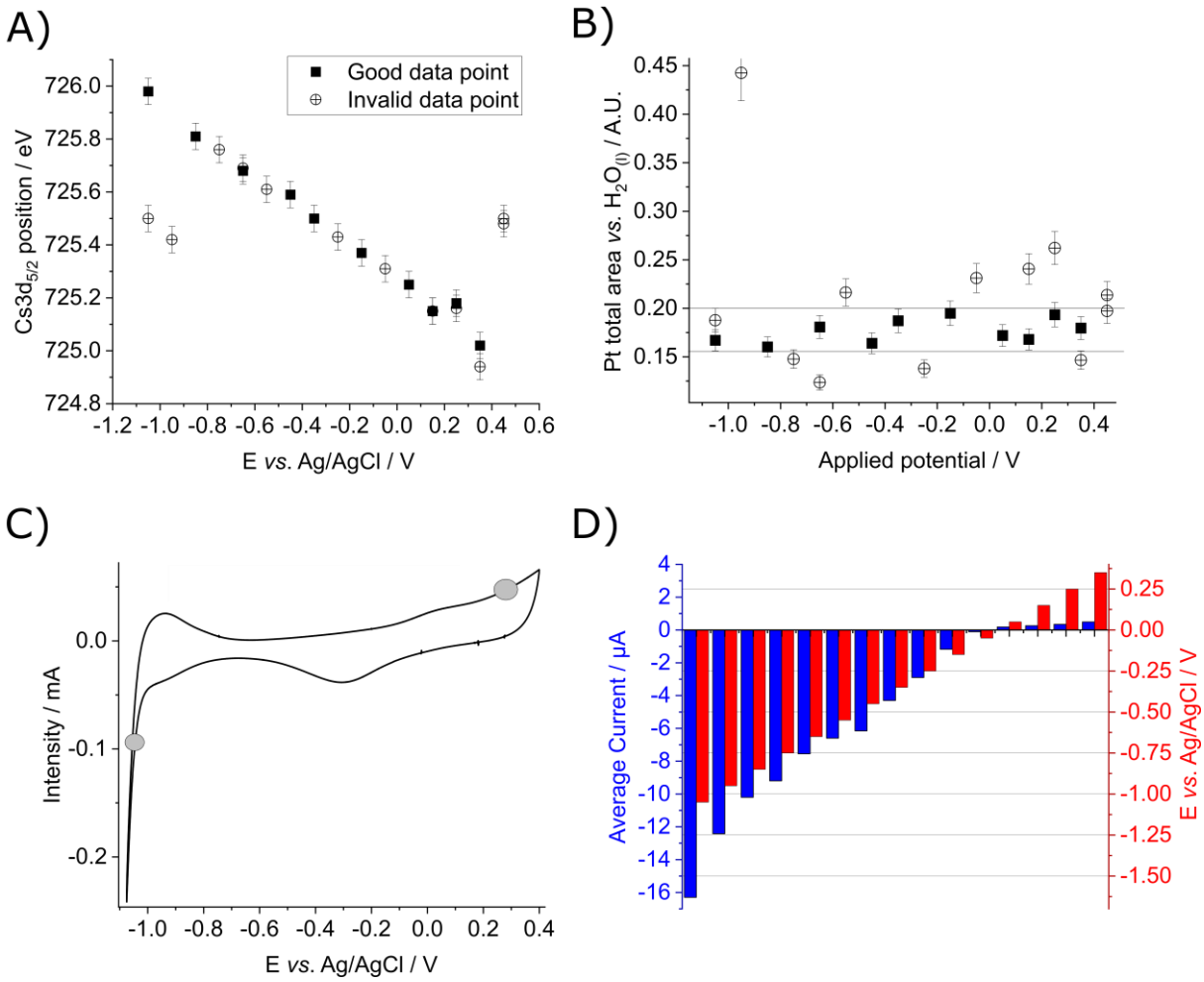

Figure 2.11: **(A)** Cs3d 5/2 peak position and **(B)** Pt4f total area versus $H_2O_{(l)}$ (O1s) area ratio depending on the applied potential during the whole dip and pull experiment. On these graphs "good" and "invalid" data points are indicated. 'Good data points' are associated to measurements satisfying both the electrode polarization (*i.e.* the Cs3d peak shift with the applied potential, figure (A)) **AND** similar electrolyte thin film thickness covering the working electrode (here we evaluated the electrolyte thickness using the relative area of Pt4f and H_2O(l)-related O1s peaks, and selected an interval for the 'valid' data, see figure (B). **(C)** Cyclic voltammogram of platinum acquired with the dip and pull setup. Scan rate is 50 mV/s, platinum foil working and counter electrodes, Ag/AgCl reference electrode, 1 M CsOH electrolyte. **(D)** Average intensity and applied voltage during the chronoamperometry throughout the dip and pull experiment. X axis represents the sequence of measurements. Average current intensity may depend on the dipping and pulling out of the electrode in the electrolyte.

Following the acquisition of the reference XPS patterns and of the Pt electrochemical fingerprint, the operando assessment of the EDL using the D&P method started following the procedure described below:

- A new potential is applied to the working electrode.
- The working electrode is dipped and pulled 2 mm above the electrolyte to renew the meniscus (distance to the electrolyte bulk up to the analysis spot was 25~35 mm).
- The working electrode position is adjusted to reach a reproducible electrolyte thickness compared to the previous data acquired.
- Pt4f & Cs4d, O1s and Cs3d XP spectra are then recorded.

The electrolyte thickness reproducibility was quickly assessed in real time by trying to get roughly the same ratio between Cs4d (electrolyte related) and Pt4f (electrode related) peak intensities (see **Figure 2.12.A**). A quantitative thickness of the obtained electrolyte is estimated using **Equation 2.1** that allows determination of the electrolyte thickness (d) depending on the electrode XPS peak intensity (Pt4f) ratio between the emerged (I_{em}) and immersed electrode (I_{im}, *i.e.,* observed through the meniscus), and the electrons IMFP in water at the kinetic energy associated to the measured peak (λ_{IMFP}).[74] The obtained thickness is then estimated as ~13 nm in this case.

Equation 2.1 : $d = \lambda \times ln\left(\frac{I_{im}}{I_{em}}\right)$

After recording XP spectra between –1.05 and +0.45 V, each XPS scan (5 scans per D&P step) was analysed individually, and the ones showing a stable signal are summed up to maximise signal-to-noise ratio. The obtained processed spectra are then fitted using the Pt4f, Cs3d and Cs4d fitting parameters determined during the analysis without electrolyte (for Pt electrode) and in a thick meniscus (for the electrolyte) (**Figure 2.9** and **Figure 2.10**). The O1s was fitted using $H_2O_{(l)}$ and $HO^-_{(aq)}$ only. These two peaks fitting procedure is justified by (i) the good fit resulting from this model and (ii) the low contribution expected from adsorbates at the Pt surface along with their closeness in binding energy to the $OH^-_{(aq)}$, which would result in an imprecise and subjective fitting. This hypothesis is supported by space-integrating **Equation 1.8**, to estimate the signal quantity received from the layer between d and d' distance (as described in **Equation 2.2**, with λ_{IMFP} the electron IMFP, *d* and *d'* the distances from the liquid/air interface and I_0 the intensity emitted by a material's layer in absence of electron inelastic scattering). Note that a monolayer of oxygen-containing adsorbates buried under a ~13 nm thick water layer should then contribute around ~0.5 % of the

total liquid phase O1s signal, and is considered negligible compared to the XPS signal-to-noise ratio estimated at ~3 %.

Equation 2.2 : $I(d,d') = \int_d^{d'} I_0 \times e^{-\frac{x}{\lambda_{IMFP}}} dx = \left[e^{-\frac{d}{\lambda_{IMFP}}} - e^{-\frac{d'}{\lambda_{IMFP}}} \right] \times \frac{I_0}{\lambda_{IMFP}}$

The $Cs3d_{5/2}$ peak (as the most intense one and with the clearest background) position depending on the applied potential is represented on **Figure 2.11.A**. As expected, due to its presence in the electrolyte, the peak position shifts towards lower binding energies with increasing potential. This confirms that the observed Cs is impacted by the potential applied to the working electrode. A linear trend can be observed from −1.05 to +0.35 V(δV = +1.4 V) where the peak position decreases from 726 to 725 eV (δBE=1 eV). The slope is −0.71 eV/V. As explained in the previous section, one should expect a 1 eV/V trend, indicating that the operating conditions are not 'ideal' in the meniscus. We believe that this discrepancy mainly arises from (i) the ohmic losses through the meniscus, which lead to a lower potential 'felt' in the meniscus that in the electrolyte pool (*i.e.,* the bulk of the beaker); (ii) the specific properties of the meniscus, in terms of electrolyte concentration, pH, *etc.* which are different from the electrolyte pool. Some data points in this plot are out of the trend. This indicates the absence of electrode polarization due to a loss in the ionic conduction between the analysed spot and the bulk of electrolyte. One will note that, in absence of electrolyte connection the $Cs3d_{5/2}$ peak tends to be positioned around 725.5 eV, which corresponds to the $Cs3d_{5/2}$ peak in absence of polarization. Those points are included in the "invalid data point" group on **Figure 2.11**, and will not be part of figures discussed in what follows. Similarly, the relative area ratio between Pt4f and $H_2O_{(l)}$-related O1s was computed and is displayed on **Figure 2.11.B.** This ratio is used here as a way to follow the stability of the meniscus thickness between each measurement, aiming to only compare experiments with a similar electrolyte thickness. As such, points which gave a ratio out of the 0.15 and 0.20 interval are considered "invalid". <u>As a consequence, the points which were kept for the following discussion are only those which both showed polarization and a meniscus of the adequate thickness.</u>

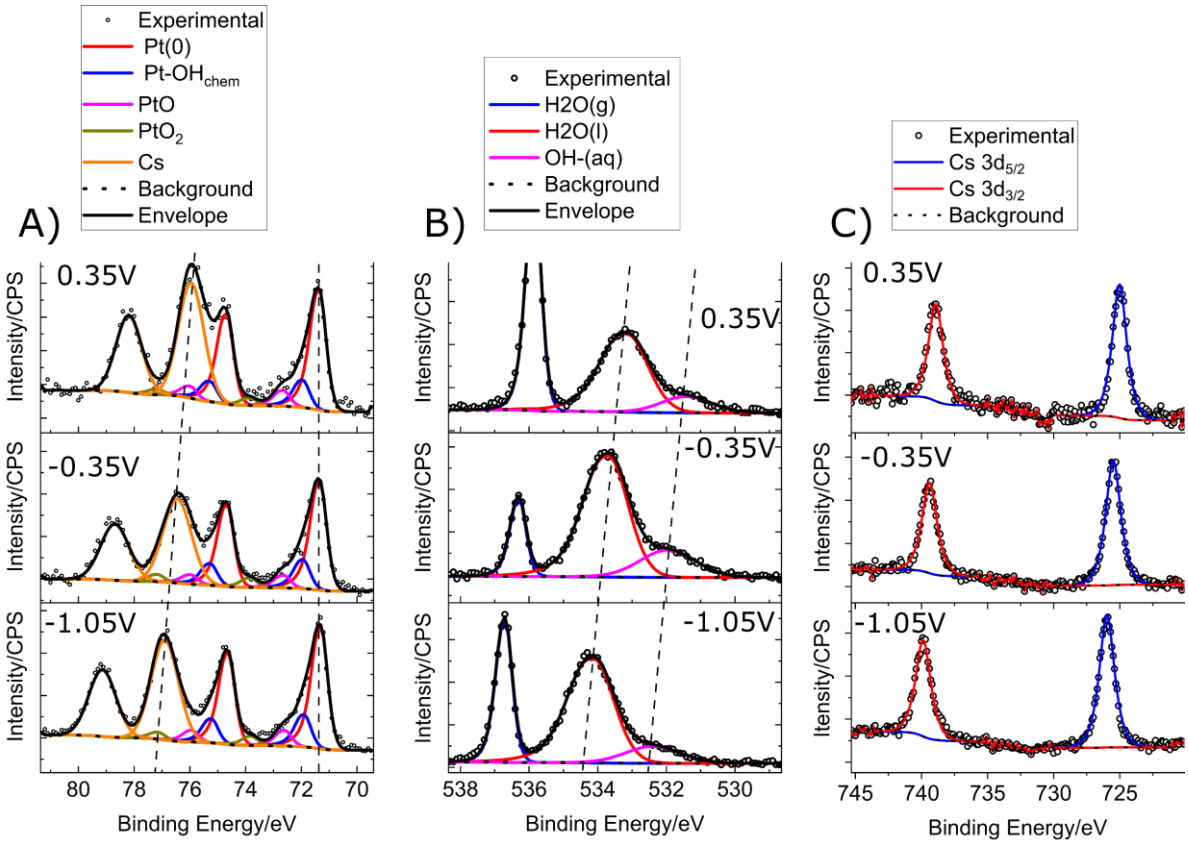

Figure 2.12: **(A)** Pt4f & Cs4d, **(B)** O1s and **(C)** Cs3d XP spectra obtained from D&P setup at 0.35, –0.35 and –1.05 V vs Ag/AgCl in 1 M CsOH. $Pt4f_{7/2}$, $Cs4d_{5/2}$, $H_2O_{(l)}$ and $HO^-_{(aq)}$ O1s peak position shifting is highlighted. Photon energy is 1.8 keV.

A set of three valid XPS measurements (at +0.35 V, −0.35 V and −1.05 V) are displayed on **Figure 2.12**. One notes the absence of Pt4f shifting and the consistent shifting of each liquid associated peaks (Cs, $H_2O_{(l)}$, $HO^-_{(aq)}$) and $H_2O_{(g)}$ peak, as the latter is not electrically connected to the ground (through the working electrode), but its potential shall mainly depend on the EDL, with a contribution of the electrolyte-air electrical potential difference, a second interface which is also still poorly understood.[179,180] The fitting procedure seems valid as well as no shoulder or peak is unconsistent with the envelope proposed. As a consequence, the platinum composition, the peak relative intensity and the FWHM depending on the applied potential are displayed on **Figure 2.13**.

Relative contributions of the four different components of the Pt4f (Pt(0), $Pt\text{-}OH_{(ads)}$, PtO, PtO_2) in the total Pt4f signal as a function of the applied potential is shown in **Figure 2.13.A**. The expected and observed main component is Pt(0), as only modifications within the first atomic layer(s) are expected. However, the constant

presence of Pt-$OH_{(ads)}$, PtO and PtO_2 even at potentials below the Pt oxides formation (*i.e.,* 0 V as seen from CV in **Figure 2.11.C**) is counterintuitive. Indeed, the approximate 30% contribution from oxides to the Pt4f signal corresponds to ~6 to 7 Å thick oxide layer (~2 monolayers). Albeit the estimation of the oxide contribution may be imprecise due to the experimental inaccuracy (*e.g.*, noise, fitting errors, absence of experimental reference spectra in our setup), we believe that the key reason behind the high Pt oxide contribution is the presence of oxide clusters/islands on the electrode surface. Indeed, PtO_x contribution might come from oxide 3D clusters/islands, in addition to a thin passivation layer. The full reduction of such islands being much slower than a 2D layer, this could explain the absence of apparent oxidation modification in the sample on the timescale of the analysis. This hypothesis is supported by the rather strong current obtained during the analysis (see **Figure 2.11.D**) under reductive potentials (<−0.4 V) compared to −0.1 V value (above the PtO_x reduction potential), and which should quickly diminish over time in the case of a 2D passivation layer, despite a possible contribution of oxygen reduction reaction in those conditions. Indeed, literature data confirms that oxidation/reduction of Pt electrodes is a complex multistep process involving subsurface oxygen species as well as 2D and 3D oxide structures.[181,182] One should also consider that high electrolyte concentration (estimated above as ~10 M for CsOH) may significantly slow down the electrode kinetics (including the kinetics of the Pt oxide reduction) due to the low fraction of 'free' water molecules (that is molecules which do not belong to the ions solvation shells).[183] Finally and despite an apparent potential-independent presence of Pt oxides in the XP spectra, it was experimentally observed during the experiment that the Pt wettability changed when increasing the potential > 0 V (*i.e.,* the surface became much more hydrophilic), which would be indicative of the Pt surface oxidation above this potential (and/or, of Pt oxide reduction below this potential).

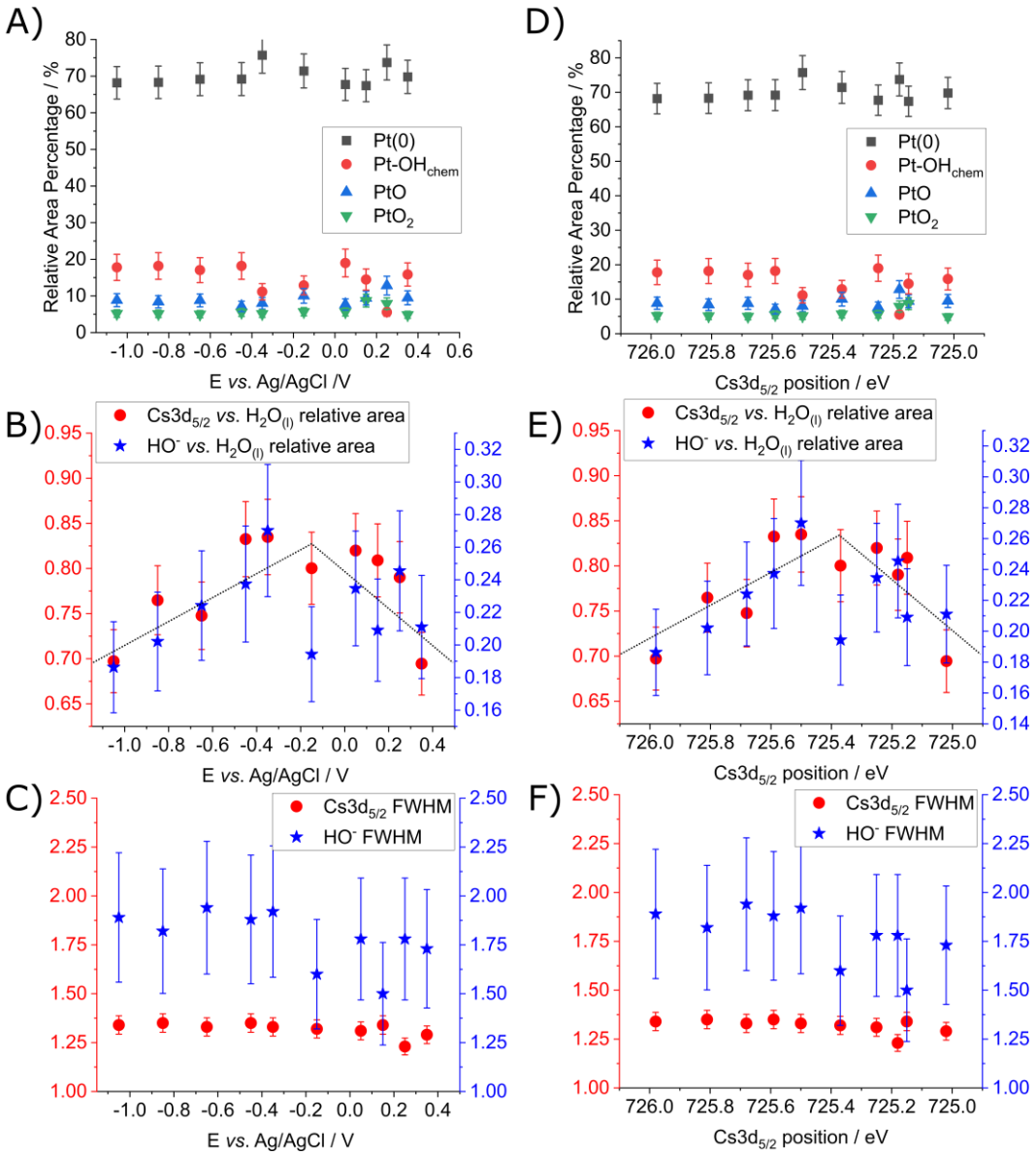

Figure 2.13: **(A,D)** Relative area percentage of different Pt contribution, **(B,E)** Electrolyte anions relative area versus liquid water, **(C,F)** HO^- (O1s) and $Cs3d_{5/2}$ full width at half maximum (FWHM) depending on the applied potential and $Cs3d_{5/2}$ position respectively. Uncertainties were roughly estimated by fitting results differences, taking different extremum background values.

To evaluate any further change in the concentration ratio between the alkali cations and H_2O, the Cs3d and HO^- (O1s) relative area versus the $H_2O_{(l)}$ (O1s) area are plotted as a function of the applied potential and of the $Cs3d_{5/2}$ binding energy (see **Figure 2.13.B** and **E**). One can observe that despite a strong noise in the computed values, a trend is observed, as the ion peak areas increase versus liquid water up to $-0.25\ V < E < 0.25\ V$, before decreasing again. This is indicative that from −1 V to

−0.25 V < E < 0.25 V, the salt concentration in the meniscus is gradually increasing, despite the fact that the meniscus is renewed between each experiment. A possible reason for that trend would be the change of the surface chemistry depending on the applied potential, which impact the electrolyte thin film mobility on the electrode surface. In particular, the oxide formation on the electrode surface could drastically impact the molecular reorganisation of the interface, which may explain the trend change in the alkali concentration depending on potential at ~ -0.25 V (approximatively the Pt oxidation 'onset' potential).

In parallel, the FWHM trends observed for OH^-(O1s) and $Cs3d_{5/2}$ do not indicate (i) the clear presence of the PZC (which would have been identified by a minima in FWHM) and (ii) a broadening of the FWHM around said PZC induced by the potential distribution within the EDL (see **Figure 2.13.C** and **F**). This indicates that it is impossible to clearly observe the EDL on a Pt electrode in 1M CsOH in our operating conditions, and to deconvolute precisely enough the FWHM signal, owing to the increased concentration in Cs^+/OH^- in the meniscus and the resulting small Debye length and low contribution of the EDL to the overall XPS signal.

2.4.2 Pt / NaOH 0.1 M interface

A second set of Pt/alkaline media interface was studied using 0.1 M NaOH electrolyte. The reasoning behind this choice stems from the interest of studying the effect of another cation, which is believed to impact the properties of the EDL. Na^+ is a smaller cation, with a larger solvation sphere ($r_{solvation}(Na^+)$ = 2.44 Å, $r_{solvation}(Cs^+)$ = 1.73 Å), resulting in a lower diffusion coefficient ($D(Na^+)=13.5\times10^{-10}$ $m^2.s^{-1}$, $D(Cs^+)=19\times10^{-10}$ $m^2.s^{-1}$).[184] The use of a lower concentration aims to overcome the limitation that was observed in the previous section, *i.e.,* the low Debye length and the resulting impossibility to observe the EDL, as a lower concentration in salt in the meniscus should result in a thicker EDL. The experimental approach, and identification of 'invalid' data was performed as for the Pt / 1M CsOH, while following the Pt4f, Na2s and O1s XPS peaks. The choice of the Na2s as a characteristic peak to follow reside in (i) its low binding energy (64.2 eV) resulting in a higher kinetic energy for the emitted photoelectron (*i.e.* higher λ_{IMFP} in liquid water) and higher sensitivity to the electrolyte depth, (ii) as well as a convenient position as it allowed us to simultaneously record Pt4f and Na2s and choose a repeatable electrolyte thickness at the different applied

potentials. The identification of the 'valid' points is presented in **Figure 2.14.A** and **B**, whereas the cyclic voltammogram of the Pt / 0.1 M NaOH is illustrated in **Figure 2.14.C**. The electrochemical signal is far more defined than for 1 M CsOH (due to the quality of the salts used and the intrinsic effect of the cation [185] on the Pt CV). One notices an upshift of the observed potential range and of the Pt characteristic peaks by ~ 60 mV *vs.* 1 M CsOH, which is consistent with the decrease in pH from 14 to 13. In terms of electrolyte thickness, only the points in the range indicated on **Figure 2.14.B** were kept. The electrolyte thickness is estimated to be within the range of **18~22 nm**. This is thicker than the previous subsection with the Pt/CsOH 1 M interface, due to the lower Na2s cross section (2.6×10^{-21}cm^2 at $h\nu$=2000 eV) compared to Cs3d$_{5/2}$ (130×10^{-21}cm^2 at $h\nu$=2000 eV) [186,187], which require a thicker electrolyte to get a reasonable signal. While the prepared electrolyte had a 0.1 M NaOH concentration, the relative O1s signal specific to HO^- once again shows a ~1:5 area ratio compared to the $H_2O_{(l)}$ peak corresponding to a ~10 M actual concentration in the meniscus, indicating that the alkali accumulation within the meniscus seems to be independent of the concentration in the beaker, but rather determined by the pressure in the vacuum chamber (as discussed in **Section 2.4.1**).

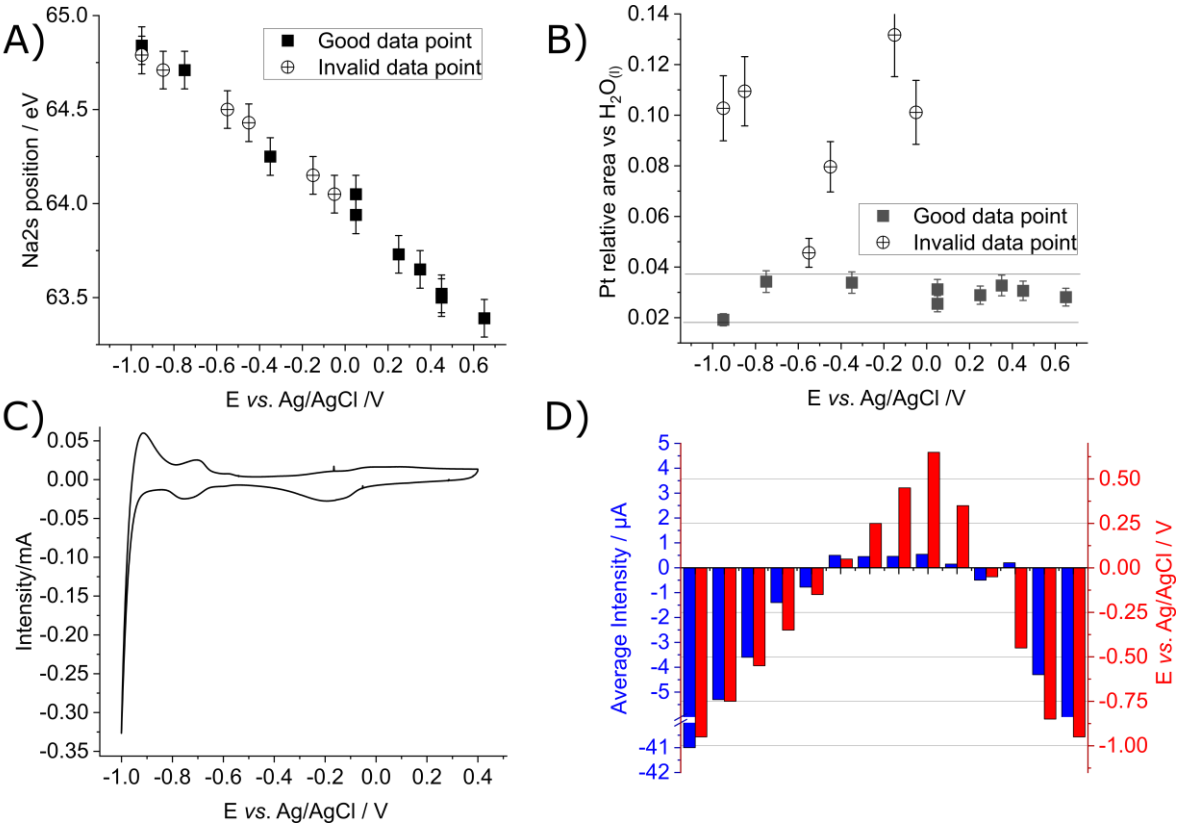

Figure 2.14: **(A)** Na2s binding energy peak position depending on the applied potential, **(B)** Pt4f peak relative area compared to $H_2O_{(l)}$ O1s peak, and **(C)** Cyclic voltammogram at 20 mV/s in the dip and pull setup with Pt foil as working electrode and counter electrode, Ag/AgCl reference electrode, NaOH 0.1 M electrolyte. **(D)** Average current and applied potential during the chronoamperometry throughout the dip and pull experiment. X axis represents the sequence of successive measurements. Average current may depend on the dipping and pulling out of the electrode, in addition to the applied potential.

Figure 2.15 represent series of XPS measurements at 3 different potentials (+0.35, −0.05 and –0.95 V). Similarly to Pt / CsOH 1 M, the Na2s (as well as the O1s of the various oxygen peaks) binding energy shifts toward lower binding energies with the increasing potential, thus being consistent with the fact that the Na^+ is present in the electrolyte. The Pt4f binding energy remains stable. Interestingly, as observed in **Figure 2.14.A**, (i) excellent polarization was achieved throughout the experiment and (ii) the slope is close to the –1 eV/V, *i.e.,* –0.9 eV/V. This last observation is probably due to lower ohmic losses in the meniscus due to thicker electrolyte layer compared to the Pt / CsOH 1 M experimental series.

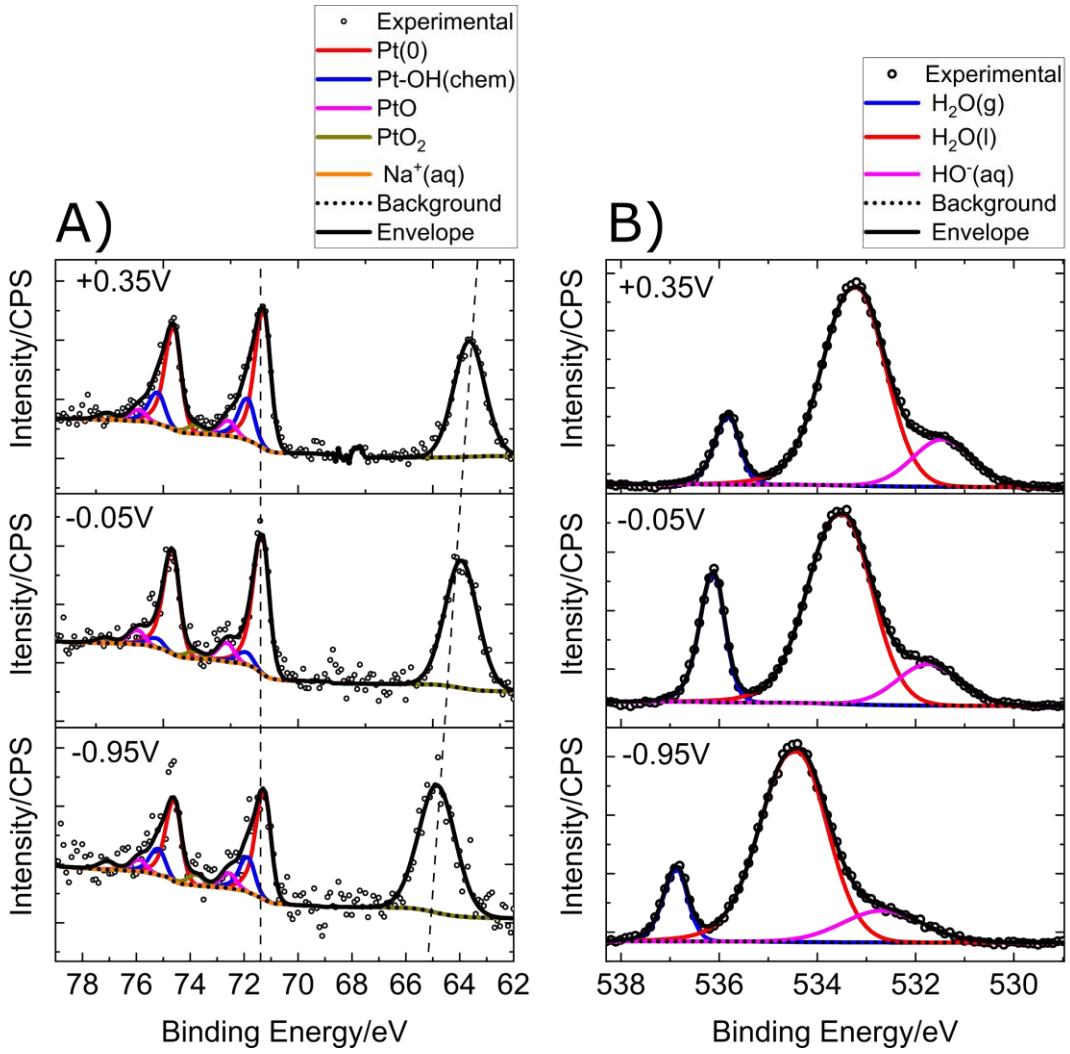

Figure 2.15: **(A)** Pt4f and Na2s, **(B)** O1s XP spectra obtained at +0.35, –0.05 and –0.95 V vs Ag/AgCl in dip and pull spectro-electrochemical operando setup using Pt foil as working electrode and NaOH 0.1M as electrolyte. Photon energy is 1.8 keV

Pt oxidation depending on the applied potential on **Figure 2.16.A** and **D** did not show a different result from the one in 1 M CsOH subsection. Once again, the Pt oxide signal is observed even in the low potential region, therefore implying that the underlining phenomena are similar to those discussed above. Furthermore, the FWHM of the O1s HO^- component seems to have a decreasing trend with the potential increase (**Figure 2.16.C** and **F**). The rather thick electrolyte compared to the thin EDL (owing to the concentration) is an argument against the EDL playing a major role in this trend, as well as the lack of a similar trend for Na^+. Moreover, one could expect a 'V' shape when it comes to FWHM *vs.* applied potential (**Figure 2.7**), as a minimum must be reached (albeit in less concentrated electrolyte) around the PZC of Pt (–0.3 V to ~ 0 V vs Ag/AgCl [134]).

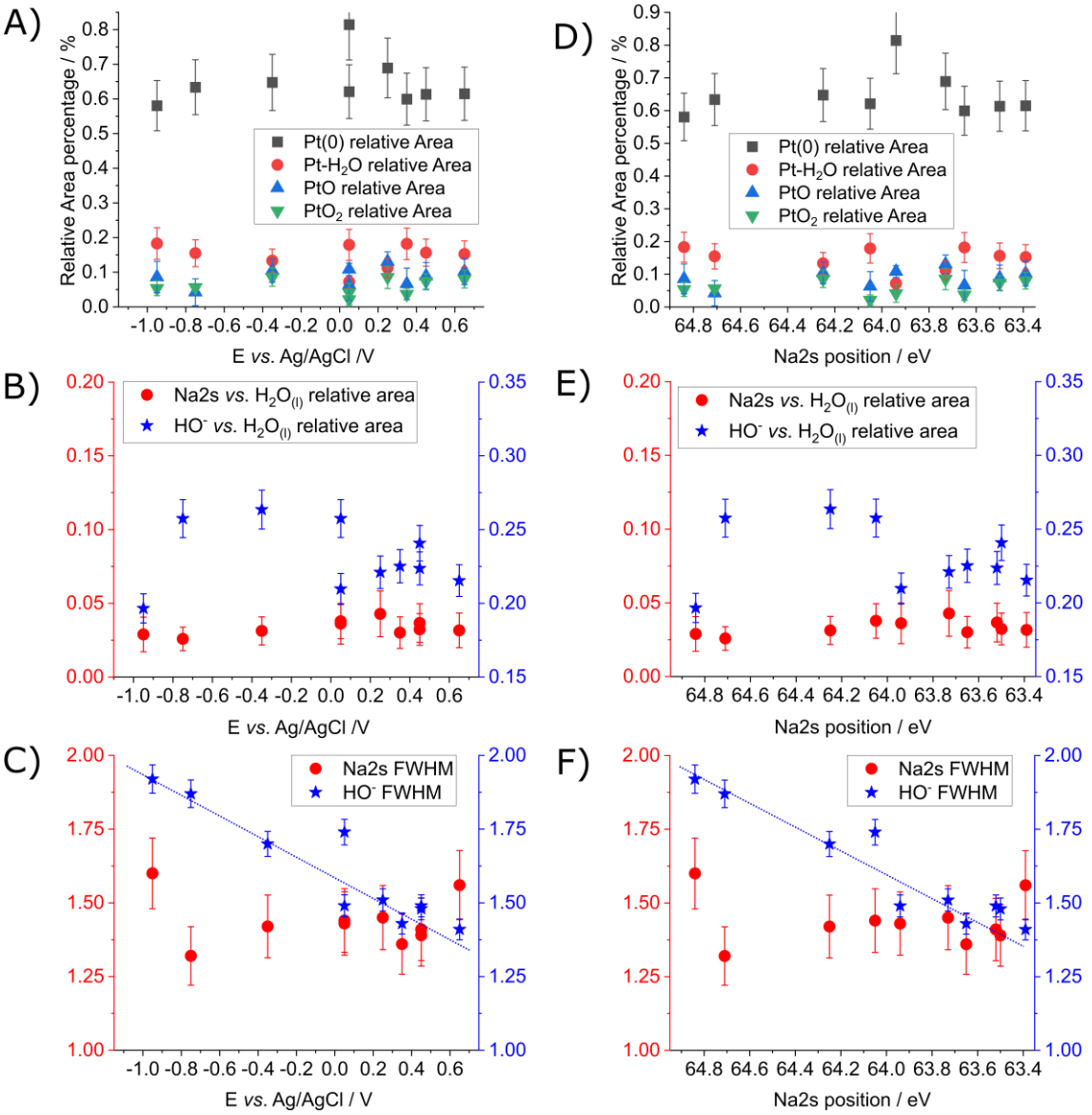

Figure 2.16: XPS fitting results regarding the dip and pull electrochemical system with Pt foil as working electrode and NaOH 0.1 M as bulk electrolyte. **(A)** Pt4f component relative area, **(B)** Na2s and $HO^-_{(aq)}$ O1s components relative area compared to the O1s $H_2O(l)$ component and **(C)** H_2O, HO^- O1s contributions and Na2s FWHM depending on the applied potential.**(D),(E)** and **(F)** are identical to (A),(B), and (C) but plotted against the Na2s position in order to fit the actual working electrode potential. Uncertainties were roughly estimated by fitting results differences, taking different background values.

The most relevant hypothesis would then be a non-homogeneous electrolyte thickness on the analysis spot, resulting in a signal broadening, which is supported by the lower number of valid points in the cathodic region, due to a more difficult electrolyte thickness control (see **Figure 2.13.B** and **E**). Furthermore, a variation of the meniscus

shape in between the analysis points could result in a variation of the OH^- distribution at the gas/liquid interface, which would be reflected in the FHWM. *However the complexity and the insufficient understanding of the electrolyte/gas interface limit the possibility of drawing definite conclusion without any simulation.* Finally we should keep in mind that due to the high electrolyte concentration and the low quantity of 'free' water molecules not involved in Cs^+ and OH^- solvation, the EDL behaviour may be hard to perceive.

2.4.3 Glassy Carbon Electrode / 1 M CsOH

While platinum foil use as a working electrode is convenient (easier to clean, good conductivity in the whole electrode, well known electrochemical behaviour), we know the electrode behaviour diverged from an ideally polarisable electrode. The extreme reactivity of platinum surface and its strong water dissociation capability may add different phenomena on top of the EDL effects. An interesting replacement to the Pt as working electrode may be the Glassy Carbon Electrode (GCE), its low reactivity towards water oxidation and reduction allowing the exploration of a larger potential window. Additionally, its well-known cleaning procedure and good flatness control makes it a good candidate for theoretical EDL studies. In this part we therefore tried the EDL D&P study using GCE working electrode and CsOH 1 M as electrolyte.

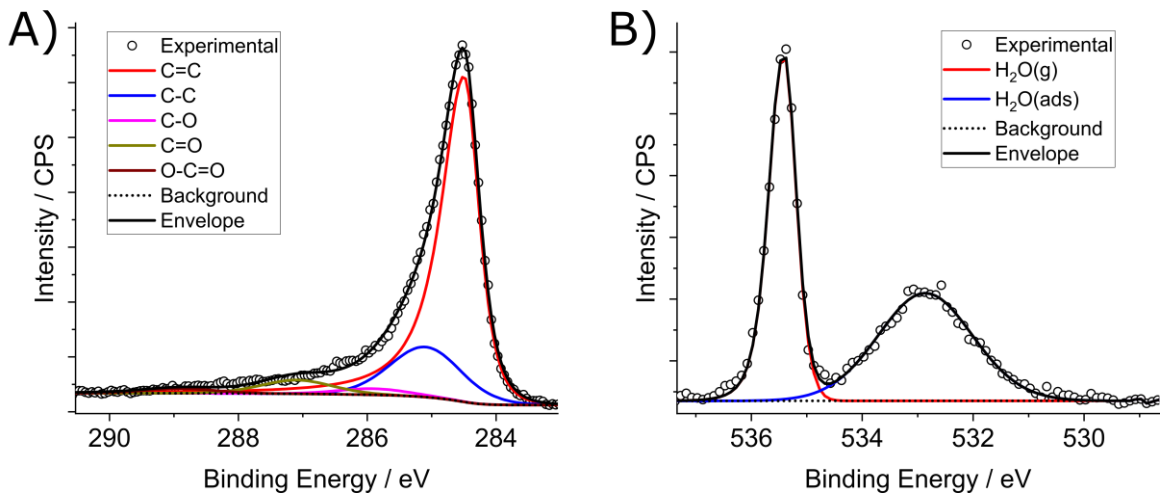

Figure 2.17: **(A)** C1s and **(B)** O1s XP spectra obtained from pristine glassy carbon electrode prior to dip and pull experiment. Photon energy is 1.8 keV.

The initial XPS GCE signal without electrolyte is shown on **Figure 2.17**. The C1s signal (**Figure 2.17.A**) is fitted using functions described in **Table 2.1**. The BE values were

taken from literature and adapted to propose the best fit throughout the experiment [202]–[204]. The binding energy of the graphitic (C=C) peak was set at 284.5 eV and kept constant for the rest of the experiment. The O1s signal (**Figure 2.17.B**) shows only two contributions, $H_2O_{(g)}$ and $H_2O_{(ads)}$.[190] This is different from the pristine Pt surface which showed an additional $HO^-_{(chem)}$ component (**Figure 2.9.B**) but consistent, as GCE does not have strong H_2O dissociation capability. The GCE / 1 M CsOH cyclic voltammogram is shown on **Figure 2.18.C** and is similar to the signal expected from a GCE. The low currents compared to Pt CVs shown previously, and the sluggish OER and HER confirm the low reactivity of GCE, while a small redox peak around -0.25 V is observed and could be associated to quinone/hydroquinone redox transition,[191] and/or dioxygen reduction. Currents above ~0.4 V may be attributed to the oxidation of carbon and OER occurring simultaneously.[192] Surprisingly, despite the higher glassy carbon hydrophobicity compared to Pt, the obtained meniscus was rather stable (**Figure 2.18.D**) from one measurement to another and estimated to ~11 nm. The polarization at the meniscus point was intermediate to what was observed for 0.1 M NaOH and 1 M CsOH on Pt (**Figure 2.10.A** and **Figure 2.17.A**), *i.e.,* a ~ –0.8 eV/V slope (**Figure 2.18.A**), this intermediate result might be explained by stronger ionic resistivity through the layer (due to thinner electrolyte layer) but an overall lower ohmic losses due to lower currents (~1 µA at 0.5 V for Pt / CsOH 1 M system *vs* ~0.3 µA at 0.5V for GCE / CsOH 1 M). The HO^--to-H_2O O1s relative area remained around 1:5 in the meniscus during the whole experiment, meaning the actual CsOH electrolyte concentration at the analysis spot is similar to previous experiments and around **~10 M**.

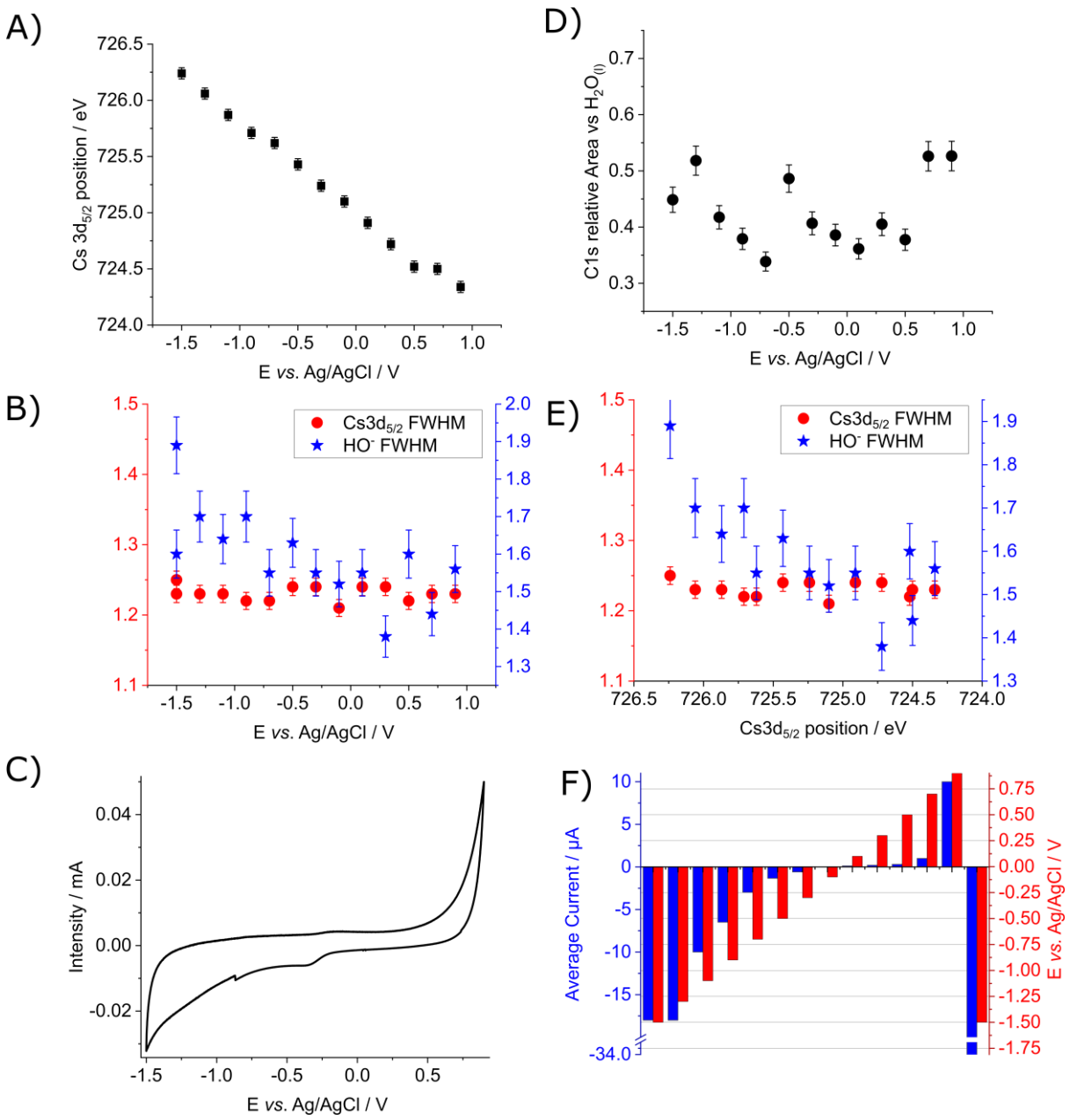

Figure 2.18: XPS fitting results regarding the dip and pull electrochemical system with GCE as working electrode, Pt foil as counter electrode, and CsOH 1 M as electrolyte. **(A)** $Cs3d_{5/2}$ position, **(B)** $Cs3d_{5/2}$, $HO^-_{(aq)}$ and $H_2O_{(l)}$ (O1s) FWHM, and **(C)** C1s relative area compared to O1s of $H_2O_{(l)}$ depending on the applied potential. **(D)** Cyclic voltammogram obtained in the spectro-electrochemical setup prior to the dip and pull experiment at 20 mV/s scan rate. **(E)** $Cs3d_{5/2}$, $HO^-_{(aq)}$ and $H_2O_{(l)}$ O1s FWHM depending on the $Cs3d_{5/2}$ peak position. **(F)** Average current and applied potential during the chronoamperometry throughout the dip and pull experiment. X axis represent the successive measurements sequence of the experiments. Average current may depend on the dipping and pulling out of the electrode, in addition to the applied potential. Uncertainties were roughly estimated by fitting results differences, taking different extremum background values.

On **Figure 2.19** one can observe a set of C1s, Cs3d and O1s XP spectra on that system at 3 different potentials (−1.5 V, −0.3 V and +0.9 V vs Ag/AgCl). One observes that similarly to previous systems, electrolyte-related peaks shift with the potential. However, contrary to the Pt4f peak, which did not shift with potential, the electrode-related C1s signal changes both the shape and the position (**Figure 2.19.A**). The shape of the C1s peak under polarization is rather different from the one observed without electrolyte, and despite several attempts, no consistent fitting was found for the whole range of potentials explored. Thus, in what follows it will be analysed qualitatively. **The C1s peak shifting with potential the same way as the electrolyte-related peaks** (~ –1.9 eV shift between –1.5 V and +0.9 V on the peak maxima), the shift cannot be related to the oxidation degree changes on the electrode surface, as oxidation of the surface would result in a shift towards higher binding energies. The fact that the shift of the C1s peak follows the electrolyte-related peaks indicates that the XPS-probed carbon surface layer is electrically 'disconnected' from the GCE. This could be explained by formation of a resistive layer on top of the GCE surface, likely formed under positive electrode polarization during the pre-analysis potential cycling (**Figure 2.18.C**). This hypothesis is supported by (i) the C1s peak shape changes compared to the reference C1s spectrum taken before electrochemical measurements (**Figure 2.17.A**), (ii) the too low binding energy position of C1s at 0.9V (284.3eV, which is lower than the reference C=C position 284.5 eV), and (iii) the cyclic voltammetry (**Figure 2.18.C**) which highlights electrochemical oxidation reaction occurring under positive polarization. The shape of the C1s peak is also affected by the influence of potential on the oxidation state of carbon. One would expect that application of anodic potentials would results in a lower contribution of graphitic carbon (low binding energy) and higher contribution of oxygen-containing groups (higher binding energy). Indeed, one may see that a shoulder on the low BE side (~285 eV) of the of the C1s peak observed at –1.5 V, which could be attributed to the C=C and C-C components, is absent at higher potentials. This suggests an oxidation of the carbon surface at positive potentials. The formation of a resistive layer on the GCE surface would additionally explain difficulties encountered to fit the C1s signal as there would be a superposition of shifted peaks (from the resistive layer) and non-shifted peaks (from the GCE bulk electrically connected to the ground). *The formation of that resistive layer would then question the validity of GCE as a working electrode for the EDL study as it would strongly impact the interface.*

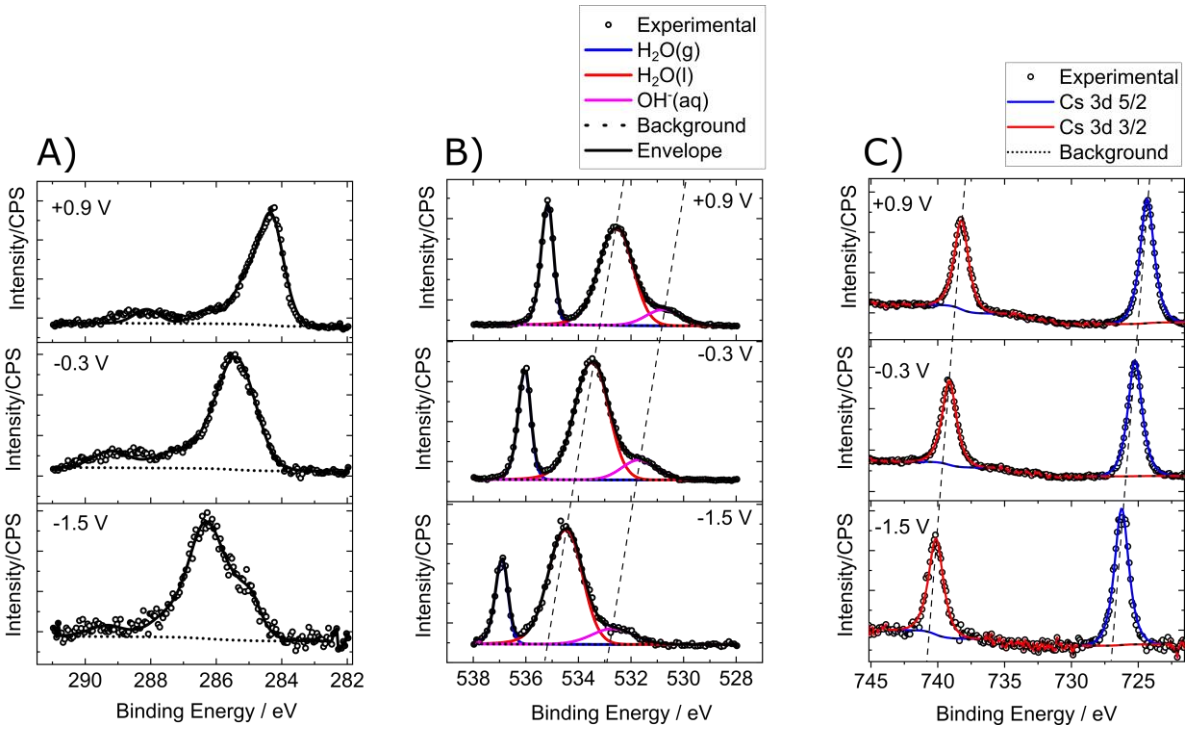

Figure 2.19: **(A)** C1s, **(B)** O1s and **(C)** $Cs3d_{5/2}$ XP spectra obtained at +0.9 V, −0.3 V and −1.5 V *vs.* Ag/AgCl in dip and pull spectro-electrochemical operando setup using Pt foil as working electrode and CsOH 1M as electrolyte. Photon energy is 1.8 keV.

2.5 A discussion on the challenges, limits and interest of the dip and pull method as a tool to assess the electrode-electrolyte interface

Operando spectro-electrochemical measurements are challenging from a technical standpoint, and the dynamic nature of the D&P system (*i.e.,* meniscus stability, evaporation, etc.) further amplifies those difficulties. Here, we discuss the different aspects that impact the assessment of the electrode-electrolyte interface by the D&P method, and the mitigation methods to decrease their effect. The reader is invited to refer to **Figure 2.20**, which illustrates the different challenges discussed in the following section. Then, we conclude on the advantages and disadvantages of the D&P method for studying the EDL, based on our results and those discussed in the literature.

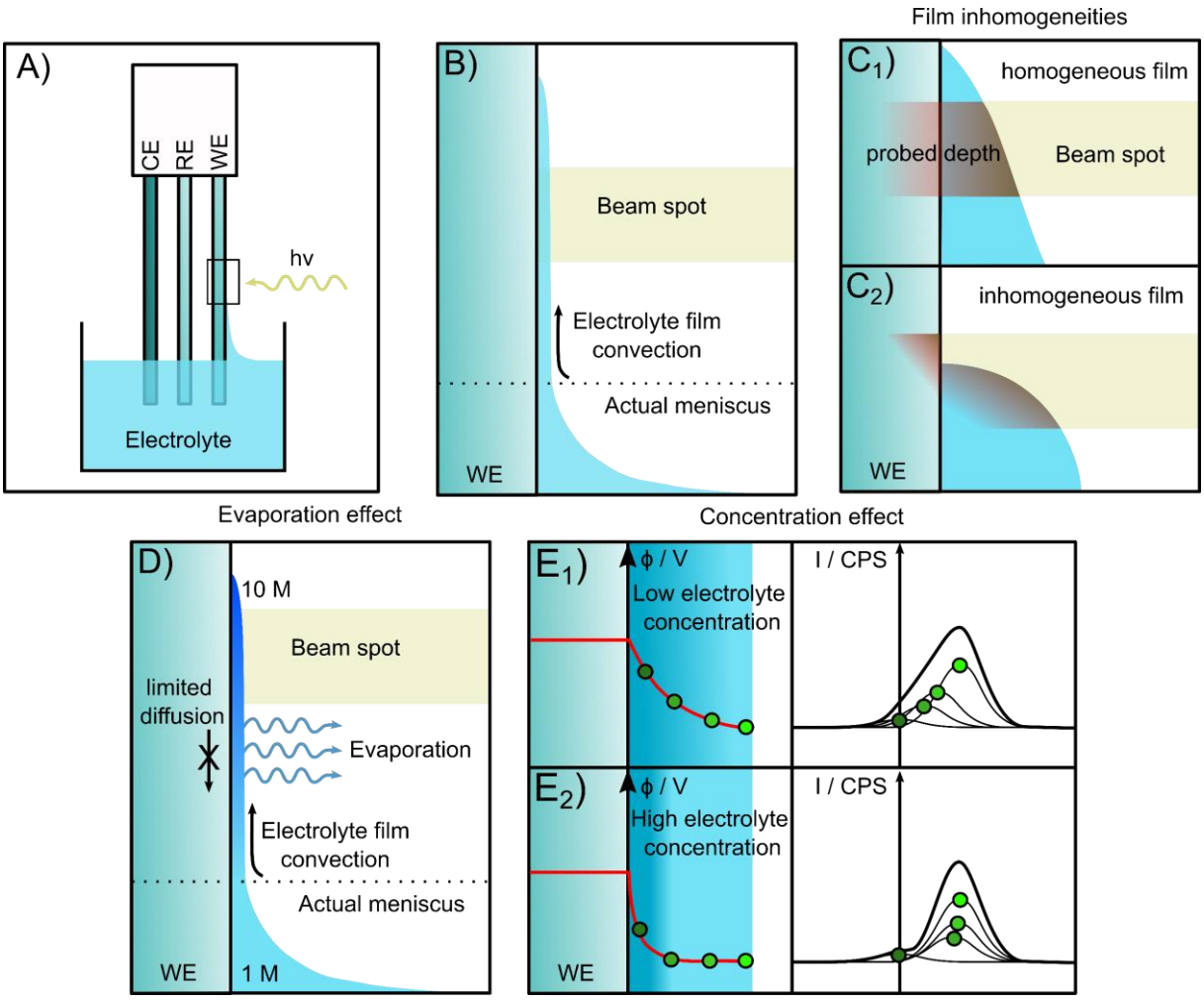

Figure 2.20: **(A)** Dip and pull experimental setup scheme, highlighting the analysis spot position which zoom is shown on **(B)**. **(C)** panel represent issues originating from the electrolyte film inhomogeneity, that might result in a wrong interpretation of the XPS signal. **(C_1)** is a 'proper' film meniscus that is rather homogeneous and allows the probe of the electrode and the electrolyte due to low thickness. **(C_2)** illustrates the case of electrolyte being non-homogeneously spread on the surface, with some electrolyte part avoiding electrode probing due to excessive thickness, and some part of the electrode not being connected to the electrolyte and thus not having a meaningful result, despite the signal able to show both electrode and electrolyte-related specific peaks. **(D)** illustrates the effect of evaporation on the electrolyte concentration on the analysis spot. **(E)** panel shows the effect of electrolyte concentration on the XPS peak broadening of soluble and solvent species, with the case of **(E_1)** low and **(E_2)** high electrolyte concentration.

2.5.1 Meniscus shape and thickness

In the D&P setup, the obtained XPS signal is the signal average on the whole beam spot (*i.e.* analysed spot, ~10 µm×25 µm with ~20 nm depth sensitivity depending on

the photoelectron kinetic energy). In order to get a result that can be trusted, the system must be (i) homogeneous on the whole analysis spot and (ii) remain stable during the whole measurement. The electrolyte film in particular determines the electrochemical activity of the working electrode and the XPS intensity corresponding to the interface. Therefore, one of the key parameters to control in such setup is the meniscus shape and thickness.

Firstly it is important to note that despite the use of the term 'meniscus' for the electrolyte covering the working electrode on the analysis spot, the analysed electrolyte rather resembles a mobile thin liquid film formed by the electrolyte molecule displacement on the electrode surface, up to the analysis spot (see **Figure 2.20.B**). This liquid thin film can extend as far as few mm from the actual visible meniscus, which was formed by the electrode immersion into the electrolyte. Said motion is dependent onto the surface hydrophobicity, and therefore, chemistry and morphology. The role of the working electrode, not only as electrocatalytic material, but also as the meniscus support, is then not to be underestimated. The chosen material hydrophilicity (or hydrophobicity) can strongly impact the electrolyte meniscus length and thickness. However, the choice of the electrode for the D&P is also controlled by the analysis of the signal, *i.e.,* the use of a porous electrode would result in a surface roughness that would greatly impact (i) the meniscus shape and properties (*e.g.,* the formation of a thin film might be far more challenging) and (ii) lead to a signal that is actually a sum of signals corresponding to pores of different depth, making analysis extremely difficult.

Depending on the working electrode and potential window, chemical changes might happen on the electrode surface during the measurement. This is illustrated for the GCE / 1 M CsOH system in **Figure 2.21**, where the C1s XP spectra of the 1st, 5th and 10th scan at −0.5 V (**A**) and −1.5 V (**B**) are shown. At −0.5 V, the C1s peak shows shape changes, probably resulting from the carbon oxidation and formation of a poorly conducting layer on the surface of the electrode, which might result in the C1s peak splitting into the signals from 'connected' and electrically 'disconnected' parts of the electrode. Similarly on the −1.5 V measurement a shift is observed both in case of the C1s (**B**) and Cs3d (**C**), which would indicate that the potential seen by the meniscus at this 'high' current density (*i.e.,* 34 µA, see **Figure 2.18.F**) is not stable, owing to changes in the ohmic losses and chemical organization within the meniscus and at the GCE surface.

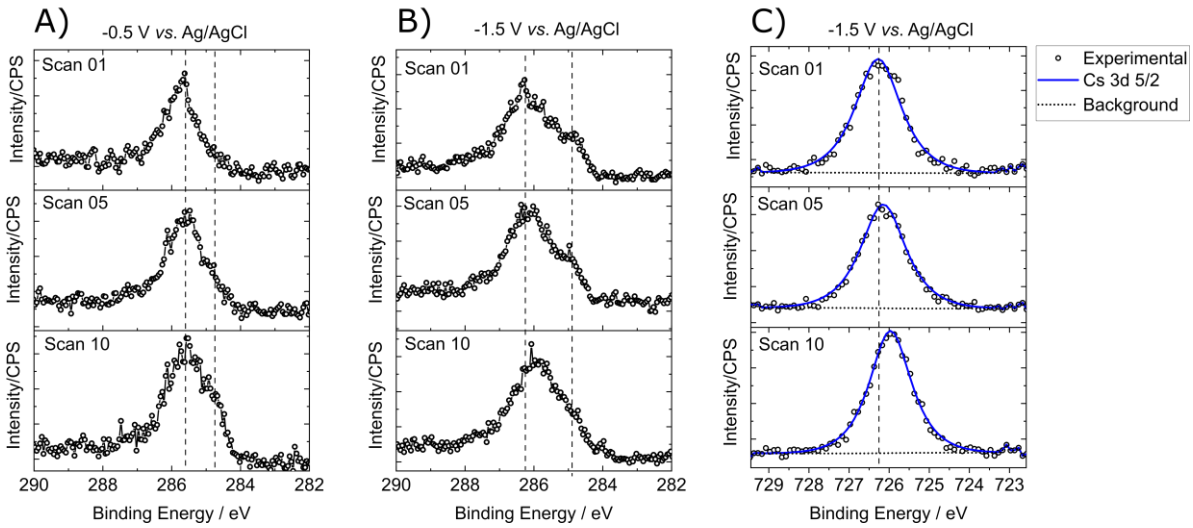

Figure 2.21: Example of the spectral evolution with time. Each panel shows the 1st, 5th and 10th scan of sequential XP spectra at a given potential: **(A)** C1s at –0.5 V, **(B)** C1s at –1.5V and **(C)** $Cs3d_{5/2}$ at –1.5V vs Ag/AgCl XP spectra obtained in GCE / CsOH 1 M dip and pull spectro-electrochemical setup. (~55 s per scan loop. 1 scan loop is 1 scan C1s spectra, followed by 1 scan O1s spectra, followed by 1 scan Cs3d spectra).

In case of a surface which is too hydrophobic, the topmost part of the electrolyte film can be sharp (see **Figure 2.20.C2**) resulting in an inhomogeneous electrolyte coverage of the analysis spot. In that case, the whole measurement is jeopardised as the measurement spot is not ionically connected to the electrolyte bulk, and the electrolyte thickness can therefore not be assessed correctly. It is important to note that there is no way to verify that we are not in such situation once the experiment is performed. But a careful investigation of the electrolyte presence just above the analysed spot before recording the XP spectra can prevent this error. An adequate protocol for the acquisition of the spectra would then be (i) finding the right spot of a desired electrolyte thickness, (ii) verify the electrolyte presence right above the beam spot and (iii) move back to the initial spot. In this case the electrolyte film should be homogeneous (see **Figure 2.20.C1**) in the investigated region. That method was applied during our experiments to minimize the probability of a film inhomogeneities on the analysis spot during the spectra recording.

2.5.2 Meniscus stability

As the electrolyte film formation depends highly on the surface chemistry, the film formation is actually dynamic. Due to the beam irradiation, the potential-induced changes in the surface chemistry or the distance between the electrolyte reservoir and

the analysis spot, the surface properties and the resulting hydrophilicity might quickly change. This is illustrated on **Figure 2.22**, taken from Pt / 1 M CsOH experiment. The measurement at –0.75 V *vs.* Ag/AgCl (**Figure 2.22.A)** illustrates a decrease in the thickness, shown by the increase of the Pt4f contribution (71.3 and 74.4 eV peaks) compared to the electrolyte Cs 3d peaks. At higher potentials (+0.35 V *vs.* Ag/AgCl, **Figure 2.22.B**) the electrode surface was probably slightly more oxidized, resulting in a more hydrophilic behaviour, and this despite the absence of visible oxidation of Pt surface in XPS (see Pt / CsOH 1 M and Pt / NaOH 0.1 M **subsections, 2.4.1** and **2.4.2** respectively). The absence of strong oxidation signal in the XP spectra, however, does not constitute an argument against this hypothesis, as only the chemistry of the very first external atomic layer of the metal is impacting the hydrophilicity of the surface. In this case the Pt 4f peaks intensity decreased until their disappearance, indicative of an electrolyte film thickness > 30 nm.

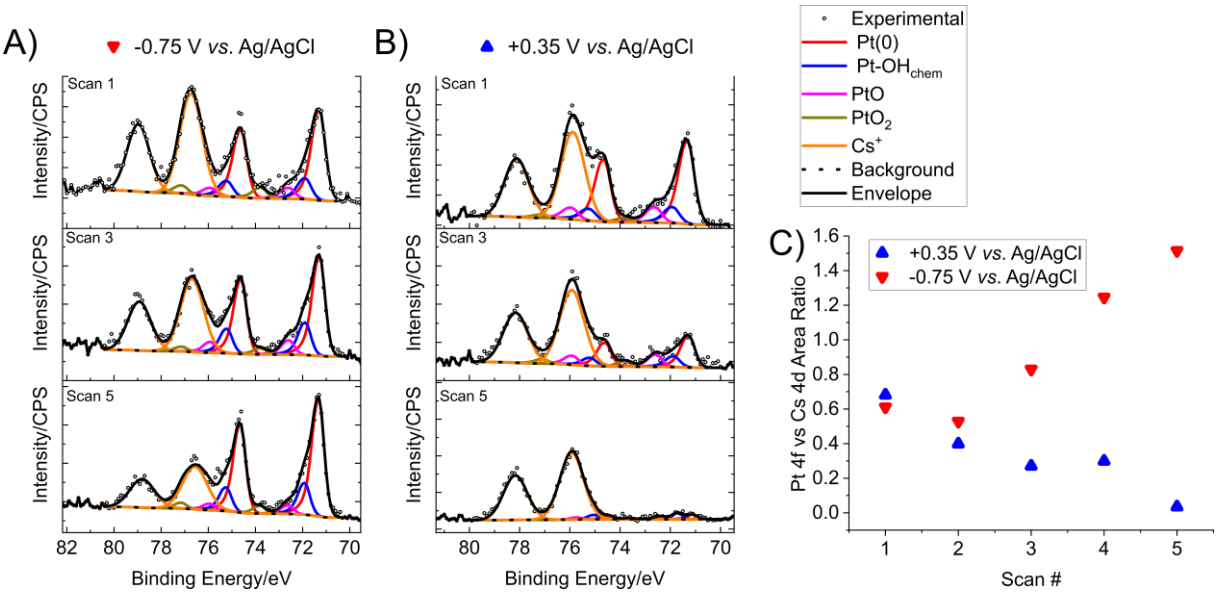

Figure 2.22: Examples of a bad meniscus control during 'dip and pull' experiments. Pt4f and Cs 3d XP spectra of the 1st,3rd and 5th scan at the same potential. **(A)** Spectra obtained at -0.75 V *vs.* Ag/AgCl, highlighting the meniscus thickness decrease due to surface hydrophobicity. **(B)** Spectra obtained at +0.35 V *vs.* Ag/AgCl, highlighting an electrolyte thickness increasing due to high hydrophilicity. **(C)** Pt 4f 7/2 and Cs 3d 5/2 peak area ratio evolution with the scan number. ~60 s per scan loop. 1 scan loop is 1 scan per region. Photon energy is 1.8 keV.

The surface chemistry changes being one challenge, the study of the electrode-electrolyte interface during an electrochemical reaction (*e.g.,* OER, HER) is another

one, as the ionic charge carrier's concentration shall vary during said reactions. This phenomenon was reported in the literature by Stoerzinger *et al.* [164,193] who proposed the addition of supporting electrolyte salt (KF 0.1 M) to prevent film instabilities (due to proton or hydroxide ions consumption in HER or OER regions, respectively). This led to a stable signal for as long as 2 hours under the OER conditions. The origin of this phenomenon was later rationalised by Marco Favaro [177] using stochastic simulations for ion diffusion in D&P systems and showed that diffusion was limited to the orthogonal direction of the interface in thin liquid electrolyte layers, therefore preventing electrolyte replenishment in hydroxyl consumption regions in case of OER in alkaline media.

2.5.3 Evaporation effect

The meniscus evaporation has a strong influence on the measurement. Due to the electron limited IMFP in the gas phase in case of soft X-Rays, working at low pressure is often required to get a more intense signal, but the lower the pressure, the stronger is the water evaporation in the meniscus. In our work, the concentration reached as high as **~10 M** at the analysed spot (assuming a homogeneous concentration in the liquid film), independently of the initial concentration in the bulk (1 M CsOH or 0.1 M NaOH). A combination of a low volume of electrolyte dispersed and dynamically spreading on a large electrode surface exposed to a pressure lower than the saturated vapor pressure, in permanent pumping, might explain this strong evaporation (see **Figure 2.20.D**). The fact that two different electrolyte concentrations tested resulted in the same hydroxide concentration at the interface highlights that the concentration at the top of the liquid film is probably thermodynamically controlled by the chamber pressure (filled mostly with gaseous water). Hence, water in the meniscus should evaporate until the concentration of the solution reaches the associated water vapor saturating pressure. This hypothesis is supported by the vapor saturating pressure in NaOH solution shown on **Figure 2.23**, where we observe that a water pressure of ~15 mbar is associated to a ~10 M NaOH concentration. To limit the evaporation effect, one could (i) cool down the electrolyte and the working electrode, to diminish the saturated vapor pressure, as already done in the literature [194], or (ii) work at higher pressure in the analysis chamber. This second option is the one used by the D&P studies presented in **Section 2.3.2**, where the authors used a 30 mbar pressure in the chamber (close to pure water vapor pressure). Yet, this option decreases significantly

the XPS signal measured and therefore increases the time required to record a spectrum of similar quality.

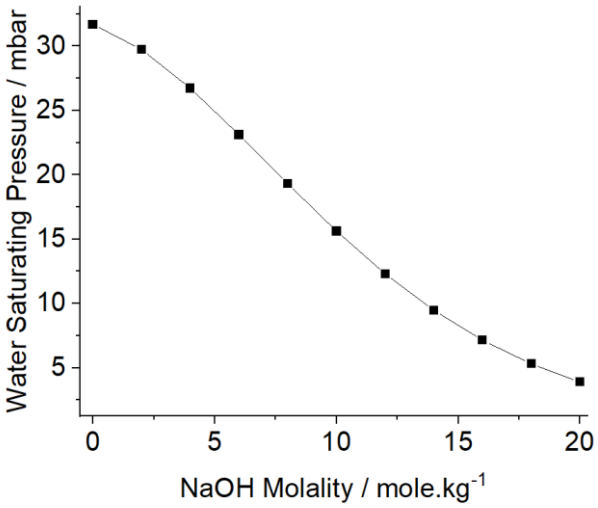

Figure 2.23: Water vapor saturating pressure depending on the NaOH molality (mole of solute per kg of solvent) at 25°C. Data reproduced from Ref.[195].

The high concentration of the electrolyte is one of the main reasons for the inability of our experiments to provide at least a semi-quantitative mapping of the EDL. Indeed the EDL thickness is significantly decreasing with the electrolyte concentration (**Figure 2.1.C**) [102]. As the EDL is thinner, the local electrical potential drops sharply and reaches a constant value much closer to the interface, which therefore diminishes the electrolyte XPS peak broadening changes that can be observed (see **Figure 2.20.E1** and **E2**). This phenomenon was theorised by Lichterman *et al.* [109] who estimated a ~2.5% change in the FWHM value with a film thickness of 10 nm at 1 M electrolyte concentration, while a 32% change may be expected at 3.2×10^{-3} M with a similar film thickness. Controlling the electrolyte concentration through the mitigation of evaporation effect is therefore critical to obtain significative trends in the FWHM variations.

2.5.4 XP spectra intensity

As the XPS peak broadening is shown to be hardly distinguishable, it is important to identify the key parameters that can positively (or negatively) influence the EDL study in dip and pull setup. Firstly, despite the fact that **the concentration** has a negative influence on the peak broadening as discussed above, a non-negligeable ion concentration is required in the view to record a decent XPS signal. Since XPS is

quantitative, the concentration decrease will impact proportionally the recorded signal. Secondly, in order to increase the signal intensity, and in the specific case whether we can choose the electrolyte salt, one should pay a careful attention to **cations cross-sections** (which can be found from several sources, the most recent one being calculations from Trzhaskonvskaya *et al.* [186,187,196]). Overall, the cross section increases with the Z element number, while also depending on the considered transition. It is therefore easier to get a good signal using Cs cations, rather than Li or Na cations ($\sigma(Cs3d_{5/2})$ = ~130×10^{-21} cm^{-2}; $\sigma(Na2s)$ = ~2.6×10^{-21} cm^{-2}; $\sigma(Li\ 1s)$ = ~0.26×10^{-21} cm^{-2} at 2 keV photon energy). Finally the **measured photoelectron kinetic energy** is a parameter that can be modified either (i) by choosing to follow low binding energy peaks (depends mostly on the system constituting elements) or (ii) by working at higher beam energy. As the depth probed by XPS depends on the electron kinetic energy (see **Equation 1.8**), it is important to choose an energy that suits the desired depth of analysis. Low kinetic energies are suitable for surface studies, while high kinetic energies are suitable for analysis deeper in the material. For example, in **Section 2.3** [96,103,109,164] a ~4keV (tender X-Ray) beam energy was used to analyse sample with a ~35 nm thick electrolyte film. Under such configuration, the electron photoemission from a Pt4f peak (KE = $h\nu$ − BE = ~3.9 keV , $\lambda_{IMPF,3.9keV}$ ~12 nm) is reduced to 5% of the electrolyte-free intensity, while a similar electrolyte thickness and using 1.8 keV beam energy ($\lambda_{IMFP,1.7keV}$ ~ 6 nm) reduces the signal down to 0.3% of the electrolyte-free intensity. While it is not a serious problem when it comes to electrode surface analysis (as long as the signal is intense enough for the measurement), this is a great challenge when it comes to EDL studies, as the interface layer signal is superposed to the rest of the electrolyte XPS signal. One therefore should privilege higher beam energies when it comes to EDL studies, to amplify the contribution from the electrode-electrolyte interface, whereas the aforementioned intensity is not as important for the electrode surface studies, as it would, to the contrary, decrease the signal surface sensibility.

2.5.5 Is the dip and pull setup suitable for the EDL study?

As explained above, D&P is a technically challenging method. In the particular case of the EDL study, experimental conditions such as the analysis chamber pressure and the electrolyte concentration must be controlled in a way that greatly decrease the cation signal intensity (high pressure, low concentration). This raises the question of

D&P being a suitable technique to the EDL study. To answer this question, it is important to remember that EDL study via spectroscopic methods is extremely challenging altogether. Despite the raising number of spectroscopic and microscopic techniques (XAS, SERS, AFM, *etc.*)[197–200] that aim to study the electrolyte/electrode interface, as well as the compact layer, no other techniques (to author's knowledge) may offer the possibility to probe the ionic concentration depending on the electrode distance (diffuse layer). The few proofs of concept which were already published and discussed in **Section 2.3** highlight the opportunities of this method when it comes to the EDL study. However, even though those studies [103,109] took good care of avoiding evaporation effects and to work in low concentration electrolyte, while having access to tender X-Ray beam (4 keV, *vs.* 1.8 keV for us) in order to maximise FWHM changes with the applied potential, the low ion-related signal/noise ratio did not provide conclusive information regarding the EDL structure. In the case of Lichterman *et al.*, the measurement uncertainty was too high to conclude, while Favaro *et al*. was forced to work with $H_2O_{(l)}$ and non-ionic molecular probe (pyrazine, N1s) XPS signals, which did provide PZC potential information, but eludes the ionic concentration profile with the electrode-electrolyte interface distance.

Since the main limitations related to this method are due to the poor signal intensity compared to the low changes that may be observed, one may play on parameters such as beam energy in view to be more sensible to the buried electrode-electrolyte interface, an adapted choice of probed elements in view to improve the photoelectron intensity, or a longer signal recording (which may be of limited value due to liquid film instabilities). *However, the overall issue for EDL studies using D&P method will remain the trade-off between this signal intensity improvement using greater electrolyte concentration, and the extent of the signal variation (linked to the EDL Debye length) using lower electrolyte concentration, preventing conclusive results*.

To author's opinion, one could expect future technical improvements of synchrotrons to improve the incident beam intensity and therefore improve the technique sensitivity to EDL changes, just like they allowed the measurement of XP spectra to move from vacuum to near-ambient pressure in the two last decades.

2.6 Conclusion

As electrochemical reactions occur at the electrode-electrolyte interface, the local reaction environment there and, specifically, the electrochemical double layer, is prone have an instrumental role in their mechanism, as such, its structure/composition is a key part of the understanding of any electrochemical system. Incidentally, it is also one of the less understood. While theories were elaborated to describe it and correlate it to observed macroscopic behaviours, only few experimental studies were carried out to truly witness the EDL morphology, owing to the technical challenges encountered to study this side of the interface.

The recently developed D&P setup was discussed here as a mean to observe the EDL, as (i) the work function at the location of the detected species depends on the local electrical potential, and (ii) said electrical potential is deeply intertwined to the EDL architecture. Hence, a deconvolution of the XP spectra might lead to a mapping of several species of interest in the EDL. Preliminary studies were conducted in the literature, using XP probes and $H_2O_{(l)}$ peak broadening, to obtain information on the PZC of given surfaces. However, by following the signal of the cations themselves, one might hope to obtain additional information when it comes to the local concentration distribution.

In this chapter, we studied three different systems in D&P configuration, using Pt foil or GCE as the working electrode, and CsOH 1 M or NaOH 0.1 M as electrolyte. We managed to get a stable electrolyte film as thin as 10-20 nm, polarise the electrode within this electrolyte layer, and developed a method to verify the experimental validity and comparability in a given set of measurement. However, we also observed that the meniscus region of the electrolyte, analysed by XPS, is widely different than the electrolyte bulk. Due to its thin film dimensions and its distance to the electrolyte beaker, evaporation induced by the low pressure chamber strongly concentrated the electrolyte in the meniscus, up to 10 M. This prevented the observation of cation distribution at the interface and determination of the PZC in any of the investigated systems and further deconvolution of electrolyte XP spectra.

This is not the only limitation of the D&P for such studies. Among the latter, the liquid electrolyte film is a common denominator, as (i) the control of its homogeneity, and stability are critical to get meaningful results, as (ii) it contains the probed species (in

case of the EDL study), and as (iii) it defines the electrochemical conditions of the analysed spot. While some issues can be addressed by a careful recording and data treatment (meniscus stability and homogeneity), other intrinsically limit the EDL study, such as the electrolyte initial concentration and its evaporation in the analysis chamber, which optimization directly impact the quality of the recorded XPS signal, by increasing the pressure in the chamber and/or decreasing the electrolyte initial concentration.

Ultimately, it is clear that any realistic electrochemical system is far from ideal to be assessed by D&P, and that a system optimized for a D&P assessment shall be remote from any meaningful electrochemical operating conditions. Thinking outside of this signal-to-electrochemistry trade-off is then critical, and meaningful working directions could be found in working with parameters that do not directly impact the electrochemistry, as working at higher beam energy (higher sensitivity to the electrode-electrolyte interface), intensity (through the development of the new generation of synchrotrons and workstations) working with elements with a higher cross section. In conclusion, the D&P remains far from being able to study the EDL of realistic systems. It can, however (even using state-of-the-art workstations and detectors) provide a semi-quantitative information onto the EDL of model, adapted for the D&P systems, and, owing to substantial improvements in terms of synchrotron intensity, might be able to eventually move to more realistic electrochemical EDLs.

2.7 Experimental

Beamline speciation

The measurements presented in the previous sections were performed at MAX IV laboratory on HIPPIE beamline, which setup and its potential applications are presented in literature.[201]

Electrolyte preparation

We prepared CsOH 1 M electrolyte diluting 17.43 mL of CsOH 50 wt% in 100 mL of distilled water and NaOH 0.1M electrolyte diluting 528 µL of NaOH 50 wt% in 100 mL of distilled water. Electrolyte was degassed in low vacuum using external vacuum chamber prior to the experiment.

Electrode preparation

Pt foils are used as a WE and CE while Ag/AgCl eDAQ leakless mini electrode is used as reference electrode. The surface of the Pt foil is (i) polished using diamond paste by successive use of 9 µm, 3 µm, 1 µm and 0.25 µm diamond suspension, then rinsed with water and (ii) heated up to 950°C (10 °C/min) to clean the surface. The slow heating and cooling ramp used in this experimental procedure could be the reason for the formation of PtO_x cluster assumed in **Section 2.4**.

The surface of the glassy carbon working electrode (GCE) surface was carefully cleaned using Kimtech® paper and sonicated in acetone, absolute ethanol, and distilled water (>5 minutes each).

Cell assembling and preparation in the analysis chamber

Once assembled on the electrode holder, the reference electrode tip was immersed in the electrolyte to avoid potential drying of the reference electrode, while the working electrode was still out of the electrolyte.

The analysis chamber was then slowly put under vacuum with pressure controlled down to 15~25 mbar. The pumping station of the analysis chamber was working permanently at a low flow rate in the view to lower the pressure and increase the signal intensity. Platinum and FCE were firstly analysed out of the electrolyte. To verify cleanliness of the surface (see **Figure 2.9** and **Figure 2.17**), and to calibrate the analyser we used the Pt(0) peak, positioned at 71.3 eV [67] or C1s peak (C=C) at 284.5 eV.[188]

Table 2.1: XPS Peak fitting detailed functions and restrictions used in this chapter

Transition	Component attribution	Function	Position restriction / eV	FWHM restriction / eV	Area restriction
Pt4f $_{7/2}$	Pt(0) Pt-OH PtO PtO2	GL(40)T(1.6) GL(40)T(1.6) GL(40)T(1.6) GL(40)T(1.6)	71.3 +/- 0.5 Pt(0) + 0.6 Pt(0) + 1.3 Pt(0) + 2.5	0.57 ; 0.59 Pt(0)*1 Pt(0)*1 Pt(0)*1	Free
Pt4f $_{5/2}$		Same as 7/2	$4f_{7/2}$ + 3.33	$4f_{7/2}$ * 1	$4f_{7/2}$ × 0.75
C1s	C=C C-C C-O C=O O-C=O	LA(1.2,2.5,5) GL(30) GL(30) GL(30) GL(30)	284.5 (C=C) + 0.6 (C=C) + 1.4 (C=C) + 2.6 (C=C) + 4.4	[0.4 ; 0.8] [0.9 ; 1.3] (C-C) × 1 (C-C) × 1 (C-C)× 1	Free
O1s	$H_2O_{(g)}$ $H_2O_{(l)}$ $HO^-_{(aq)}$ $H_2O_{(chem)}$ $HO^-_{(chem)}$	GL(50)T(2) GL(20)T(2) GL(20) GL(20) GL(20)	Free $H2O_{(l)}$ − 1.73V Free	Free Free $H_2O_{(chem)}$ ×1	Free
$Cs4d_{5/2}$	$Cs^+_{(aq)}$	GL(10)	Free	Free	Free
$Cs4d_{3/2}$		Same as 5/2	$4d_{5/2}$ + 2.24	$4d_{5/2}$ × 1	$4d_{5/2}$×0.67
$Cs3d_{5/2}$	$Cs^+_{(aq)}$	GL(80)	Free	Free	Free
$Cs3d_{3/2}$		Same as 5/2	$3d_{5/2}$ + 13.89	$3d_{5/2}$ ×1	$3d_{5/2}$×0.73
Na2s	$Na^+_{(aq)}$	GL(20)	Free	Free	Free

Chapter 3: Operando study of the instability of cobalt-based polyoxometalates during the oxygen evolution reaction

3.1 General introduction

In **Chapter 2** X-Ray Photoelectron spectroscopy measurements are carried out in D&P configuration, which, additionally to the points discussed previously, presents two other limitations: (i) the proximity of the detector to the meniscus and the electrolyte greatly limits its use to study reactions that generate bubbles, the most notable being the OER and HER, keys to the hydrogen cycle; (ii) it is limited to model electrodes, with a low roughness factor. This specific geometry allows for a semi-quantitative and in depth sensitivity to the changes in the electrode and in the electrolyte. However, despite their 'model' geometry, such catalytic surfaces might present complex (electro)chemistry. As exhibited in **Chapter 2**, glassy carbon undergoes significant chemistry changes as a function of potential, whereas platinum presents oxides clusters, along with structural defects and, ultimately, different chemical environments of atoms in the near-surface region. Therefore, when an electrochemical reaction occurs, the involvement of various active sites is difficult to distinguish, both from a reactivity and spectroscopic standpoint, which complexifies the detailed understanding of the changes happening at the interface.[202]

In this **Chapter 3**, we therefore move toward a more complex interaction between the electrode and the electrolyte, *i.e.,* from the absence of faradaic reaction to the oxygen evolution reaction (OER). However, we concomitantly decrease the complexity of the electrocatalyst, by focusing on a model molecular OER catalyst, whose metal active site and chemical environment are well defined. We use X-Ray Absorption and Photoelectron Spectroscopies (XAS and XPS) under *in-situ* and *operando* conditions

aiming to understand the OER mechanism on such 'ideal' molecular catalyst and explore the chemical changes undergone by such system under water oxidation conditions.

Our focus then is complexes of cobalt(II) stabilised by lacunary polyoxometalates (Co-POM), which are highly discussed water oxidation catalysts (WOC). While their activity and/or (in)stability in the oxygen evolution reaction (OER) have been widely explored, there is still no consensus between those who claim Co-POMs being OER active and stable and those who insist on CoPOMs rather acting as pre-catalysts, which degrade into an OER-active heterogeneous CoO_x catalyst. We therefore use *operando* XAS and XPS alongside with electrochemical methods (cyclic voltammetry, chronoamperometry) to assess the activity and stability of $[Co_4(H_2O)_2(PW_9O_{34})_2]^{10-}$ (Co_4−POM) and $[Co_9(H_2O)_6(OH)_3(HPO_4)_2(PW_9O_{34})_3]^{16-}$ (Co_9−POM) under various operational conditions, to provide an answer to the following questions:

(i) *Are the Co-POMs stable in OER operating conditions?*

(ii) *If unstable, can the operating conditions be tuned to stabilize them?*

(iii) *Can we observe, on a model, 'mono-site', electrocatalyst, the OER intermediate (here, presumably a Co(III)-POM) by spectroscopic means?*

3.2 State of the Art

3.2.1 Polyoxometalates general introduction

Polyoxometalates (POM) are a class of metal oxide cluster anions, which are constituted of transition metals, usually V, Mo or W, as primary constituents, also called *addenda* atoms. Those addenda atoms are coordinated by oxygen and can adopt tetrahedral (4-coordinated) or octahedral (6-coordinated) geometries and can share one or several oxygens with the neighbouring addenda atoms, forming complex structures [203].

This family of species is usually divided into two categories: isopolyanions (IPA) (an example is shown on **Figure 3.1.A**), of general formula $[M_mO_y]^{q-}$ (M = Addenda atoms V, Mo, W…), and heteropolyanions (HPA). The second category includes an additional heteroatom (X=P, S, As, S, Cl…) based tetrahedral substructure such as phosphate (PO_4^{3-}) or silicate (SiO_4^{3-}) and therefore adopts a general formula $[X_rM_mO_y]^{q-}$. POMs can adopt an extremely large variety of structures by the arrangement of several

octahedral and tetrahedral oxoanions, but two most representative HPA structures are the Keggin and Wells-Dawson. Keggin structure was first reported in 1933 [204], and is composed of a central tetrahedral hetero-oxoanion (XO_4^{3-}) surrounded by 12 octahedral oxometallates (MO_6^{q-}). The octahedral oxometallates are arranged in 4 triades, where each metalate shares an edge with the two other metalates of the triade, and a corner with the central hetero-oxoanion. The most common α isomer of the Keggin structure is shown on **Figure 3.1.B**, but it is noteworthy that the respective rotation of 1, 2, 3 or 4 metalates triade result in the formation of β, γ, δ and ε isomers of the structure. Dawson structure (whose alpha isomer is shown in **Figure 3.1.C**) was described a bit later (1953) [205] and is composed of two identical parts. Each part is organised around the tetrahedral hetero-oxoanion, which is surrounded by nine octahedral oxometallates. Similar to Keggin structure, the rotation of each unit by 120° compared to the other results in the isomeric β structure [206].

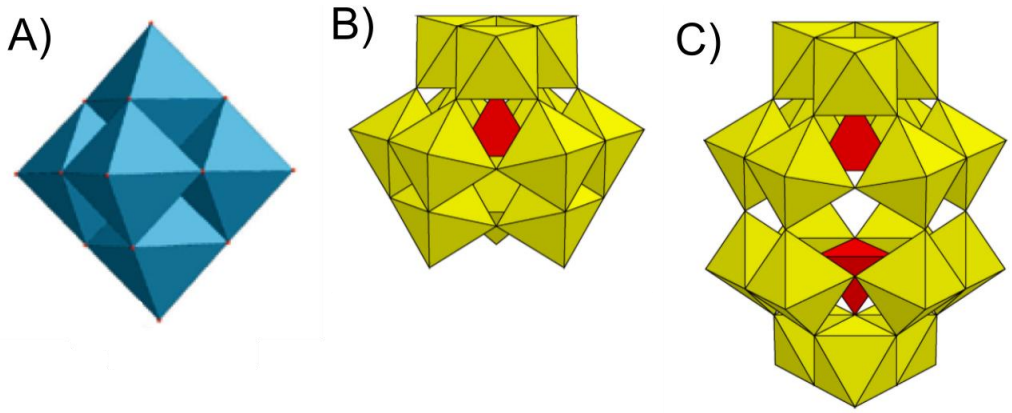

Figure 3.1: **(A)** Isopolyanion M_6O_{16} Lindqvist structure. Reproduced from Ref.[206]. **(B)** Heteropolyanion $XM_{12}O_{40}q^-$ α-Keggin structure. **(C)** Heteropolyanion $X_2M_{18}O_{62}q^-$ α-Wells-Dawson structure. Reproduced from Ref.[207]. Blue and yellow octahedra are representing MO_6^{q-} metalates (M=Mo, V, W, etc.), red tetrahedra are representing XO_4^{q-} hetero-oxoanions (X=P, As, Si, Cl, etc.).

Due to the wide variety of structures and chemical compositions that are included in the POM family, it is hard to give a general description of their synthesis. Yet, the simplest method to prepare HPA is the acidification of an aqueous alkaline mixture of metal-oxoanions and hetero-oxoanions. Acidification of the solution results in the condensation of oxoanions and the formation of POMs (*e.g.* Keggin $[PMo_{12}O_{40}]^{3-}$ POM condensation, **Equation 3.1**). The resulting product will therefore depend on several

parameters: the M/X atomic ratio in the reaction media, the temperature, the final pH value, the solvent nature, and the counter-ion nature.[208]

Equation 3.1 $12\ MoO_4^{2-} + H_3PO_4 + 21\ H^+ = [PMo_{12}O_{40}]^{3-} + 12\ H_2O$

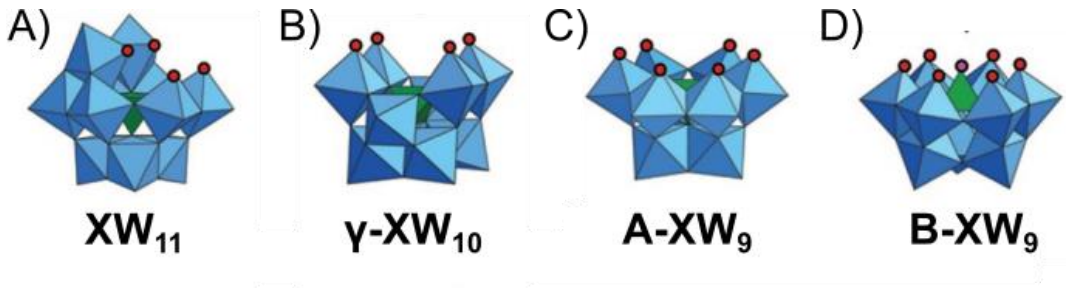

Figure 3.2: (A) mono-lacunary **(B)** bilacunary **(C)** trilacunary A isomer and **(D)** trilacunary B isomer Keggin polyoxometalates. Reproduced from Ref.[209].

As this condensation reaction is an equilibrium, each POM structure has a range of pH stability. The acidification of the aqueous media may therefore result in further condensation (if possible), while the pH increase would result in a partial or total hydrolysis of the POMs. Under mild pH conditions, one can obtain lacunary POM structures, such as lacunary Keggin structures, obtained by the removal of one, two or three (**Figure 3.2**) metalate octahedra. Due to their lacunary nature, oxygen atoms that were previously bridged to another metalate in those structures (highlighted in red in **Figure 3.2**) are likely to behave as electron donor, and can therefore act as ligands in metal complexes.

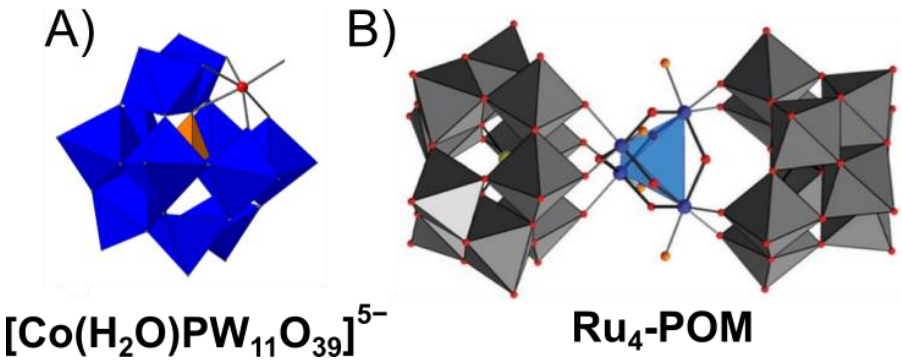

Figure 3.3: Metal complexes stabilised by Keggin-based lacunary polyoxometalates. **(A)** $[Co(H_2O)PW_{11}O_{39}]^{5-}$ is a mono-metal complex that was examined for its potential activity regarding the OER. Reproduced from Ref.[210]. **(B)** $[\{Ru_4(\mu\text{-}O)_4(\mu\text{-}OH)_2(H2O)_4\}(\gamma\text{-}SiW_{10}O_{36})_2]^{10-}$ is one of the most studied M-POM complexes as it showed good stability and performance regarding water oxidation catalysis. Reproduced from Ref.[211].

The obtained complexes can be mono-metallic (**Figure 3.3.A**) or sandwich-type (**Figure 3.3.B**) and are interesting because of the polydentate nature of the lacunary POM ligand, providing stability to the complex structure while containing for instance a catalytically active metal center.[206,207,212] We will refer to this kind of species as metal-stabilised polyoxometalates (M-POM).

3.2.2 M-POM as catalyst and electrocatalyst

POMs science is regarded as a mature field as it is attracting much attention since the 1960's. The commercial availability of basic Keggin POM structure such as $H_3PMo_{12}O_{40}$, $H_3PW_{12}O_{40}$, $H_3SiMo_{12}O_{40}$, as well as the large number of studies published around it make them convenient starting materials for a wide range of POM derivative synthesis [213]. They have shown to be useful in a large range of applications related to medicine, biochemistry, material science, molecular magnetism, electrochemistry, and catalysis, mainly because of their exceptional redox properties. Indeed, POMs possess capacity to bear and release several electrons from their addenda atoms, which is why they are recognised as electron reservoirs. The associated electron transitions can be mono- or multi-electron processes, may be coupled with proton exchange, localised or delocalised among several sites depending on the pH and the considered POM composition and structure. Despite the fact that Keggin and Wells-Dawson electrochemical behaviour is documented, the electrochemical properties of M-POM are very different from those of the corresponding parent POMs, and the relation between these two is still to be clearly understood [207,214,215]. Yet, POM redox characteristics creates unique chemical properties for M-POM species which make them particularly interesting for photo and electro-catalysis [216,217] notably for the HER [218], OER [212], CO_2 reduction [219,220] and other energy-related applications, such as energy storage.[221]

3.2.3 Cobalt-based polyoxometalates as OER electrocatalyst

The use of M-POM for water oxidation catalysis started around 2004 with the development of noble-metal-based POM complexes [222,223]. One of the most famous examples is $[\{Ru_4(\mu\text{-}O)_4(\mu\text{-}OH)_2(H_2O)_4\}(\gamma\text{-}SiW_{10}O_{36})_2]^{10-}$, which is consisting of a Ru_4O_4 core stabilised by two bilacunary Keggin POMs acting as inorganic tetradentate oxygen donor ligands (Ru_4-POM, **Figure 3.3.B**) [224,225]. Ru_4-POM is rather interesting because it offers 4 redox active Ru(IV) sites, it is stable under neutral

and acid pH, it has shown to be a water oxidation catalyst under chemical oxidation conditions (*i.e.* in the presence of a chemical oxidant), both at acidic and neutral pH [224,225], and as an OER electrocatalyst in neutral pH conditions [226]. Interestingly, this specie shows good stability and a good capacity to be functionalised onto graphene-based electrodes (modified carbon nanotubes [226] and graphene layers [227,228] for instance) while retaining its OER activity and electrochemical behaviour.

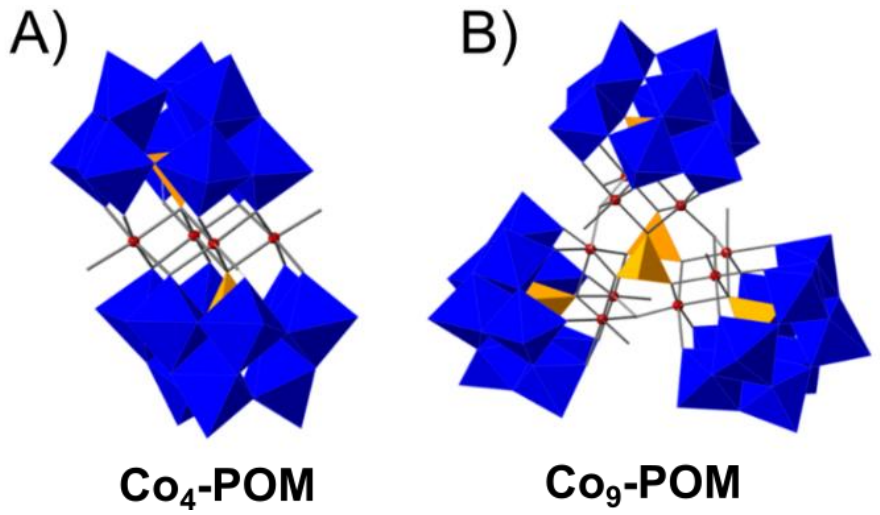

Figure 3.4: **(A)** $[Co_4(H_2O)_2(A\text{-}PW_9O_{34})_2]^{10-}$ (Co_4-POM) and **(B)** $[Co_9(H_2O)_6(OH)_3(HPO_4)_2(A\text{-}PW_9O_{34})_3]^{16-}$ (Co_9-POM) structure representation. Blue octahedra are WO_6, yellow tetrahedra are PO_4, red spheres are Co(II), and pending sticks are labile water molecules. Co(II) connected to those water molecules are the suspected active sites of these catalysts for water oxidation. Reproduced from Ref.[210].

In order to create novel noble-metal-free electrocatalysts, the development of new M-POM electrocatalysts involving transition metal ion-stabilised POM (mainly Ni [229], Mn [230,231], and Co [232,233]) started in 2010 with the assessment of an apparent OER activity of $[Co_4(H_2O)_2(PW_9O_{34})_2]^{10-}$ (Co_4-POM, **Figure 3.4.A**) by Hill *et al.* [234] under chemical and electrochemical oxidation conditions. This study was followed by further research regarding this complex and other Co-POM derivatives, including $[Co_9(H_2O)_6(OH)_3(HPO_4)_2(PW_9O_{34})_3]^{16-}$ (Co_9-POM, **Figure 3.4.B**). In what follows we will focus on both of the proposed catalysts:

3.2.4 Co_4-POM state of the art

Co_4-POM is composed of four Co centres that are stabilised by two trilacunary Keggin POMs. It was firstly synthesized in 1973 by Weakley *et al.* [235]. However it is only in 2010 that a true interest emerged for that complex, as Hill *et al.* [234] reported its

activity both as WOC and OER catalyst at neutral pH conditions (pH 8). In this first study, authors studied Co_4-POM in solution to determine its pH stability range (pH 3.5 to pH 9) through UV-Vis spectroscopy and ^{31}P-Nuclear Magnetic Resonance (NMR). They additionally highlighted the Co_4-POM electrocatalytic behaviour which showed OER activity signs above 1.7 V vs RHE (**Figure 3.5.A**), and O_2 production was observed when the catalyst was exposed to sacrificial tris(2,2′-bipyridyl)triperchlororuthenium(III) ($[Ru(bpy)3]^{3+}$) oxidant, sparking the interest of the scientific community in Co-POM species as OER catalyst under chemical oxidation and electrochemical condition (denominated as *chemical* and *electrochemical OER* for the rest of this chapter).

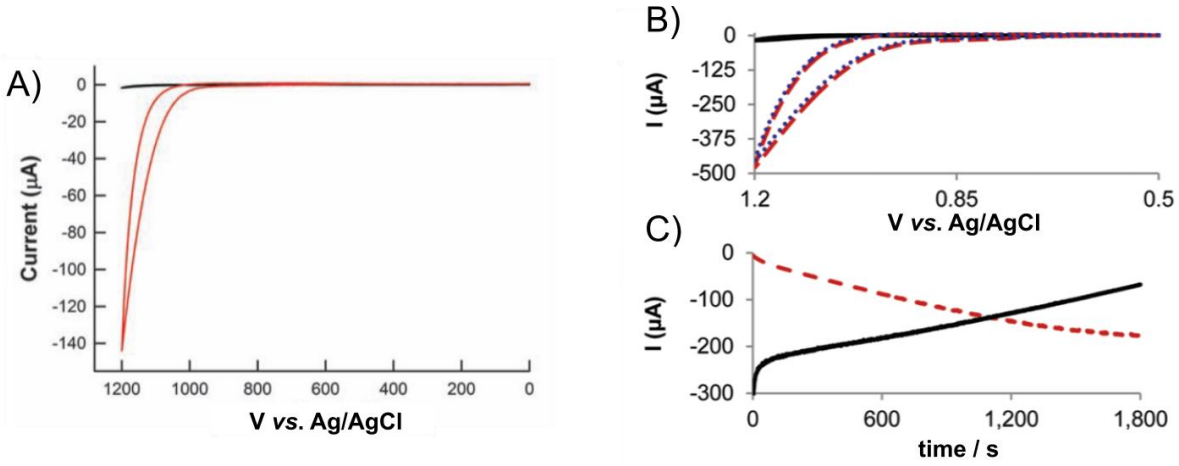

Figure 3.5: **(A)** Cyclic voltammetry (CV) of 50 mM sodium phosphate buffer solution at pH 8 alone (black) and with 1mM of Co_4-POM (red). Scan rate 25 mV/s, potential is reported versus Ag/AgCl reference electrode (E(Ag/AgCl) = 0.68 V *vs.* RHE) reproduced from [234]. **(B)** CV of 0.5 mM Co_4-POM in 0.1 M NaPi buffer at pH 8 immediately after dissolution (black), after 30 minutes of chronoamperometry at 1.1 V *vs.* Ag/AgCl (red dashed curve) and after the working electrode was washed with water and placed in pure buffer solution (blue dotted curve). Scan rate 100mV/s, glassy carbon used as a working electrode. **(C)** Chronoamperometry (CA) of 0.5 mM Co_4-POM in 0.1M NaPi buffer at pH 8 and 1.1 V *vs.* Ag/AgCl (black solid curve), and the one of the same working electrodes after the solid black curve CA, after working electrode rinsing and in sodium phosphate buffer solution alone (red dotted line). Glassy carbon is used as a working electrode. Data in panels (B) and (C) are reproduced from Ref.[236]. *Note that the American plotting conventions are used on this graph (i.e., inverted current sign and potential axes).*

When this first article was published, Nocera *et al.* [237] (2008) already highlighted that neutral pH sodium phosphate buffer solution (NaPi 0.1 M, pH 7) containing Co^{2+}(aq)

under oxidative conditions (1.71V vs RHE) would form *in-situ* a heterogeneous CoO_x OER electrocatalyst on the working electrode. Naturally, one could wonder if Co_4-POM could partially be hydrolytically dissociated (**Equation 3.2**) to form Co^{2+}(aq), which could form a CoO_x electrocatalyst, making Co_4-POM a pre-catalyst. Yet, Hill *et al.* discarded the possibility of Co_4-POM degradation and contribution of Co^{2+}(aq) to the OER activity in the case of WOC. To verify this, an excess of 2,2′-bipyridine (bpy) was added to the Co_4-POM solution, allowing the *in-situ* complexation (**Equation 3.3**) of the leached Co^{2+}(aq), cancelling its OER activity, as $[Co(bpy)_3]^{+3}$ is not active for that reaction. Despite bpy addition to the reaction media, the solution remained active towards water oxidation under chemical oxidation conditions.[234]

Equation 3.2: $Co_yPOM^{q-} + 6\,H_2O = Co_{y-1}POM^{(q+2)-} + [Co(H_2O)_6]^{2+}$

Equation 3.3*:* $Co^{2+} + 3\,bpy = [Co(bpy)_3]^{2+}$

Following this paper, and knowing that M-POM can be subjected to hydrolysis (**Equation 3.2**), Finke *et al.*[236] focused on whether the Co_4-POM is a true catalyst in that reaction or it is rather a CoO_x degradation layer. In the first study they focused on a more detailed electrochemical analysis of Co_4-POM solution in similar conditions as described by Hill, and obtained the CV (**Figure 3.5.B**) and chronoamperometry (CA, **Figure 3.5.C**) signature of the working electrode *after the electrolysis of Co_4-POM solution* under strong oxidative conditions (1.8 V vs RHE). The OER activity of the Co_4-POM solution right after dilution (**Figure 3.5.B** black solid curve), compared to the working electrode OER activity after 30 minutes of electrolysis (red dashed curve in Co_4-POM 0.5 mM, blue dotted line in buffer solution only after electrolysis) led the authors to conclude that the OER activity could be mainly attributed to a heterogeneous degradation layer formed onto the working electrode during the electrolysis. *Post-Mortem* EDX analysis of the working electrode surface confirmed the presence of a Co, P and O containing layer, similar to what was reported by Nocera *et al.* [237] and confirming the degradation of Co_4-POM under electrochemical conditions in those specific conditions. In 2013, the same group performed further studies regarding the Co_4-POM stability and activity under lower concentration conditions (2.5 µM Co_4-POM, pH 5.8 and pH 8) [238] and inferred that the Co^{2+}(aq) concentration leached from Co_4-POM dissociation could not fully explain the OER activity of the system. They thus concluded that Co_4-POM *could* be the actual OER electrocatalyst, but that hypothesis of the CoO_x formation and acting as an OER catalyst could not be discarded either.

While the Co_4-POM stability and activity regarding the OER under electrocatalytic conditions remained elusive, other groups focused on the water oxidation catalysis under chemical oxidation (or photo-induced oxidation) conditions using $[Ru(bpy)3]^{3+}$ as an oxidant. On this topic, several groups checked the Co_4-POM WOC activity and its stability either with or without light [239–244], essentially concluding that Co_4-POM was an active and stable WOC.

3.2.5 Co_9-POM state of the art

As Co_4-POM and Co_9-POM are both complexes composed of Co(II) ions stabilised by the same Keggin tri-lacunary POMs, their chemistry is relatively similar, with similar questions rising, *i.e.,* are they true catalysts for OER or only precatalysts forming CoO_x species under oxidative conditions which are OER active?

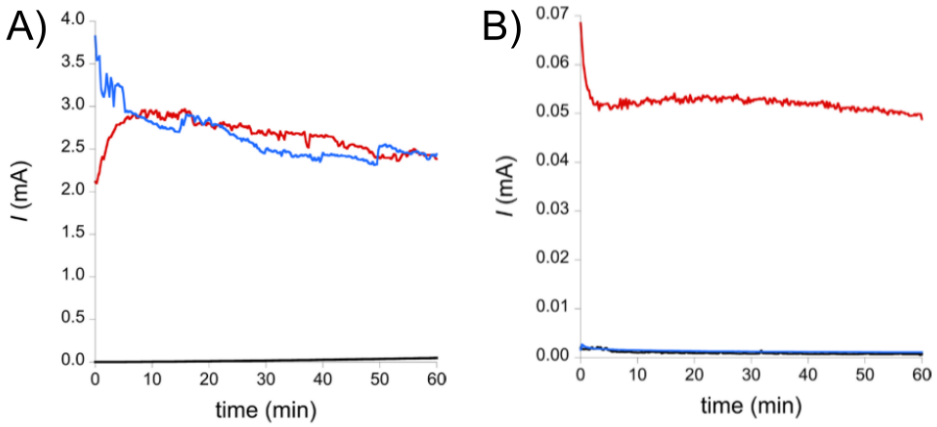

Figure 3.6: Chronoamperometry (CA) in Co_9-POM 1 mM containing solution (red) and *post-mortem* CA (blue) compared to the blank CA (black). **(A)** In absence and **(B)** presence of 2.8 mM bpy (10-fold bpy excess compared to leached $Co^{2+}(aq)$). Experiments were performed in 50 mM NaPi buffer pH 7, and 1 M $NaNO_3$ supporting electrolyte. Reproduced from Ref.[245].

Co_9-POM was firstly reported as a WOC and OER active catalyst in 2012 by Galan-Mascaros *et al*. who investigated its activity using CA experiments (**Figure 3.6**) and chemical oxidation experiment using NaClO as oxidant [245]. Under electrochemical conditions, the first CA was performed using 1 mM Co_9-POM in 50 mM NaPi buffer solution at pH 7 (**Figure 3.6.A**). The authors noticed that despite the fact the Co_9-POM was showing strong OER activity (red curve), the working electrode post-mortem, in buffer solution only (blue curve) also had a significant OER activity compared to the initial CA (black). This highlights the formation of CoO_x onto the electrode. In the view to poison CoO_x formation, authors used the same method as Hill *et al.* and introduced

an excess of bpy in solution (**Figure 3.6.B**). This second electrochemical experiment showed that bpy was successfully preventing the CoO_x formation, as the *post-mortem* CA (blue) showed a similar activity compared to the initial CA (black). The most important observation is the higher current amplitude during the CA in presence of Co_9-POM and bpy excess, despite a substantial decrease in the current compared to bpy-free experiment. This led the authors to conclude that Co_9-POM was indeed an OER electrocatalyst, despite the fact that CoO_x formation could be observed under bpy-free experimental conditions. In a second set of experiments, the activity of Co_9-POM as WOC using NaClO as oxidant in presence of 10-fold excess of bpy was investigated and showed a good oxygen efficiency, even after several NaClO additions (up to 10^5 equivalents added) over a week-long experiment.

3.2.6 The common stability and activity questions around Co_4 and Co_9-POM

Few studies included both Co_9-POM and Co_4-POM in the same stability [246,247] and mechanistic studies [248]. A remarkable study aiming to answer the common question of Co-POMs (Co_4-POM, Co_9-POM and other similar complexes) stability and activity towards OER was performed in 2018 by Folkmann *et al.* [210], who (i) rationalized the different hypotheses regarding what could happen to the catalytic system upon oxidation conditions (see **Figure 3.7.A**) that could explain its OER activity, (ii) quantified $Co^{2+}_{(aq)}$ leached from the different Co-POMs studied from pH 5.8 to pH 9, and (iii) assessed the ratio between the OER activity of the Co-POM solution and the one from a $Co^{2+}_{(aq)}$ solution whose concentration matches the previously quantified CoPOM hydrolysis. This study highlighted in particular the fact that no Co-POM complex is immune to hydrolysis, and that the leached $Co^{2+}_{(aq)}$ quantity depends on the type of Co_x-POM and the experimental conditions. For example, for Co_4-POM and Co_9-POM, 0.5% and 1.7% of Co ions leached into the solution after 3 hours ageing at pH = 5.8, respectively (see **Figure 3.7.B** for further details). Interestingly, in the case of these two electrocatalysts, the OER activity measured for the Co-POM containing solution could not be attributed fully to the OER activity of leached $Co^{2+}_{(aq)}$ ions alone, once again suggesting that Co_4-POM and Co_9-POM could be the actual OER electrocatalyst. Yet the authors insisted that due to the activity differences between homogeneous Co-POMs and *in-situ* formed CoO_x (Co-POMs being 35 to 150 less

active than an equivalent quantity of CoO_x), even minor changes in the Co^{2+}(aq) concentration could reverse the conclusions.

A)

1. The Co-POM is the true molecular catalyst.

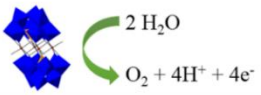

2. There is insidious Co(II) counter ion impurity which forms the catalyst.

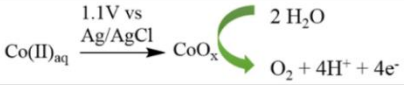

3. The Co-POM releases Co(II) to form CoO_x as the catalyst.

4. The Co-POM acts as a direct precursor to CoO_x on the electrode

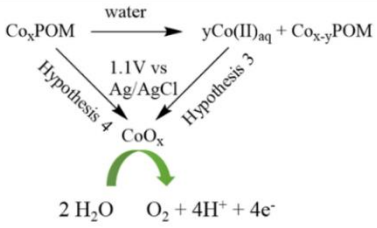

5. An unidentified species is the catalyst.

6. A combination of any of the above.

B)

polyoxometalate	$[Co(II)_{aq}]$ by ^{31}P NMR, μM (% Co(II) after 3 h) 0.1 M NaPi pH 5.8 [data range]	$[Co(II)_{aq}]$ by ^{31}P NMR, μM (% Co(II) after 3 h) 0.1 M NaPi pH 8.0 [data range]	$[Co(II)_{aq}]$ by cathodic stripping, μM (% Co(II) after 3 h) 0.1 M NaB pH 9.0 [data range]
$Co_4P_2W_{18}$	11 ± 3 (**0.5 ± 0.2%**)	55 ± 3 (**2.8 ± 0.3%**)	44 ± 5 (**2.2 ± 0.3%**)
$Co_9P_5W_{27}$	75 ± 2 (**1.7 ± 0.1%**)	37 ± 2 (**0.8 ± 0.1%**)	44 ± 5 (**1.0 ± 0.1%**)

Figure 3.7: **(A)** List of hypotheses regarding the OER activity of CoPOMs. **(B)** Leached $Co^{2+}_{(aq)}$ quantification resulting from the dilution of Co_4-POM and Co_9-POM in different systems. Reproduced from Ref. [210].

In order to avoid Co-POM hydrolysis and the ensuing stability questions that are inherent to homogenous electrocatalysis, several teams attempted to integrate them in electrodes, using molecular Co-POMs either incorporated into metal organic frameworks [249], grafted on functionalised surfaces [250–252], by using insoluble Co-POM salts of Ba or Cs, or by elaboration of a composite electrode [253–257]. The last method interestingly allowed the developed catalyst layer to operate well for the OER under acidic or alkaline solutions, outside of the respective Co-POMs pH stability range.

3.2.7 Summary and objectives

Despite Co_4-POM and Co_9-POM being debated as OER electrocatalyst for a decade, there is still no consensus on whether they are actually true active species under electrochemical oxidation conditions or just act as pre-catalyst. It is aknowledged that

since Co-POMs are in equilibrium with $Co^{2+}_{(aq)}$ due to the complex hydrolytic dissociation, CoO_x can be formed *in-situ* and account for a large majority of the overall system activity. This equilibrium is depending on the specific system conditions [210,243] (*i.e.* pH, buffer type, solution ionic strength, *etc.*) and therefore impacts the part of the OER that can be accounted to Co-POM. Yet, those species are extremely interesting as they may serve as (i) OER molecular homogeneous electrocatalyst and (ii) are stable in neutral pH media. This family of compounds therefore offers a potential model for the theoretical study of the OER catalytic cycle, in contrast to heterogeneous catalyst that are usually comprised of a variety of active sites [258,259].

It is important to note that either for Co_4-POM or Co_9-POM, to the best of our knowledge, *no operando studies were performed, which would allow to unambiguously conclude on the nature of the catalytically active component* (molecular Co_x-POM against heterogeneous oxide layer resulting from the degradation of the above). Furthermore, *no systematic electrochemical study was published* (*i.e.* systematic screening of CVs in different potential windows). Additionally, the electrochemical activity and stability studies were performed at high overpotential (>1.7 V *vs.* RHE, that is, a >500 mV OER overpotential), which could be the reason for the catalyst quick ageing/degradation.[260,261] This means the Co-POM degradation origin in published studies could be primarily due to strong oxidative conditions leading to the Co-POM destabilization, rather than spontaneous $Co^{2+}_{(aq)}$ leaching over the entire OER range.

In the following sections, we examine whether Co-POM are the true active species for the water oxidation reaction and are stable while performing the OER catalytic cycles. To do so, we first perform an electrochemical study of a Co-POM solution in oxidative conditions and the characterization of its degradation products using *post-mortem* XAS and XPS, followed by a set of *operando* XAS analysis. We start with Co-POM *operando* analysis under OER electrocatalytic conditions, in absence and in presence of bpy to avoid CoO_x formation, and under chemical oxidation conditions (using NaClO as oxidant), followed by the investigation of the Co-POM oxidation as an heterogeneous catalyst using XAS in-situ analysis.

3.3 Co-POM - electrochemical behaviour

Since literature focused on electrochemical studies under strong oxidation conditions (>1.7 V *vs.* RHE) and in low buffer concentration conditions (from 50 mM to 0.1 M NaPi), we perform a systematic study of Co-POMs oxidation behaviour to determine if more gentle conditions could result in a better stability under the OER conditions. Indeed, too high overpotentials could result in faster catalyst degradation [260,261], whereas a strong OER current alongside a low buffer concentration dramatically decreases pH at the electrode vicinity [134,262,263], both conditions that can promote Co-POM degradation (pH stability range between, pH~4 and pH~8) and CoO_x formation. Therefore, the stability of the Co_4-POM and Co_9-POM during the electrochemical OER was studied with CV and CA followed by *post-mortem* X-ray spectroscopy characterizations of the WE to detect eventual electrodeposition of a Co-containing layer. The buffer solution used is 0.72 M NaPi at pH 6.0, a rather high concentration which was chosen to minimise local pH variations due to the OER. *For the rest of this section, potentials indicated will be given versus RHE*.

Figure 3.8 shows sequential CV cycles applied to a glassy carbon electrode (GCE) in a 1 mM Co_4-POM (**A-C**) and Co_9-POM (**D-F**) solution in different potential intervals: first between 0.7 and 1.7 V for Co_4-POM (**Figure 3.8.A**) and 0.7 to 1.65 V for Co_9-POM (**Figure 3.8.D**). The OER manifests itself by the current increase above ~1.5 V, and one can note that CVs consecutive scan in **Figure 3.8.A** and **D** are reproducible, thus confirming the Co_4-POM and Co_9-POM stability at potentials below 1.7 V and 1.65 V, respectively. However, even a slight increase of the electrode potential of 0.025 V (**Figure 3.8.B and E**) results in a qualitative change of behaviour: the anodic currents increase in sequential CV cycles, and a cathodic peak at 1.45 V appears in the negative scan, suggesting formation of a Co-containing layer on the GC surface.

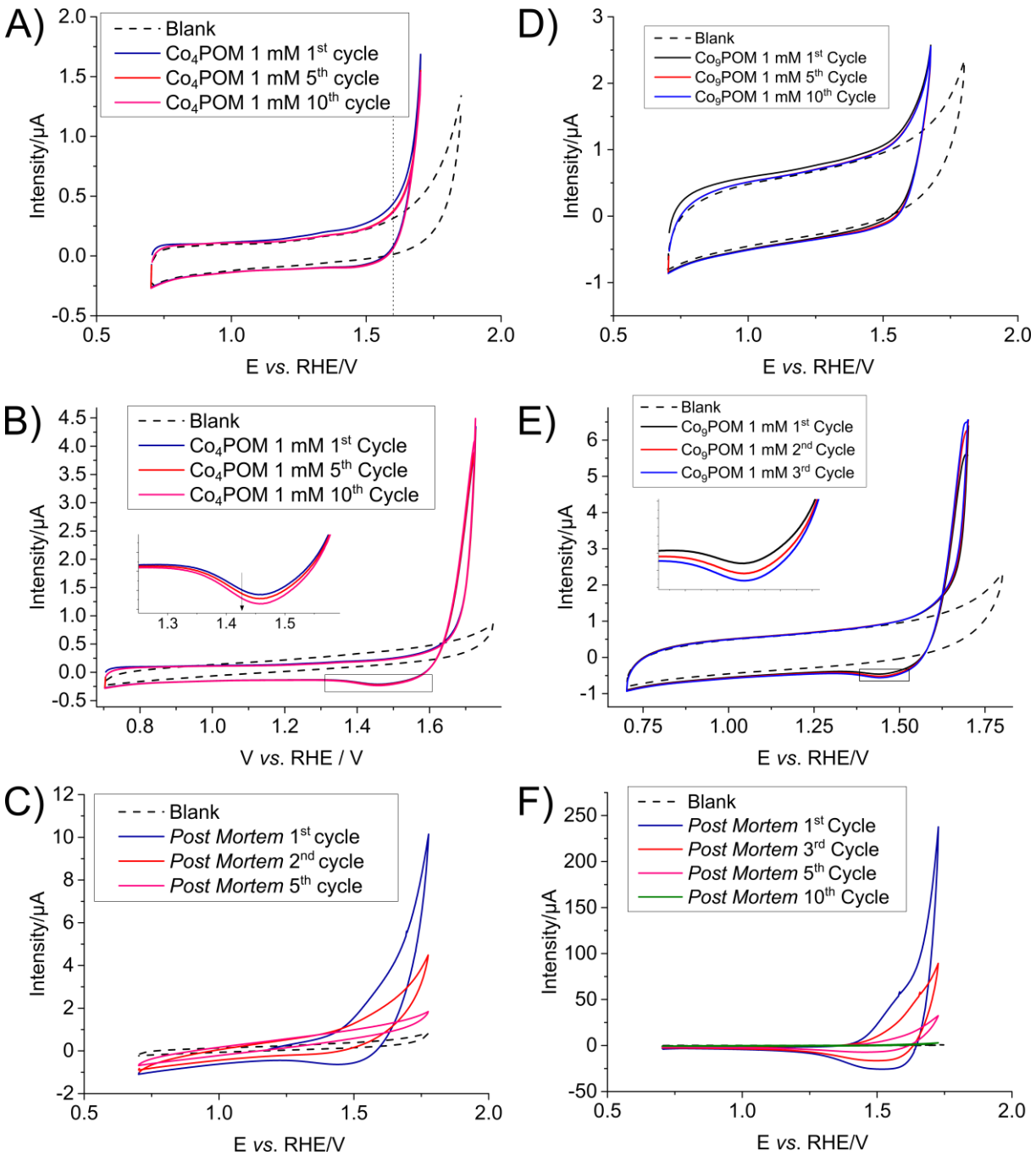

Figure 3.8: 1 mM Co_4-POM cyclic voltammetry (CV) at different anodic potential limits: (A) 0.7 V to 1.7 V, **(B)** 0.7 V to 1.725 V. **(C)** *Post-mortem* CV taken in a Co-POM-free buffer solution after 20 minutes chronoamperometry (CA) in Co_4-POM 1 mM solution at 1.6 V. CV is taken from 0.7 V to 1.775 V vs RHE; **1 mM Co_9-POM CV at different anodic potential limits**: **(D)** 0.7 V to 1.65 V and **(E)** 0.7 V to 1.675 V. **(F)** *Post-mortem* CV taken in a Co-POM-free buffer solution after CAs of 20 minutes in Co-$_9$POM 1 mM solution at 1.6V. CV is taken from 0.7 V to 1.725 V vs RHE. Electrolyte is 0.72 M sodium phosphate buffer at pH 6. Scan rate is 20mV/s. Glassy carbon was used as a working electrode. All potentials indicated are given *vs.* RHE.

To verify whether the CoPOM stability is related to the applied potential or rather to the number of imposed catalytic cycles (and hence the amount of transferred charge), constant-potential chronoamperometry measurements were performed at 1.6 V for 20 min (**Figure 3.9.A**), *i.e.,* at potentials below the degradation potential observed in **Figure 3.8.A.** The analysis reveals an increase in the current for Co_9-POM after ~10 sec of electrolysis (~ 150 s for Co_4-POM, which is consistent with the lower potential of instability for Co_9-POM *vs.* Co_4-POM), once again suggesting formation of a heterogeneous Co-containing layer on the electrode surface. The WEs were therefore transferred in an electrochemical cell filled with a Co-POM-free NaPi buffer solution after the CA. The significantly higher anodic currents (compared to the pristine GC electrode, see **Figure 3.8.C** and **F**) along with the appearance of the anodic and cathodic peaks typical for redox transitions of Co oxides [237,264], both testify in favour of a Co oxide layer deposition during the OER in a Co-POM solution, and prove that *the degradation is not directly related to the electrode potential but rather to the amount of charge transferred* (and thus the number of catalytic cycles performed by the Co-POM, even if those were done at low OER overpotentials).

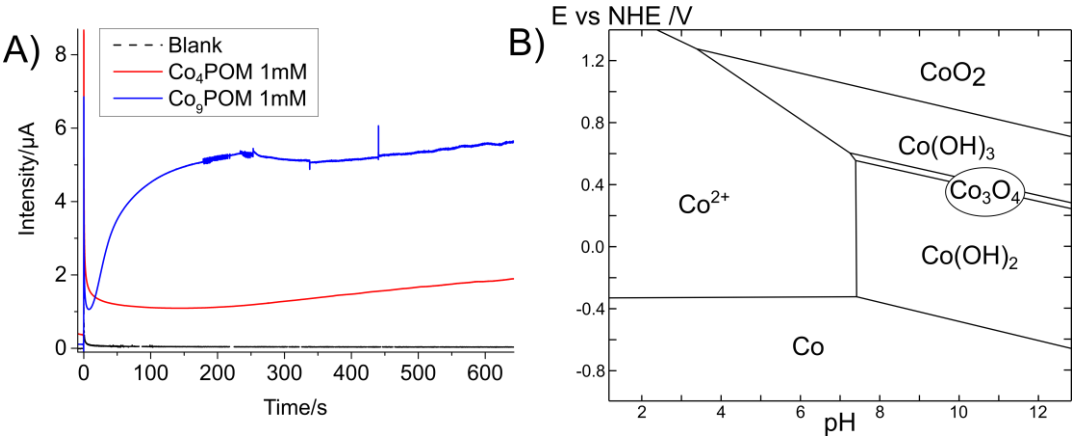

Figure 3.9: **(A)** Co_4-POM 1mM (red curve) and Co_9-POM 1 mM (blue curve) chronoamperometry at 1.6 V *vs.* RHE, in 0.72M NaPi buffer at pH 6.0 compared to buffer only solution (black dashed curve). **(B)** Cobalt Pourbaix diagram in aqueous solution. Total cobalt concentration taken at 10^{-2} M, and at 25°C. Data from **(B)** was taken from [265].

Note that the continuous decrease of the currents revealed by repetitive CV cycles in the Co-POM-free NaPi buffer is in agreement with the Pourbaix diagram of Co pointing to solubility of Co(II) (hydr)oxide at pH < 6 [265] (**Figure 3.9.B**) and accelerated by the OER induced acidification of the electrode/electrolyte interface due to the OER ($H_2O \rightarrow O_2 + 4\underline{H^+} + 4e^-$). The observed difference between the potentials (1.7 *vs.* 1.65

V for Co_4-POM and Co_9-POM respectively) causing the degradation during the CV measurements and the initial currents after the CA (10 *vs.* 250 µA at 1.6 V for Co_4-POM and Co_9-POM respectively, see **Figure 3.8)**, must be due to differences in the leached $Co^{2+}_{(aq)}$ concentration because of hydrolytic dissociation equilibrium constant difference between the two complexes (which is consistent with the data presented in **Figure 3.7.** at low pHs), or (ii) differences in the complex ageing after several OER catalytic cycles (turnover-number, TON).

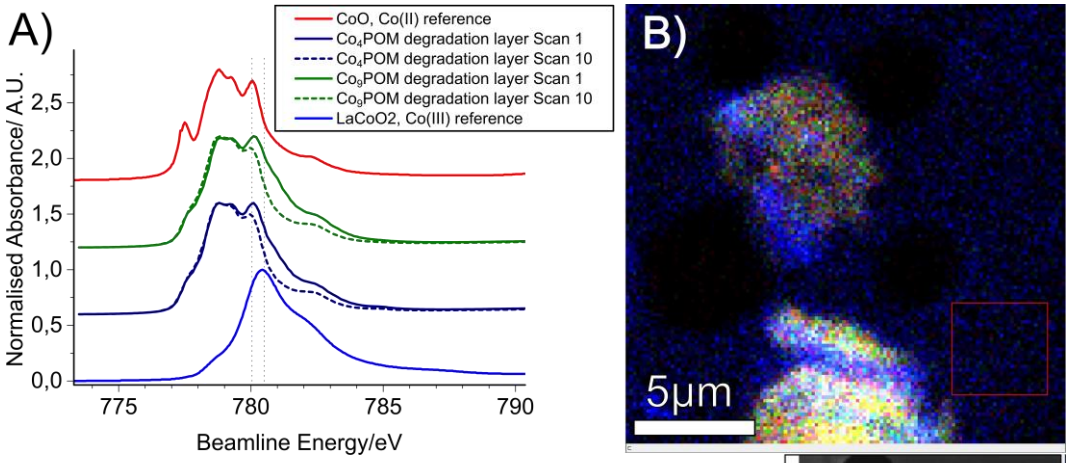

C)	Co_4POM	Co_9 POM
Co	11%	17%
O	85%	77%
P	4%	5%
W	0%	1%

Figure 3.10: Analyses of the degradation product formed on a GC working electrode surface after subjecting it to 1.6 V *vs.* RHE in 1 mM Co_xPOM in 0.1 M NaPi buffer pH 6 for 300 s. **(A)** Co L-edge spectra acquired in the total electron yield collected via a Faraday cup, via the first aperture of the differential pumping system with an applied accelerating voltage [266]. Spectra obtained at Bessy II, ISISS Beamline. **(B)** EDX mapping of the Co_4-POM degradation layer scratched from the GC surface. Red=Co, green=P, blue=W; **(C)** Atomic fractions of the elements extracted from laboratory XPS analysis of the related working electrodes surfaces, hv=8.05 keV.

Additional *post-mortem* analyses of the GC electrode surface exposed to a 20 min CA at 1.6 V in presence of Co_4-POM or Co_9-POM were performed by XAS at the Co L-edge (**Figure 3.10.A**), TEM-EDX (**B**) and XPS (**C**) and revealed an amorphous, inhomogeneous Co, P and O containing layer on the surface. Interestingly, XPS

measurements show a negligeable concentration of W in the deposit, while in pristine Co_9-POM and Co_4-POM complexes the atomic fraction of W is 3 and 2 times higher than that of Co, respectively. Finally, an XA spectrum at Co L-edge reveal an initial mix of Co(III)/Co(II) species in the layer (see shoulders at 780.5 eV specific of Co(III) on solid curves in **Figure 3.10.A**). However, after acquisition of several consecutive spectra, Co(III) is fully reduced in Co(II) due to the beam damage (dashed curves). In summary, this series of experiments on solutions containing Co-POM shows that under mild OER conditions (*i.e.,* low overpotentials) the Co-POM nevertheless degrades and forms a layer of CoO_x. Post-mortem analyses indicate that this inhomogeneous and amorphous layer is composed of a mixture of Co(III)/Co(II) oxides or phosphates. This conclusion agrees with that of *Stracke and Finke* who studied Co_4POM [236] albeit under harsher conditions (1.9 V *vs.* RHE).

As a conclusion to this electrochemical study, one can note that Co-POM degradation into CoO_x layer might mainly be driven by the charge exchanged at the interface, rather than potential driven, as the degradation ultimately occurs at potentials lower than the degradation potentials identified by cyclic voltammetries. This CoO_x degradation layer could result either from the (i) CoPOM metal-ligand dissociation equilibrium and hence non-zero concentration of Co^{2+}_{aq} leached in solution, or (ii) CoPOM degradation due to the local environment acidification resulting from the OER, or (iii) CoPOM instability resulting from the cobalt oxidation and change of coordination as part of the catalytic cycle. To differentiate between these options and eventually shed light on the changes of the oxidation state and local chemical environment of Co during the catalytic cycle, operando XAS measurements were performed under different experimental conditions.

3.4 Co-POM operando oxidation study

To investigate the behaviour of Co-POM under the OER conditions, we used a fluorescence spectro-electrochemical cell at the Lucia beamline of the Synchrotron Soleil [267,268]. In this setup the electrolyte is flowing in a close loop, through the cell, where the counter electrode (Pt foil), reference electrode (Ag wire) and working electrode (GCE foil) are placed, the X-Ray illuminating the solution *through the working electrode*, and the fluorescence signal being recorded 45° from the X-Ray beam (see **Figure 3.11**). As a photon-out detection technique is used here, the technique is bulk-

sensitive and one can easily isolate the liquid electrolyte from the analysis chamber, which is under low vacuum to maximize signal intensity.

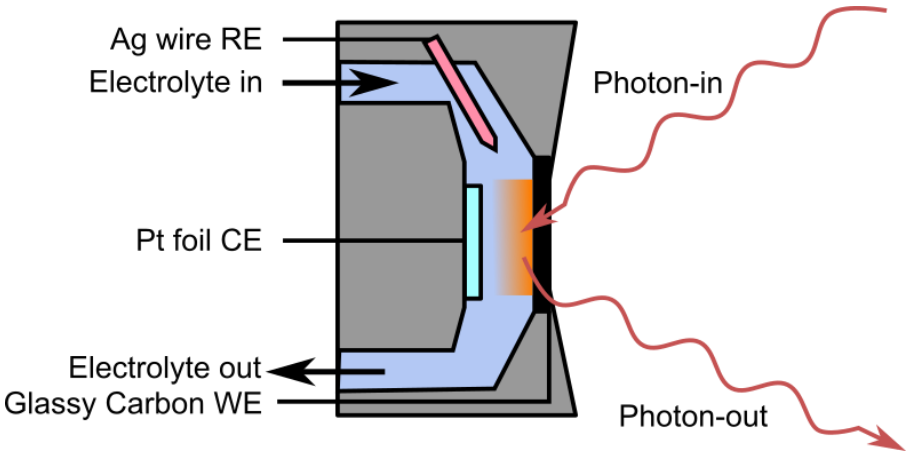

Figure 3.11: schematic representation of the XAS spectro-electrochemical cell used at Lucia beamline in this work. Here the cell is composed of a microfluidic system that carry the electrode into a PPP container containing a small, squared cavity with a window. On the back of the cavity, the counter electrode (Pt foil) is sticked to the PPP container. To close the window, the working electrode (0.06 mm × 10 mm × 10 mm glassy carbon electrode) is hermetically compressed with a cap, so that the X-Ray (2 mm×2 mm) can pass into the cell and irradiate the electrolyte, which fluoresces and emits back an X-Ray fluorescence signal to the detector. The floating reference electrode is a simple Ag wire sticked into the microfluidic system, close to the cavity. More detail on the setup can be found in Ref.[268].

Note that in this part, the applied potential was extrapolated from the Fc^{+}/Fc redox peak recorded in a separate experiment, using a 10 mM $[Fe(CN)_6]^{3-}$ in the same buffer solution, and might present some differences compared to the true applied potential. Additionally, we decided to focus for this set of experiment on Co_9-POM catalyst, as it offers a stronger Co K-edge fluorescence signal at a similar concentration along with the biggest electrochemical changes during the OER, as shown in ***section 3.3****.* We started the experiment under electrochemical oxidation conditions, reproducing the conditions exposed in **Section 3.3** (Co_9-POM 1mM, NaPi 0.72 M pH 6).

3.4.1 Operando XAS study of Co-POMs during electrochemical OER

Bpy-free experiment

Operando XAS spectra at the Co K-edge were collected for a Co_9-POM solution with different potentials applied to the GC working electrode. We note that the shape of CVs (**Figure 3.12.D**) acquired in the spectro-electrochemical cell was similar to the one

obtained in a three-electrode electrochemical cell (**Figure 3.8.D**) with an additional reversible redox peak being observed around 0.15 V *vs.* Fc/Fc^+ (0.6 V *vs.* RHE) which may be attributed to quinone/hydroquinone couple on the GC electrode [191]. The shape of the CV was used to identify the potentials of interest that were further investigated by XAS: the Co K-edge spectra were recorded at the open-circuit potential (OCP ~0.45 V *vs.* Fc^+/Fc), at the OER 'onset' at 1.05 V *vs.* Fc^+/Fc (corresponding to ~1.5 V *vs.* RHE), during the OER at 1.1 V *vs.* Fc^+/Fc (corresponding to ~1.55 V *vs.* RHE, albeit this value might slightly differ from **Section 3.3**, as aforementioned) (as illustrated in **Figure 3.12.C**) as well as *post-mortem* after flushing the spectro-electrochemical cell with ultra-pure water without exposing the working electrode to the ambient atmosphere. The spectra are shown in **Figure 3.12.A**, and the associated Fourier Transform-EXAFS (FT-EXAFS) spectra in **Figure 3.12.C**.

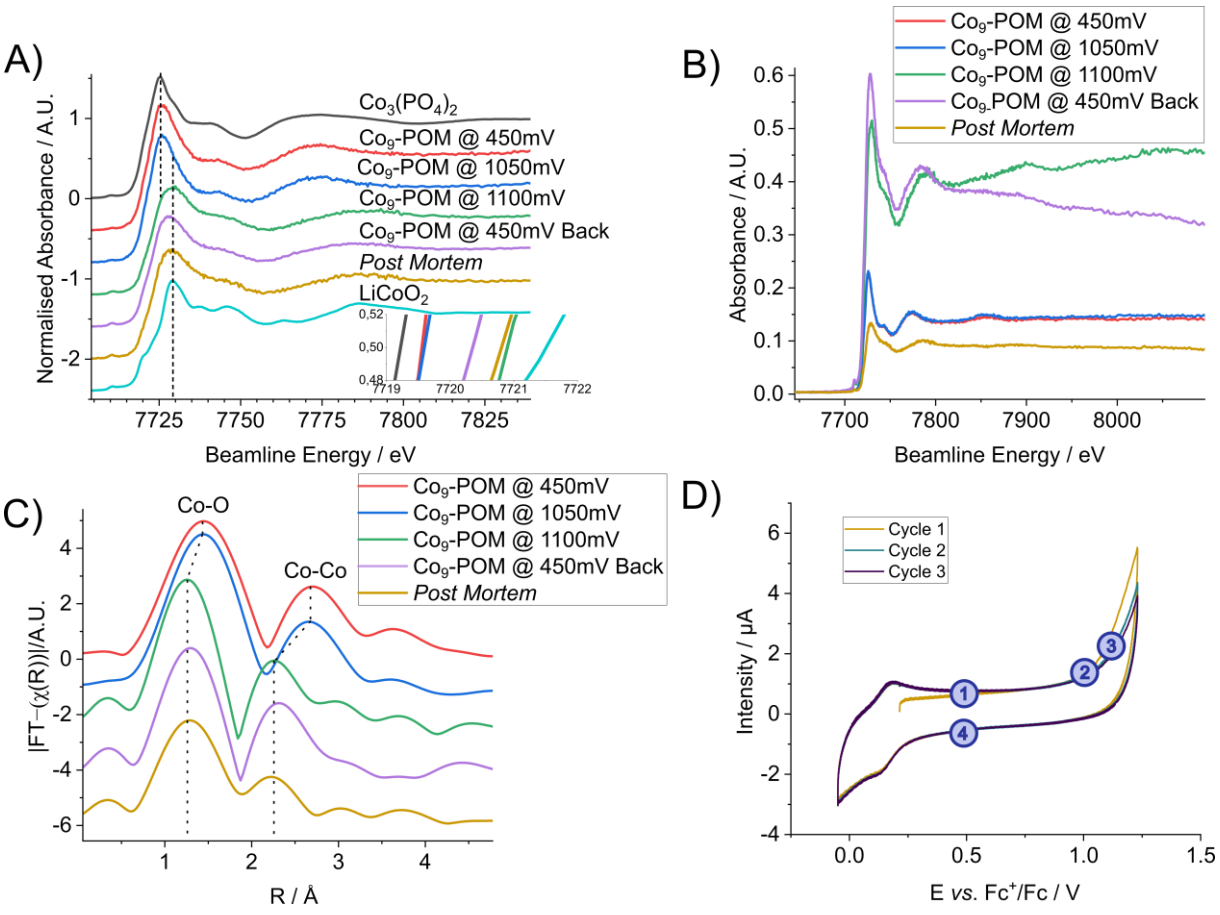

Figure 3.12: Operando measurements of 1 mM Co_9-POM in 0.72 M NaPi buffer pH 6 at different applied potentials. Potentials were estimated against a floating Fc^+/Fc reference electrode prior to the experiment, in similar conditions. **(A)** Normalised and **(B)** non-normalised Co K-Edge XAS spectra. Inset window of figure A highlight the half-edge jump shift of the different spectra without offset. The spectra of the $Co(II)_3(PO_4)_2$ and $LiCo(III)O_2$ references are

shown for comparison. **(C)** Corresponding Fourier Transform-EXAFS spectra acquired at potentials indicated in the plots. The *post-mortem* spectra were measured after the replacement of the electrolyte in the spectro-electrochemical cell by ultra-pure water. Distances indicated on the graph are apparent interatomic distances, which are about 0.5 Å shorter than the actual ones. **(D)** CVs obtained in the spectro-electrochemical cell with the potential of analysis highlighted. Scan Rate = 20 mV/s.

Neither K-edge Co spectra in **Figure 3.12.A** nor FT-EXAFS spectra in **Figure 3.12.C** show noticeable changes when the potential of the WE is increased from 450 mV to 1050 mV *vs.* Fc^+/Fc. This implies that no degradation of the Co_9-POM occurred under the applied conditions despite the OER 'onset' observed at this potential. As the OER starts at this potential according to the CV in **Figure 3.12.D**, this also indicates that the concentration of the OER reactive intermediate (RI) is below the XAS detection limit due to its low concentration (controlled by the reaction equilibrium). Indeed, in addition to follow the eventual degradation process of the Co_9-POM, the XAS can be used to capture the RI of the Co_9-POM-catalyzed OER. Previous computational studies suggested POM-Co(III)-$O^{\bullet}$ as the OER RI, which so far has never been detected experimentally [248]. Its absence at this potential being explained either by the low reaction rate at the OER 'onset' or short lifetime of the RI.

When the electrode potential is increased to 1.1 V *vs.* Fc^+/Fc, a strong shift in the Co K-edge white line is observed (**Figure 3.12.A).** While the XAS Co K-edge spectra taken at the OCP and at the OER onset are similar to the Co(II) reference ($Co_3(PO_4)_2$), the spectrum taken at 1.1 V *vs.* Fc^+/Fc is closer to the Co(III) reference ($LiCoO_2$), as confirmed by the white line position and the half-edge jump energy position (**Figure 3.12.A** inset window), suggesting that Co(II) is oxidized into Co(III) during the OER. These changes are accompanied by shortening of the Co-O (from 1.45 Å to 1.25 Å) and Co-Co (from 2.67 Å to 2.25 Å) apparent distances highlighted from the FT-EXAFS spectra (**Figure 3.12.C**) which is consistent with the reduction of the bond length and/or modifications in the Co coordination sphere due to the oxidation of Co(II).[269] These changes are irreversible since stepping back to the OCP does not allow one to restore the initial spectrum.

Similarly to what was observed in the conventional electrochemical cell (**Figure 3.9.A**), one may assume that Co_9-POM degrades during the electrolysis (in agreement with **Section 3.3**) leaving behind a Co-containing precipitate on the GCE surface. To prove

this, a XAS Co K-edge spectrum was measured *post mortem* after removing the electrolyte from the spectro-electrochemical cell and filling the latter with ultra-pure water without opening the cell and exposing it to the ambient atmosphere. The *post-mortem* spectrum confirms formation of an oxide layer consisting in Co(III) (**Figure 3.12.A and C**) in agreement with *ex situ* findings reported in the literature [210,245]. Furthermore, an increase of the Co K-edge intensity is observed on the non-normalized XANES spectra shown in **Figure 3.12.B**. Specifically, at 1.1 V *vs.* Fc^+/Fc, the edge absorbance intensity is increasing, indicating the accumulation of a CoO_x layer on the electrode. Back at 0.45 V, the edge absorbance intensity decreases, *i.e.,* the CoO_x layer dissolves, similarly to what was observed in **Figure 3.8.C** and **F**. Those changes are both observable on the overall spectra intensity, and the spectra background (>7800 eV region), as the layer electrodeposition/dissolution is a time dependant process, and each spectrum took about 20 minutes to be recorded. Finally, one should note that changes observed on non-normalised spectra should be analysed carefully as they may be subject to spectroscopic artifacts, without real meaning regarding the actual electrochemical system. However in our case, those observations are supported by the above mentioned changes in XANES and FT-EXAFS spectra.

Considering the similarities between the '*post-mortem*' XA spectrum, and the one taken under the OER conditions (at 1.1 V *vs.* Fc^+/Fc) we conclude that the Co_9-POM is degrading under the OER conditions, (despite the OER current being relatively small) and that the Co(III) degradation product deposited on the WE dominates the spectrum, which impedes the *in-situ* observation of reactive intermediate in solution.

Adding bpy to the reaction media

As we wonder if the CoO_x layer is coming from $Co^{2+}_{(aq)}$ leached in solution due to Co-POM hydrolytic dissociation equilibria (potentially impacted by the OER local pH modification) or due to Co-POM direct oxidation, we use an approach previously described in the literature [234,245], which consists in the addition of bpy to a Co_xPOM solution. The idea is to convert $Co^{2+}_{(aq)}$ ions into a $Co(bpy)_3^{2+}$ complex which is expected to be inactive towards the OER [234]. To this end, the conditions of the experiment presented in **Figure 3.12** were modified by adding three bpy equivalents per Co atom (27 eq. per Co_9-POM). The two sets of data (**Figure 3.12** *vs.* **Figure 3.13**) are then compared to determine if the cobalt oxidation can be observed without degradation as a proof of the CoPOM stability and reactivity under the OER conditions.

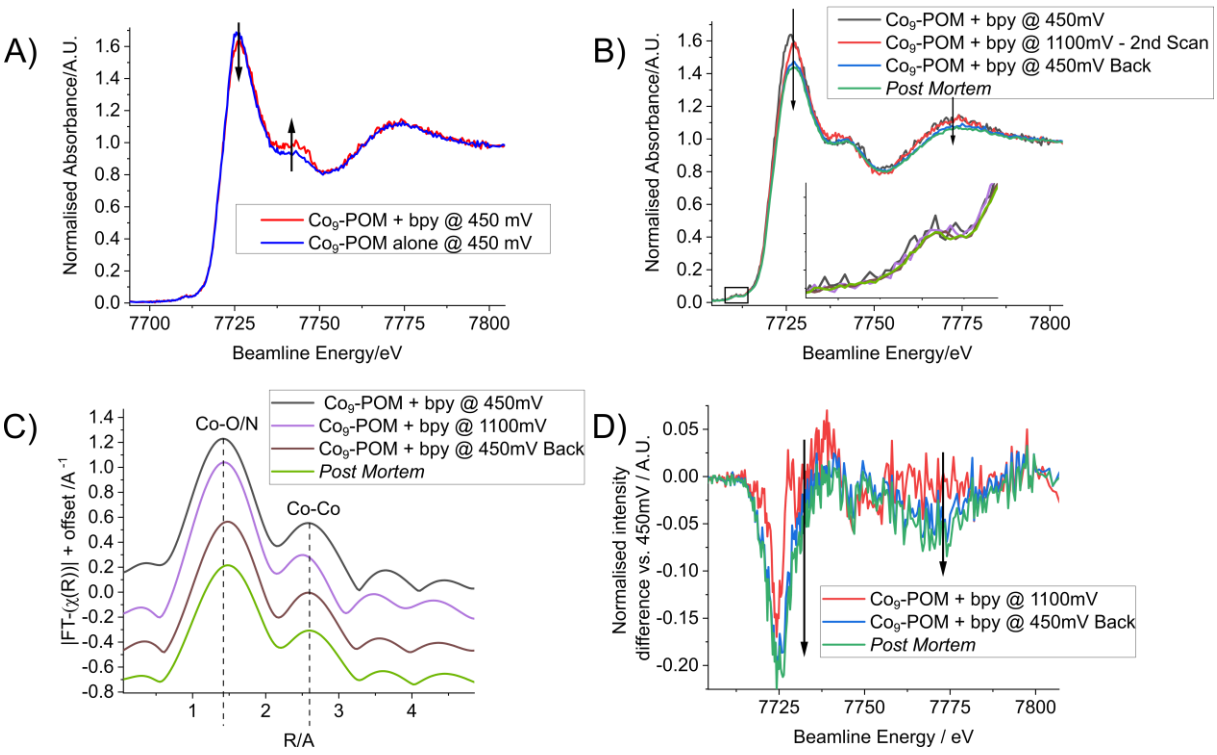

Figure 3.13: Operando measurements of 1 mM Co_9-POM in 0.72 M NaPi buffer pH 6 in the presence of 27 mM 2-2' bipyridine (bpy, 3 eq. per Co). **(A)** Comparison of X-ray Absorption Co K-edge spectra at the OCP (0.45 V *vs.* Fc^+/Fc reference) in the presence and in the absence of bpy. **(B)** Co K-Edge XAS spectra and **(C)** corresponding FT-EXAFS spectra acquired in the presence of bpy at potentials indicated in the plots. Distances indicated on the graph are apparent interatomic distances, which are about 0.5 Å shorter than the actual ones. **(D)** draws the difference between the XAS spectra shown in figure (B) at 1100 mV, 450 mV back after the analysis and *post mortem*, *vs*. the initial spectra at 450 mV. The *post mortem* spectra were measured after the replacement of the electrolyte in the spectro-electrochemical cell by ultra-pure water. All potentials are indicated *vs.* Fc^+/Fc.

Firstly, the XANES fingerprints between the Co_9-POM solution alone and Co_9-POM+bpy solution are compared at 1.1 V (**Figure 3.13.A**.). While the general shape of the XA spectra is retained and does not highlight any change in the cobalt oxidation degree, the white line and the maxima at 7743 eV evolved, suggesting that bpy influences the local environment of cobalt cations. This can be explained by the expected formation of Co(II)-bpy complexes, presumably $Co(bpy)_3^{2+}$. Changes in the spectra can also be explained by a shift in Co-POM hydrolytic dissociation equilibria, due to the bpy excess presence, which is complexing $Co^{2+}_{(aq)}$.

Then we compare the XANES spectra and the associated FT-EXAFS under *operando* conditions, shown on **Figure 3.13.B** and **C**. Similarly to the protocol applied in previous section, we started from a potential close to the OCP (450 mV), then we increased up to 1100 mV (maximum potential reached for the bpy free experiment), finally we went back to 450 mV to determine system reversibility, and performed a *post-mortem* analysis of the WE surface by the replacement of the electrolyte by ultrapure water. One can observe that regardless of the potential applied on the system, the white line position is slightly increasing towards high energy (7726 eV to 7727 eV), while its intensity slightly decreased as well as the maximum intensity of the 7773 eV peak (changes more visible on **Figure 3.13.D**, illustrating the difference between the spectrum at 1100 mV and post-mortems one, *vs.* the initial one at 450 mV). Those observations are hinting at an irreversible change in the structure of the Co-containing species and is further supported with the visual observation of the formation of a beige precipitate in the solution. The intense Co K-edge signal in the post-mortem spectra confirm the presence of an insoluble Co-containing species on the electrode surface. Therefore, we can conclude that an insoluble specie is formed during the measurements and eventually dominates the Co-K edge signal. $Co(bpy)_3^{2+}$ has good solubility in water [270] and no precipitation was reported in the literature following the addition of bpy in Co_xPOM solutions [234,245]. Hence, the precipitate was not ascribed to $Co(bpy)_3^{2+}$. However, it was reported in literature that the bpy ligands can link to Co(II) directly from cobalt-polyoxometalates complexes to form new complexes or organic-inorganic polymers [271,272], which is consistent with the lack of strong changes in relative intensity of the Co-Co band (*i.e.,* this indicates that CoPOM-derivatives are present in the precipitate). Hence, the precipitate was assumed to be a Co-POM-bpy insoluble species, formed under the experimental conditions described in this section (*i.e.,* applied potential, high bpy concentration).

From these observations, it appears that bpy greatly impacts the Co_9-POM transformations during the OER. It does prevent the formation of the $Co(III)O_x$ layer on the working electrode, instead leading to the precipitation Co(II)-bpy-POM. This indicates that the bpy does not avoid the degradation process, but rather changes the chemistry of the final degradation product. While the literature describes bpy reaction as Co^{2+} complexation, we rather observed irreversible chemical environment changes for the cobalt species, jointly with the formation of precipitate, suggesting the formation

of Co-POM-bpy species. But the question still remains, 'Does the Co-POM degradation arise from the local pH variation during the electrochemical OER or is it induced by an intrinsic instability of the Co-POM during the catalytic cycle?'. We attempt to answer this question in the next section.

3.4.2 Operando XAS study of CoPOMs during chemical OER

Local pH changes being strongly tied to heterogeneous electrochemical OER [262,263], we investigated the homogeneous chemical OER (WOC) in the presence of a chemical oxidant. As the reaction is occurring in the solution bulk rather than being localised near the GC electrode/electrolyte interface (with which the Co-POM must interact to complete its catalytic cycle), the pH modification resulting from OER is mitigated more efficiently by the buffer. To this end, we used NaClO as an oxidant, similarly to previous studies addressing the Co_9-POM activity for the OER [245,246]. Here, operando XAS is used to access stability of Co_9-POM depending on the number of oxidation equivalents (*i.e.,* 0, 1, 2, 4 and 8) of NaClO per Co atom (which corresponds to 0, 9, 18, 36 and 72 mM of NaClO added in total, *i.e.* the successive addition of 0, 9, 9, 18 and 36 eq. of NaClO). Two types of spectral acquisitions were used: 'quick' XAS, to detect Co oxidation immediately after the addition of NaClO (*i.e.* 3 scans of 3.5 min each), followed by a 'high quality' XAS (*i.e.* 2 scans of 40 min each) to obtain more precise information regarding the oxidation state and local environment of Co after the redox cycle.

The results are presented in **Figure 3.14.** Regardless the number of NaClO equivalents, no shift in the Co K-edge was observed during the 'quick' XAS measurements performed right after the NaClO addition (**Figure 3.14.A**), *i.e.,* no Co(III) was observed after the addition of NaClO, confirming the short lifetime of the Co(III) reactive intermediates, the latter reacting fast with water to produce O_2 and Co(II). The 'high quality' spectra (**Figure 3.14.B**) obtained 30 min after the addition of NaClO show a slight change in the main Co K-edge peak. This indicates a modification in the Co chemical environment as soon as 2 eq. of NaClO are added. The resulting FT-EXAFS (**Figure 3.14.C**) shows a strong decrease of the FT-EXAFS features with the increasing NaClO quantity added, highlighting the global loss of organisation around the cobalt cations. In addition, one may observe a slight increase of the Co K-pre-edge absorption, the latter related to the $Co_{1s} \rightarrow Co_{3d}$ transition. These changes may be tentatively attributed to the increase of the probability of a $Co_{1s} \rightarrow Co_{3d}$ transition with

the NaClO addition, due to the loss of the octahedral chemical environment around cobalt. The higher probability of transition would result from a stronger dipole transition character to the 3d orbital, due to a stronger 3d-4p mixing compared to pure quadripolar transition to the 3d orbitals in non-deformed octahedral environment.[273,274]

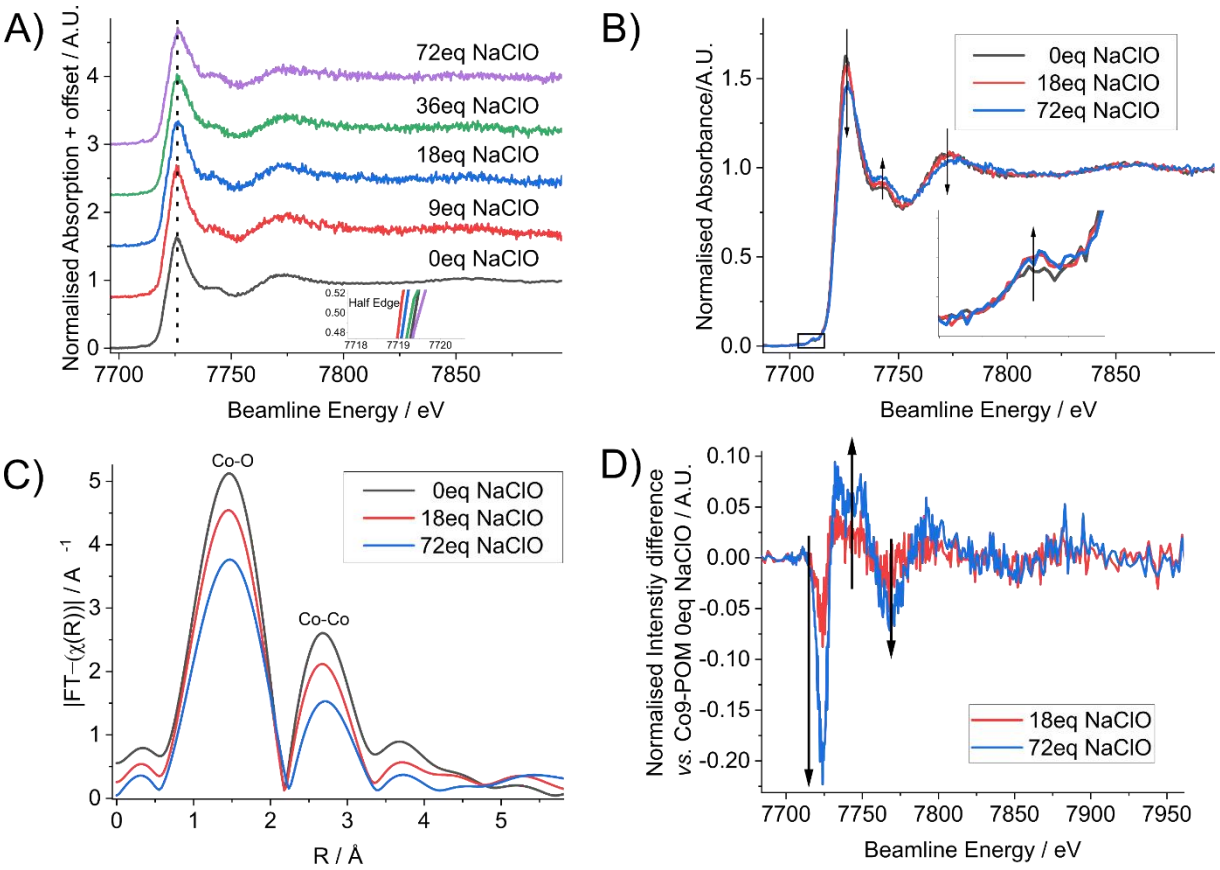

Figure 3.14: Operando Co K-edge analysis after 0, 9, 18, 36 and 72 mM of NaClO added in 1mM Co_9−POM solution, in phosphate buffer 0.72M pH = 7. **(A)** Fast XANES Co K-edge acquisition, immediately after NaClO addition. **(B)** Precise XANES spectra 30 min after the last NaClO addition. **(C)** EXAFS Fourier Transform of the (B) related spectra. Distances indicated on the graph are apparent interatomic distances, which are about 0.5 Å shorter than the actual ones. **(D)** Differential Co-K edge spectra shown figure (B) between the spectra after 18 eq and 72 eq of NaClO added, *vs.* the initial CoPOM solution.

Overall, the changes of the XAS spectra are attributed to both (i) the loss of cobalt in Co_9-POM complexes (i.*e.,* Co_9-POM → $Co_{(9-x)}$-POM) and (ii) the loss of the octahedral environment. The absence of modification in the Co-O bond indicates that no Co-Cl (1.94 Å apparent distance) bonds were formed to the detriment of the Co-O (1.61 Å apparent distance) bonds, ruling out a possible POM/chloride competition as Co

complexation agents [275]. Consequently, the Co_9POM degradation and the Co leaching arise from the OER catalytic cycle itself. The results indicate that NaClO must have effectively oxidized CoPOM, but that this oxidation, or the following reduction during the H_2O oxidation is leading to an irreversible degradation of the Co_9POM structure, resulting into the formation of $Co_{(9-x)}$POM and leached Co^{2+}_{aq}.

3.5 Foray into the use of Co-POM as a heterogeneous catalyst.

As highlighted by our *operando* electrochemical study under both electrochemical and chemical OER conditions, Co-POMs are subject to degradation in any oxidative condition, which answers the initial query of our investigation. However, there is still an interest to 'catch' the reactive intermediate for the OER, which, in such conditions, is tricky. In order to detect the reactive species in water oxidation catalytic cycle involving Co-POMs complexes, while avoiding the problematic dissociation and degradation, we attempted to transfer Co-POMs from homogeneous media (dissolved in aqueous solution) to heterogeneous media (grafted or deposited on the working electrode surface), as the chemical environment changes could improve Co-POM stability. In this section we will explore two methods to transfer POMs into a heterogeneous form, first by the preparation of Co-POM adsorbed on positively charged modified graphene (molecular form), then by the crystallisation of Co-POM in an insoluble form.

3.5.1 XPS study of Co-POMs adsorbed on positively charged modified graphene

POM and M-POM functionalisation onto surface is complex, and several methods exist to do so [203,276]. As any other molecular species, one can distinguish two different types of functionalisation depending on the interactions between the species to be functionalised and the substrate: covalent functionalisation and weak-interaction/adsorption. Several ways to covalently functionalise M-POM and POM onto a surface have been reported, most of them rely on a metalate unit replacement or modification (MO_6 octahedra) by one or several other atoms that are linked to an organic spacer [203,276,277]. This functionalisation method requires replacement of a metalate unit. Since, in our case, Keggin based ligands are already at their highest lacunary degree it is, at a first glance, not possible to go through this method to functionalise our Co-POMs from the molecular complex without its degradation or changing completely the synthesis method. The adsorption through weak interaction

is a bit easier to carry on, and once again several methods exist. As POMs and M−POMs are negatively charged, it is possible to form layer-by-layer assembling, using cationic organic molecules (such as tetrabutylammonium or porphyrins) [216,278–280]. It is worth noting that this method encapsulates the POM-based species into a polymer matrix. The accessibility of the active site is therefore hard to establish compared to the molecular dissolved species, decreasing the interest of this method in the frame of this study. Finally, it is reported that POM and M−POM can be easily adsorbed on graphene and graphene derivatives (reduced graphene oxide, and graphene modified by the addition of functional groups for instance) [203,281].This last method is the most preferable one as it retains the initial molecular structure of Co−POM complex and keeps the catalyst on the very surface of the substrate (preferable for further spectro-electrochemical *operando* analysis, as the electrochemical reaction will happen at the electrode-electrolyte interface).

Despite several experimental attempts to adsorb Co-POM on graphene and reduced graphene oxide (not detailed in this manuscript), the functionalisation of the catalyst onto such substrate remained unsuccessful (or in quantities undetectable by XPS characterization). It was then decided to improve the Co−POM / graphene interaction by the chemical modification of graphene through the addition of trimethyl ammonium functions ($R-NMe_3^+$), which would add electrostatic interactions between the Co−POM and the modified-graphene layer. This method was used successfully with the Ru_4−POM by Hadad *et al.* [227,228], another lacunary Keggin-base M-POM used for the OER.

Ammonium functionalised few layers of graphene (f−FLG) was therefore prepared following the procedure described by Hadad *et al.* This procedure and the obtained modified graphene suspension characterization are detailed in **Section 3.7.4**. Reaction scheme of FLG functionalisation and Co-POM adsorption is represented on **Figure 3.15**. In a nutshell, f−FLG is prepared from suspended FLG in dimethyl formamide (DMF), and let to react with *in-situ* prepared 4-trimethylammonium benzene diazonium (step D on **Figure 3.15**) [282,283], the resulting f-FLG suspension is cleaned, then transferred into water. To prepare the Co_4-POM and Co_9-POM grafted f-FLG, 20 µL of the f-FLG suspension (0.1mg/mL) was drop-casted on a clean and polished GCE. Once dried, the surface is immersed in 5 mM Co-POM solution and let to rest overnight (step E on **Figure 3.15**). The Co-POM/f-FLG/GCE obtained is finally gently immersed

in water for 30 s to remove weakly adsorbed Co-POM, and then analysed using XPS. The sample analysis revealed presence of Co, W, P and O in addition to the carbon substrate.

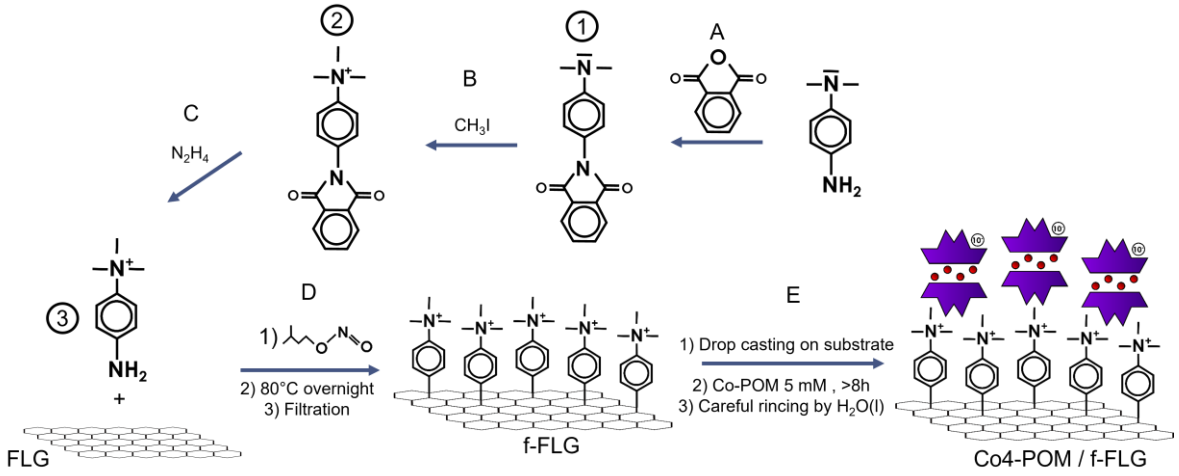

Figure 3.15: Reactional scheme of Co-POM/f-FLG. **(A)** primary amine function of *N,N-dimethyle-p-phenylendiamine* is protected using *phthalic anhydride*. **(B)** The protected molecule **1** is then methylated thanks to *iodomethane* to get the trimethylammonium function. **(C)** The obtained molecule **2** is then deprotected, and **(D) 3** is mixed with *3-methylbutylnitrite* and *few layers graphene* (FLG) suspension to generate in-situ *4-trimethylammonium benzene diazonium* and functionalise FLG. **(E)** After proper separation and isolation of functionalised FLG, the suspension is drop casted on the desired substrate. Once dry, the substrate is finally immersed in 5 mM Co-POM containing solution overnight, and rinsed in ultrapure water. The detailed synthesis method is given in **Section 3.7.4**.

Co and W XP spectra fitting (**Figure 3.16.A-D**) followed by relative element concentration estimation was therefore performed (**Figure 3.16.E**, **Equation 1.10**) According to the elemental ratio computed, the Co:W ratio is not preserved when the Co-POM is grafted onto the functionalised graphene either for the Co_4-POM or the Co_9-sample. Co:W = **22:78** and **33:67** are expected for Co_4-POM and Co_9-POM samples, respectively, while we measure an actual ratio of **80:20** for both Co-POM/f-FLG/GCE samples. Since no particular treatment was made on the Co-POM and no other product was added during the functionalisation, the ratio modification must come from a dissociation and reorganisation of the complex on the f-FLG surface. The fact that the two obtained Co-POM/f-FLG/GCE layers shows a similar ratio between Co and W, despite the initial element ratio difference between the two Co-POM, and the similarity on the XP spectra obtained, both support this hypothesis, and suggest the formation

of a thermodynamically more stable species on the modified graphene surface. *Due to the wide range of degradation products possibilities and the limited value that would provide its identification, we did not perform further investigation in that direction.*

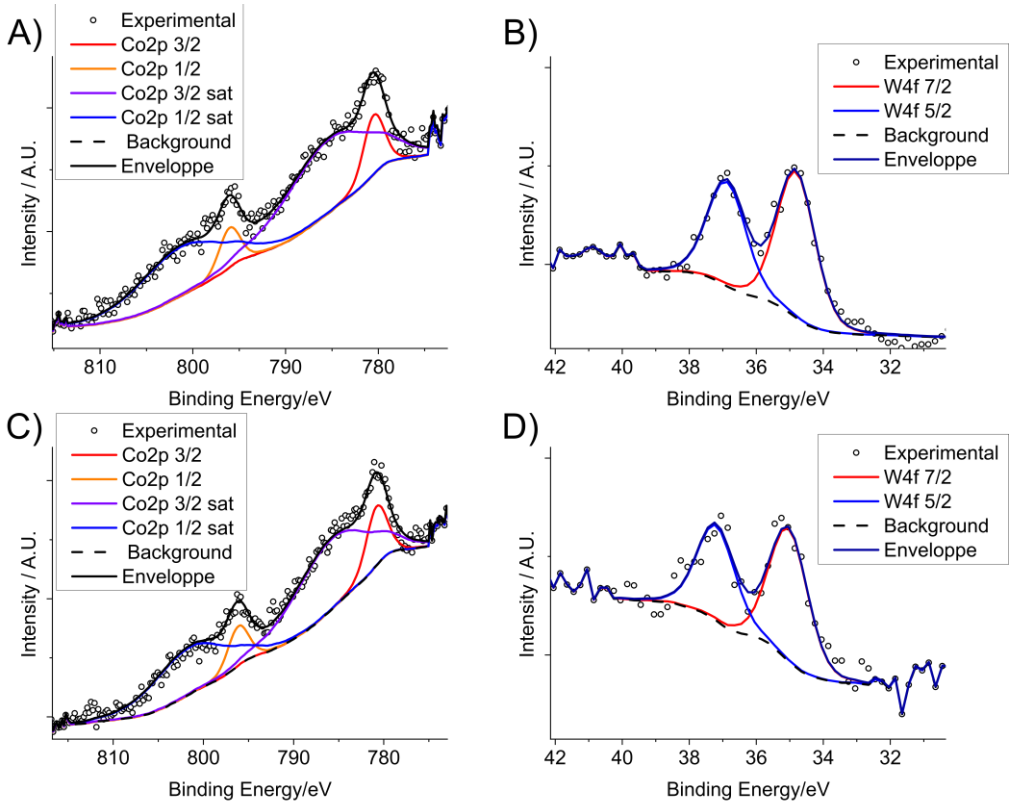

E)

Sample	Co_{2p}	W_{4f}
Co4-POM/f-FLG/GCE	82%	18%
Co4-POM (theoretical)	22%	78%
Co9-POM/f-FLG/GCE	79%	21%
Co9-POM (theoretical)	33%	67%

Figure 3.16: Co_4-POM/f-FLG/GCE **(A)** Co 2p and **(B)** W 4f XP spectra. Co_9-POM/f-FLG/GCE **(C)** Co2p and **(D)** W4f XP spectra. Data recorded at HIPPIE beamline at MAX IV synchrotron under vacuum conditions. Beam energy = 1200 eV. **(E)** XPS relative atomic ratio between Co and W, for the experimental samples and the expected ratio according to the Co-POM theoretical composition. Cobalt and tungsten area were roughly fitted using Shirley background and pure Lorentzian function, to give a first approximation of the peaks area.

This section highlights difficulties that can be encountered when it comes to Co-POM grafting on a surface. Even though the use of weak interaction (electrostatic) between the complex and the modified surface allowed the adsorption of a Co, W, P, O containing species, the Co-POM degradation was assessed due to the strong difference between the measured Co:W elemental ratio measured and the theoretical

one. This degradation once again questions the stability of those species altogether, as no particular treatment was made on the complex, except an exposure to negatively charged modified graphene layer.

3.5.2 In situ-XAS Co-POM oxidation under crystalline form

Apart from the M-POM molecular adsorption onto a surface, some groups studied those species as heterogeneous catalysts after crystallisation into insoluble Ba and Cs salts. In their solid crystalline form, the Co-POMs are supposed to be resistant to a wider range of pH, which allowed *Galan-Mascaros et al.* to explore this heterogeneous catalyst activity in acidic and alkaline media [253,254,256]. Hence, we explored the Co-POM oxidation behaviour as a crystal, using *in-situ* XAS Co-L edge measurements with Co-POM crystals drop-casted onto a gold foil and exposed alternatively to oxidative N_2O(g) and reductive H_2O(g) gases (as water oxidation catalysts, Co−POMs oxidized forms should be reduced by water). The preparation of Co-POM crystals will be detailed in **Section 3.7.4**, and a TEM imaging characterization of the obtained Co_9−POM crystals drop-casted on a TEM-grid is shown in **Figure 3.17.D,** highlighting the nanometric structure of the crystals (dimensions as small as ~100 nm). To increase signal intensity and minimise atmospheric effects on the signal, XAS spectra were measured under vacuum conditions after the gas exposure (see **Figure 3.17.C** for the experimental roadmap).

Co-POMs Co-L edge XAS spectra were measured:

(i) prior to any exposure (Vacuum 1, see **Figure 3.17.A** and **B**);
(ii) then, after being exposed to 1 mbar of N_2O for ~1 h to oxidize the Co−POM and back in vacuum (Vacuum 2);
(iii) then, after being reduced by exposure to H_2O ~1 mbar for 1 h.

In the absence of any changes in the Co L-edge spectra, the same sequence procedure was repeated at stronger oxidative conditions (1 bar N_2O for 8h). Despite the surface sensitivity of the detection method (Total Electron Yield method, ~5 nm depth sensitive) and the long exposure time in strong oxidative conditions (8 h at 1 bar N_2O), no changes in the Co oxidation degree have been observed, *i.e.,* no appearance of a shoulder at 780.3 eV, corresponding to Co(III) [284] (see **Section 4.4** for further XAS Co L-edge detailed analysis). While this method already showed oxidation degree modification on other OER electrocatalysts [285] (**section 4.6**), and since we let

enough time to the system to reach a steady state, we concluded that either (i) no cobalt centres were oxidized in those conditions or (ii) the amount of Co(III) formed is too low to be detected, or (iii) Co(III) formed in the oxidative atmosphere degraded due to eventual beam-damage effects. This absence or limited cobalt oxidation could be related to the low mobility of cobalt and lacunary POM ligands in the crystalline structure. However, the absence of Co(III) identification, compared to the findings of **Section 4.4.2** on $CoFe_2O_4$@Fe_3O_4 catalysts, brings further questions onto the capabilities of Co-POM as an OER electrocatalyst, owing to its lack of changes in oxidation degree under oxidative conditions.

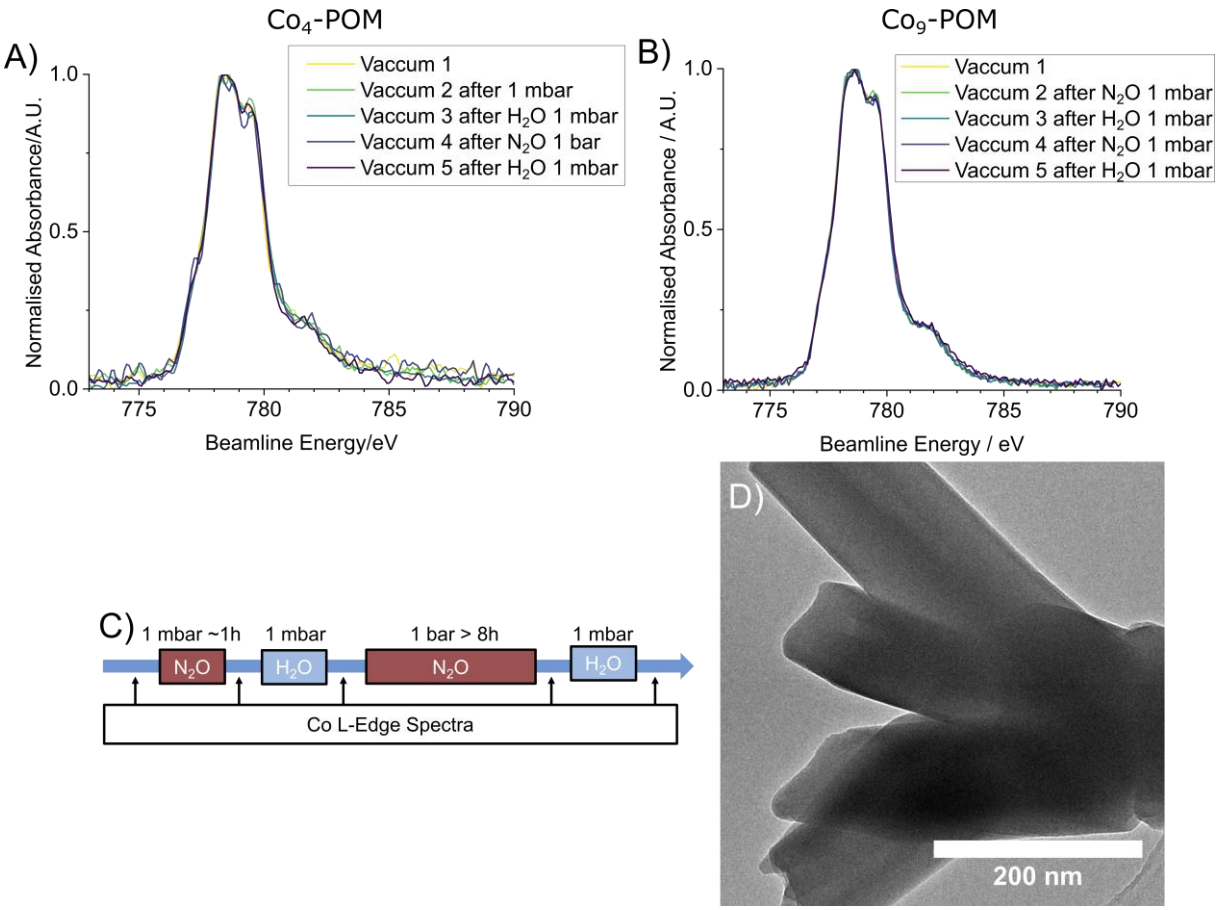

Figure 3.17: Co-L edge X-Ray absorption spectra of **(A)** Co_4−POM crystals and **(B)** Co_9−POM crystals drop-casted on the gold foil substrate and acquired following the protocol detailed in panel **(C).** Each spectrum was taken under vacuum after the exposure to the gas. **(D)** TEM image of Co_9−POM crystals.

3.6 Conclusion

Table 3.1: Co_9-POM stability towards oxidative conditions explored in this chapter. Note that RHE potentials are indicative and may differ due to issues related to the reference electrode stability (Ag wire floating reference electrode, calibrated vs Fc^+/Fc).

Phase	Oxidation condition	Co_9-POM
1 mM solution 0.72M NaPi buffer	1.55 V *vs.* RHE, CA, pH = 6 (1.1 V *vs*. Fc^+/Fc)	CoO_x formation
	1.55 V vs RHE, CA, pH = 6 (1.1 V *vs*. Fc^+/Fc) 2-2' bipyridine 3eq/Co	Insoluble Co-POM-bpy species precipitation
	NaClO >2eq/Co pH 7	Co-POM chemical environment alteration
Crystalline	$N_2O_{(g)}$ 1 bar 8h	No changes
Adsorbed on f-FLG	None	Co:W ratio alteration

$[Co_4(H_2O)_2(A\text{-}PW_9O_{34})_2]^{10-}$ (Co_4-POM) and $[Co_9(H_2O)_6(OH)_3(HPO_4)_2(PW_9O_{34})_3]^{16-}$ (Co_9−POM) are highly discussed in the literature since 2010's because they offer noble-metal-free molecular model water oxidation catalysts. Quickly after their respective growth in interest, it was observed that, in OER conditions, CoO_x formation occurs, the latter being active for the OER. This rose the question of whether the Co-POMs were true OER electrocatalysts or only precatalysts.

In this **Chapter**, we aimed, through a combination of spectroscopy and electrochemistry, to provide a clear answer to this question. To this end we:

(i) by electrochemical means and *operando* measurements, evidenced that, even at low OER overpotential, the Co-POM presence in the electrolyte leads to the formation of a layer of a heterogeneous phase at the electrode surface. This layer was characterized post-mortem using XAS and XPS and identified as a Co(III/II) oxide layer, tungsten-free, evidencing the Co-POMs instability during electrochemical OER.

(ii) by operando XAS coupled with electrochemistry, evidenced that the presence of a chelating agent, the bipyridine, prevents the growth of this Co(III/II) oxide layer, but leads to another degradation product, assumedly a

Co-POM-bpy precipitate. This clearly indicates the Co-POM instability under the conditions of electrochemical OER, likely provoked by the OER-induced local acidification at the electrode-electrolyte interface.

(iii) By operando XAS coupled with chemical water oxidation, we finally evidenced that, even when Co-POM is used homogeneously in solution (and is hence exempt of local pH changes), it also undergoes irreversible changes in its chemical structure, putting a last nail in the coffin of the Co-POM potential as a water oxidation catalyst.

Furthermore, none of the aforementioned systems allowed us to catch a glimpse of the Co(III)-based Co-POM intermediate for the OER/water oxidation. A final attempt was carried in in-situ oxidation of Co-POM nanometric crystals under N_2O atmosphere, but even the harsher conditions (N_2O 1 bar, 8h) were not sufficient to trigger the Co-POM oxidation, suggesting the cobalt center oxidation requires a flexible (non-crystalline, and/or more labile) environment, in order to be oxidized, on top of a long-term stability.

Such a clear conclusion could not have been reached without the support of spectroscopic tools: XAS and XPS were critical in the post-mortem degradation products characterization, as the quantification and Co(III) detection could only be done through XPS and XAS respectively. In addition, the XAS K-edge *operando* measurements were essential as they allowed a clear monitoring of the chemical environment modifications of the cobalt in the complex under different oxidative conditions. However one could still question the presence of a short-lived oxidized form of Co-POM which was not ‘caught’ during the operando measurements, and could pledge in favour of Co-POM being able to sustain few OER catalytic cycles, albeit this still does not guarantee their viability as OER electrocatalysts. This underlines one of the main limitations of XAS shared with XPS, which is the time-frame necessary to obtain a spectrum (>10 s), compared to reactive intermediates lifespan (< 1 ms),[286] and therefore limits the *operando* studies to steady-states or long-lived intermediate states whose characteristic time is longer than the typical scan recording time. However, progresses has been observed in the field of 'time-resolved' operando spectroscopy, which specifically aims to obtain < 1 ms information onto a given electrochemical system and catch a glimpse of reactive intermediate. The interested reader can find some meaningful examples in the following references.[287–292]

3.7 Experimental

3.7.1 Co_xPOM synthesis and characterization

Co_4-POM and Co_9-POM used in this chapter were synthesized at the *Institut Parisien de Chimie Moléculaire* (Sorbonne Université, Paris, France) following an optimized method inspired by Refs. [293,294] and described underneath. The purity of each product was verified using IR-spectroscopy and P^{31}-NMR spectroscopy before use (see **Figure 3.18**) and water content in the crystal evaluated using thermogravimetric analysis.

$Na_{10}[Co_4(H_2O)_2(PW_9O_{34})_2]$ (Co_4−POM):

Firstly 0.41 g (1.4 mmol) of $Co(NO_3)_2{\cdot}6H_2O$ is dissolved in 15 mL of distilled water. 2 g (0.83 mmol) of $Na_8HPW_9O_{34}$ is added under stirring. The mixture is then heated (at about 80°C) and stirred until a homogeneous purple solution is obtained. About 5 g of NaCl is then added and the mixture is stirred until dissolution, and then left at ambient temperature for crystallisation. After a few hours, a precipitate is filtered and dried on a sintered glass. The solid obtained is diluted in about 5 mL of hot water and then left at 5°C for re-crystallisation. After one night at low temperature Co_4POM is filtered and dried on a sintered glass. About 0.5 g (0.1 mmol) of solid is obtained. The yield is about 30%.

$Na_{16}[Co_9(H_2O)_6(OH)_3(HPO_4)_2(PW_9O_{34})_3]$ (Co_9−POM):

$Na_{16}[Co_9(H_2O)_6(OH)_3(HPO_4)_2(PW_9O_{34})_3]$ was first reported as an eventual byproduct during the Co_4POM synthesis [295]. The aim was then to improve the yield and to extract Co_9POM from the mixture. Firstly 33 g (100 mmol) of $Na_2WO_4 \cdot 2H_2O$ and 3.3 g (22 mmol) of Na_2HPO_4 are added to 100 mL of distilled water. Once dissolved, acetic acid is added until the pH of the solution reaches 7.5. At the same time 9 g (35 mmol) of $Co(OOCCH_3)_2{\cdot}4H_2O$ is dissolved in 30 mL of distilled water. Then the cobalt solution is added slowly to the tungstate solution to obtain a violet suspension which is stirred under reflux (100°C). After 2 hours the solution is hot-filtered, and an excess of $K(OOCCH_3)$ (2 g) is added. The solution is filtered again and cooled down at room temperature. About 20 g of a Co_4−POM and Co_9−POM mixture were obtained and filtered off. The filtrate is then stored at 5°C for one or two days leading to the formation of long pink needle crystals of Co_9−POM. A second filtration of the solution is therefore

performed and allows the isolation of ~0.5 g of pure Co_9−POM. The filtrate can then be stored in the fridge for a few days and future fractions of Co_9−POM can be recovered after filtration and are sometimes less and less pure in Co_9−POM and rich in acetate salts and other byproducts.

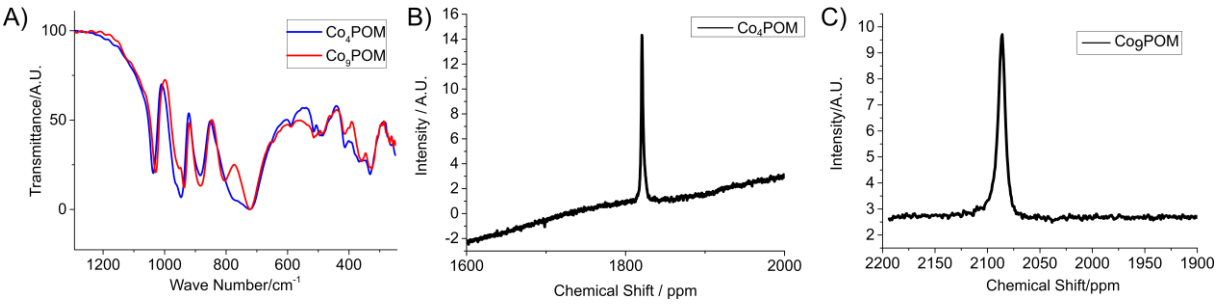

Figure 3.18: (A) Infrared spectra for Co_4−POM and Co_9−POM in the wavenumber interval characteristic of the POM. The absorption bands can be assigned as follows: 1030 cm^{-1} - P-O stretching; 940 cm^{-1} - W-O stretching; 885 cm^{-1} - W-O-W corner-sharing bending; 720 cm^{-1} - W-O-W edge sharing bending. 31P-NMR analysis of Co_4−POM **(B)** and Co_9−POM **(C)**. Samples are diluted in D_2O, dwell Time: 1 s, spectral width: 500 kHz, spectrometer frequency: 121.49 MHz, observation frequency: 121.70 MHz.

3.7.2 Electrochemical study

Sodium phosphate buffer preparation

Sodium phosphate buffer (NaPi) was prepared by dilution of an 85 wt. % H_3PO_4 solution in ultrapure water followed by neutralisation with 50 wt. % NaOH to reach pH 6, which was controlled with a calibrated pH-meter. Concentrations were calculated considering the dilution effect. Co-POM solutions were freshly prepared before each experiment and tested in a glass electrochemical cell, cleaned in Caroic acid.

Laboratory electrochemistry experiment

The electrolyte was degassed by N_2 purging for at least 10 min before the experiment, and during experiments. A 5 mm diameter glassy carbon electrode, polished by alumina (1 µm → 0.3 µm → 0.05 µm) and sonicated for 5 minutes in acetone, absolute ethanol, and water, was used as a working electrode. A flame-cleaned Pt wire was used as a counter electrode, and a mercury sulphate electrode as a reference electrode. The reference electrode was calibrated in the same electrolyte, using a platinized Pt reference hydrogen electrode, prior to experiments.

3.7.3 Co-POM in solution *operando* oxidation study

XAS beamline and cell information

Ex-situ, in-situ and operando XAS Co K-edge measurements were performed at the LUCIA beamline [267] of synchrotron SOLEIL, with a ring current of 500 mA and a nominal energy of 2.75 GeV. The beamline energy was selected by means of a Si(111) double-crystal monochromator and the beam size was 2 x 2 mm^2 on the sample. The data were collected in total fluorescence yield with a single-channel silicon drift detector from Bruker. Data reduction, normalization, and Fourier-Transforms were performed with the Athena software [296]. All data were normalized to the intensity of the incident beam. The spectro-electrochemical cell, represented on **Figure 3.11** and introduced in Ref.[268], is composed of a 0.06 mm*10 mm*10 mm glassy carbon (GC) electrode carefully washed by successive sonication in acetone, absolute ethanol, and water, 5 min each, a Pt plate counter electrode, and a silver wire floating reference electrode. The reference electrode was calibrated using the Fc^+/Fc redox peaks of a ~10 mM ferro/ferri cyanide solution. During the measurements, the electrolyte was continuously flowing in a closed loop with a peristaltic pump, coupled to an electrolyte container of 5 mL. For all spectro-electrochemical experiments, CV was performed prior to chronoamperometry and spectra accumulation.

Spectra acquisition parameters

XAS spectra of reference compounds were collected on BN pellets with 10 wt. % concentration. The spectra acquisition parameters of 'high quality spectra are detailed in .

Table 3.1: 'High quality' spectra acquisition parameters used in this chapter.

Energy range / eV	[7620,7700]	[7700,7740]	[7740,7800]	[7800,7900]	[7900,8100]
Step size / eV	2	0.2	0.5	1	2
Acquisition time / s	2	2	5	4	8

'*Quick' spectra* were taken in the 'fly mode' *i.e.* continuous change in the incident beam energy. Spectra were recorded in the [7620,7900] eV range, 1 point every 200 ms (~ 0.3 eV).

Co-POM chemical oxidation

A 1 mM Co_9-POM solution in 0.72 M NaPi at pH 7.0 was obtained by direct dilution of Co_9-POM into the desired electrolyte. In parallel, a NaClO 100 mM solution in 0.72 M NaPi at pH 7.0 was prepared by: (i) neutralization of a 50 wt. % NaClO solution with NaPi (pH4.0), up to pH 7 and (ii) dilution of the obtained intermediate solution by 0.72 M NaPi with pH 7.0. Operando chemical oxidation analysis was performed by successive addition of the desired amount of the solution containing 100 mM of NaClO into the 1 mM Co_9POM in NaPi 0.72 M solution. XAS spectra were taken in the 'quick' mode immediately after each addition of the NaClO solution, and then in a "high quality".

3.7.4 Co-POM heterogeneous oxidation study

f-FLG preparation and characterization (reactional scheme in Figure 3.15)

Step 0:Few Layers Graphene (FLG) suspension

1 g expanded graphene is suspended in 200 mL dimethyl formamide (DMF) and left under sonication (*Branson* sonication probe, Intensity=30%) for 4 hours. The resulting dispersion is centrifugated and supernatant separated, and sonicated again for 4 hours in the same conditions. FLG concentration was evaluated to be ~0.1 mg/mL by weighting the dry product of 10 mL from the suspension.

Step A: 2-(4-(dimethylamino)phenyl)isoindoline-1,3-dione (**1**)

8.00 g N,N dimethyl phenyl diamine (58.75 mmol, 1 eq) and 16.40 g phthalic anhydride (110.7 mmol, 1.9 eq) are mixed in 200 mL toluene and 4 mL triethyl amine at 130°C in Dean-Stark apparatus. Reaction advance is followed by thin-layer chromatography (TLC) until total reaction of limiting reactant. The media is then evaporated down to ~40 mL, filtrated and cleaned by toluene, methanol, and ethanol. Final product is characterised by H-NMR and weighted. 14.03 g of **1** (52.6 mmol, 89.7% yield) are obtained.

Step B: 4-(1,3-dioxoisoindolin-2-yl)-N,N,N-trimethylbenzenaminium, iodide (**2**)

14.03 g of **1** (52.6 mmol, 1 eq) are dissolved in 200 mL chloroform in a Schlenk tube, then 14 mL of iodomethane (225 mmol, 4.6 eq) are added to the reaction media. The system is heated at 50°C for ~24h. The mixture is filtrated and cleaned by chloroform and ethanol. 12.85 g of **2** are obtained (31.7 mmol, 60% yield).

Step C: 4-amino-N,N,N-trimethylbenzene ammonium, iodide (**3**)

12.85 g of **2** (31.4 mmol) are diluted in 450 mL ethanol and 7 mL hydrazine and stirred overnight at room temperature. The reaction media is then filtrated and the filtrate is evaporated, and recrystallised in 200mL ethanol. We obtain 3.42 g of **3** (39% yield) which were characterised by H-NMR.

Step D: functionalised-Few Layers Graphene (**f-FLG)**

220 mg of **3** (1.45 mmol, 1 eq) are diluted in 3 mL H_2O(l) and mixed with 45 mL of FLG suspension (0.1 mg/mL in DMF). The reaction mixture is sonicated for few minutes (ultrasound bath) and 270µL (1.45 mmol, 1 eq) of isopentyl nitrite are added. The reaction media is heated for 80°C overnight, cooled down to room temperature and filtered on polypropylene paper (0.45µm). The filtration paper is then sonicated in 100mL DMF to disperse f-FLG back and the procedure is repeated twice in methanol and once in diethyl ether. The filtration paper is finally sonicated in 25.0 mL water to obtain a 0.16 mg/mL f-FLG dispersion in water. The obtained suspension is finally drop-casted and characterised by Raman spectroscopy, transmission electron microscopy and scanning electron microscopy (**Figure 3.19**).

Raman spectroscopy highlights increase in the concentration of defects in the FLG once functionalised, as the D1 and D2 bands (linked to graphene structure defects) increases compared to the G band (graphene monolayer related) (see **Figure 3.19.A**), which was related to graphene functionalisation. In the meantime, electron microscopy images confirmed the graphene surface was rather clean as no particles of different composition (EDX not shown here) on the surface was detected, and determined the f-FLG suspension could be defined as a suspension of several graphene layers (3 to 5 layers observed on **Figure 3.19.B**) with a typical width of 3~5 µm. XP spectroscopy was attempted to quantify nitrogen on the surface and evaluate the FLG functionalisation degree, but the low intensity of the N1s peak prevented such characterization.

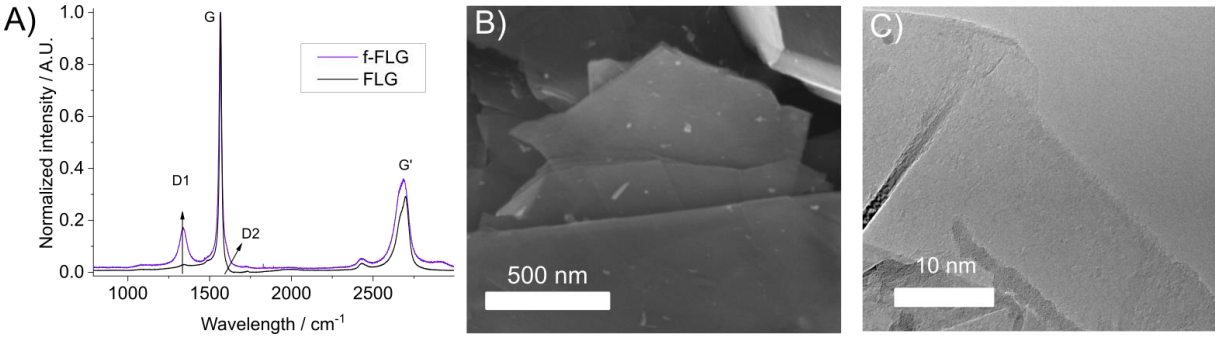

Figure 3.19: **(A)** non-modified few layer graphene suspension (FLG) and functionalised few layers of graphene drop casted on gold substrate, Raman spectroscopy. **(B)** Scattering Electron Microscopy images of f-FLG, and **(C)** Transmission Electron Microscopy image of f-FLG.

Co-POM crystal drop casting method

Co_4-POM and Co_9-POM crystals used in **Section 3.5.2** were prepared from drop-casting of Co-POM suspension in isopropanol:water (75:25 v:v) solution. To do so, 20 mg of Co-POM was dissolved in 0.33 mL of ultrapure water, then the aqueous solution is mixed drop by drop (~ 25 µL) in 1 mL isopropanol under strong magnetic stirring. Co−POM salt being poorly soluble in organic media, the crystal precipitation can be observed as the solution takes a pale blueish and opaque colour. Transmission electron microscopy was used to determine crystallite average size, which was about ~100 nm in the shortest dimension (**Figure 3.17.D**).

Chapter 4: *Operando* and *in-situ* study of the shell thickness on the OER mechanism in Fe_3O_4@$CoFe_2O_4$ core-shell nanoparticles

Sections 4.3 and **4.4** of this chapter are based on published work:

[71]: Royer L., Bonnefont A., Asset T., **Rotonnelli B.**, Velasco-Vélez J. J., Holdcroft S., Hettler S., Arenal R., Pichon B., & Savinova E. (2023). Cooperative Redox Transitions Drive Electrocatalysis of the Oxygen Evolution Reaction on Cobalt-Iron Core-Shell Nanoparticles. ACS Catalysis, 13(1), 280–286.

[1]: Royer L., Makarchuk I., Hettler S., Arenal R., Asset T., **Rotonnelli B.**, Bonnefont A., Savinova E., & Pichon, B. (2023). Core–shell Fe_3O_4@$CoFe_2O_4$ nanoparticles as high-performance anode catalysts for enhanced oxygen evolution reaction. Sustainable Energy & Fuels, 7(14), 3239–3243.

4.1 General introduction

Chapter 2 and **Chapter 3** focused on the XAS and XPS *operando* study of model systems, first with the D&P and a 2D-model electrode in absence of faradaic reaction, then with a model molecular electrocatalyst, but applied to the OER. However, not every system can be reduced to such simple objects. This is particularly true when it comes to dealing with catalysts for which the 'extended' chemical environment, or the catalyst size and shape matters for electrocatalytic activity. Such complex systems offer more perspectives from an industrial standpoint than their model, molecular counterparts. In that frame, we propose in this chapter the study of core@shell (C@S) nanoparticles (NPs) composed of $CoFe_2O_4$@Fe_3O_4 for the OER electrocatalysis in alkaline media. We therefore use a promising nanostructured OER electrocatalyst stable in *operating* conditions, while retaining some of the model electrocatalytic features, as those C@S are mono-disperse and present extremely low structural variation from particle to particle.

Transition metal oxides are widely studied OER electrocatalysts in alkaline media, since they are based on abundant elements, inexpensive and their structure/composition can be tuned to provide high activity. However the mechanism of the OER on said structure is complex, electrocatalyst-dependent, and has yet to be fully understood. This need of understanding is further increased when tackling the case of multi-metallic oxides containing Fe. It is widely accepted that the presence of Fe in addition to another transition metal cation such as Co (or Ni) increases the OER activity of an oxide material, which justifies the design of our C@S, *i.e.,* a conductive Fe_3O_4 core surrounded by a $CoFe_2O_4$ shell. However, the C@S electrocatalytic activity for the OER far surpasses the one of its individual components [1] hinting toward a synergistic interaction between the core and the shell. Using *operando* XAS, we are able to propose a first hypothesis regarding their OER mechanism and how the core-Fe(II) participates in the electrocatalytic process. To explore this hypothesis further, we decide to investigate three types of C@S NPs of various shell thickness, as the latter would impact the interactions between the shell and the core-Fe(II). The activity, durability, and structural changes under *in-situ* conditions, simulating the first steps of the OER, are investigated. Our objective is to understand how, in $CoFe_2O_4$@Fe_3O_4 nanoparticles, the shell thickness impacts the OER mechanism, aiming through this study to gather further insights on the mechanism itself.

4.2 State of the art: from transition metal oxides to $CoFe_2O_4$@Fe_3O_4 core@shell nanoparticles as OER electrocatalysts

4.2.1 The 'Fe effect'

In **Chapter 1**, a wide variety of materials used as OER electrocatalysts are discussed. Among them, transition metal oxides (TMO) have received significant attention in recent years. [297–300] Some of the TMOs demonstrated an activity comparable to that of iridium oxides, while being based on inexpensive earth-abundant elements, and stable in alkaline environment. Cobalt is one of the most studied and promising elements in that category, alongside nickel [301–304]. The combination of multiple transition metals in the same oxide material exhibits an even more interesting OER activity, especially when considering the Co-Fe (and Ni-Fe) oxide families [305–309]. This is despite iron being a relatively poor OER electrocatalyst. A review by Anantharaj *et al.* [308], highlights this so-called 'Fe-effect', which is still not fully understood, leading to several hypotheses about the activity enhancement when iron is combined with other transition metals in the OER. Possible explanations include:

- **the incorporation of Fe in the material increases its conductivity, influencing the measured catalyst's activity**. It was found by Boettcher *et al*.[310] that the incorporation of Fe into $Ni(OH)_2$/NiOOH film increases its activity concomitantly with its conductivity. Authors established a correlation between those two parameters among several electrocatalysts, and concluded that conductivity was a parameter positively influencing the catalyst activity, a result supported by other studies.[311] However it was also found that some effects (such as ageing [312]) which are negatively affecting the conductivity, could positively affect the catalyst activity, suggesting the conductivity is not the only parameter responsible for the Fe-effect.
- **the incorporation of Fe in the oxide matrix modifies its crystallography and/or impacts the chemical environment of the active site**. Several studies highlighted that the ageing of Fe incorporated/doped NiOOH [310] and CoOOH [313] systems lead to the formation of so-called 'layered double hydroxides' (LDH) structures which were proven to be more active than the Fe-free electrocatalyst. The latter was attributed to a larger number of active sites compared to the original oxyhydroxide.[310,313] Different crystallographic

changes, such as confinement of Co in specific crystalline sites due to the Fe incorporation in the structure, were observed in other systems, suggesting the LDH is not the only structural change that Fe presence can induce in transition metal oxides, and that these structural changes may be linked to the OER activity enhancement.[314,315]

- **combination of Co (or Ni) and Fe results in the formation of a unique ensemble comprised of both Co (or Ni) and Fe, resulting in an exceptionally high OER activity**. It was demonstrated through operando XAS spectroscopy combined with theoretical calculation, by Friebel *et al*., that Fe incorporation into $Ni_xFe_{1-x}OOH$ structure leads to a linear variation of the Fe−O and the Ni−O bound lengths with increasing Fe content, and results in the formation of Ni-O-Fe motives presenting an exceptionally low overpotential, therefore suggesting the existence of bimetallic highly active sites in Fe-containing TMO.[316]
- **the incorporation of Fe in the original Co or Ni oxide matrix modifies potentials of the redox transitions of the material, making it more difficult to reach high valence states**. While it is observed that the redox transition of Ni and Co oxyhydroxides is impacted by Fe impurities in solution as low as 1ppm (anodic shift with Fe impurities, [310,313,317]), it has been shown that under the OER conditions, the redox behaviour of $Ni_xFe_{1-x}OOH$ electrocatalyst under OER potential is unusual. Fe remains in a trivalent state independently of the potential, while Ni oxidation state highly depends on the Fe content, exhibiting lower oxidation states with greater Fe content. Thanks to a combination of *operando* differential electrochemical mass spectroscopy (DEMS, which gives an information about the OER faradaic efficiency, as the OER competes with the Ni(III) → Ni(IV) transition) and *in-situ* XAS analysis, the authors determined that the greater the Fe content in the oxyhydroxide, the lower the Ni oxidation state, and the higher the OER faradaic efficiency, owing to a more reduced Ni. An increasing content of Fe inside the structure can therefore prevent the Ni oxidation and positively impact the material's OER activity. [318,319]

4.2.2 Oxides with a spinel structure for the oxygen evolution reaction

As highlighted in the frame of the Fe-effect, both the crystallographic state of the catalyst and its eventual surface reconstruction during electrocatalysis, affect the activity, as they define the chemical environment of the active site. Various oxide structures have been studied for the OER applications, such as perovskites [320–322], hydroxides [323,324] and spinels [325–328]. Among these, spinels stand out as one of the most promising OER electrocatalysts due to their stability, conductivity, tuneable composition, and high activity.

A spinel has a chemical formula of AB_2O_4, where A and B represent di- and trivalent cations, respectively. Spinel crystals belong to the Fd3m space group, exhibiting face-centred cubic (fcc) cell symmetry with oxygen atoms arranged in a cubic-closed packed (ccp) lattice. The A cations occupy tetrahedral sites, while B cations occupy octahedral sites, as depicted in **Figure 4.1.A**. A variation of this structure known as "inversed spinel" consists in the inversion of A(II) cations with half of B(III) cations in the structure. Consequently, A and half of B cations share the octahedral sites, while the other half of B cations occupy the tetrahedral sites.

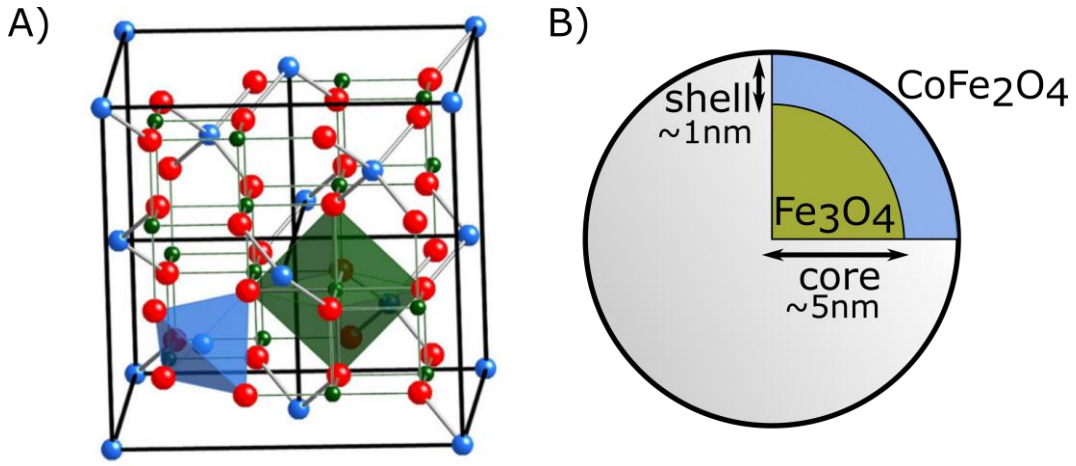

Figure 4.1: **(A)** Spinel crystallographic structure representation (blue: tetrahedral sites, green: octahedral sites, red: oxygen). Reproduced from Ref.[329]. **(B)** Schematic representation of Fe_3O_4@$CoFe_2O_4$ nanoparticles core-shell. The exact particle dimensions are given in the **section 4.8.1**, **Table 4.1**.

One of spinel advantages regarding their catalytic activity may actually be related to this chemical environment diversity for the cations, where both tetrahedral and octahedral geometry are represented. Indeed, the 3d orbitals splitting is different

depending on the coordination geometry of the anions around the cation: octahedral geometry resulting in e_g and t_{2g} orbital groups splitting, and tetrahedral geometry resulting in t_2 and e groups.[330–332]

Using spinel structures as OER electrocatalysts is not a new concept, and numerous studies have proposed OER mechanisms on transition metal oxides in alkaline media. Two mechanisms seem to be at work during the OER on transition metal oxides. The first is the 'conventional mechanism,' also known as the 'adsorbate evolution mechanism', which is the most commonly proposed. It suggests that the reaction occurs on the surface, and that the metal acts as the primary active site during the reaction (**Figure 4.2**.**a**), with formation of M−OH hydroxide intermediate that later reacts to form M−OOH peroxo-intermediate. This mechanism aligns with the Sabatier principle, which links the strength of the M-O bond to the catalyst activity. However, studies aiming to understand the parameters influencing the OER performance highlighted the existence of a second mechanism, often referred to as the 'lattice oxygen mechanism.' This alternative mechanism proposes the participation of oxygen from the crystalline lattice in the OER and highlights that the cation may not be the sole active site in the catalyst (**Figure 4.2.b**). The lattice oxygen mechanism explains the out-of-trend activity observed for some electrocatalysts (*e.g.,* perovskites with certain compositions) when assessing them in the prism of the adsorbate evolution mechanism. [297,332,333]

Even if Co spinels are generally considered stable in alkaline media under oxidative potentials, durability studies coupled with XAS and XPS analyses carried out by Calvillo *et al.* proved $Co_xFe_{3-x}O_4$ materials suffer from partial restructuring of the surface (that may be induced by partial dissolution/redeposition of the surface cations, see **Figure 4.2.c)**. This was confirmed by several other works [333–337]. Similarly, an operando X-Ray surface diffraction study of the OER on Co_3O_4 surfaces by Magnussen *et al.* proved the formation of a thin CoOOH layer at potentials > 1.2 V *vs* RHE [337]. These studies conclude that CoOOH resulting from the Co_3O_4 electrochemical oxidation is required for the OER electrocatalysis and propose Co(IV) as a reactive intermediate.

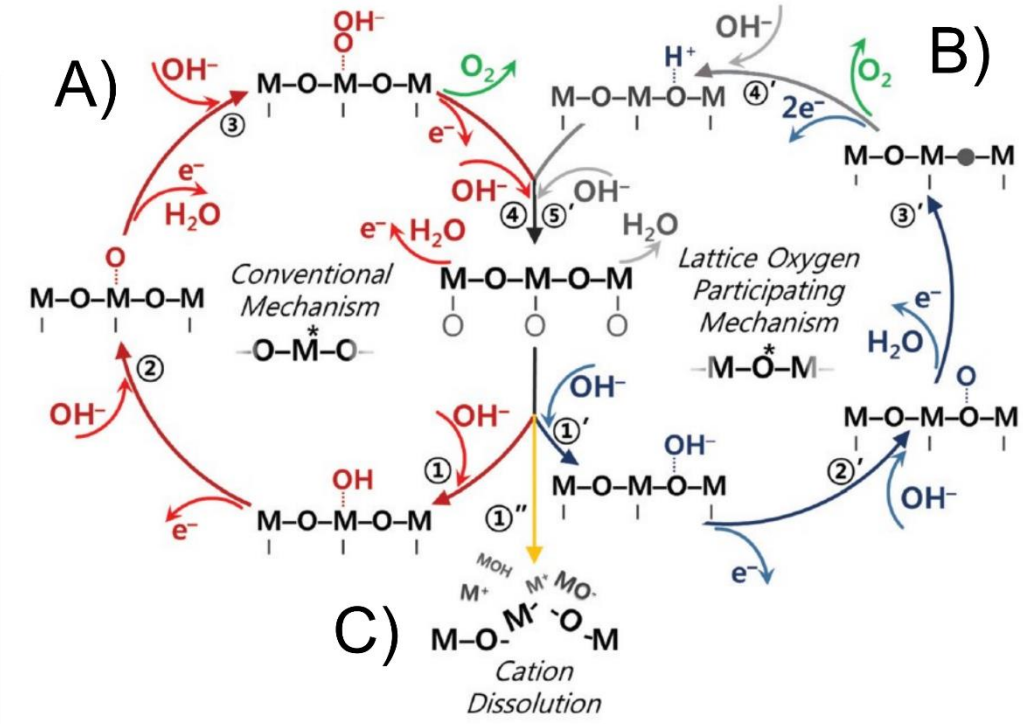

Figure 4.2: Current hypotheses regarding the OER mechanism on perovskites going through **(a)** the conventional adsorbate mechanism and **(b)** the lattice oxygen participating mechanism. **(c)** represents a potential surface dissolution of the cations, which can be redeposited to form a hydroxide layer on top of the catalyst. Figure reproduced from Ref.[29].

To increase even more the activity, the electrocatalysts morphology at the nanoscale (*e.g.,* shape, size, etc.) is of great importance. Indeed, the use of nanometric particles (NPs) leads to a greatly enhanced surface-to-mass ratio compared to macroscopic materials, due to their extremely small dimensions. This allows to develop highly active catalytic layers while using substantially less material. Furthermore, in addition to the impact of the surface-to-mass ratio, complementary benefits may come from nano-size induced effects. [338] NPs are already used as OER electrocatalysts, [93,339–341] yet those materials could be improved even-more using a core@shell (C@S) design. A different composition of materials for the core and for the surface (shell) can lead to a combination of both material properties and eventual synergistic effects which improve the overall properties of the nanostructure.[342–344]

4.2.3 Objectives

In **Section 4.2,** we explored different parameters that can influence a catalyst activity: its composition, its nanostructure, and finally its composite nature, such as a C@S structure that could benefit from synergistic effects between the core and the shell. In

the following subsections, we propose to study a novel OER promising electrocatalyst: Fe_3O_4@$CoFe_2O_4$ (C@S) nanoparticles. We aim to minimize the cobalt use in the electrocatalyst and improve its conductivity, as well as exploring and exploiting the poorly understood Fe-effect in OER electrocatalysts. To that end, the nanoparticles' design is thought as (i) a core composed of a conductive, but OER inactive, Fe_3O_4 magnetite, that will provide a good electron conductivity to the whole surface of the electrochemically active shell and (ii) a thin shell presenting a minimal amount of Co, supposedly OER active due to its $CoFe_2O_4$ composition, but which suffers on contrary from its lack of conductivity. Combination of these two complementary materials into an advantageous architecture is therefore promising from an electrocatalytic point of view. In the following part, we will discuss the activity of these C@S nanoparticles for the OER, along with the mechanism of said reaction on those catalytic nanostructures, unveiled through the use of *in-situ* and *operando* XAS.

4.3 Evaluation of the electrocatalytic activity of core@shell nanoparticles

To assess the C@S architecture effect on the OER activity, a first set of nanoparticles was prepared: Fe_3O_4 (⌀ = 12.4 nm), $CoFe_2O_4$ (⌀ = 9.8 nm) and Fe_3O_4@$CoFe_2O_4$ (core ⌀ = 12.7 nm, core@shell ⌀ = 14 nm) which will be called C@S-0.65nm referring to the shell thickness. More details regarding the synthesis and characterization, as well as a summary of the different particles used in the chapter is given in **Section 4.8**. *For the rest of this chapter, unless stated otherwise, the potentials will be given versus RHE.*

The different nanoparticle suspensions were diluted to reach the same final concentration (~0.04 µg/µL), and 10 µL was drop-cast onto a clean ⌀ = 0.5 cm Glassy Carbon Electrode (GCE) disc, resulting in a ~2 µg/cm^2 nanoparticle loading on the surface. This dilution step and control of the loading is important as previous studies [345] demonstrated the influence of the catalyst layer thickness on the mass activity. Nevertheless, it is important to note that the solvent volatility (chloroform), the stability of colloidal nanoparticles in low concentration solutions, and the shaping method for the catalyst layer (drop-casting) are two main obstacles to the precise control of the NP loading and the catalyst layer homogeneity. After deposition, and prior to any electrochemical analysis, NP surface was systematically cleaned by cyclic

voltammetry in a restricted potential interval from 0.8 V to 1.44 V *vs* RHE (150 cycles at 100 mV/s) to remove organic ligands from the NPs surface.

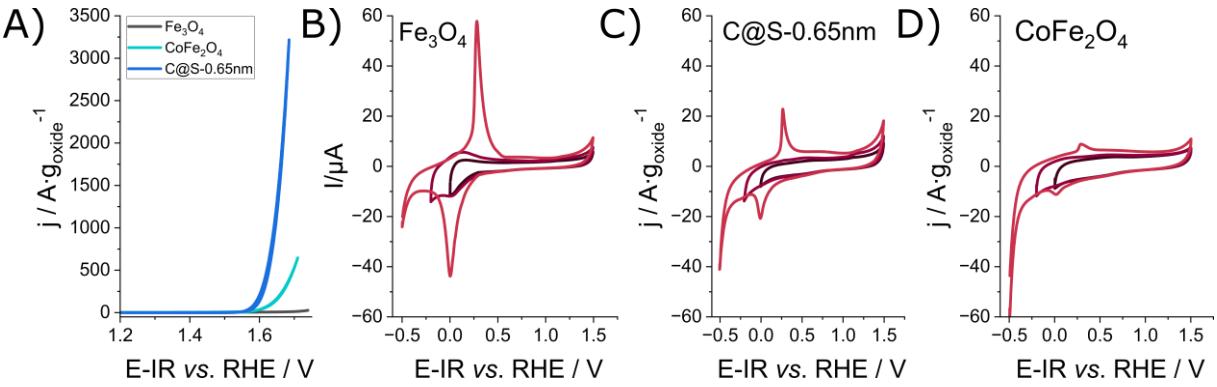

Figure 4.3: Influence of the core@shell architecture on electrochemical and electrocatalytic properties of NPs. **(A)** OER activity normalised per oxide mass for Fe_3O_4, $CoFe_2O_4$ and C@S-0.65 nm sample. CVs were obtained in 0.1 M NaOH with 10 mV/s scan rate, working electrode rotation at 1000 rpm, with the temperature controlled at 25°C. **(B) (C)** and **(D)** are the second cycle of CVs at low potentials for Fe_3O_4, C@S-0.65nm and $CoFe_2O_4$ nanoparticles, respectively. CVs obtained in 0.1 M NaOH with 20 mV/s scan rate, working electrode rotation at 1000 rpm and temperature controlled at 25°C.

Two types of analyses were performed. First, the NPs activity under the OER conditions was recorded (see **Figure 4.3.A**) and normalised by the catalyst mass. One observes that both the Fe_3O_4 and $CoFe_2O_4$ nanoparticles exhibit a rather low activity (20 A/g_{oxide} and 120 A/g_{oxide} at 1.65 V, respectively) compared to C@S-0.65nm which exhibits a much higher activity (750 A/g_{oxide} at 1.65 V). This first activity comparison perfectly illustrates the advantage of the C@S architecture that dramatically improves the nanoparticle activity through the combination of the two oxides: $CoFe_2O_4$ confined within the shell and Fe_3O_4 within the core. This activity enhancement can be explained by (i) the conductivity enhancement of the $CoFe_2O_4$ material due to the presence of the Fe_3O_4 core, and/or (ii) the 'Fe-effect', due to the presence of Fe(II) (in the core) near the $CoFe_2O_4$ shell. Indeed, while combining Co and Fe in a crystalline structure results in the activity enhancement, (*e.g.,* as shown here or by Saddeler *et al.,* that showed that a $Co_xFe_{3-x}O_4$ nanostructure with an optimum Co fraction can outperform either Fe_3O_4 or Co_3O_4 spinel [306]) this alone is not sufficient to explain the higher activity of C@S-0.65nm compared to single-phase $CoFe_2O_4$ NPs.

Then, cyclic voltammograms are recorded at low potentials down to –0.5 V for the same set of nanoparticles. One observes that $CoFe_2O_4$ (**Figure 4.3.D**), Fe_3O_4 and

C@S-0.65nm do show a redox transition with cathodic and anodic peaks at 0.0 and 0.28 V *vs.* RHE correspondingly. These peaks can be associated to the Fe_3O_4 to Fe(II) hydroxide transition [346]. The amplitude of the peaks corresponding to this transition is decreasing from the Fe_3O_4, to the C@S sample, with a lowest peak for $CoFe_2O_4$ NPs, which can be explained by the lower accessibility of Fe_3O_4 for this transition in the case of the C@S NPs, due to the shell covering the Fe_3O_4 core, and a disadvantaged transition in $CoFe_2O_4$ oxide due to the absence of Fe(II) in the structure. Though, as the redox transition happens at the surface of the material, one should expect the same redox peak intensity between $CoFe_2O_4$ and C@S-0.65nm, which is not the case. The higher $Fe_3O_4/Fe(OH)_2$ transition in C@S sample could be explained by some defects in the structure: either (i) in the microstructure (*e.g.,* part of the core is exposed as the shell may not be fully homogeneous), or (ii) in the lattice, with some Fe_3O_4 or Fe(II)CoFe(III)O_4 defects in the shell crystalline structure, as both could explain the presence of Fe(II), which is in theory required for this redox transition at the NP surface. The 2nd explanation justifies as well for the presence of the redox peak on the $CoFe_2O_4$ NPs, as defects of Fe(II) in the surface would allow to a lower extent the transition.

As a first conclusion, we observed a strong activity enhancement due to the C@S architecture. To shed light on the OER mechanism in this system and understand the mechanism behind the strong activity enhancement of C@S-0.65nm compared to the Fe_3O_4 and $CoFe_2O_4$ respective activities, we performed an *operando* XAS study under OER conditions for these C@S nanoparticles.

4.4 Operando assessment of the OER mechanism with $CoFe_2O_4$@Fe_3O_4 nanoparticles

To gather information related to the chemical and structural modifications undergone by the C@S catalyst during the OER, an operando study by X-ray absorption spectroscopy of C@S-0.65 nm at the L_3-edges of Co and Fe was carried out. The experiments were performed in total electron yield (electron-out detection), which is sensitive to the surface (~5 nm) as explained in **Section 1.3.3**. Two sets of experiments are presented here. The first one is used to characterize the sample changes under reductive conditions, while the second one is used for the *operando*

observation of the OER. The details for this spectro-electrochemical cell and sample preparation are given in **Section 4.8.4**.

4.4.1 Nanoparticle reduction operando study

In the first experiment, the cyclic voltammogram of the working electrode is recorded and can be observed on **Figure 4.4.C**. One observes two small redox peaks: a cathodic peak around -0.1 V and anodic peak around +0.2 V. This transition is similar to the one observed on **Figure 4.3.C**, which is tentatively attributed to the $Fe_3O_4/Fe(OH)_2$ transition. One also notes that those peaks are slightly shifted compared to the **Figure 4.3.C** CV (-0.1 V shifting), probably due to reference electrode calibration and stability issues in *operando* setups, rather than a physically meaningful change between the systems. Then, the XA spectra were recorded at constant potential, which was set at 1.0 V, -0.2 V and -0.4 V. Between application of each cathodic potential, 1.0 V was applied once again to verify the reversibility of transformations. One can observe Fe and Co L-edge at the different potentials in **Figure 4.4.A** and **B**.

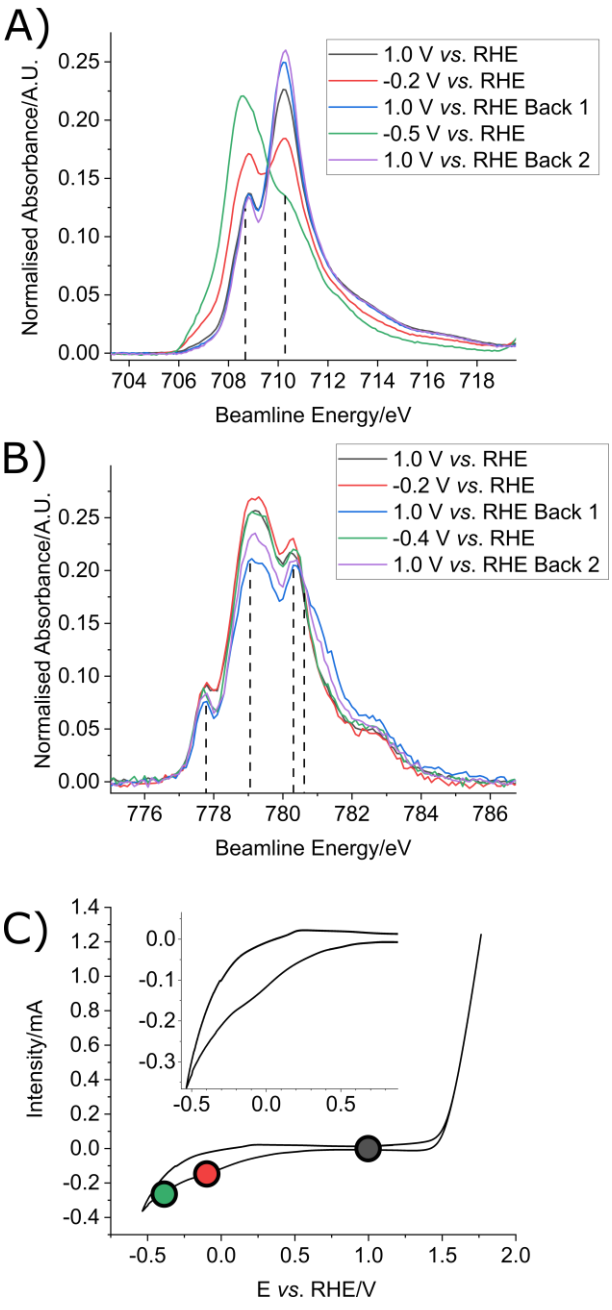

Figure 4.4*: C@S-0.65nm study of NPs in a spectro-electrochemical cell in the potential interval from 1.0 to −0.5 V vs. RHE:* ***(A)*** *Fe L_3-edge,* ***(B)*** *Co L_3-edge and* ***(C)*** *cyclic voltammogram acquired in the spectro-electrochemical cell prior to the experiment. C@S-0.65nm NPs are deposited on Fumatech membrane using bilayer of graphene as current collector, electrolyte is 0.1 M NaOH, scan rate 20 mV/s.*

To determine the Fe and Co oxidation degree and follow their evolution as a function of the potential, XAS reference spectra

were acquired experimentally or taken from the literature,[28] as presented on **Figure 4.5**. FeO (Fe(II) octahedral environment) is characterized by a main peak at 708.6 eV (Fe-α peak on the figure); while Fe_2O_3 (Fe(III) octahedral environment) is characterized by a main peak at 710.2 eV (Fe-β peak on the figure) and a smaller feature at 708.7 eV. Due to the close position of this feature and the Fe-α peak, it is impossible to distinguish both when a mix of Fe(II) and Fe(III) is present. The qualitative sample oxidation or reduction is then assessed through the variation of Fe-α and Fe-β relative peak intensity. Co reference spectra can be observed in **Figure 4.5.B** where CoO (Co(II) octahedral environment) and $LiCoO_2$ (Co(III) octahedral environment) are represented. Co(II) spectra are composed of several peaks: Co-α (777.7 eV), Co-β (779.0 eV) and Co-γ (780.2 eV) while Co(III) only has one main peak at 780.6 eV (peak Co-δ). Due to Co-δ slightly higher energy position compared to Co-γ, the Co(II) oxidation to Co(III) often appears as a growing shoulder in the high energy interval of the Co(II) peak, with a change in the Co-β /Co-γ intensity ratio.

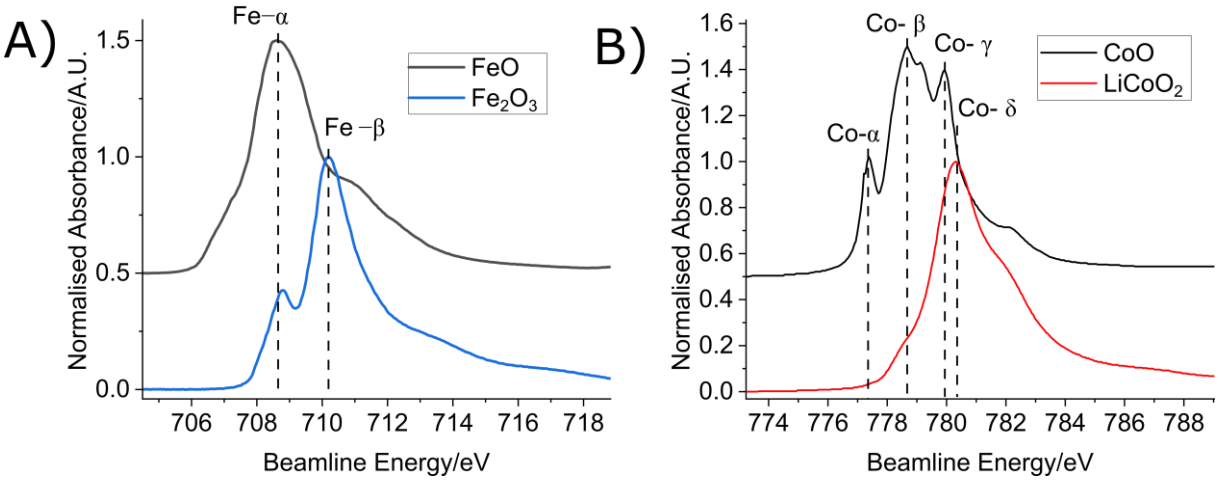

Figure 4.5: Reference **(A)** Fe L_3-edge of FeO and Fe_2O_3 and **(B)** Co L_3-edge of CoO and $LiCoO_2$ X-Ray absorption spectra, cobalt references are taken from Ref.[347]. XAS spectra are normalised to the peak maxima.

For the C@S-0.65nm NP**,** the application of −0.2 V *vs* RHE results in a Fe-α peak intensity increase and a lowering the Fe-β peak intensity, indicating a reduction of Fe(III) to Fe(II) (see **Figure 4.4.A**). This observation is coherent with the interpretation of the CVs presented in **Figure 4.3** and the attribution of the redox peak at 0 V to Fe(III)/Fe(II) transition from Fe_3O_4 to $Fe(OH)_2$. The application of −0.5 V showed a stronger reduction trend. The signal back at 1.0 V showed a good reversibility with the

return of the Fe signal close to the 1.0 V initial signal. It is thus concluded that within the depth of analysis (~5 nm) the observed iron can reversibly be reduced from Fe_3O_4 to a Fe(II) structure, probably corresponding to $Fe_3O_4 \leftrightarrow Fe(OH)_2$ transition [265,348].

The application of a reductive potential did not have any significant impact on the Co L-edge signal (see **Figure 4.4.B**). The initial cobalt oxidation degree already being Co(II) in the structure, the application of -0.5 V is not enough to reduce cobalt to its metallic state. However, the spectrum measured after stepping potential back at 1.0 V *vs.* RHE did show a slight oxidation of Co compared to the initial spectrum at 1.0 V *vs.* RHE. This is highlighted by the lowering of the Co(II) Co-α and Co-β peaks, and the appearance of a shoulder around 781 eV. This might be induced by the phase transition from Fe_3O_4 to Fe-hydroxide under potential and the return to the initial Fe_3O_4 phase at OCP. Such crystallographic changes might impact the defects density within the crystalline structure, as well as the Co and Fe distribution in the NPs. Note that Co(II) → Co(III) redox transition starts around 1 V *vs.* RHE (see **Section 4.4.2** and discussion therein), which could explain slight increase of the Co(III) contribution when stepping to 1.0 V *vs.* RHE. *Post-mortem* TEM imaging and electron energy loss spectroscopy (EELS) mapping confirmed a modification of the NP's shape (from 'perfectly' spherical transforming into NPs with rough edges) as well as cobalt redistribution within NPs after the reductive treatment, suggesting a loss of the C@S architecture [71]. The observed changes in **Figure 4.4.B.** thus suggest that loss of the C@S morphology favours accumulation of Co(III) at positive potentials.

Those results first confirm that reduction at potentials as low as -0.5 V for an extended time (10~20 min) does not reduce Fe to its metallic state, and that the $Fe_3O_4/Fe(OH)_2$ transformation is essentially reversible in this system. However, the C@S structure is lost after such a reductive treatment and the defect concentration may increase within the crystalline structure [71], impacting redox behaviour of Co, as reflected by the increased concentration in Co(III) at 1.0 V. *Additionally, it confirms that the spectro-electrochemical cell used for those experiments allows to follow changes in the oxidation state of Co and Fe when a potential is applied, meaning the part of the working electrode which is assessed by X-rays is indeed polarized.*

4.4.2 *Operando* study of the OER

The second experiment consists in the study of the electrocatalyst properties under OER conditions. The cyclic voltammetry is represented on **Figure 4.6.C**. A first redox cathodic peak is observed at ≈ 1.05 V and an anodic peak at ≈ 1.1 V. Those peaks are attributed to Co(III)/Co(II) transition, which in the literature was associated with a transformation from Co_3O_4 to CoOOH [337]. A second cathodic peak (with the corresponding anodic peak hidden in the OER current rise) is observed at 1.3 V and associated in the literature to the Co(IV)/Co(III) transition.[337,349,350] The fact that these redox transitions are little or not observable in the liquid electrochemical cell with NPs deposited on a GC disc (**Figure 4.3**) can be attributed to high pseudo-capacitance of the GC, the latter hiding features related to the NPs given their small loading. One will note that OER is starting earlier in the spectro-electrochemical cell compared to the conventional electrochemical cell (see CVs presented on **Figure 4.3.A**). This could be explained by difficulties in reference electrode stability and calibration (Ag/AgCl) in our operando system as well as to a higher NP loading in the *operando experiment*.

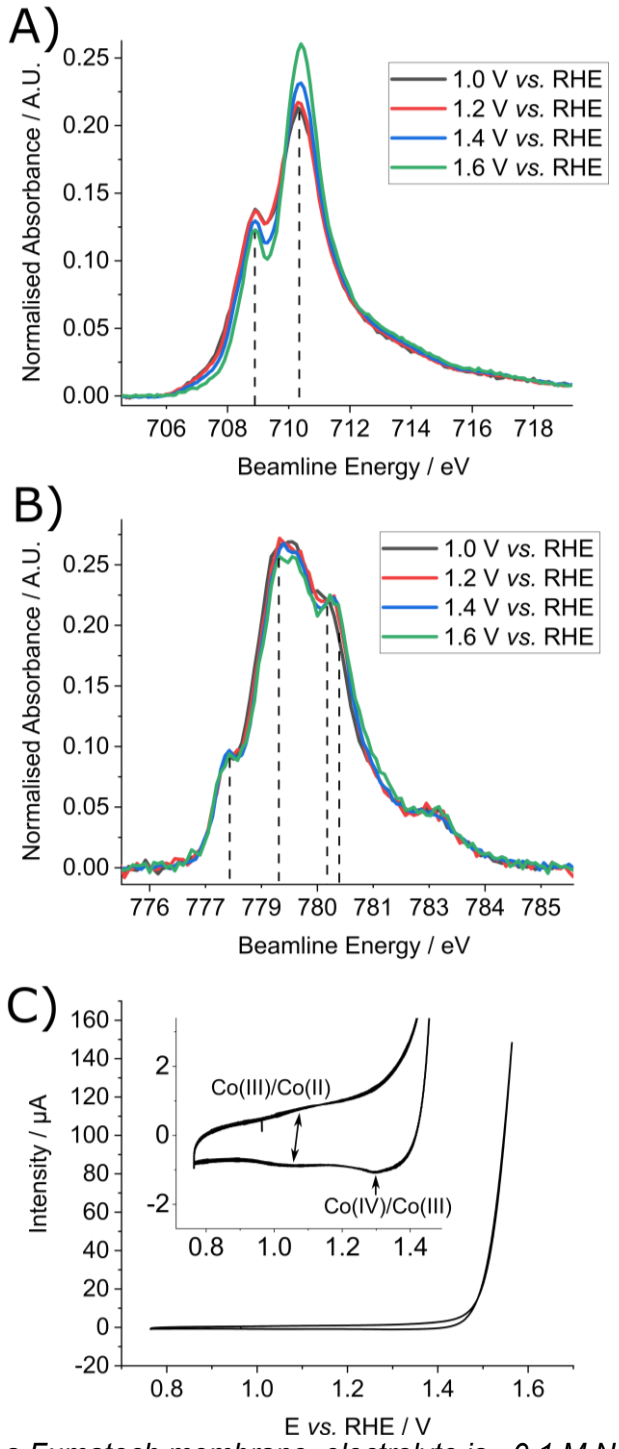

Figure 4.6: *Study of C@S-0.65nm NPs in a spectro-electrochemical cell in the potential interval from 1.0 to 1.6 V vs. RHE:* ***(A)*** *Fe and* ***(B)*** *Co L_3-Edge XAS operando analysis under different successive oxidative potentials.* ***(C)*** *Cyclic voltammetry in the spectro-electrochemical cell prior to the experiment. C@S-0.65nm NPs deposited on a Fumatech membrane, electrolyte is −0.1 M NaOH, scan rate 20 mV/s.*

Similarly to the previous experiment, the Fe and Co L-Edge spectra were acquired under potentiostatic conditions. Potentials were increased step by step in the view to observe transformations occurring at different increasing potentials, namely 1.0 V (starting potential much below the OER); 1.2 V (above Co(II)/Co(III) transition according to the CV); 1.4 V (just before the OER onset) and 1.6 V (during the OER itself), with a reversibility analysis back at 1.0 V after each oxidative potential application. The obtained spectra can be observed on **Figure 4.6** and **Figure 4.7**.

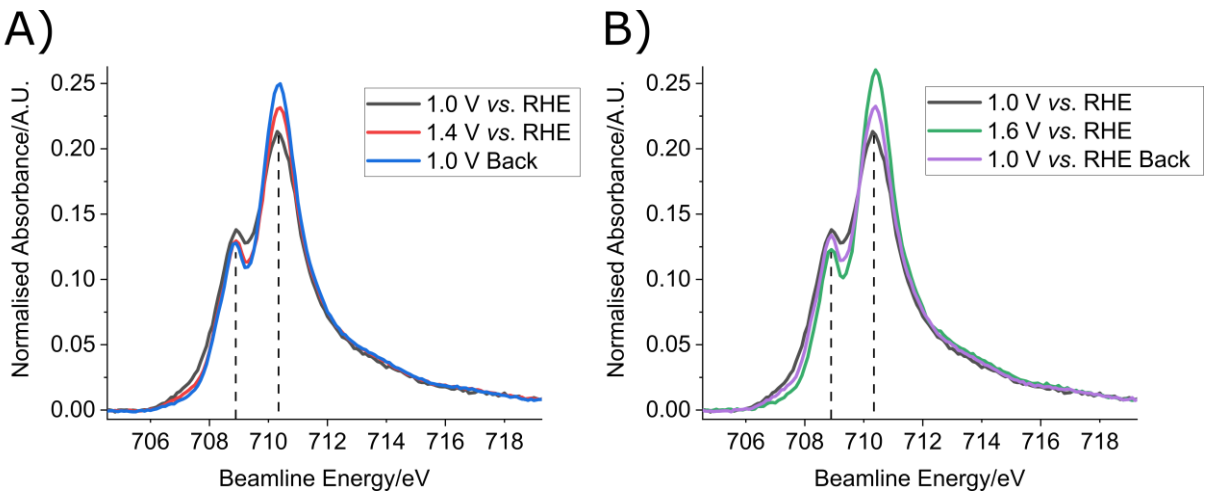

Figure 4.7: Fe L_3-Edge NEXAFS spectra reversibility at 1.0 V *vs.* RHE after applying **(A)** 1.4 V and **(B)** 1.6 V *vs.* RHE, respectively.

No change is observed in the Co and Fe L-edges when the potential is increased from 1 V to 1.2 V despite the CV indicating the transformation of Co(II) to Co(III) before 1.2 V. At 1.4 V, one can observe the increase of the Fe-β resonance and decrease of the Fe-α resonance, meaning the Fe(II) is oxidized to Fe(III) despite Fe(II) being only present in the NP core. In the meantime, the Co L-edge spectra showed little change suggesting that despite a slight decrease of the Co(II) peaks and the 780.1 eV shoulder growing, resulting from minor cobalt oxidation towards Co(III), the initial Co(II) oxidation state and its octahedral environment are mostly retained under anodic potentials. Regarding the Fe L_3-Edge spectrum acquired after stepping back to 1.0 V after the application of 1.4 V (**Figure 4.7.A**), one may observe a more oxidized Fe than the one at 1.4 V itself, suggesting a non-reversible Fe oxidation at this potential. This apparent stronger oxidation may result from the spectra acquisition procedure and oxidation occurring during the measurements. Indeed, Fe and Co L-edge spectra were measured in sequence. Hence, at the end of the Fe L_3-edge spectrum acquisition at 1.4 V, steady-state was probably not reached, hence Fe(II) → Fe(III) transformation

continued during the acquisition of the Co L-edge spectrum at the same potential. When 1.0 V was applied and Fe L-edge spectrum was measured again, Fe was oxidized to higher extent than at 1.4 V. The spectrum subsequently acquired at 1.6 V shows higher Fe oxidation state than that observed after stepping back to 1.0 V. This result would suggest a partially reversible Fe oxidation when a higher potential is applied, which would be apparently in opposition with the aforementioned conclusion. Hence, we believe that either (i) the differences in the behaviour between the experiments at two different potentials might result from bubble formation and catalyst contact loss with the current collector, which incidentally limited our capability to acquire patterns at potentials greater than 1.6 V *vs.* RHE; (ii) or that, independently of the potential, the Fe(II) → Fe(III) transition is partially, or totally, reversible, but that at 1.6 V on the Fe L-edge pattern, the Fe already reached its steady-state whereas, as explained above, it continued to oxidize at 1.4 V (*i.e.,* the L-edge pattern at 1.4 V widely underestimates the oxidation degree of Fe) during the Co L-edge acquisition. Hence, when exposed back to 1.0 V, both experiments led to a partial reduction of Fe(III), but, in the case of the previously at 1.4 V pattern, it was 'off-set' by the hidden increase in Fe-β during the Co L-edge acquisition at 1.4 V.

From these experimental observations, we propose a mechanistic hypothesis illustrated in **Figure 4.8**. As indicated by the cyclic voltammetry, Co(III)/Co(II) transition must already happen at 1.1 V. However, the Co L-edge spectrum does not exhibit significant changes, meaning no Co(III) accumulation happened. Hence, we believe that part of the Fe(II) oxidized to Fe(III) observed at 1.4 and 1.6 V results from an electron transfer from Fe(II) to a short-lived Co(III), the latter returning to its pristine Co(II) state, while Fe(II) transforms in Fe(III). As Fe(II) is only present in the NPs core, the oxidation from Fe(II) to Fe(III) must happen in the core; most probably at the C@S interface, in the cobalt vicinity. To preserve the electroneutrality in the core, there are two possible options: either (i) the newly formed Fe(III) diffuses through the shell to the NP surface, forming a new crystalline phase, and/or (ii) there is oxygen diffusion from the particle shell/electrolyte interface to the core, forming a new phase between the core and the shell. The newly formed phase would probably be Fe_2O_3. However, this material is not conductive. Hence, a layer of Fe_2O_3 between the core and the shell would then have a negative effect on the electronic conductivity within the NP and thus, on its activity (which was not observed, see discussion in **Section 4.5**). The most

interesting result consists in the Co(II) stabilisation under oxidative potentials. This observation was already discussed in the literature using DFT+U computation. While Co in the absence of Fe does stabilise in a trivalent state [351], the presence of a monolayer of Fe cations close to the Co sites stabilises the divalent state of the latter [352]. Therefore, a mechanism involving the formation of CoOOH and its oxidation up to Co(IV) as suggested in the literature [337] is rather unlikely in our case. Rather, we observed the Fe-induced reduction of the Co(III) formed at potentials below the OER and its following stabilization as Co(II), due to the presence of Fe(III)/Fe(II) cations in the Co vicinity, despite the Co(IV)/Co(III) redox transition observed on CV. This leads us to the conclusion that the OER active site is most probably a short-lived trivalent Co, or an ensemble comprised of short-lived Co(III) and Fe(II/III).

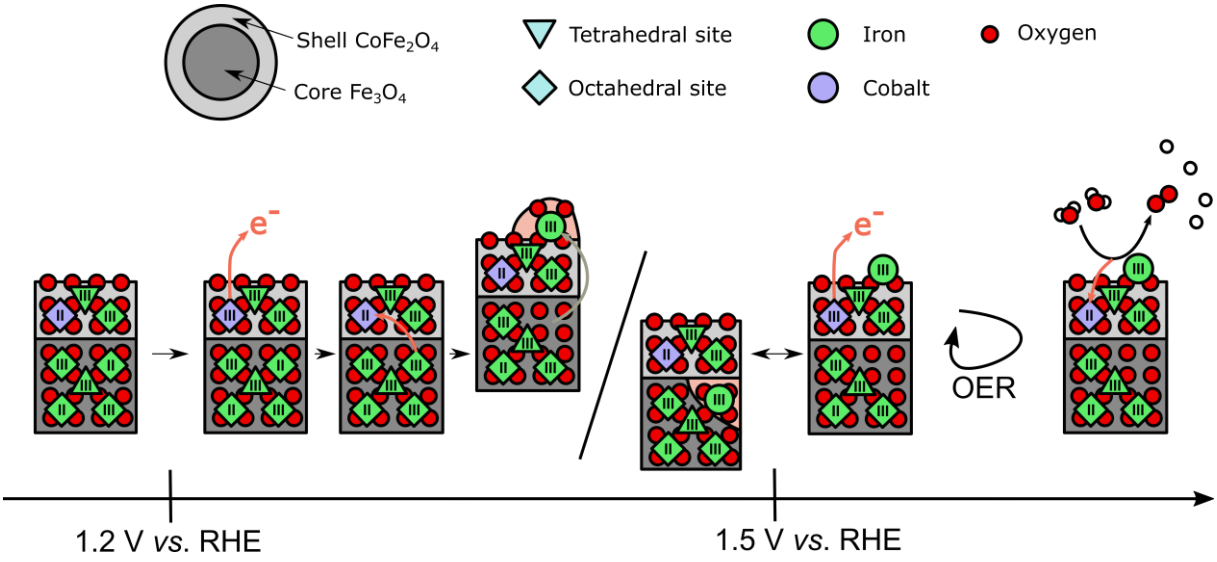

Figure 4.8: Hypothesis of redox transformations happening at positive potentials and during the OER in Fe_3O_4@$CoFe_2O_4$ core@shell nanoparticles, supported by *operando* NEXAFS measurements.

This set of experiments highlighted the low oxidation state of Co cations in the C@S structure during the OER, which was explained by electron hopping and divalent Co(II) state stabilisation due to Fe(II) → Fe(III) transition in the core. This observation raises several questions: if Fe(II) is irreversibly transformed and/or diffuses through the shell during the catalytic cycle, would its depletion result in the loss of the C@S activity? As Co(II) is stabilised thanks to the Fe(II) vicinity, how the shell thickness (*i.e.,* Fe(II)−Co(III)/Co(II) distance) influences the OER activity and the cobalt stabilisation? To answer those questions, we decide to study a set of C@S nanoparticles with

different shell thickness. Therefore, we introduce two additional samples: C@S-0.1nm and C@S-2nm with respective shell thicknesses of 0.1 nm and 2 nm of $CoFe_2O_4$ on the Fe_3O_4 core (more details about those sample on **Table 4.1, Section 4.8.1**). The durability of those samples was studied (**Section 4.5**) to determine if the Fe(II) depletion results in the OER activity loss of the sample. Furthermore, the early steps of the OER (cobalt oxidation or stabilisation due to Fe(II) presence) are studied by a XAS *in-situ* experiment, through exposure of the NPs to oxidative and reductive gases (**Section 4.6**).

4.5 Shell thickness influence on the OER activity and durability of core@shell nanoparticles

The activity of C@S-0.1nm and C@S-2nm for the OER was assessed (see **Figure 4.9.A**). Similarly to C@S-0.65nm, both C@S-2nm (430 A/g_{oxide} at 1.65V) and C@S-0.1nm (350 A/g_{oxide} at 1.65V) exhibit a higher activity than either $CoFe_2O_4$ or Fe_3O_4 NPs. However, their activity is not as high as C@S-0.65nm (750 A/g_{oxide} at 1.65V). This observation suggests that the shell thickness of the C@S NPs is impacting their activity, the latter reaching a maximum between 0.1 and 2 nm shell thickness. Cyclic voltammograms in the interval of potentials from 1.5 to – 0.5 V *vs.* RHE (**Figure 4.9.C−G**) show the same Fe(III)/Fe(II) transition attributed to $Fe_3O_4/Fe(OH)_2$ transformation for all NP samples. The amplitude of the redox peaks is higher for the Fe_3O_4 sample compared to $CoFe_2O_4$ sample, with the C@S samples exhibiting an intermediate behaviour between Fe_3O_4 and $CoFe_2O_4$. As elaborated on in **Section 4.3,** this might be explained by defects in the C@S structure: either Fe_3O_4 core exposed to the NP surface (*i.e.* lack of the shell continuity) or crystalline defects in the $CoFe_2O_4$ shell (either in composition: $Co_{(1-x)}Fe_2O_4$, or lattice: $Fe(II)Co(III)Fe(III)O_4$). Deeper analysis on the NPs crystalline defects density should be carried out (X-ray magnetic circular dichroism, XMCD, for instance, and high resolution EELS mapping in TEM, to provide a clear representation of the NP shell homogeneity and defects quantity) to be able to correlate this redox transition and the defect density in the shell.

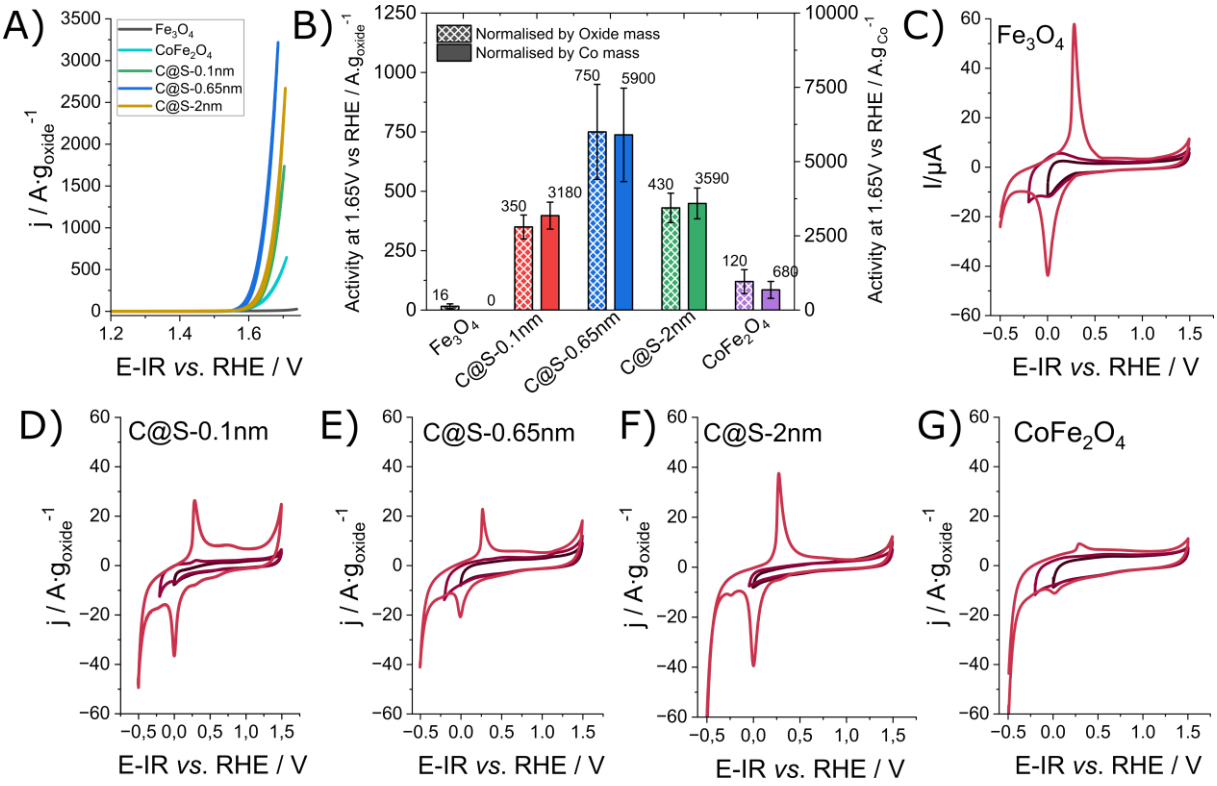

Figure 4.9: Electrochemical characterisation of Fe_3O_4, $CoFe_2O_4$, C@S-0.1nm, C@S-0.65nm and C@S-2nm NPs: **(A)** Cyclic voltammetry in 0.1 M NaOH, scan rate 10mV/s, rotation at 1000rpm and temperature 25°C. **(B)** OER activity at 1.65 V *vs*. RHE per gram of oxide and per gram of Co. Error bars are result of standard deviation from repeatability measurements. (at least 3 experiments were performed per sample) **(C)**, **(D)**, **(E)**, **(F)** and **(G)** are CVs at 20 mV/s scan rate potentials in the interval from 1.5 to -0.5 V vs. RHE for Fe_3O_4, $CoFe_2O_4$, C@S-0.1nm, C@S-0.65nm and C@S-2nm NPs respectively.

Since we question the role of Fe(II) in the OER mechanism, namely whether or not its oxidation through Co(III) hopping (see **Figure 4.8**) is a step in the OER catalytic cycle, and if Fe(II) depletion may have a negative effect on the particle activity, we turn to the ageing study of those particles using a 3 h chronoamperometry at 1.65 V. This method is chosen over accelerated ageing procedure (repetitive CVs) as we aim to push forward an eventual chemical reactivity change through the Fe(II) depletion. The results are shown on **Figure 4.9.** It can be observed that during the first minutes of the 1.65 V *vs.* RHE potential application, each of the C@S NP samples show a fast activity increase, for the C@S-0.65nm reaching up to 750 A/g_{oxide} after 6 minutes. Then the activity slowly increases over time from 30% to 70% between 10 min and 3h depending on the C@S sample, meaning that a chemical reorganisation might occurs which is advantageous for the OER. As we do not observe such phenomenon by CV, it means

the time scale for such changes must take longer time than the CV characteristic time. After subjecting the samples to 1.65 V *vs.* RHE for 3 hours, the OER activity was measured by cyclic voltammetry (End of Life, EoL) as shown and compared to the initial OER currents (Beginning of Life, BoL) on **Figure 4.10.** It is interesting to note that the OER currents measured by cyclic voltammetry do not show an enhancement comparable to the one observed in the chronoamperometry experiment, albeit no relevant activity drop is observed. This may be attributed to a reversible structural evolution of C@S NPs during the CA, which then return to their 'fundamental' state once exposed to E < 1.0 V *vs.* RHE. Some complementary experiments should be performed to better understand the nature of these modifications, their characteristic lifetime and potential required to lift this modification and return NPs to their initial state, *e.g.,* the immediate CV analysis of NPs after CA of different timescale, with a cathodic scanning starting at E = 1.8 V *vs.* RHE.

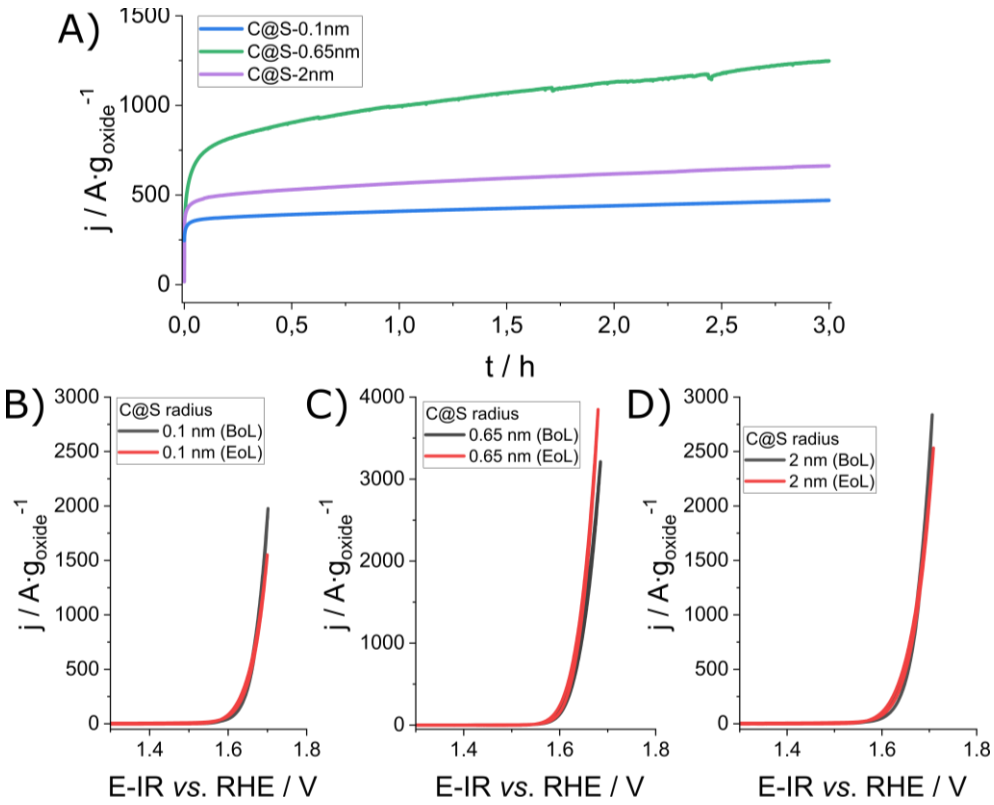

Figure 4.10: C@S durability **(A)** C@S-0.1nm, C@S-0.65nm and C@S-2nm nanoparticles chronoamperometry for 3h at 1.65V vs RHE in NaOH 0.1 M, WE rotation speed at 1000rpm to remove bubble formation, and thermostated at 25°C. The current intensity amplitude increases by 28%, 66% and 36% for C@S-0.1nm, C@S-0.65nm and C@S-2nm, respectively between the 10th minute and after 3h of CA. Beginning of Life (BoL) and End of Life (EoL) OER CVs are presented on **(B) (C)** and **(D)** figure for C@S-0.1nm, C@S-0.65nm, C@S-2nm, respectively.

As the 3h long chronoamperometry does not lead to any activity decrease, we assume that the Fe(II) → Fe(III) oxidation is not the step controlling the OER rate on C@S NPs. This hypothesis could be strengthen by a theoretical calculation of the time required to fully oxidize all of the Fe(II) present within the electrocatalyst, based on the dedicated exchanged for the Co(II) → Co(III) transition during the CA, which would require a calculation of the OER FE (*e.g.,* by DEMS, as discussed in **Section 4.1**) *vs.* the Co(II) → Co(III) transition, Nevertheless, we provided some 'back-of-the-enveloppe' estimation, based on a FE_{O2} of 90% (see [318,319]) at 1.65 V *vs.* RHE (*i.e.,* a $FE_{Fe(II)\rightarrow Fe(III)}$ = 10%), which would lead to a complete depletion of the Fe(II) in 10~20 s for C@S-0.65nm, *i.e.,* far below the time of the CA.On the contrary, a slight activity increase during the OER is observed and might be linked to some ageing-induced positive effects, such as the nanoparticles roughening or the reversible formation of another phase such as the state-of-the-art observed cobalt (oxy)hydroxide [95] or a Co(III/II)Fe(III) pattern on the NPs surface. Finally, as the activity does not drop during the OER, the formation of non-conductive Fe_2O_3 phase (as hypothesised in **Section Figure 4.8**) is unlikely.

Last but not least, the C@S activity study on three different shell thicknesses shows a maximum of activity for the C@S-0.65 nm sample, instead of the thinner (0.1 nm) and thicker (2 nm) shells. This implies that a maximum of activity could be found between 0.1 nm and 2 nm shell thicknesses, the latter being possibly controlled by (i) the number of active site (*i.e.,* Co(II)) in case of thin shells and (ii) the Fe(II)-Co distance in the case of thick shells.

4.6 Influence of the shell thickness on the catalytically active species in core@shell nanoparticles

To better understand the influence of the shell thickness and Fe(II) vicinity on the Co(II) oxidation during the OER, we studied the NPs oxidation state in-situ, by measuring the Co and Fe L-Edge XAS after exposure to an oxidative gas (N_2O). The objective was here to decorrelate the Co(II) → Co(III) and the core influence on said oxidation, without any influence of the OER or of the potential. Here, we focused onto the Fe_3O_4 and $CoFe_2O_4$ samples, and the C@S-0.1nm and C@S-2nm as they are the core@shell NPs with the thinnest and the thickest shell. Sample preparation is detailed

in **Section 4.8.3**. Prior to the experiment, NPs were plasma-cleaned under O_2 atmosphere for 2 minutes to remove organic ligands from the NPs surface.

Then they were exposed to a series of different gases, at 1 mbar pressure:

1) H_2O to eventually reduce back the NPs after the plasma cleaning induced oxidation;
2) N_2O to oxidize the NPs;
3) H_2 to eventually reduce the NPs with a more reductive gas than H_2O;
4) H_2O to eventually reduce the NPs by mimicking the OER.

Notably, during the exposure to different gases, the NEXAFS signal was recorded, hence the samples were also exposed to the beam. Between each exposure the Co and Fe L_3-edge were recorded under vacuum, using a drain current method (electron-out, ~5 nm depth analysis) to have a surface sensitive detection method.[353] The obtained spectra are presented in **Figure 4.11** with a reminder of the experimental plan.

The Fe_3O_4 NPs do not show any Fe oxidation degree modification throughout the whole experiment. C@S-0.1nm shows a slight Co oxidation, when exposed to oxidative $N_2O_{(g)}$, and then partially reduced back after reductive $H_2O_{(g)}$ exposure. This oxidation is visible in the change of the intensity of the Co-β and Co-γ resonances and accompanies a slight irreversible oxidation of Fe with the change in the intensity ratio of the Fe-α and Fe-β resonances. C@S-2nm and $CoFe_2O_4$ shows a stronger Co oxidation, with a shoulder appearance at 781 eV and the Co-γ peak intensity increase compared to the Co-β peak. This oxidation is reversible after the exposure to H_2 and H_2O reductive gases. Yet, no Fe oxidation is observed. Thus, *in-situ* study performed under the oxidative $N_2O_{(g)}$ confirms Co(II) to Co(III) oxidation depends on the shell thickness, with the stabilisation of Co in its Co(II) state in the thin shell nanostructures due to its proximity to the Fe(II) in the core.

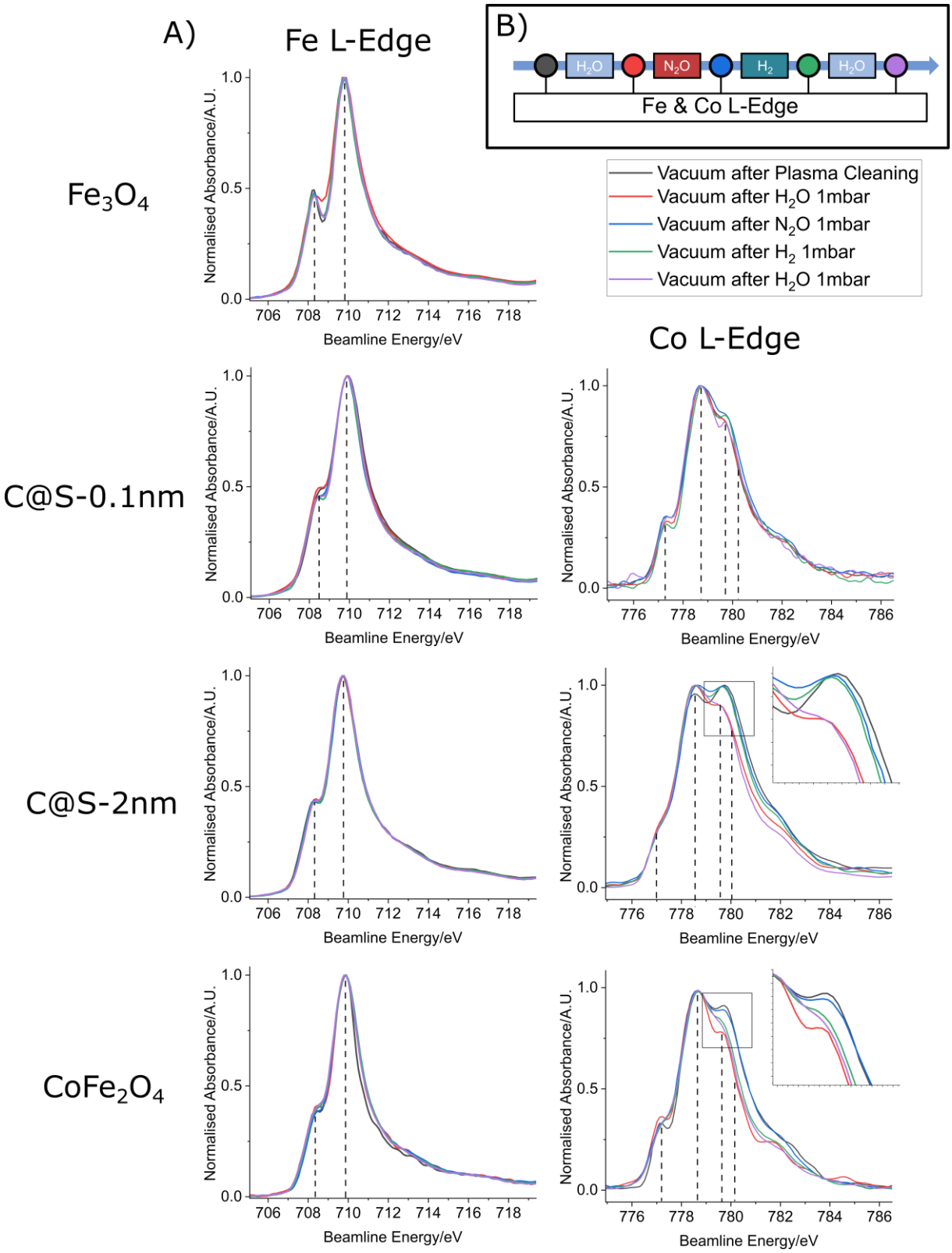

Figure 4.11: (A) Fe L_3-edge for the Fe_3O_4 NP under different oxidative or reductive gaz. **(B)** Detailed experimental plan. **(C)**, (**D)** C@S-0.1nm; (**E), (F)** C@S-2nm and **(G), (H)** $CoFe_2O_4$ NPs Fe-L edge and Co L-Edge under vacuum after exposure to the different oxidative or reductive atmospheres. Spectra were normalised by the peak maximum.

The difference of the profile in the Fe L_3-edge spectra between Fe_3O_4 NPs (*i.e.,* higher Fe-α relative intensity) and the other samples can be explained by a combination of several factors: (i) the detection method used for the spectra recording here is surface-sensitive; (ii) Fe(II) is only present in Fe_3O_4; *i.e*. in the core of C@S NPs. The Fe(II) component is therefore expected to be more pronounced for the Fe_3O_4 sample compared to the other samples, whose shell should only contain Fe(III); (ii) initial differences in the Co and Fe L-edges (*i.e.,* black curves on **Figure 4.11**) might arise from heterogeneities in structural defects in the spinel structure.

When considering the trends in oxidation, iron stability in oxidative conditions implies that: (i) in Fe_3O_4 NPs, Fe(II) needs Co(III) and electron hopping to be oxidized (similar to **Section 4.5**) and/or a thin Fe_2O_3 passivating layer is protecting the Fe_3O_4 NP (being absent on the C@S NPs); (ii) in C@S-2nm, the thickness of the shell limits any information that can be obtained on the core chemistry, while in $CoFe_2O_4$ there is no Fe(II) only Fe(III) and/or that the shell is too thick to fully allow electron hopping and Fe(II) → Fe(III) transformation; (iii) in C@S-0.1nm, where iron is being slightly oxidized, the shell is thin enough that chemical changes of the core can be observed by XAS. In that frame, these observations are consistent with the proposed mechanism in **Figure 4.8**, *i.e.,* the Fe(II) from the core is oxidized due to electron hopping from Co(III), resulting in retaining Co in its initial Co(II) oxidation state even under strongly oxidative conditions. This hopping seems to be limited by the distance between the Co at the shell surface and the Fe(II) in the core, as C@S-0.1nm showed only minor Co oxidation, while C@S-2nm NPs exhibited noticeable Co(II) to Co(III) oxidation when exposed to $N_2O_{(g)}$. Therefore, the electron hopping is clearly facilitated for thin shells, albeit it cannot be fully excluded for C@S-2nm, due to the depth of analysis limitations. Yet those results are in accordance with **Section 4.5** conclusions, *i.e.* that thick shells seem detrimental for the C@S OER activity.

Interestingly, in the case of C@S-0.1nm and C@S-2nm, H_2 does not show any reductive effect while H_2 seems to reduce the $CoFe_2O_4$ sample, therefore highlighting some differences in the reducible nature of those different samples by H_2. While $H_2O_{(g)}$ seems to have a reductive effect in this study, it is important to note that, as aforementioned, the samples were still exposed to the highly ionizing X-ray beam under $H_2O_{(g)}$ atmosphere. Since it is well known that soft X-rays do strongly ionize water, it is then possible that what did reduce our sample was not water but more

reactive radicals resulting from water dissociation under the beam. Any reductive effect of the beam *alone* was discarded as degradation test under beams are performed prior to the measurement.

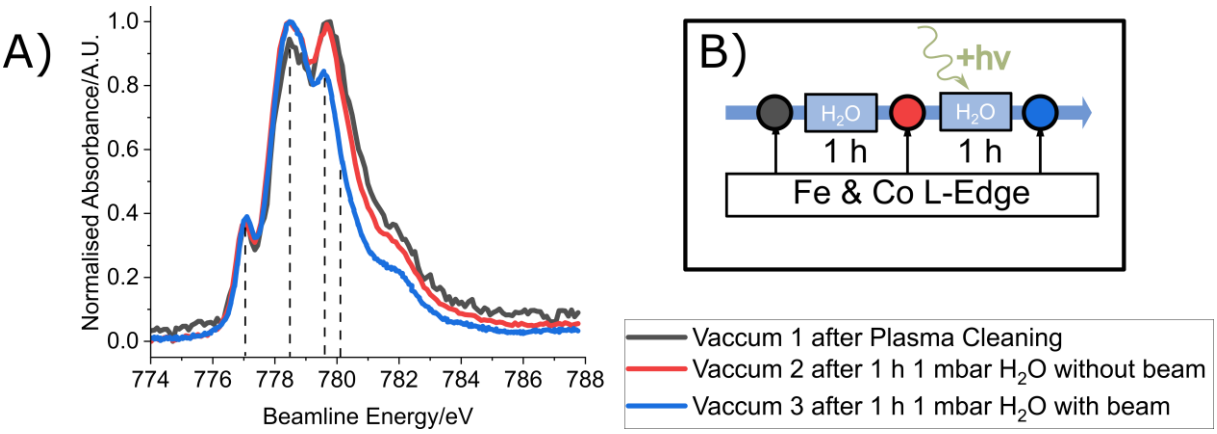

Figure 4.12: $CoFe_2O_4$ nanoparticles *in-situ* X-Ray Absorption Spectra (XAS) study of water and water + beam reduction power. **(A)** Co L_3-Edge XAS in vacuum after Plasma Cleaning (NP surface oxidized) (dark grey), after exposure to 1mBar water atmosphere for 1h (red) and after exposure to 1mbar water with the beam on. **(B)** Experimental roadmap representation.

To properly assess this phenomenon, an additional experiment was performed: XAS Co L_3-edge was recorded before and after exposing the oxidized $CoFe_2O_4$ NPs (directly after plasma cleaning) to 1 mbar of water atmosphere without beam exposure. Then the sample was exposed to 1 mbar of water with beam exposure. As it can be seen in **Figure 4.12**, a 1h exposure to water with the beam shutter closed resulted in only a slight reduction of the NP surface, with a slight increase of the Co-β peak compared to Co-γ, specific of a Co(III)/Co(II) ratio increase. However, the exposure of the NP to $H_2O_{(g)}$ under the beam for 1h results in a strong reduction of Co, with a noticeable decrease of the shoulder at 781 eV and the decrease of the Co-γ peak. This experiment reveals that water does not have a strong reductive effect and that the beam is actually necessary to reduce back the particles. As a conclusion, oxidation of the C@S using $N_2O_{(g)}$, despite leading to an increased Co oxidation degree, is not sufficient to then oxidize water and reduce efficiently the particle. This suggests that the OER intermediates are formed only during electrochemical polarization and not during chemical oxidation of NPs by $N_2O_{(g)}$.

4.7 Conclusion

In this chapter, we have shown that Fe_3O_4@$CoFe_2O_4$ C@S nanoparticles far exceed the activity of the homogenous Fe_3O_4 and $CoFe_2O_4$ NPs of similar dimensions. This increase in activity cannot be solely explained by the combination of the conductivity enhancement due to the Fe_3O_4 core and of the intrinsic OER activity of the $CoFe_2O_4$ catalyst. The OER operando XAS study of C@S-0.65nm shows a stabilisation of cobalt under a divalent oxidation state, concomitantly to an oxidation of Fe(II) to Fe(III) under oxidative potentials. This stabilisation probably results from electron hopping from Co(III) in the shell to Fe(II) in the core, which seems crucial to justify the C@S superior activity.

This 'stabilisation' was further investigated both by (i) studying the C@S stability under the OER conditions and (ii) comparing C@S with different shell thickness. 3 h chronoamperometries at 1.65 V *vs.* RHE shows a good retaining of the OER activity for the C@S, independently of the shell thickness. This implies that the electron-hopping step and the resulting Fe(II) → Fe(III) irreversible oxidation is not quantitatively linked to the OER and does not limit the catalyst durability. In addition, the C@S activity as a function of the shell thickness results in the identification of an optimum shell thickness (C@S-0.65nm), indicating that the shell should be neither too thick nor too thin, and that a fine tuning of the shell thickness might lead to an even higher activity improvement.

In-situ XAS analysis of different C@S, Fe_3O_4 and $CoFe_2O_4$ after exposure to oxidative atmosphere shows that the Fe(II)-Co distance is critical to the cobalt stabilisation under a divalent state by Fe(II). Indeed, while the 0.1 nm shell is thin enough to greatly limit the Co oxidation under oxidative conditions, the 2 nm shell does not show qualitative difference compared to the $CoFe_2O_4$ nanoparticles.

To complete this study, (i) a *post-mortem* analysis of the C@S particles after a durability test should help understand the structural changes and how they tie back to the slight increase in the OER activity observed during 3 hour durability tests. This study could be combined with an (ii) operando assessment of the C@S structural properties during the OER, as a function of the shell thickness, to confirm the insights that were provided by the *in-situ* analysis.

In this chapter, L-edge X-Ray Absorption spectroscopy using the electron-out detection mode was a key to obtain reliable results under *operando* and *in-situ* conditions. Indeed, the high surface sensitivity of the method ensures the acquisition of spectra whose main changes could be attributed to the NPs shell in contact with reactive environment (*i.e.* electrolyte or oxidative atmosphere). Finally, the complementarity of *in-situ* characterization to *operando* is exemplified through the **Section 4.6** as the absence of OER reaction during the analysis allows the isolation of an oxidized form of the electrocatalyst and avoid questions regarding the influence of other transformations onto the observed spectral changes. As *in-situ* conditions are easier to characterise compared to operando because of their relative simplicity, they appear as a convenient and sometimes necessary pre-step in the reaction analysis. Yet, they cannot replace *operando* as they fail to represent the complete reality of an electrochemical system, *e.g.,* with the full set of interactions with the reactants, intermediates, and products.

4.8 Experimental part

4.8.1 Particle synthesis and characterization.

The synthesis of the different Fe_3O_4@$CoFe_2O_4$ nanoparticles and homogenous nanoparticles was performed by Dr. Lisa Royer and Dr. Iryna Makarchuk at IPCMS UMR 7504 and full detail are given in published articles [345,354]. The synthesis is composed of two steps, each of them consisting in thermal decomposition of stearate metal complexes. First, the synthesis of the Fe_3O_4 core is done and characterised. It is then followed by the crystalline epitaxial growth of $CoFe_2O_4$ on top of the previously synthesized core. The obtained nanoparticles are suspended in chloroform media and sterically stabilised by stearate organic molecules. The only exception is C@S-0.1nm nanoparticles, whose extremely thin shell was prepared using diffusion method of cobalt into Fe_3O_4 nanoparticle.

The different materials and suspension were characterised with X-Ray Diffraction (XRD) for the crystalline phase verification, Transmission Electron Microscopy (TEM) for size distribution and Inductively Coupled Plasma Mass Spectrometry (ICP-MS) for the precise concentration determination of the oxide suspension. **Table 4.1** presents a list of different samples used in this chapter and their related particle size.

Table 4.1: Nanoparticle sample named Fe_3O_4 and $CoFe_2O_4$ are pure nanoparticles composed of the named material. C@S-0.1nm, C@S-0.65nm and C@S@2nm are core-shell nanoparticles with a Fe_3O_4 core and $CoFe_2O_4$ shell, the number referring to the shell thickness in nanometres. Indicated size are the average size of a large number (> 300) of nanoparticles on TEM images. This size was corroborated by granulometry measurements. More details can be found in Ref.[1].

Sample name	Core diameter	core@shell particle diameter
Fe_3O_4	12.4	
C@S-0.1nm	9.1	9.3
C@S-0.65nm	12.7	14
C@S-2nm	12.4	16.4
$CoFe_2O_4$	9.8	

The C@S architecture of C@S-0.65nm was characterised by XPS using the depth-profiling method, under vacuum conditions at ISISS beamline at Bessy II. This method lay on the electron IMFP with the kinetic energy. Different incident energies are used to record the Co2p and Fe2p XPS signal (shown on **Figure 4.13.A** and **B**), from which the corresponding quantification of cobalt and iron was calculated, taking into account the cross sections for the two elements at the energies used. As the incident energy increases, the photoelectron kinetic energy and therefore the photoelectrons IMFP (see **Figure 1.5.B**) increase as well, and the quantification is more and more sensible to the material's depth. The result is given in **Figure 4.13.C** as the function of the calculated photoelectron IMFP (λ_{IMFP}, calculated thanks to *QUASES-IMFP-TPP2M* Ver. 3.0 software, based on Ref.[161]) at the corresponding kinetic energy. One can observe that the relative iron content atomic ratio increases when the IMFP increases up to ~0.8 nm before levelling off. This result qualitatively demonstrates the lower concentration of iron (*i.e.,* higher concentration of cobalt) on the nanoparticle near-surface region in accordance to the C@S structure. The Fe content increase can be explained by both (i) the decreasing exponential trend in the electron detection (see **Equation 1.8**), meaning that core signal contributes even at the lowest IMFP and becomes stronger with the higher IMFP values (as 63% of the signal is coming from $1\times\lambda_{IMFP}$ sample depth, and 95% from $3\times\lambda_{IMFP}$) [355], and (ii) the presence of the cobalt only in the NPs shell. Interestingly, the cobalt atomic ratio reaches up to 50% at the

lowest IMFP, which is richer in cobalt than the theoretical shell ($CoFe_2O_4$). Those findings were confirmed by TEM and EELS mapping [1]. Those observations suggest that despite a clear C@S architecture, the nanoparticles have a non-constant shell composition, with a higher cobalt concentration at the nanoparticle surface (up to $Co_xFe_{3-x}O_4$ with x=1.5), which diminishes with the distance to the surface.

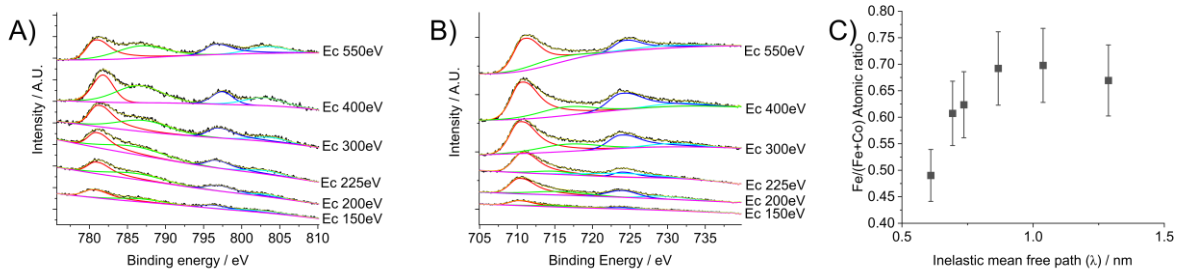

Figure 4.13: C@S−0.65nm X-Ray Photoelectron Spectroscopy (XPS) depth profiling characterization: **(A)** Fe2p XPS signal and **(B)** Co2p XPS signal obtained at kinetic energy about 150, 200, 225, 300, 400 and 550eV. **(C)** Depth profiling analysis with Fe/(Co+Fe) atomic ratio detected as a function of the electron inelastic mean-free path.

4.8.2 Operando OER study at ISISS beamline of BESSY II synchrotron facility

Section 4.4 presents results in operando conditions during OER on Fe_3O_4@$CoFe_2O_4$ nanoparticles. The spectra presented were recorded at ISISS beamline at BESSY II synchrotron (Berlin, Germany) and obtained thanks to a spectro-electrochemical cell represented on **Figure 4.14.A** and **B**, with the beam arriving from the working electrode side. The cell and the analysis chamber (~10^{-7} mbar) are separated thanks to a graphene bilayer.

The nanoparticles dispersion was directly drop-casted by 4.2 µg of CS@0.65nm in 10 µL chloroform suspension onto Fumatech Anion Exchange Membrane (AEM) (Fumasep® FAS-50) prior to a graphene bilayer deposition on the AEM surface and cell assembly. The AEM was permanently soaked in a NaOH 0.1M solution. A three-electrode cell was finally elaborated by introduction of a Ag/AgCl reference electrode, a platinum counter electrode, while the graphene bilayer acts as a current collector for the working electrode side as it is in contact with the catalyst (**Figure 4.14.C**).

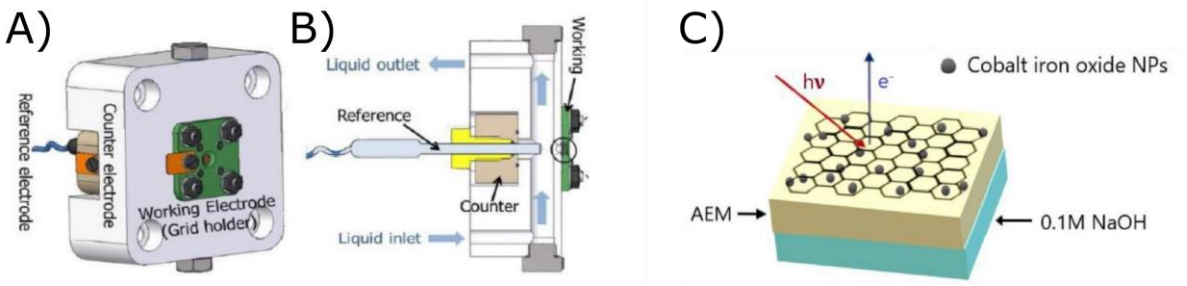

Figure 4.14: **(A)** Front and **(B)** lateral representation of the electrochemical cell developed at Fritz Haber Institute (Berlin, Germany) and used during this operando experiment. Image reproduced from Ref.[356], **(C)** schematic representation of the working electrode assembly for the operando setup: a graphene layer is used as current collector and separates the catalyst from the low-pressure atmosphere. Nanoparticles are dispersed on graphene layer and sandwiched between this layer and a Fumatech anion exchange membrane (AEM). Liquid electrolyte flows behind the AEM, providing continuous hydration to the catalyst surface.

4.8.3 In-situ analysis of NPs exposed to different gases at TEMPO beamline

In-situ X-Ray Absorption analysis of NPs after gas exposure shown in **Section 4.6** were performed at TEMPO beamline at synchrotron SOLEIL. The samples were prepared by direct drop-casting of a diluted nanoparticle suspension in chloroform, onto silicon wafer substrate, aiming to obtain bout a monolayer of nanoparticles. The sample was then plasma-cleaned for two minutes in oxygen atmosphere, to remove organics from the nanoparticles surface prior to analysis. Preliminary X-Ray photoelectron spectra were recorded to verify the nanoparticle layer thickness. The spot were chosen so that the signal of the nanoparticles and silicon wafer were observed at the same time to confirm the small thickness of the NP's layer. The beamline energy was calibrated using Au4f XPS signal from a reference Au foil.

4.8.4 Electrochemistry details

Electrochemical experiments shown in **section 4.3** and **4.4** are performed using Gamry Ref 600 potentiostat in a three electrode electrochemical cell priorly washed by immersion in Caroic acid, and made of Teflon to prevent carbonates. Counter electrode is a Pt wire, Reference electrode is a Hg/HgO calibrated *vs.* RHE prior to experiment. The 0.1 NaOH electrolyte is prepared by dilution of 1.316 mL of NaOH 50 wt. % in 250 mL ultrapure water (18.2 MΩ). The working electrode consists of a glassy carbon support carefully polished using 1 µm, 0.3 µm and 0.05 µm Al_2O_3 powder and

sonication in acetone, ethanol, and water after each step, on which 10µL of electrocatalyst suspension is deposited, corresponding to a final loading of ~2 µg.cm^{-2}. The determination of that loading is done thanks to Inductively Coupled Plasma Mass Spectrometry (ICP-MS) to measure the initial suspension concentration (after synthesis). The corresponding concentration are evaluated in the same timeframe of the electrochemical experiments, in order to avoid $CHCl_3$ evaporation, and are given in **Table 4.2.** Those suspensions are therefore diluted in order to reach ~0.4 µg/10 µL and drop-casted onto the clean carbon substrate. The side of the electrode were finally covered with Teflon tape and 150 CV cycles were performed as a way to remove remaining organics (and especially stearates) from the NPs surface and start the presented electrochemical experiments presented in this chapter.

Table 4.2: Nanoparticle suspension concentrations obtained by ICP-MS, and the determined dilutions to perform in order to obtain a ~2 µg/cm^2 loading onto the glassy carbon working electrode, after drop casting of 10µL of diluted solution.

Sample Name	**Fe_3O_4**	**C@S−0.1nm**	**C@S−0.65nm**	**C@S−2nm**	**$CoFe_2O_4$**
d (Core/Core-Shell) / nm		9.1/9.3	12.7/14	12.4/16.4	9.8
Initial [Fe] / g/L **[Fe_3O_4] / g/L**	1.32 1.84	4.08 4.48	0.39 0.40	11.5 12.23	1.59 2.89
Initial [Co] / g/L **[$CoFe_2O_4$] / g/L**	-	0.88 3.50	0.103 0.41	2.8 11.14	0.51 2.89
[oxide] g/L **[Fe_3O_4 + $CoFe_2O_4$]**	1.84	7.99	0.81	23.37	2.89
Dilution factor	50	200	20	550	72
Loading on 0.5 cm^2 / µg.cm^{-2}	1.84	2.00	2.025	2.12	2.06

General conclusions and outlook

This PhD manuscript aims to understand the stakes, opportunities, and technical limits that *operando* and *in-situ* analysis using X-Ray Absorption Spectroscopy (XAS) and X-Ray Photoelectron spectroscopy (XPS) present regarding the study of electrocatalytic reactions in electrochemical systems of various complexity.

Therefore, in **Chapter 1**. we demonstrate that the resolution of the global-scale problematic of global warming, which could be tackled by the decrease of our dependence to fossil fuels, depends on the maturity of the water electrolysis technology for hydrogen production (green hydrogen). This technology competitivity *vs.* carbon-based molecules reforming technologies (grey and blue hydrogen), depends on the development of inexpensive, based on earth abundant elements, and active oxygen evolution reaction (OER) electrocatalysts, a reaction which is still poorly understood. The comprehension of the chemical changes occurring during the reaction at the electrode-electrolyte interface, the cornerstone of any electrochemical reaction, is therefore fundamental to engineer the next generation of electrocatalysts.

XA and XP spectroscopies are unique and complementary tools to probe this interface. First, both are element-specific techniques, which is extremely advantageous when it comes to the study of complex, heterogeneous systems. Then, they present a chemical environment and oxidation degree sensitivity at different extents, which is suitable for electrochemical reactions when aiming to determine the atomic centres involved in reduction or oxidation processes. While XPS ease the quantification and separation of different components in a spectrum, in simple systems, XAS offers the opportunity to quantify the number and the distance of the neighbouring atoms to the probed element. Finally, depending on the detection method, XAS can be either bulk sensitive (photon-out) or surface sensitive (electron-out), while XPS is limited to surface sensitivity. The surface sensitivity resulting from the photo-electron intensity measurement, is however desired, as electrocatalysis happens at the electrode surface (or near-surface). Although, due to the limited inelastic mean free path of electrons in gaseous and liquid environments, surface sensitivity comes to the price of technical challenges, since spectro-electrochemical cells must be able to operate in low pressure environment,

whereas the synchrotrons and analysers must be adapted to non-vacuum conditions. This challenge, by opposition, does not exist when using a photon-out method.

Those technical challenges are illustrated in **Chapter 2** with the **study of the electrochemical double layer (EDL) using dip and pull (D&P) XPS**. The EDL greatly impacts the electrochemical behaviour and activity of a system. However, it is still poorly experimentally explored. Hence, we aimed here to determine the extent of the information that XPS can gather regarding this part of the interface. Theoretically, D&P XPS is a perfect match for an EDL study. Indeed, (i) the setup geometry, consisting of a model 2D-electrode covered by a nanometric-thick electrolyte film and (ii) the XPS sensitivity to the local electrical potential, give the unique opportunity to probe the variations of electrical potential and ion concentration depending on the distance to the electrode (*i.e.* which are directly linked to the EDL properties). Albeit the D&P is a great tool to semi-quantitatively study the electrode chemical changes and the extent of those changes in the electrode depth, the EDL study proved challenging. Indeed, here, the method suffers from the trade-off between the signal intensity (determined by experimental conditions and increasing with the electrolyte concentration) and the EDL thickness and, thus, observable nature (decreasing with the electrolyte concentration). This trade-off prevents the EDL study to be performed in realistic conditions until further technical improvements are available regarding the synchrotron beam intensities, or photoelectron detections.

To work in conditions of greater relevance to the hydrogen cycle, in **Chapter 3** we leave non-faradaic conditions to study the OER electrocatalysis in neutral media. Doing so, we choose to work with a homogeneous molecular model-electrocatalyst: a complex of **cobalt based polyoxometalates (Co-POM).** To answer the long-standing question of those species' **stability and activity towards the OER**, we present a series of *in-situ* and *operando* XAS experiments that complement the electrochemical data presented in the literature (and extended in this work). The chemical environment sensitivity of FT-EXAFS allowed to determine that Co-POMs are unstable in the operating conditions relevant for the water electrochemical and chemical oxidations, while not being oxidized under crystalline form when exposed to an oxidative atmosphere ($N_2O_{(g)}$ 1 bar for >8h). Yet even though the specie instability was confirmed, it remains hard to conclude that Co-POM does not undergo few undetected OER catalytic cycles before being degraded into a Co(III)/Co(II) oxidation under

operando conditions due to the time necessary to record a XA spectrum, which is greater than the reactive intermediates lifespan. In the light of this time limitation, information that *operando* and *in-situ* experiments can provide regarding the chemical changes happening during the OER (or any other chemical transformations) are put on condition that the system reaches a steady-state in which the specie of interest is present or that chemical changes are slower than the spectra recording.

In the **Chapter 4**, we therefore move to the study of more stable and industrially compatible OER electrocatalyst: **$CoFe_2O_4$@Fe_3O_4 core@shell nanoparticles** (C@S, NPs). In this chapter, we **investigate the role of iron in the cobalt driven OER mechanism**. Initial electrochemical study reveals that the C@S NPs exhibit an exceptional activity that far surpasses the activity of the pure core and shell materials. This exceptional activity is investigated by operando XAS spectroscopy, where we show that Fe(II) is responsible for Co stabilisation in its divalent state, even under OER conditions. Finally, an electrochemical investigation concomitantly to in-situ XAS spectroscopy on samples with different shell thicknesses allows to highlight the importance of the Fe(II)-Co distance for the OER activity. The shell should neither be too thick nor too thin to provide an optimal activity, and the Co(II) stabilisation effect is stronger for thinner shells. This set of experiments illustrates the differences between *in-situ* and *operando* methods. Indeed, while operando is rich of information regarding the true system, the plentiful of origins that can lead to any observed change can sometimes make it hard to distinguish between the reaction (OER), a degradation or experimental issues (loss of contact for instance). *In-situ* therefore appears as a convenient pre-step to *operando* in order to isolate the unaltered catalyst in oxidative conditions. These *in*-situ studies cannot however replace operando studies, as ageing, along with (in our specific case) performing the full OER cycle on the active site, are keys to the electrochemical system and must be taken into account when aiming to fully understand it.

To conclude this manuscript, one can observe that XAS and XPS are powerful techniques that, once coupled to *operando* or *in-situ* experiments, allow to gather precious information regarding the oxidation state and chemical environment changes of the probed element. Those techniques appear to be complementary in number of characteristics (summarised in **Table C.1**) and adapted to electrocatalytic studies.

Table C.1: Overview of XAS and XPS characteristics explored in this manuscript

X-Ray Photoelectron Spectroscopy	X-Ray Absorption Spectroscopy
Element sensitive	
Quantitative	
Oxidation degree sensitive	
Single-energy X-Ray beam irradiation *(can be performed on lab scale)*	Requires a source offering a continuum spectrum of X-Rays
Easy element quantification in complex environment	Difficult element quantification in absence of reliable references
Indirect information on the chemical environment *(XPS peak shift)*	Precise probing of the chemical environment through FT-EXAFS *(number of neighbours depending on the distance to absorbing atom)*
Local electrical potential sensitive	Insensitive to local electrical potential
Tuneable surface sensitivity from 5 nm to 30 nm	Either bulk or surface sensitive *(~5 nm)*
Operando setup technically challenging	Operando setup easier to develop *(in photon-out method)*
Timescale to record 1 spectrum in this work ~ 1 min	Timescale to record 1 spectrum in this work ~15 min

However, one should remember that when it comes to the development of new electrocatalysts, those techniques are neither an end by themselves nor absolute. Performing a complete electrochemical study remains a fundamental requirement to assess the activity and durability of the electrocatalyst as well as initial and *post-mortem* characterizations, where more invasive/destructive and adapted method can be used (Transmission or Scanning Electron Microscopy, X-Ray Diffraction, FT-Infrared spectroscopy, Raman, Thermogravimetric analysis, *etc*., to provide a global picture of their physico-chemical characteristics). *Operando* XAS and XPS methods therefore appear as tools to get insights about the dynamic changes that happen during the reaction (*i.e.* between the initial catalyst and the *post-mortem*, during the electrochemical reaction) and require a deliberated preparation in terms of (i) how to meaningfully assess the observed signal based on adequate references samples, (ii) how to adequately design the spectro-electrochemical cell and (iii) how to critically

analyse the obtained spectro-electrochemical data through a clear understanding of the system.

- Reference samples: *operando* measurements can be complicated to analyse due to the reactions happening during the analysis. ***References samples*** are therefore essential to correlate ***the observed signals to changes in chemical environment and oxidation degree, based on this comparison with well-defined ex-situ samples.*** In some specific cases, to give another step-by-step information, ***in-situ measurements offer a solution to isolate the catalyst into its oxidized (or reduced) form, therefore widening the spectrum of references samples.***

- Spectroelectrochemical cell: XAS and XPS are spectroscopy techniques that can be challenging to perform when combined with electrochemistry, due to the need to use near ambient pressure conditions for techniques that are fundamentally easier in vacuum. Designing a cell and adapting it to the system to be ***sensible to electrode-electrolyte interface***, while ***maximizing the signal***, is therefore as crucial as it is difficult.

- The relevance of the results: As the system must be adapted to fit the XAS and XPS analysis conditions, the question "*are those operando conditions similar to our real system?*" is fundamental. It is therefore important to **know**, prior to the measurement, **how the system should behave in more realistic conditions** and how this behaviour is modified when moving to the spectroelectrochemical conditions, in order to correlate the *operando* system to the system in conventional electrochemistry conditions. Furthermore, it is essential to always have a critical look on the spectro-electrochemical data, to avoid any misinterpretation. *Operando XAS and XPS coupled with electrochemistry are extremely challenging methods, which require substantial preparation time, are mentally and physically exhausting to perform, and thus lead to the innate desire to see meaningfulness in the results. However, although it is a cruel teaching, one must remain impartial in his analysis and interpretation of the experimental data and objectively accept them for what they are, and not what one want them to be.*

*As we illustrate through **Figure C.1**, the understanding of electrocatalytic reactions at the interface therefore lay on our capacity to study the electrocatalyst before, after and during the reaction, while addressing the crucial questions inherent to operando methods regarding the results coherence, and their comparison with reference data.*

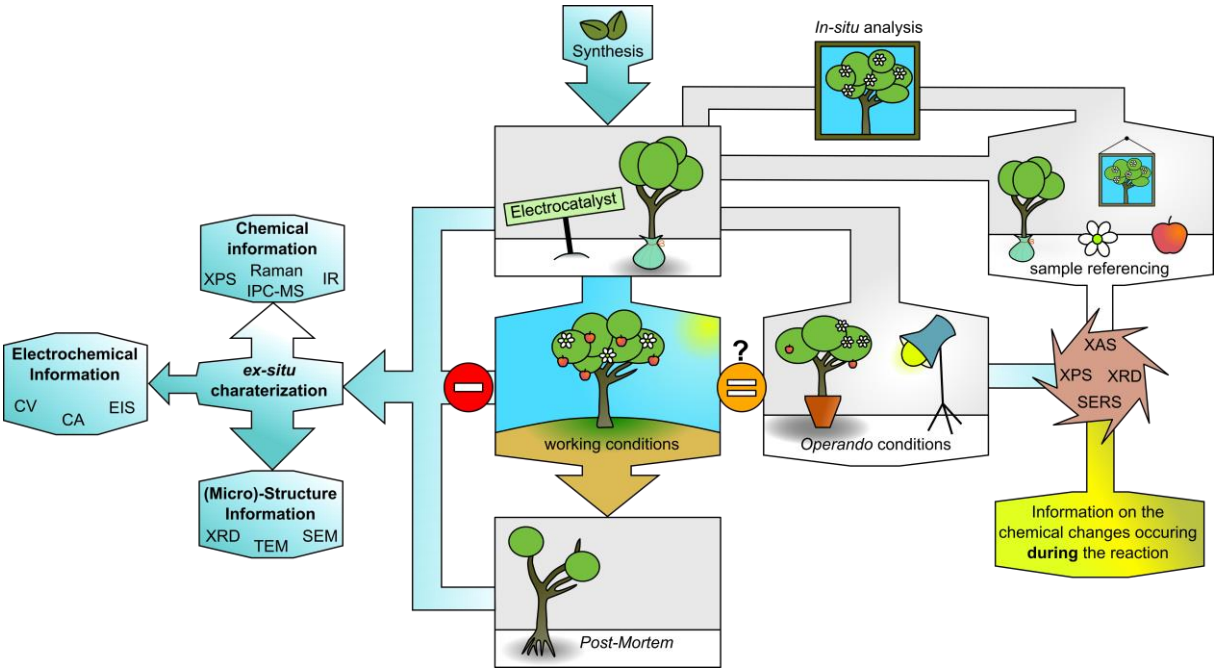

Figure C.1: Illustration of the characterization roadmap for an electrocatalyst study.

In addition, there are technical limits that restrict information that can be gathered from *in-situ* and *operando* XAS and XPS. Examples are the signal intensity and the spectra resolution, which limits the detection of the tinniest changes triggered by the operando conditions, as well as the time-resolution which is still a limit to detect short-lived intermediates. Several methods are designed to cope with those problematics such as the fixed energy or energy dispersive XAS but those remain limited due to their innate technical limits and the low number of synchrotron facilities that able to perform them. Hopefully, the ongoing technical improvement of the aforementioned facilities will push even further the capabilities of those techniques, and unlock the remaining knowledge barriers to the OER understanding.

Finally one should not neglect other *operando* characterisation techniques, which altogether can help to further improve our understanding of the electrocatalyst in *operando* conditions. Examples of those are X-ray scattering techniques (small angle X-ray scattering, wide angle X-ray scattering) that are able to provide information regarding the crystalline organisation of the electrocatalyst; Raman derived techniques

(surface enhanced and tip enhanced Raman) that provide insights on the reactive intermediates and their interactions with the reactive interface; or scanning probe electrochemical microscopy that allow to further explore the electrochemical interface and its local environment variations, *etc.*[357] A wise, and adapted, use of those methods alongside the XP and XA *operando* spectroscopies, is therefore essential in the understanding of electrocatalysis.

References

[1] Lisa Royer, Iryna Makarchuk, Simon Hettler, Raul Arenal, Tristan Asset, Benjamin Rotonnelli, Antoine Bonnefont, Elena Savinova, B. P. Pichon, *Core–shell Fe3O4@CoFe2O4 nanoparticles as high-performance anode catalysts for enhanced oxygen evolution reaction*, Sustain Energy Fuels. 7 (**2023**) 3239–3243.

[2] B. Rotonnelli, M.-S.D. Fernandes, F. Bournel, J.-J. Gallet, B. Lassalle-Kaiser, *In situ/operando X-ray absorption and photoelectron spectroscopies applied to water-splitting electrocatalysis*, Curr Opin Electrochem. 40 (**2023**) 101314.

[3] G.E. Halkos, E.-C. Gkampoura, *Reviewing Usage, Potentials, and Limitations of Renewable Energy Sources*, Energies (Basel). 13 (**2020**) 2906.

[4] I. Dincer, C.O. Colpan, F. Kadioglu, eds., Causes, Impacts and Solutions to Global Warming, Springer New York, New York, NY, **2013**.

[5] Emissions Trends and Drivers, in: Climate Change 2022 - Mitigation of Climate Change, Cambridge University Press, **2023**: pp. 215–294.

[6] S. Rehman, L.M. Al-Hadhrami, Md.M. Alam, *Pumped hydro energy storage system: A technological review*, Renewable and Sustainable Energy Reviews. 44 (**2015**) 586–598.

[7] T. Bashir, S.A. Ismail, Y. Song, R.M. Irfan, S. Yang, S. Zhou, J. Zhao, L. Gao, *A review of the energy storage aspects of chemical elements for lithium-ion based batteries*, Energy Materials. 1 (**2022**) 100019.

[8] M. Aneke, M. Wang, *Energy storage technologies and real life applications – A state of the art review*, Appl Energy. 179 (**2016**) 350–377.

[9] M.K. Singla, P. Nijhawan, A.S. Oberoi, *Hydrogen fuel and fuel cell technology for cleaner future: a review*, Environmental Science and Pollution Research. 28 (**2021**) 15607–15626.

[10] J. Incer-Valverde, A. Korayem, G. Tsatsaronis, T. Morosuk, *"Colors" of hydrogen: Definitions and carbon intensity*, Energy Convers Manag. 291 (**2023**) 117294.

[11] M. El-Shafie, *Hydrogen production by water electrolysis technologies: A review*, Results in Engineering. 20 (**2023**) 101426.

[12] O. Massarweh, M. Al-khuzaei, M. Al-Shafi, Y. Bicer, A.S. Abushaikha, *Blue hydrogen production from natural gas reservoirs: A review of application and feasibility*, Journal of CO2 Utilization. 70 (**2023**) 102438.

[13] *Blue, green, gray: the colors of hydrogen*, (n.d.).

[14] P.P. Edwards, V.L. Kuznetsov, W.I.F. David, *Hydrogen energy*, Philosophical Transactions of the Royal Society A: Mathematical, Physical and Engineering Sciences. 365 (**2007**) 1043–1056.

[15] N. Armaroli, V. Balzani, *The Hydrogen Issue*, ChemSusChem. 4 (**2011**) 21–36.

[16] A. Nechache, S. Hody, *Alternative and innovative solid oxide electrolysis cell materials: A short review*, Renewable and Sustainable Energy Reviews. 149 (**2021**) 111322.

[17] Q. Feng, X. Yuan, G. Liu, B. Wei, Z. Zhang, H. Li, H. Wang, *A review of proton exchange membrane water electrolysis on degradation mechanisms and mitigation strategies*, J Power Sources. 366 (**2017**) 33–55.

[18] J. Brauns, J. Schönebeck, M.R. Kraglund, D. Aili, J. Hnát, J. Žitka, W. Mues, J.O. Jensen, K. Bouzek, T. Turek, *Evaluation of Diaphragms and Membranes as Separators for Alkaline Water Electrolysis*, J Electrochem Soc. 168 (**2021**) 014510.

[19] F. Safizadeh, E. Ghali, G. Houlachi, *Electrocatalysis developments for hydrogen evolution reaction in alkaline solutions – A Review*, Int J Hydrogen Energy. 40 (**2015**) 256–274.

[20] S.W. Sharshir, A. Joseph, M.M. Elsayad, A.A. Tareemi, A.W. Kandeal, M.R. Elkadeem, *A review of recent advances in alkaline electrolyzer for green hydrogen production: Performance improvement and applications*, Int J Hydrogen Energy. (**2023**).

[21] K. Zeng, D. Zhang, *Recent progress in alkaline water electrolysis for hydrogen production and applications*, Prog Energy Combust Sci. 36 (**2010**) 307–326.

[22] D. Henkensmeier, M. Najibah, C. Harms, J. Žitka, J. Hnát, K. Bouzek, *Overview: State-of-the Art Commercial Membranes for Anion Exchange Membrane Water Electrolysis*, (**2020**).

[23] K. Ayers, *The potential of proton exchange membrane–based electrolysis technology*, Curr Opin Electrochem. 18 (**2019**) 9–15.

[24] T.B. Ferriday, P.H. Middleton, *Alkaline fuel cell technology - A review*, Int J Hydrogen Energy. 46 (**2021**) 18489–18510.

[25] J. Durst, A. Siebel, C. Simon, F. Hasché, H. Hasché, J. Herranz, H.A. Gasteiger, *New insights into the electrochemical hydrogen oxidation and evolution reaction mechanism †*, (**2014**).

[26] P.J. Rheinländer, J. Herranz, J. Durst, H.A. Gasteiger, *Kinetics of the Hydrogen Oxidation/Evolution Reaction on Polycrystalline Platinum in Alkaline Electrolyte Reaction Order with Respect to Hydrogen Pressure*, J Electrochem Soc. 161 (**2014**) F1448–F1457.

[27] E.S. Davydova, S. Mukerjee, F. Jaouen, D.R. Dekel, *Electrocatalysts for Hydrogen Oxidation Reaction in Alkaline Electrolytes*, ACS Catal. 8 (**2018**) 6665–6690.

[28] M. Mandal, *Recent Advancement on Anion Exchange Membranes for Fuel Cell and Water Electrolysis*, ChemElectroChem. 8 (**2021**) 36–45.

[29] H.A. Miller, K. Bouzek, J. Hnat, S. Loos, C.I. Bernäcker, T. Weißgärber, L. Röntzsch, J. Meier-Haack, *Green hydrogen from anion exchange membrane water electrolysis: a review of recent developments in critical materials and operating conditions*, Sustain Energy Fuels. 4 (**2020**) 2114–2133.

[30] K.M. Hugar, H.A. Kostalik, G.W. Coates, *Imidazolium Cations with Exceptional Alkaline Stability: A Systematic Study of Structure-Stability Relationships*, J Am Chem Soc. 137 (**2015**) 8730–8737.

[31] J. Fan, A.G. Wright, B. Britton, T. Weissbach, T.J.G. Skalski, J. Ward, T.J. Peckham, S. Holdcroft, *Cationic Polyelectrolytes, Stable in 10 M KOH(aq) at 100°c*, ACS Macro Lett. 6 (**2017**) 1089–1093.

[32] S. Dresp, F. Dionigi, M. Klingenhof, P. Strasser, *Direct electrolytic splitting of seawater: Opportunities and challenges*, ACS Energy Lett. 4 (**2019**) 933–942.

[33] X. Xiao, L. Yang, W. Sun, Y. Chen, H. Yu, K. Li, B. Jia, L. Zhang, T. Ma, *Electrocatalytic Water Splitting: From Harsh and Mild Conditions to Natural Seawater*, Small. 2105830 (**2021**) 1–16.

[34] M. Delpisheh, M.A. Haghghi, H. Athari, M. Mehrpooya, *Desalinated water and hydrogen generation from seawater via a desalination unit and a low temperature electrolysis using a novel solar-based setup*, Int J Hydrogen Energy. 46 (**2021**) 7211–7229.

[35] G. Gauglitz, T. Vo-Dinh, eds., Handbook of Spectroscopy, Wiley-VCH GmbH & Ci. KGaA, Weinheim, **2003**.

[36] J.M. Hollas, ed., Modern Spectroscopy, 4th edition, John Wiley & Sons, Ltd, **2004**.

[37] J. Ryczkowski, *IR spectroscopy in catalysis*, Catal Today. 68 (**2001**) 263–381.

[38] S. Liu, L. D'Amario, S. Jiang, H. Dau, *Selected applications of operando Raman spectroscopy in electrocatalysis research*, Curr Opin Electrochem. 35 (**2022**) 101042.

[39] A. Orlando, F. Franceschini, C. Muscas, S. Pidkova, M. Bartoli, M. Rovere, A. Tagliaferro, *A Comprehensive Review on Raman Spectroscopy Applications*, Chemosensors. 9 (**2021**) 262.

[40] C.A. Mesa, E. Pastor, L. Francàs, C. Roth, A. Simonov, *UV-Vis operando spectroelectrochemistry for (photo)electrocatalysis: Principles and guidelines*, (**2022**).

[41] M.C.O. Monteiro, M.T.M. Koper, *Measuring local pH in electrochemistry*, Curr Opin Electrochem. 25 (**2021**) 100649.

[42] Y. Zhu, T.-R. Kuo, Y.-H. Li, M.-Y. Qi, G. Chen, J. Wang, Y.-J. Xu, H.M. Chen, *Emerging dynamic structure of electrocatalysts unveiled by* in situ *X-ray diffraction/absorption spectroscopy*, Energy Environ Sci. 14 (**2021**) 1928–1958.

[43] M.P. Seah, W.A. Dench, *Quantitative Electron Spectroscopy of Surfaces: A Standard Data Base for Electron Inelastic Mean Free Paths in Solids*, Surface and Interface Analysis. 1 (**1979**).

[44] D. Briggs, M. Seah, Practical Surface Analysis, second edition, John Wiley & Sons, New York, **1990**.

[45] G.H. Major, V. Fernandez, N. Fairley, M.R. Linford, *A detailed view of the Gaussian–Lorentzian sum and product functions and their comparison with the Voigt function*, Surface and Interface Analysis. 54 (**2022**) 262–269.

[46] J.T. Grant, *Methods for quantitative analysis in XPS and AES*, Surface and Interface Analysis. 14 (**1989**) 271–283.

[47] V. Jain, M.C. Biesinger, M.R. Linford, *The Gaussian-Lorentzian Sum, Product, and Convolution (Voigt) functions in the context of peak fitting X-ray photoelectron spectroscopy (XPS) narrow scans*, (**2018**).

[48] A.G. Shard, *Practical guides for x-ray photoelectron spectroscopy: Quantitative XPS*, Journal of Vacuum Science & Technology A: Vacuum, Surfaces, and Films. 38 (**2020**) 41201.

[49] Paul van der Heide, X-Ray Photoelectron Spectroscopy: an Introduction to Principles and Practices, John Wiley & Sons, Inc., **1962**.

[50] D.E. Sayers, E.A. Stern, F.W. Lytle, *New Technique for Investigating Noncrystalline Structures: Fourier Analysis of the Extended X-Ray—Absorption Fine Structure*, Phys Rev Lett. 27 (**1971**) 1204–1207.

[51] Y. Cauchois, C. Bonnelle, G. Missoni, *First X-Spectra of the orbital radiation of the FRASCATI synchrotron*, Aca. de Sci. Fr. 257 (**1963**) 409–1242.

[52] R. Stumm von Bordwehr, *A History of X-ray absorption fine structure*, Ann Phys (Paris). 14 (**1989**) 377–465.

[53] L. Galoisy, G. Calas, M.A. Arrio, *High-resolution XANES spectra of iron in minerals and glasses: structural information from the pre-edge region*, Chem Geol. 174 (**2001**) 307–319.

[54] G. Bunker, Introduction to XAFS, Cambridge University press, **2010**.

[55] Y. Yang, Y. Xiong, R. Zeng, X. Lu, M. Krumov, X. Huang, W. Xu, H. Wang, F.J. DiSalvo, Joel.D. Brock, D.A. Muller, H.D. Abruña, Operando *Methods in Electrocatalysis*, ACS Catal. 11 (**2021**) 1136–1178.

[56] R. Arrigo, In situ X-ray spectroscopic characterization techniques for electrocatalysis, Elsevier B.V., **2022**.

[57] B. Lassalle-Kaiser, S. Gul, J. Kern, V.K. Yachandra, J. Yano, *In situ/Operando studies of electrocatalysts using hard X-ray spectroscopy*, J Electron Spectros Relat Phenomena. 221 (**2017**) 18–27.

[58] F.J. Scott, C. Roth, D.E. Ramaker, *Kinetics of CO Poisoning in Simulated Reformate and Effect of Ru Island Morphology on PtRu Fuel Cell Catalysts As Determined by Operando X-ray Absorption Near Edge Spectroscopy*, (**2007**).

[59] W.E. O'Grady, K.I. Pandya, K.E. Swider, D.A. Corrigan, *In Situ X-Ray Absorption Near-Edge Structure Evidence for Quadrivalent Nickel in Nickel Battery Electrodes*, J Electrochem Soc. 143 (**1996**) 1613–1617.

[60] D.E. Starr, Z. Liu, M. Hävecker, A. Knop-Gericke, H. Bluhm, *Investigation of solid/vapor interfaces using ambient pressure X-ray photoelectron spectroscopy*, Chem Soc Rev. 42 (**2013**) 5833–5857.

[61] D.F. Ogletree, H. Bluhm, G. Lebedev, C.S. Fadley, Z. Hussain, M. Salmeron, *A differentially pumped electrostatic lens system for photoemission studies in the millibar range*, Review of Scientific Instruments. 73 (**2002**) 3872–3877.

[62] J.J. Velasco-Velez, L.J. Falling, D. Bernsmeier, M.J. Sear, P.C.J. Clark, T.S. Chan, E. Stotz, M. Hävecker, R. Kraehnert, A. Knop-Gericke, C.H. Chuang, D.E. Starr, M. Favaro, R. V. Mom, *A comparative study of electrochemical cells for in situ x-ray spectroscopies in the soft and tender x-ray range*, J Phys D Appl Phys. 54 (**2021**).

[63] L.J. Falling, R. V. Mom, L.E. Sandoval Diaz, S. Nakhaie, E. Stotz, D. Ivanov, M. Hävecker, T. Lunkenbein, A. Knop-Gericke, R. Schlögl, J.J. Velasco-Vélez, *Graphene-Capped Liquid Thin Films for Electrochemical Operando X-ray Spectroscopy and Scanning Electron Microscopy*, ACS Appl Mater Interfaces. 12 (**2020**) 37680–37692.

[64] R. Mom, L. Frevel, J.J. Velasco-Vélez, M. Plodinec, A. Knop-Gericke, R. Schlögl, *The Oxidation of Platinum under Wet Conditions Observed by Electrochemical X-ray Photoelectron Spectroscopy*, J Am Chem Soc. 141 (**2019**) 6537–6544.

[65] L.J. Frevel, R. Mom, J.J. Velasco-Vélez, M. Plodinec, A. Knop-Gericke, R. Schlögl, T.E. Jones, *In situ X-ray spectroscopy of the electrochemical development of iridium nanoparticles in confined electrolyte*, Journal of Physical Chemistry C. 123 (**2019**) 9146–9152.

[66] V. Pfeifer, T.E. Jones, J.J. Velasco Vélez, R. Arrigo, S. Piccinin, M. Hävecker, A. Knop-Gericke, R. Schlögl, *In situ observation of reactive oxygen species forming on oxygen-evolving iridium surfaces*, Chem Sci. 8 (**2017**) 2143–2149.

[67] V.A. Saveleva, V. Papaefthimiou, M.K. Daletou, W.H. Doh, C. Ulhaq-Bouillet, M. Diebold, S. Zafeiratos, E.R. Savinova, *Operando Near Ambient Pressure XPS (NAP-XPS) Study of the Pt Electrochemical Oxidation in H2O and H2O/O2 Ambients*, Journal of Physical Chemistry C. 120 (**2016**) 15930–15940.

[68] V.A. Saveleva, L. Wang, W. Luo, S. Zafeiratos, C. Ulhaq-Bouillet, A.S. Gago, K.A. Friedrich, E.R. Savinova, *Uncovering the Stabilization Mechanism in Bimetallic Ruthenium-Iridium Anodes for Proton Exchange Membrane Electrolyzers*, Journal of Physical Chemistry Letters. 7 (**2016**) 3240–3245.

[69] P. Lettenmeier, J. Majchel, L. Wang, V.A. Saveleva, S. Zafeiratos, E.R. Savinova, J.J. Gallet, F. Bournel, A.S. Gago, K.A. Friedrich, *Highly active nano-sized iridium catalysts: Synthesis and operando spectroscopy in a proton exchange membrane electrolyzer*, Chem Sci. 9 (**2018**) 3570–3579.

[70] J.J. Velasco Vélez, D. Bernsmeier, T.E. Jones, P. Zeller, E. Carbonio, C.H. Chuang, L.J. Falling, V. Streibel, R. V. Mom, A. Hammud, M. Hävecker, R. Arrigo, E. Stotz, T. Lunkenbein, A. Knop-Gericke, R. Krähnert, R. Schlögl, *The rise of electrochemical NAPXPS operated in the soft X-ray regime exemplified*

by the oxygen evolution reaction on IrOx electrocatalysts, Faraday Discuss. 236 (**2022**) 103–125.

[71] L. Royer, A. Bonnefont, T. Asset, B. Rotonnelli, J.J. Velasco-Vélez, S. Holdcroft, S. Hettler, R. Arenal, B. Pichon, E. Savinova, *Cooperative Redox Transitions Drive Electrocatalysis of the Oxygen Evolution Reaction on Cobalt-Iron Core-Shell Nanoparticles*, ACS Catal. 13 (**2023**) 280–286.

[72] V.A. Saveleva, L. Wang, D. Teschner, T. Jones, A.S. Gago, K.A. Friedrich, S. Zafeiratos, R. Schlögl, E.R. Savinova, *Operando Evidence for a Universal Oxygen Evolution Mechanism on Thermal and Electrochemical Iridium Oxides*, Journal of Physical Chemistry Letters. 9 (**2018**) 3154–3160.

[73] L. Lukashuk, N. Yigit, H. Li, J. Bernardi, K. Föttinger, G. Rupprechter, *Operando XAS and NAP-XPS investigation of CO oxidation on meso- and nanoscale CoO catalysts*, Catal Today. 336 (**2019**) 139–147.

[74] S. Axnanda, E.J. Crumlin, B. Mao, S. Rani, R. Chang, P.G. Karlsson, M.O.M. Edwards, M. Lundqvist, R. Moberg, P. Ross, Z. Hussain, Z. Liu, *Using "Tender" X-ray Ambient Pressure X-Ray Photoelectron Spectroscopy as A Direct Probe of Solid-Liquid Interface*, Sci Rep. 5 (**2015**) 9788.

[75] B.-J. Kim, E. Fabbri, M. Borlaf, D.F. Abbott, I.E. Castelli, M. Nachtegaal, T. Graule, T.J. Schmidt, *Oxygen evolution reaction activity and underlying mechanism of perovskite electrocatalysts at different pH*, Mater Adv. 2 (**2021**) 345–355.

[76] M. Chatenet, B.G. Pollet, D.R. Dekel, F. Dionigi, J. Deseure, P. Millet, R.D. Braatz, M.Z. Bazant, M. Eikerling, I. Staffell, P. Balcombe, Y. Shao-Horn, H. Schäfer, *Water electrolysis: from textbook knowledge to the latest scientific strategies and industrial developments*, Chem Soc Rev. 51 (**2022**) 4583–4762.

[77] T. Reier, H.N. Nong, D. Teschner, R. Schlögl, P. Strasser, *Electrocatalytic Oxygen Evolution Reaction in Acidic Environments – Reaction Mechanisms and Catalysts*, Adv Energy Mater. 7 (**2017**).

[78] S. Wang, T. Shen, C. Yang, G. Luo, D. Wang, *Engineering Iridium-Based Oxygen Evolution Reaction Electrocatalysts for Proton Exchange Membrane Water Electrolyzers*, ACS Catal. 13 (**2023**) 8670–8691.

[79] C.E. Beall, E. Fabbri, T.J. Schmidt, *Perovskite Oxide Based Electrodes for the Oxygen Reduction and Evolution Reactions: The Underlying Mechanism*, ACS Catal. 11 (**2021**) 3094–3114.

[80] Y.-C. Zhang, C. Han, J. Gao, L. Pan, J. Wu, X.-D. Zhu, J.-J. Zou, *NiCo-Based Electrocatalysts for the Alkaline Oxygen Evolution Reaction: A Review*, ACS Catal. 11 (**2021**) 12485–12509.

[81] J. Song, C. Wei, Z.-F. Huang, C. Liu, L. Zeng, X. Wang, Z.J. Xu, *A review on fundamentals for designing oxygen evolution electrocatalysts*, Chem Soc Rev. 49 (**2020**) 2196–2214.

[82] M.-I. Jamesh, M. Harb, *Tuning the electronic structure of the earth-abundant electrocatalysts for oxygen evolution reaction (OER) to achieve efficient alkaline water splitting – A review*, Journal of Energy Chemistry. 56 (**2021**) 299–342.

[83] G. Liu, *Oxygen evolution reaction electrocatalysts for seawater splitting: A review*, Journal of Electroanalytical Chemistry. 923 (**2022**) 116805.

[84] T. Naito, T. Shinagawa, T. Nishimoto, K. Takanabe, *Recent advances in understanding oxygen evolution reaction mechanisms over iridium oxide*, Inorg Chem Front. 8 (**2021**) 2900–2917.

[85] H.G. Sanchez Casalongue, M.L. Ng, S. Kaya, D. Friebel, H. Ogasawara, A. Nilsson, *In Situ Observation of Surface Species on Iridium Oxide Nanoparticles during the Oxygen Evolution Reaction*, Angewandte Chemie International Edition. 53 (**2014**) 7169–7172.

[86] O. Kasian, J. Grote, S. Geiger, S. Cherevko, K.J.J. Mayrhofer, *The Common Intermediates of Oxygen Evolution and Dissolution Reactions during Water Electrolysis on Iridium*, Angewandte Chemie International Edition. 57 (**2018**) 2488–2491.

[87] S. Czioska, A. Boubnov, D. Escalera-López, J. Geppert, A. Zagalskaya, P. Röse, E. Saraçi, V. Alexandrov, U. Krewer, S. Cherevko, J.-D. Grunwaldt, *Increased Ir–Ir Interaction in Iridium Oxide during the Oxygen Evolution Reaction at High Potentials Probed by Operando Spectroscopy*, ACS Catal. 11 (**2021**) 10043–10057.

[88] V. Pfeifer, T.E. Jones, S. Wrabetz, C. Massué, J.J. Velasco Vélez, R. Arrigo, M. Scherzer, S. Piccinin, M. Hävecker, A. Knop-Gericke, R. Schlögl, *Reactive oxygen species in iridium-based OER catalysts*, Chem Sci. 7 (**2016**) 6791–6795.

[89] V. Saveleva, Investigation of the anodes of PEM water electrolyzers by operando synchrotron-based photoemission spectroscopy, **2018**.

[90] R. V. Mom, L.J. Falling, O. Kasian, G. Algara-Siller, D. Teschner, R.H. Crabtree, A. Knop-Gericke, K.J.J. Mayrhofer, J.-J. Velasco-Vélez, T.E. Jones, *Operando Structure–Activity–Stability Relationship of Iridium Oxides during the Oxygen Evolution Reaction*, ACS Catal. 12 (**2022**) 5174–5184.

[91] J.J. Velasco-Vélez, T.E. Jones, V. Streibel, M. Hävecker, C.-H. Chuang, L. Frevel, M. Plodinec, A. Centeno, A. Zurutuza, R. Wang, R. Arrigo, R. Mom, S. Hofmann, R. Schlögl, A. Knop-Gericke, *Electrochemically active Ir NPs on graphene for OER in acidic aqueous electrolyte investigated by in situ and ex situ spectroscopies*, Surf Sci. 681 (**2019**) 1–8.

[92] M. Elmaalouf, M. Odziomek, S. Duran, M. Gayrard, M. Bahri, C. Tard, A. Zitolo, B. Lassalle-Kaiser, J.Y. Piquemal, O. Ersen, C. Boissière, C. Sanchez, M. Giraud, M. Faustini, J. Peron, *The origin of the high electrochemical activity of pseudo-amorphous iridium oxides*, Nat Commun. 12 (**2021**).

[93] H.N. Nong, L. Gan, E. Willinger, D. Teschner, P. Strasser, *IrOx core-shell nanocatalysts for cost- and energy-efficient electrochemical water splitting*, Chem Sci. 5 (**2014**) 2955–2963.

[94] Y. Zhao, D.P. Adiyeri Saseendran, C. Huang, C.A. Triana, W.R. Marks, H. Chen, H. Zhao, G.R. Patzke, *Oxygen Evolution/Reduction Reaction Catalysts: From* In Situ *Monitoring and Reaction Mechanisms to Rational Design*, Chem Rev. 123 (**2023**) 6257–6358.

[95] Y. Han, S. Axnanda, E.J. Crumlin, R. Chang, B. Mao, Z. Hussain, P.N. Ross, Y. Li, Z. Liu, *Observing the Electrochemical Oxidation of Co Metal at the Solid/Liquid Interface Using Ambient Pressure X-ray Photoelectron Spectroscopy*, Journal of Physical Chemistry B. 122 (**2018**) 666–671.

[96] M. Favaro, J. Yang, S. Nappini, *Understanding the OER mechanism on CoOx using operando ambient pressure X-ray Photoelectron Spectroscopy*, (**2017**).

[97] J. Timoshenko, F.T. Haase, S. Saddeler, M. Rüscher, H.S. Jeon, A. Herzog, U. Hejral, A. Bergmann, S. Schulz, B. Roldan Cuenya, *Deciphering the Structural and Chemical Transformations of Oxide Catalysts during Oxygen Evolution Reaction Using Quick X-ray Absorption Spectroscopy and Machine Learning*, J Am Chem Soc. 145 (**2023**) 4065–4080.

[98] A. Frumkin, *Wasserstoffüberspannung und Struktur der Doppelschicht*, Zeitschrift Für Physikalische Chemie. 164A (**1933**) 121–133.

[99] W. Schmickler, *Double layer theory*, Journal of Solid State Electrochemistry. 24 (**2020**) 2175–2176.

[100] S. Sakong, J. Huang, M. Eikerling, A. Groß, *The structure of the electric double layer: Atomistic versus continuum approaches*, Curr Opin Electrochem. 33 (**2022**) 100953.

[101] J. Wu, *Understanding the Electric Double-Layer Structure, Capacitance, and Charging Dynamics*, Chem Rev. 122 (**2022**) 10821–10859.

[102] K. Doblhoff-Dier, M.T.M. Koper, *Electric double layer of Pt(111): Known unknowns and unknown knowns*, Curr Opin Electrochem. 39 (**2023**).

[103] M. Favaro, B. Jeong, P.N. Ross, J. Yano, Z. Hussain, Z. Liu, E.J. Crumlin, *Unravelling the electrochemical double layer by direct probing of the solid/liquid interface*, Nat Commun. 7 (**2016**) 12695.

[104] A.J. Bard, L.R. Faulkner, Electrochemical Methods: Fundamentals and Applications, 2nd Edition, John Wiley & Sons, INC., **2001**.

[105] J.O. Bockris, B.E. Conway, E. Yeager, Comprehensive Treatise of Electrochemistry, Spinger Science, Business Media, LCC, **1980**.

[106] L. Scalfi, T. Dufils, K.G. Reeves, B. Rotenberg, M. Salanne, *A semiclassical Thomas-Fermi model to tune the metallicity of electrodes in molecular simulations*, Journal of Chemical Physics. 153 (**2020**).

[107] A. Serva, L. Scalfi, B. Rotenberg, M. Salanne, *Effect of the metallicity on the capacitance of gold-aqueous sodium chloride interfaces*, Journal of Chemical Physics. 155 (**2021**).

[108] B.B. Damaskin, O.A. Petrii, *Historical development of theories of the electrochemical double layer*, Journal of Solid State Electrochemistry. 15 (**2011**) 1317–1334.

[109] M.F. Lichterman, M.H. Richter, B.S. Brunschwig, N.S. Lewis, H.J. Lewerenz, *Operando X-ray photoelectron spectroscopic investigations of the electrochemical double layer at Ir/KOH(aq) interfaces*, J Electron Spectros Relat Phenomena. 221 (**2017**) 99–105.

[110] C.Y. Li, M. Chen, S. Liu, X. Lu, J. Meng, J. Yan, H.D. Abruña, G. Feng, T. Lian, *Unconventional interfacial water structure of highly concentrated aqueous electrolytes at negative electrode polarizations*, Nature Communications 2022 13:1. 13 (**2022**) 1–10.

[111] S. Soo Lee, A. Koishi, I.C. Bourg, P. Fenter, *Ion correlations drive charge overscreening and heterogeneous nucleation at solid-aqueous electrolyte interfaces*, 118 (**2021**) 2105154118.

[112] P. Li, Y. Liu, S. Chen, *Microscopic EDL structures and charge-potential relation on stepped platinum surface: Insights from the ab initio molecular dynamics simulations*, Journal of Chemical Physics. 156 (**2022**).

[113] M.A. Brown, A. Goel, Z. Abbas, *Effect of Electrolyte Concentration on the Stern Layer Thickness at a Charged Interface*, Angewandte Chemie. 128 (**2016**) 3854–3858.

[114] J. Huang, M. Li, M.J. Eslamibidgoli, M. Eikerling, A. Groß, *Cation Overcrowding Effect on the Oxygen Evolution Reaction*, JACS Au. 1 (**2021**) 1752–1765.

[115] Z. Lin, P.L. Taberna, P. Simon, *Electrochemical double layer capacitors: What is next beyond the corner?*, Curr Opin Electrochem. 6 (**2017**) 115–119.

[116] G. Jeanmairet, B. Rotenberg, M. Salanne, *Microscopic Simulations of Electrochemical Double-Layer Capacitors*, Chem Rev. 122 (**2022**) 10860–10898.

[117] M. Dunwell, Y. Yan, B. Xu, Understanding the Influence of the Electrochemical Double-Layer on Heterogeneous Electrochemical Reactions, **2018**.

[118] J. Wu, *Understanding the Electric Double-Layer Structure, Capacitance, and Charging Dynamics*, Chem Rev. 122 (**2022**) 10821–10859.

[119] H.L.F. Von Helmoltz, , Ann. Physik. (**1853**) 211.

[120] G. Gouy, , Compt. Rend. 149 (**1910**).

[121] G. Gouy, , J. Phys. Radium. 9 (**1910**).

[122] D.L. Chapman, , Phil. Mag. 25 (**1913**).

[123] G.H. Bolt, *Analysis of the validity of the Gouy-Chapman theory of the electric double layer*, J Colloid Sci. 10 (**1955**) 206–218.

[124] G.M. Torrie, J.P. Valleau, *Electrical double layers. 4. Limitations of the Gouy-Chapman theory*, Journal of Physical Chemistry. 86 (**1982**) 3251–3257.

[125] O. Stern, , Elektrochem. 30 (**1924**).

[126] R. Parsons, *Electrical Double Layer: Recent Experimental and Theoretical Developments*, Chem Rev. 90 (**1990**) 813–826.

[127] D.C. Grahame, *The electrical double layer and the theory of electrocapillarity*, Chem Rev. 41 (**1947**) 441–501.

[128] D.C. Grahame, R. Parsons, *Components of Charge and Potential in the Inner Region of the Electrical Double Layer: Aqueous Potassium Chloride Solutions in Contact with Mercury at 25°*, J Am Chem Soc. 83 (**1961**) 1291–1296.

[129] R.W. Gurney, *Theory of Electrical Double Layers in Adsorbed Films*, Physical Review. 47 (**1935**) 479.

[130] S. Trasatti, L.M. Doubova, *Crystal-face specificity of electrical double-layer parameters at metal/solution interfaces*, Journal of the Chemical Society, Faraday Transactions. 91 (**1995**) 3311–3325.

[131] J.O. BOCKRIS, M.A.V. DEVANATHAN, K. MÜLLER, *On the structure of charged interfaces*, Electrochemistry. (**1965**) 832–863.

[132] A.N. Frumkin, O.A. Petrii, *Potentials of zero total and zero free charge of platinum group metals*, Electrochim Acta. 20 (**1975**) 347–359.

[133] A.N. Frumkin, O.A. Petrii, B.B. Damaskin, *Potentials of Zero Charge*, Comprehensive Treatise of Electrochemistry. (**1980**) 221–289.

[134] R. Rizo, E. Sitta, E. Herrero, V. Climent, J.M. Feliu, *Towards the understanding of the interfacial pH scale at Pt(111) electrodes*, Electrochim Acta. 162 (**2015**) 138–145.

[135] Q. Deng, J. Weissmüller, *Electrocapillary coupling during electrosorption*, Langmuir. 30 (**2014**) 10522–10530.

[136] O.M. Magnussen, A. Groß, *Toward an Atomic-Scale Understanding of Electrochemical Interface Structure and Dynamics*, J Am Chem Soc. 141 (**2019**) 4777–4790.

[137] S. Levine, C.W. Outhwaite, L.B. Bhuiyan, *Statistical mechanical theories of the electric double layer*, J Electroanal Chem Interfacial Electrochem. 123 (**1981**) 105–119.

[138] A. Roudgar, A. Groß, Water bilayer on the Pd/Au(111) overlayer system: coadsorption and electric field effects, n.d.

[139] A. Michaelides, *Density functional theory simulations of water-metal interfaces: Waltzing waters, a novel 2D ice phase, and more*, Appl Phys A Mater Sci Process. 85 (**2006**) 415–425.

[140] E. Skúlason, G.S. Karlberg, J. Rossmeisl, T. Bligaard, J. Greeley, H. Jónsson, J.K. Nørskov, *Density functional theory calculations for the hydrogen evolution reaction in an electrochemical double layer on the Pt(111) electrode*, Physical Chemistry Chemical Physics. 9 (**2007**) 3241–3250.

[141] S.P. Jiang, *A comparison of O2 reduction reactions on porous (La,Sr)MnO3 and (La,Sr)(Co,Fe)O3 electrodes*, Solid State Ion. 146 (**2002**) 1–22.

[142] E. Spohr, *Computer simulation of the structure of the electrochemical double layer*, Journal of Electroanalytical Chemistry. 450 (**1998**) 327–334.

[143] E. Spohr, *Molecular simulation of the electrochemical double layer*, Electrochim Acta. 44 (**1999**) 1697–1705.

[144] S. Schnur, A. Groß, *Properties of metal-water interfaces studied from first principles*, New J Phys. 11 (**2009**).

[145] S. Sakong, A. Groß, *The electric double layer at metal-water interfaces revisited based on a charge polarization scheme*, Journal of Chemical Physics. 149 (**2018**).

[146] A. Marin-Laflèche, M. Haefele, L. Scalfi, A. Coretti, T. Dufils, G. Jeanmairet, S.K. Reed, A. Serva, R. Berthin, C. Bacon, S. Bonella, B. Rotenberg, P.A. Madden, M. Salanne, *MetalWalls: A classical molecular dynamics software dedicated to the simulation of electrochemical systems*, J Open Source Softw. 5 (**2020**) 2373.

[147] A. Coretti, C. Bacon, R. Berthin, A. Serva, L. Scalfi, I. Chubak, K. Goloviznina, M. Haefele, A. Marin-Laflèche, B. Rotenberg, S. Bonella, M. Salanne, *MetalWalls: Simulating electrochemical interfaces between polarizable electrolytes and metallic electrodes*, Journal of Chemical Physics. 157 (**2022**).

[148] H. Siegenthaler, E. Ammann, P.-F. Indermuhlet, G. Repphun, *Nanoscale Probes of the Solid-Liquid Interface*, Nanoscale Science and Technology. (**1998**) 297–315.

[149] A.J. Bard', H.D. Abruiia, C.E. Chidsey, L.R. Faulkner, S.W. Feldberg, K. Itaya, M. Majda, O. Melroy, R.W. Murray, M.D. Porter, M.P. Soriaga, H.S. White, The Electrode/Electrolyte Interface - A Status Report, **1993**.

[150] D.Y. Wu, J.F. Li, B. Ren, Z.Q. Tian, *Electrochemical surface-enhanced Raman spectroscopy of nanostructures*, Chem Soc Rev. 37 (**2008**) 1025–1041.

[151] B.Y. Wen, J.S. Lin, Y.J. Zhang, P.M. Radjenovic, X.G. Zhang, Z.Q. Tian, J.F. Li, *Probing Electric Field Distributions in the Double Layer of a Single-Crystal Electrode with Angstrom Spatial Resolution using Raman Spectroscopy*, J Am Chem Soc. 142 (**2020**) 11698–11702.

[152] S.H. Macomber, T.E. Furtak, T.M. Devine, *Enhanced RAMAN characterization of adsorbed water at the electrochemical double layer on silver*, Surf Sci. 122 (**1982**) 556–568.

[153] I. Siretanu, D. Ebeling, M.P. Andersson, S.L. Svane Stipp, A. Philipse, M.C. Stuart, D. Van Den Ende, F. Mugele, *Direct observation of ionic structure at solid-liquid interfaces: a deep look into the Stern Layer*, (**2014**).

[154] E.M. Stuve, A. Krasnopoler, D.E. Sauer, Relating the in-situ, ex-situ, and non-situ environments in surface electrochemistry, **1995**.

[155] A. Shchukarev, *XPS at solid-aqueous solution interface*, Adv Colloid Interface Sci. 122 (**2006**) 149–157.

[156] E.R. Savinova, D.Y. Zemlyanov, A. Scheybal, R. Schlögl, K. Doblhofer, *Ex Situ X-ray Photoelectron Spectroscopy Study of the Interface between a Ag(111) Electrode and an Alkaline Electrolyte. 2. Structure of the Double Layer*, (**1999**).

[157] E.R. Savinova, D. Zemlyanov, A. Scheybal, Th. Schedel-Niedrig, K. Doblhofer, R. Schlögl, *Ex Situ X-ray Photoelectron Spectroscopy Study of the Interface between a Ag(111) Electrode and an Alkaline Electrolyte. 1. Influence of the Electrode Potential on the Adsorption of Oxygen Species*, Langmuir. 15 (**1999**) 6546–6551.

[158] H.-G. Steinrück, S. Steinrück, C. Cao, Y. Tsao, C.J. Takacs, O. Konovalov, J. Vatamanu, O. Borodin, M.F. Toney, *The Nanoscale Structure of the Electrolyte-metal Oxide Interface*, (n.d.).

[159] M. Favaro, F. Abdi, E. Crumlin, Z. Liu, R. van de Krol, D. Starr, *Interface Science Using Ambient Pressure Hard X-ray Photoelectron Spectroscopy*, Surfaces. 2 (**2019**) 78–99.

[160] H. Shinotsuka, B. Da, S. Tanuma, H. Yoshikawa, C.J. Powell, D.R. Penn, *Calculations of electron inelastic mean free paths. XI. Data for liquid water for energies from 50 eV to 30 keV*, Surface and Interface Analysis. 49 (**2017**) 238–252.

[161] H. Shinotsuka, S. Tanuma, C.J. Powell, D.R. Penn, *Calculations of electron inelastic mean free paths. XII. Data for 42 inorganic compounds over the 50 eV to 200 keV range with the full Penn algorithm*, Surface and Interface Analysis. 51 (**2019**) 427–457.

[162] D. Weingarth, A. Foelske-Schmitz, A. Wokaun, R. Kötz, *In situ electrochemical XPS study of the Pt/[EMIM][BF4] system*, Electrochem Commun. 13 (**2011**) 619–622.

[163] S.G. Booth, A.M. Tripathi, I. Strashnov, R.A.W. Dryfe, A.S. Walton, *The offset droplet: a new methodology for studying the solid/water interface using x-ray photoelectron spectroscopy.*, J Phys Condens Matter. 29 (**2017**) 454001.

[164] K.A. Stoerzinger, M. Favaro, P.N. Ross, J. Yano, Z. Liu, Z. Hussain, E.J. Crumlin, *Probing the Surface of Platinum during the Hydrogen Evolution Reaction in Alkaline Electrolyte*, Journal of Physical Chemistry B. 122 (**2018**) 864–870.

[165] M. Favaro, C. Valero-Vidal, J. Eichhorn, F.M. Toma, P.N. Ross, J. Yano, Z. Liu, E.J. Crumlin, *Elucidating the alkaline oxygen evolution reaction mechanism on platinum*, J Mater Chem A Mater. 5 (**2017**) 11634–11643.

[166] I. Källquist, F. Lindgren, M.T. Lee, A. Shavorskiy, K. Edström, H. Rensmo, L. Nyholm, J. Maibach, M. Hahlin, *Probing Electrochemical Potential Differences over the Solid/Liquid Interface in Li-Ion Battery Model Systems*, ACS Appl Mater Interfaces. 13 (**2021**) 32989–32996.

[167] I. Källquist, R. Le Ruyet, H. Liu, R. Mogensen, M.-T. Lee, K. Edström, A.J. Naylor, *Advances in studying interfacial reactions in rechargeable batteries by photoelectron spectroscopy*, J Mater Chem A Mater. 10 (**2022**) 19466–19505.

[168] P. Aydogan Gokturk, R. Sujanani, J. Qian, Y. Wang, L.E. Katz, B.D. Freeman, E.J. Crumlin, *The Donnan potential revealed*, Nat Commun. 13 (**2022**).

[169] R.H. Temperton, A. Kawde, A. Eriksson, W. Wang, E. Kokkonen, R. Jones, S.M. Gericke, S. Zhu, W. Quevedo, R. Seidel, J. Schnadt, A. Shavorskiy, P. Persson, J. Uhlig, *Dip-and-pull ambient pressure photoelectron spectroscopy as a spectroelectrochemistry tool for probing molecular redox processes*, Journal of Chemical Physics. 157 (**2022**).

[170] L. Pérez Ramírez, A. Boucly, F. Saudrais, F. Bournel, J.J. Gallet, E. Maisonhaute, A.R. Milosavljević, C. Nicolas, F. Rochet, *The Fermi level as an energy reference in liquid jet X-ray photoelectron spectroscopy studies of aqueous solutions*, Physical Chemistry Chemical Physics. 23 (**2021**) 16224–16233.

[171] L.D. Chen, *Cations play an essential role in CO2 reduction*, Nature Catalysis 2021 4:8. 4 (**2021**) 641–642.

[172] J.T. Bender, A.S. Petersen, F.C. Østergaard, M.A. Wood, S.M.J. Heffernan, D.J. Milliron, J. Rossmeisl, J. Resasco, *Understanding Cation Effects on the Hydrogen Evolution Reaction*, ACS Energy Lett. 8 (**2023**) 657–665.

[173] J. Zaffran, M.B. Stevens, C.D.M. Trang, M. Nagli, M. Shehadeh, S.W. Boettcher, M. Caspary Toroker, *Influence of Electrolyte Cations on Ni(Fe)OOH Catalyzed Oxygen Evolution Reaction*, Chemistry of Materials. 29 (**2017**) 4761–4767.

[174] J.A.D. del Rosario, G. Li, M.F.M. Labata, J.D. Ocon, P.Y.A. Chuang, *Unravelling the roles of alkali-metal cations for the enhanced oxygen evolution reaction in alkaline media*, Appl Catal B. 288 (**2021**) 119981.

[175] R.W. McCabe, C. Wong, H.S. Woo, *The passivating oxidation of platinum*, J Catal. 114 (**1988**) 354–367.

[176] T.G. Avval, S. Chatterjee, G.T. Hodges, S. Bahr, P. Dietrich, M. Meyer, A. Thißen, M.R. Linford, *Oxygen gas, O2(g), by near-ambient pressure XPS*, Surface Science Spectra. 26 (**2019**) 014021.

[177] M. Favaro, *Stochastic Analysis of Electron Transfer and Mass Transport in Confined Solid/Liquid Interfaces*, Surfaces. 3 (**2020**) 392–407.

[178] S. Tanaka, H. Tajiri, O. Sakata, N. Hoshi, M. Nakamura, *Interfacial Structure of Pt(110) Electrode during Hydrogen Evolution Reaction in Alkaline Solutions*, Journal of Physical Chemistry Letters. 13 (**2022**) 8403–8408.

[179] Y. Levin, A.P. dos Santos, A. Diehl, *Ions at the Air-Water Interface: An End to a Hundred-Year-Old Mystery?*, Phys Rev Lett. 103 (**2009**) 257802.

[180] L. Dalstein, K.Y. Chiang, Y.C. Wen, *Surface Potential at Electrolyte/Air Interfaces: A Quantitative Analysis via Sum-Frequency Vibrational Spectroscopy*, Journal of Physical Chemistry B. (**2023**).

[181] L. Jacobse, V. Vonk, I.T. McCrum, C. Seitz, M.T.M. Koper, M.J. Rost, A. Stierle, *Electrochemical oxidation of Pt(111) beyond the place-exchange model*, Electrochim Acta. 407 (**2022**) 139881.

[182] H. Imai, K. Izumi, M. Matsumoto, Y. Kubo, K. Kato, Y. Imai, *In Situ and Real-Time Monitoring of Oxide Growth in a Few Monolayers at Surfaces of Platinum Nanoparticles in Aqueous Media*, J Am Chem Soc. 131 (**2009**) 6293–6300.

[183] M. Shi, Z. Zhang, M. Zhao, X. Lu, Z.L. Wang, *Reducing the Self-Discharge Rate of Supercapacitors by Suppressing Electron Transfer in the Electric Double Layer*, J Electrochem Soc. 168 (**2021**) 120548.

[184] K. Hayamizu, Y. Chiba, T. Haishi, *Dynamic ionic radius of alkali metal ions in aqueous solution: a pulsed-field gradient NMR study*, RSC Adv. 11 (**2021**) 20252–20257.

[185] D.F. Van Der Vliet, M.T.M. Koper, *Electrochemistry of Pt (100) in alkaline media: A voltammetric study*, Surf Sci. 604 (**2010**) 1912–1918.

[186] M.B. Trzhaskovskaya, V.G. Yarzhemsky, *Dirac–Fock photoionization parameters for HAXPES applications*, At Data Nucl Data Tables. 119 (**2018**) 99–174.

[187] J. Willis, C. Kalha, M.B. Trzhaskovskaya, V.G. Yarzhemsky, D.O. Scanlon, A. Regoutz, *Digitisation of Trzhaskovskaya Dirac-Fock Photoionisation parameters for HAXPES Applications (1.5-10 keV)*, Figshare. (**2020**).

[188] X. Chen, X. Wang, D. Fang, *A review on C1s XPS-spectra for some kinds of carbon materials*, Fullerenes Nanotubes and Carbon Nanostructures. (**2020**) 1048–1058.

[189] A. Dekanski, J. Stevanovic, R. Stevanovic, B.Z. Nikolic, ´ Vladislava, M. Jovanovic, *Glassy carbon electrodes I. Characterization and electrochemical activation*, Carbon N Y. 39 (**2001**) 1195–1205.

[190] Y. Yi, G. Weinberg, M. Prenzel, M. Greiner, S. Heumann, S. Becker, R. Schlögl, *Electrochemical corrosion of a glassy carbon electrode*, Catal Today. 295 (**2017**) 32–40.

[191] P.S. Guin, S. Das, P.C. Mandal, *Electrochemical Reduction of Quinones in Different Media: A Review*, International Journal of Electrochemistry. 2011 (**2011**) 1–22.

[192] I.S. Filimonenkov, C. Bouillet, G. Kéranguéven, P.A. Simonov, G.A. Tsirlina, E.R. Savinova, *Carbon materials as additives to the OER catalysts: RRDE study of carbon corrosion at high anodic potentials*, Electrochim Acta. 321 (**2019**) 134657.

[193] K.A. Stoerzinger, M. Favaro, P.N. Ross, Z. Hussain, Z. Liu, J. Yano, E.J. Crumlin, *Stabilizing the Meniscus for Operando Characterization of Platinum During the Electrolyte-Consuming Alkaline Oxygen Evolution Reaction*, Top Catal. 61 (**2018**) 2152–2160.

[194] A. Larsson, K. Simonov, J. Eidhagen, A. Grespi, X. Yue, H. Tang, A. Delblanc, M. Scardamaglia, A. Shavorskiy, J. Pan, E. Lundgren, *In situ quantitative analysis of electrochemical oxide film development on metal surfaces using ambient pressure X-ray photoelectron spectroscopy: Industrial alloys*, Appl Surf Sci. 611 (**2023**) 155714.

[195] J. Balej, *Water vapour partial pressures and water activities in potassium and sodium hydroxide solutions over wide concentration and temperature ranges*, Int J Hydrogen Energy. 10 (**1985**) 233–243.

[196] M.B. Trzhaskovskaya, V.G. Yarzhemsky, *Dirac–Fock photoionization parameters for HAXPES applications, Part II: Inner atomic shells*, At Data Nucl Data Tables. 129–130 (**2019**) 101280.

[197] J. Peng, J. Guo, P. Hapala, D. Cao, R. Ma, B. Cheng, L. Xu, M. Ondráček, P. Jelínek, E. Wang, Y. Jiang, *Weakly perturbative imaging of interfacial water with submolecular resolution by atomic force microscopy*, Nature Communications 2017 9:1. 9 (**2018**) 1–7.

[198] Y.H. Wang, S. Li, R.Y. Zhou, S. Zheng, Y.J. Zhang, J.C. Dong, Z.L. Yang, F. Pan, Z.Q. Tian, J.F. Li, *In situ electrochemical Raman spectroscopy and ab initio molecular dynamics study of interfacial water on a single-crystal surface*, Nature Protocols 2023 18:3. 18 (**2023**) 883–901.

[199] T. Petit, H. Yuzawa, M. Nagasaka, R. Yamanoi, E. Osawa, N. Kosugi, E.F. Aziz, *Probing Interfacial Water on Nanodiamonds in Colloidal Dispersion*, Journal of Physical Chemistry Letters. 6 (**2015**) 2909–2912.

[200] J.J. Velasco-Velez, C.H. Wu, T.A. Pascal, L.F. Wan, J. Guo, D. Prendergast, M. Salmeron, *The structure of interfacial water on gold electrodes studied by x-ray absorption spectroscopy*, Science (1979). 346 (**2014**) 831–834.

[201] S. Zhu, M. Scardamaglia, J. Kundsen, R. Sankari, H. Tarawneh, R. Temperton, L. Pickworth, F. Cavalca, C. Wang, H.H. Tissot, J. Weissenrieder, B. Hagman, J. Gustafson, S. Kaya, F. Lindgren, I. Källquist, J. Maibach, M. Hahlin, V. Boix, T. Gallo, F. Rehman, G. D'acunto, J. Schnadt, A. Shavorskiy, *HIPPIE: a new platform for ambient-pressure X-ray photoelectron spectroscopy at the MAX IV Laboratory*, J. Synchrotron Rad. 28 (**2021**) 624–636.

[202] A.R. Akbashev, *Electrocatalysis on oxide surfaces: Fundamental challenges and opportunities*, Curr Opin Electrochem. 35 (**2022**) 101095.

[203] J.J. Borrás-Almenar, E. Coronado, A. Müller, M. Pope, Polyoxometalate Molecular Science, Springer Netherlands, Dordrecht, **2003**.

[204] J.F. KEGGIN, *Structure of the Crystals of 12-Phosphotungstic Acid*, Nature. 132 (**1933**) 351–351.

[205] B. Dawson, *The structure of the 9(18)-heteropoly anion in potassium 9(18)-tungstophosphate, K_6 ($P_2W_{18}O_{62}$).14H_2O*, Acta Crystallogr. 6 (**1953**) 113–126.

[206] N.I. Gumerova, A. Rompel, *Synthesis, structures and applications of electron-rich polyoxometalates*, Nature Reviews Chemistry 2018 2:2. 2 (**2018**) 1–20.

[207] T. Ueda, *Electrochemistry of Polyoxometalates: From Fundamental Aspects to Applications*, ChemElectroChem. 5 (**2018**) 823–838.

[208] J.J. Borrás-Almenar, E. Coronado, A. Müller, M. Pope, eds., Polyoxometalate Molecular Science, Springer Netherlands, Dordrecht, **2003**.

[209] A. Dolbecq, E. Dumas, C.R. Mayer, P. Mialane, *Hybrid organic-inorganic polyoxometalate compounds: From structural diversity to applications*, Chem Rev. 110 (**2010**) 6009–6048.

[210] S.J. Folkman, J. Soriano-Lopez, J.R. Galán-Mascarós, R.G. Finke, *Electrochemically Driven Water-Oxidation Catalysis Beginning with Six Exemplary Cobalt Polyoxometalates: Is It Molecular, Homogeneous Catalysis or*

Electrode-Bound, Heterogeneous CoO x Catalysis?, J Am Chem Soc. 140 (**2018**) 12040–12055.

[211] Y. V. Geletii, B. Botar, P. Kögerler, D.A. Hillesheim, D.G. Musaev, C.L. Hill, *An All-Inorganic, Stable, and Highly Active Tetraruthenium Homogeneous Catalyst for Water Oxidation*, Angewandte Chemie International Edition. 47 (**2008**) 3896–3899.

[212] D. Gao, I. Trentin, L. Schwiedrzik, L. González, C. Streb, *The reactivity and stability of polyoxometalate water oxidation electrocatalysts*, Molecules. 25 (**2020**) 157.

[213] D.E. Katsoulis, *A Survey of Applications of Polyoxometalates*, Chem. Rev. 98 (**1998**) 359–387.

[214] M.S. Balulla, J.A. Gamelas, H.M. Carapuça, A.M.V. Cavaleiro, W. Schlindwein, *Electrochemical behaviour of first row transition metal substituted polyoxotungstates: A comparative study in acetonitrile*, Eur J Inorg Chem. 4 (**2004**) 619–628.

[215] B. Keita, E. Abdeljalil, L. Nadjo, B. Avisse, R. Contant, J. Canny, M. Richet, *Ligand and electrolyte effects in the electroreduction of copper-substituted heteropolyanions*, Electrochem Commun. 2 (**2000**) 145–149.

[216] B. Keita, L. Nadjo, *Polyoxometalate-based homogeneous catalysis of electrode reactions: Recent achievements*, J Mol Catal A Chem. 262 (**2007**) 190–215.

[217] C. Freire, D.M. Fernandes, M. Nunes, M. Araújo, *Polyoxometalate-based modified electrodes for electrocatalysis: From molecule sensing to renewable energy-related applications*, Advanced Electrode Materials. (**2016**) 147–212.

[218] Z. Zeb, Y. Huang, L. Chen, W. Zhou, M. Liao, Y. Jiang, H. Li, L. Wang, L. Wang, H. Wang, T. Wei, D. Zang, Z. Fan, Y. Wei, *Comprehensive overview of polyoxometalates for electrocatalytic hydrogen evolution reaction*, Coord Chem Rev. 482 (**2023**) 215058.

[219] J. Du, Y.Y. Ma, H. Tan, Z.H. Kang, Y. Li, *Progress of electrochemical CO2 reduction reactions over polyoxometalate-based materials*, Chinese Journal of Catalysis. 42 (**2021**) 920–937.

[220] D. Yang, B. Ni, X. Wang, *Heterogeneous Catalysts with Well-Defined Active Metal Sites toward CO2 Electrocatalytic Reduction*, Adv Energy Mater. 10 (**2020**) 2001142.

[221] M. Genovese, K. Lian, *Polyoxometalate modified inorganic–organic nanocomposite materials for energy storage applications: A review*, Curr Opin Solid State Mater Sci. 19 (**2015**) 126–137.

[222] S.W. Gersten, G.J. Samuels, T.J. Meyer, *Catalytic oxidation of water by an oxo-bridged ruthenium dimer*, J Am Chem Soc. 104 (**1982**) 4029–4030.

[223] A.R. Howells, A. Sankarraj, C. Shannon, *A Diruthenium-Substituted Polyoxometalate as an Electrocatalyst for Oxygen Generation*, J Am Chem Soc. 126 (**2004**) 12258–12259.

[224] A. Sartorel, M. Carraro, G. Scorrano, R. De Zorzi, S. Geremia, N.D. McDaniel, S. Bernhard, M. Bonchio, *Polyoxometalate Embedding of a Tetraruthenium(IV)-oxo-core by Template-Directed Metalation of [γ-$SiW_{10}O_{36}$]$^{8-}$: A Totally Inorganic Oxygen-Evolving Catalyst*, J Am Chem Soc. 130 (**2008**) 5006–5007.

[225] Y.V. Geletii, B. Botar, P. Kögerler, D.A. Hillesheim, D.G. Musaev, C.L. Hill, *An All-Inorganic, Stable, and Highly Active Tetraruthenium Homogeneous Catalyst for Water Oxidation*, Angewandte Chemie. 120 (**2008**) 3960–3963.

[226] F.M. Toma, A. Sartorel, M. Iurlo, M. Carraro, P. Parisse, C. Maccato, S. Rapino, B.R. Gonzalez, H. Amenitsch, T. Da Ros, L. Casalis, A. Goldoni, M. Marcaccio, G. Scorrano, G. Scoles, F. Paolucci, M. Prato, M. Bonchio, *Efficient water oxidation at carbon nanotube–polyoxometalate electrocatalytic interfaces*, Nat Chem. 2 (**2010**) 826–831.

[227] S.X. Guo, Y. Liu, C.Y. Lee, A.M. Bond, J. Zhang, Y. V. Geletii, C.L. Hill, *Graphene-supported [{Ru4O4(OH)2(H 2O)4}(γ-SiW10O36) 2]10- for highly efficient electrocatalytic water oxidation*, Energy Environ Sci. 6 (**2013**) 2654–2663.

[228] C. Hadad, X. Ke, M. Carraro, A. Sartorel, C. Bittencourt, G. Van Tendeloo, M. Bonchio, M. Quintana, M. Prato, *Positive graphene by chemical design: tuning supramolecular strategies for functional surfaces*, Chem. Commun. 50 (**2014**) 885–887.

[229] L. Yu, Y. Ding, M. Zheng, H. Chen, J. Zhao, *[{β-$SiNi_2W_{10}O_{36}(OH)_2(H_2O)$}$_4$]$^{24-}$: a new robust visible light-driven water oxidation catalyst based on nickel-containing polyoxometalate*, Chemical Communications. 52 (**2016**) 14494–14497.

[230] B. Schwarz, J. Forster, M.K. Goetz, D. Yücel, C. Berger, T. Jacob, C. Streb, *Visible-Light-Driven Water Oxidation by a Molecular Manganese Vanadium Oxide Cluster*, Angewandte Chemie International Edition. 55 (**2016**) 6329–6333.

[231] J. Kern, R. Chatterjee, I.D. Young, F.D. Fuller, L. Lassalle, M. Ibrahim, S. Gul, T. Fransson, A.S. Brewster, R. Alonso-Mori, R. Hussein, M. Zhang, L. Douthit, C. de Lichtenberg, M.H. Cheah, D. Shevela, J. Wersig, I. Seuffert, D. Sokaras, E. Pastor, C. Weninger, T. Kroll, R.G. Sierra, P. Aller, A. Butryn, A.M. Orville, M. Liang, A. Batyuk, J.E. Koglin, S. Carbajo, S. Boutet, N.W. Moriarty, J.M. Holton, H. Dobbek, P.D. Adams, U. Bergmann, N.K. Sauter, A. Zouni, J. Messinger, J. Yano, V.K. Yachandra, *Structures of the intermediates of Kok's photosynthetic water oxidation clock*, Nature 2018 563:7731. 563 (**2018**) 421–425.

[232] S.D. Adhikary, A. Tiwari, T.C. Nagaiah, D. Mandal, *Stabilization of Cobalt-Polyoxometalate over Poly(ionic liquid) Composites for Efficient Electrocatalytic Water Oxidation*, ACS Appl Mater Interfaces. 10 (**2018**) 38872–38879.

[233] H. Lv, J. Song, Y. V. Geletii, J.W. Vickers, J.M. Sumliner, D.G. Musaev, P. Kögerler, P.F. Zhuk, J. Bacsa, G. Zhu, C.L. Hill, *An exceptionally fast homogeneous carbon-free cobalt-based water oxidation catalyst*, J Am Chem Soc. 136 (**2014**) 9268–9271.

[234] Q. Yin, J.M. Tan, C. Besson, Y. V Geletii, D.G. Musaev, A.E. Kuznetsov, Z. Luo, K.I. Hardcastle, C.L. Hill, *A fast soluble carbon-free molecular water oxidation catalyst based on abundant metals*, Science (1979). 328 (**2010**) 342–345.

[235] B.J. Timothy R Weakley, H.T. Evans, J.S. Showell, G.F. Tournb, C.M. Tournq, 18-Tungstotetracobalto(11)diphosphate and Related Anions: a Novel Structural Class of Heteropolyanions, **1973**.

[236] J.J. Stracke, R.G. Finke, *Electrocatalytic Water Oxidation Beginning with the Cobalt Polyoxometalate [Co 4 (H 2 O) 2 (PW 9 O 34) 2] 10– : Identification of*

Heterogeneous CoO x as the Dominant Catalyst, J Am Chem Soc. 133 (**2011**) 14872–14875.

[237] M.W. Kanan, D.G. Nocera, *In Situ Formation of an Oxygen-Evolving Catalyst in Neutral Water Containing Phosphate and Co^{2+}*, Science (1979). 321 (**2008**) 1072–1075.

[238] J.J. Stracke, R.G. Finke, *Water oxidation catalysis beginning with 2.5 μm [Co4(H 2O)2(PW9O34)2] 10-: Investigation of the true electrochemically driven catalyst at ≥600 mV overpotential at a glassy carbon electrode*, ACS Catal. 3 (**2013**) 1209–1219.

[239] Z. Huang, Z. Luo, Y. V. Geletii, J.W. Vickers, Q. Yin, D. Wu, Y. Hou, Y. Ding, J. Song, D.G. Musaev, C.L. Hill, T. Lian, *Efficient Light-Driven Carbon-Free Cobalt-Based Molecular Catalyst for Water Oxidation*, J Am Chem Soc. 133 (**2011**) 2068–2071.

[240] D. Lieb, A. Zahl, E.F. Wilson, C. Streb, L.C. Nye, K. Meyer, I. Ivanović-Burmazović, *Water exchange reactivity and stability of cobalt polyoxometalates under catalytically relevant pH conditions: Insight into water oxidation catalysis*, Inorg Chem. 50 (**2011**) 9053–9058.

[241] M. Natali, S. Berardi, A. Sartorel, M. Bonchio, S. Campagna, F. Scandola, *Is [Co4(H2O)2(α-PW9O34)2]10− a genuine molecular catalyst in photochemical water oxidation? Answers from time-resolved hole scavenging experiments*, Chemical Communications. 48 (**2012**) 8808.

[242] R. Schiwon, K. Klingan, H. Dau, C. Limberg, *Shining light on integrity of a tetracobalt-polyoxometalate water oxidation catalyst by X-ray spectroscopy before and after catalysis*, Chem. Commun. 50 (**2014**) 100.

[243] J.W. Vickers, H. Lv, J.M. Sumliner, G. Zhu, Z. Luo, D.G. Musaev, Y. V. Geletii, C.L. Hill, *Differentiating homogeneous and heterogeneous water oxidation catalysis: Confirmation that [Co4(H2O)2(α-PW 9O34)2]10- is a molecular water oxidation catalyst*, J Am Chem Soc. 135 (**2013**) 14110–14118.

[244] C.A. Ohlin, S.J. Harley, J.G. McAlpin, R.K. Hocking, B.Q. Mercado, R.L. Johnson, E.M. Villa, M.K. Fidler, M.M. Olmstead, L. Spiccia, R.D. Britt, W.H. Casey, *Rates of water exchange for two cobalt(II) heteropolyoxotungstate*

compounds in aqueous solution, Chemistry - A European Journal. 17 (**2011**) 4408–4417.

[245] S. Goberna-Ferrón, L. Vigara, J. Soriano-López, J.R. Galán-Mascarós, *Identification of a Nonanuclear {Co(II)9} Polyoxometalate Cluster as a Homogeneous Catalyst for Water Oxidation*, Inorg Chem. 51 (**2012**) 11707–11715.

[246] S. Goberna-Ferrón, J. Soriano-López, J.R. Galán-Mascarós, M. Nyman, *Solution Speciation and Stability of Cobalt-Polyoxometalate Water Oxidation Catalysts by X-ray Scattering*, Eur J Inorg Chem. 2015 (**2015**) 2833–2840.

[247] S.J. Folkman, R.G. Finke, *Electrochemical Water Oxidation Catalysis Beginning with Co(II) Polyoxometalates: The Case of the Precatalyst Co4V2W18O6810-*, ACS Catal. 7 (**2017**) 7–16.

[248] J. Soriano-López, D.G. Musaev, C.L. Hill, J.R. Galán-Mascarós, J.J. Carbó, J.M. Poblet, *Tetracobalt-polyoxometalate catalysts for water oxidation: Key mechanistic details*, J Catal. 350 (**2017**) 56–63.

[249] G. Paille, M. Gomez-Mingot, C. Roch-Marchal, B. Lassalle-Kaiser, P. Mialane, M. Fontecave, C. Mellot-Draznieks, A. Dolbecq, *A Fully Noble Metal-Free Photosystem Based on Cobalt-Polyoxometalates Immobilized in a Porphyrinic Metal-Organic Framework for Water Oxidation*, J Am Chem Soc. 140 (**2018**) 3613–3618.

[250] K. Fan, H. Chen, B. He, J. Yu, *Cobalt polyoxometalate on N-doped carbon layer to boost photoelectrochemical water oxidation of BiVO4*, Chemical Engineering Journal. 392 (**2020**) 123744.

[251] C. Ong, Z. Chen, T.-T. Lim, Z. Dong, *Immobilization of cobalt-based polyoxometalates on titanium dioxide nanorod for enhancement in photoelectrochemical water oxidation*, Mater Chem Phys. 301 (**2023**) 127690.

[252] N. Limani, I.S. Marques, B. Jarrais, A.J.S. Fernandes, C. Freire, D.M. Fernandes, *Cobalt Phosphotungstate-Based Composites as Bifunctional Electrocatalysts for Oxygen Reactions*, Catalysts. 12 (**2022**) 357.

[253] M. Blasco-Ahicart, J. Soriano-López, J.J. Carbó, J.M. Poblet, J.R. Galan-Mascaros, *Polyoxometalate electrocatalysts based on earth-abundant metals for efficient water oxidation in acidic media*, Nat Chem. 10 (**2018**) 24–30.

[254] L. Vigara, J.J. Carbó, J. Soriano-López, J.R. Galán-Mascarós, J.M. Poblet, S. Goberna-Ferrón, *Cobalt Polyoxometalates as Heterogeneous Water Oxidation Catalysts*, Inorg Chem. 52 (**2013**) 4753–4755.

[255] K. Azmani, M. Besora, J. Soriano-López, M. Landolsi, A.-L. Teillout, P. de Oliveira, I.-M. Mbomekallé, J.M. Poblet, J.-R. Galán-Mascarós, *Understanding polyoxometalates as water oxidation catalysts through iron* vs. *cobalt reactivity*, Chem Sci. 12 (**2021**) 8755–8766.

[256] J.T. Arens, M. Blasco-Ahicart, K. Azmani, J. Soriano-López, A. García-Eguizábal, J.M. Poblet, J.R. Galan-Mascaros, *Water oxidation electrocatalysis in acidic media with Co-containing polyoxometalates*, J Catal. 389 (**2020**) 345–351.

[257] A. Haider, B.S. Bassil, J. Soriano-López, H.M. Qasim, C. Sáenz De Pipaón, M. Ibrahim, D. Dutta, Y.S. Koo, J.J. Carbó, J.M. Poblet, J.R. Galán-Mascarós, U. Kortz, *9-Cobalt(II)-Containing 27-Tungsto-3-germanate(IV): Synthesis, Structure, Computational Modeling, and Heterogeneous Water Oxidation Catalysis*, Inorg Chem. 58 (**2019**) 11622–11629.

[258] P.P. Lopes, D.Y. Chung, X. Rui, H. Zheng, H. He, P.F.B.D. Martins, D. Strmcnik, V.R. Stamenkovic, P. Zapol, J.F. Mitchell, R.F. Klie, N.M. Markovic, *Dynamically stable active sites from surface evolution of perovskite materials during the oxygen evolution reaction*, J Am Chem Soc. 143 (**2021**) 2741–2750.

[259] F. Song, L. Bai, A. Moysiadou, S. Lee, C. Hu, L. Liardet, X. Hu, *Transition Metal Oxides as Electrocatalysts for the Oxygen Evolution Reaction in Alkaline Solutions: An Application-Inspired Renaissance*, J Am Chem Soc. 140 (**2018**) 7748–7759.

[260] Anawati, G.S. Frankel, A. Agarwal, N. Sridhar, *Degradation and deactivation of Sn catalyst used for CO2 reduction as function of overpotential*, Electrochim Acta. 133 (**2014**) 188–196.

[261] F. Zeng, C. Mebrahtu, L. Liao, A.K. Beine, R. Palkovits, *Stability and deactivation of OER electrocatalysts: A review*, Journal of Energy Chemistry. 69 (**2022**) 301–329.

[262] A. Slesinski, S. Sroka, K. Fic, E. Frackowiak, J. Menzel, *Operando Monitoring of Local pH Value Changes at the Carbon Electrode Surface in Neutral Sulfate-Based Aqueous Electrochemical Capacitors*, ACS Appl Mater Interfaces. 14 (**2022**) 37782.

[263] A.T. Kuhn, C.Y. Chan, *pH changes at near-electrode surfaces*, J Appl Electrochem. 13 (**1983**) 189–207.

[264] Y. Surendranath, M.W. Kanan, D.G. Nocera, *Mechanistic studies of the oxygen evolution reaction by a cobalt-phosphate catalyst at neutral pH*, J Am Chem Soc. 132 (**2010**) 16501–16509.

[265] M. Pourbaix, Atlas of Electrochemical Equilibria in Aqueous Solutions, 2nd ed., **1974**.

[266] V. Streibel, M. Hävecker, Y. Yi, J.J. Velasco Vélez, K. Skorupska, E. Stotz, A. Knop-Gericke, R. Schlögl, R. Arrigo, *In Situ Electrochemical Cells to Study the Oxygen Evolution Reaction by Near Ambient Pressure X-ray Photoelectron Spectroscopy*, Top Catal. 61 (**2018**) 2064–2084.

[267] D. Vantelon, N. Trcera, D. Roy, T. Moreno, D. Mailly, S. Guilet, E. Metchalkov, F. Delmotte, B. Lassalle, P. Lagarde, A.M. Flank, *The LUCIA beamline at SOLEIL*, Urn:Issn:1600-5775. 23 (**2016**) 635–640.

[268] D. Mendoza, S.T. Dong, N. Kostopoulos, V. Pinty, O. Rivada-Wheelaghan, E. Anxolabéhère-Mallart, M. Robert, B. Lassalle-Kaiser, *In situ X-ray Absorption Spectroscopy in Homogeneous Conditions Reveals Interactions Between CO2 and a Doubly and Triply Reduced Iron(III) Porphyrin, then Leading to Catalysis*, ChemCatChem. 15 (**2023**) e202201298.

[269] M.D. Hall, C.K. Underwood, T.W. Failes, G.J. Foran, T.W. Hambley, *Using XANES to monitor the oxidation state of cobalt complexes*, Aust J Chem. 60 (**2007**) 180–183.

[270] Q. Wu, M. Xiao, W. Wang, C. Cui, In Situ Coordination Environment Tuning of Cobalt Sites for Efficient Water Oxidation, **2019**.

[271] C. Singh, S. Mukhopadhyay, S.K. Das, *Polyoxometalate-Supported Bis(2,2'-bipyridine)mono(aqua)nickel(II) Coordination Complex: An Efficient Electrocatalyst for Water Oxidation*, Inorg Chem. 57 (**2018**) 6479–6490.

[272] K. Yu, B. Bin Zhou, Y. Yu, Z.H. Su, G.Y. Yang, *A new organic-inorganic hybrid layered molybdenum(V) cobalt phosphate constructed from [H24(Mo16O32)Co 16(PO4)24(OH)4(C5H 4N)2(H2O)6]4- wheels and 4,4'-bipyridine linkers*, Inorg Chem. 50 (**2011**) 1862–1867.

[273] F. De Groot, G. Vankó, P. Glatzel, *The 1s x-ray absorption pre-edge structures in transition metal oxides*, Journal of Physics Condensed Matter. 21 (**2009**).

[274] D. Cabaret, A. Bordage, A. Juhin, M. Arfaoui, E. Gaudry, *First-principles calculations of X-ray absorption spectra at theK-edgeof 3dtransition metals: an electronic structure analysis of the pre-edge*, Physical Chemistry Chemical Physics. 12 (**2010**) 5502.

[275] G. Kuppuraj, M. Dudev, C. Lim, *Factors governing metal-ligand distances and coordination geometries of metal complexes*, Journal of Physical Chemistry B. 113 (**2009**) 2952–2960.

[276] A. Proust, B. Matt, R. Villanneau, G. Guillemot, P. Gouzerh, G. Izzet, *Functionalization and post-functionalization: A step towards polyoxometalate-based materials*, Chem Soc Rev. 41 (**2012**) 7605–7622.

[277] C. Allain, D. Schaming, N. Karakostas, M. Erard, J.P. Gisselbrecht, S. Sorgues, I. Lampre, L. Ruhlmann, B. Hasenknopf, *Synthesis, electrochemical and photophysical properties of covalently linked porphyrin-polyoxometalates*, Dalton Transactions. 42 (**2013**) 2745–2754.

[278] J.J. Borrás-Almenar, J.M. Clemente-Juan, M. Clemente-León, E. Coronado, J.R. Galán-Mascarós, C.J. Gómez-García, *Molecular Materials from Polyoxometalates*, Polyoxometalate Chemistry From Topology via Self-Assembly to Applications. (**2001**) 231–253.

[279] H.C. Novais, D.M. Fernandes, C. Freire, *Hybrid methyl green/cobalt-polyoxotungstate nanostructured films: Self-assembly, electrochemical and electrocatalytic properties*, Appl Surf Sci. 347 (**2015**) 40–47.

[280] I.C.M.S. Santos, S.L.H. Rebelo, M.S.S. Balula, R.L. Martins, M.Q. Sim, M. Grac, P.M.S. Neves, *Association of Keggin-type anions with cationic meso -substituted porphyrins : synthesis , characterization and oxidative catalytic studies*, 231 (**2005**) 35–45.

[281] Y. Kim, S. Shanmugam, *Polyoxometalate-reduced graphene oxide hybrid catalyst: Synthesis, structure, and electrochemical properties*, ACS Appl Mater Interfaces. 5 (**2013**) 12197–12204.

[282] C. Cougnon, N.H. Nguyen, S. Dabos-Seignon, J. Mauzeroll, D. Bélanger, *Carbon surface derivatization by electrochemical reduction of a diazonium salt in situ produced from the nitro precursor*, Journal of Electroanalytical Chemistry. 661 (**2011**) 13–19.

[283] R.O.C. Norman, J.M. Coxon, Principles of organic synthesis, third edition, Chapman & Hall, **1993**.

[284] A.M. Hibberd, H.Q. Doan, E.N. Glass, F.M.F. De Groot, C.L. Hill, T. Cuk, *Co polyoxometalates and a Co3O4 thin film investigated by L-edge X-ray absorption spectroscopy*, Journal of Physical Chemistry C. 119 (**2015**) 4173–4179.

[285] S. Sato, R. Takahashi, T. Sodesawa, K.-I. Yuma, Y. Obata, *Distinction between Surface and Bulk Oxidation of Cu through N 2 O Decomposition*, J Catal. 196 (**2000**) 195–199.

[286] J.-M. Noël, F. Kanoufi, *Probing the reactive intermediate species generated during electrocatalysis by scanning electrochemical microscopy*, Curr Opin Electrochem. 35 (**2022**) 101071.

[287] J.-J. Gallet, M.G. Silly, M. El Kazzi, F. Bournel, F. Sirotti, F. Rochet, *Chemical and kinetic insights into the Thermal Decomposition of an Oxide Layer on Si(111) from Millisecond Photoelectron Spectroscopy*, Sci Rep. 7 (**2017**) 14257.

[288] A. Minguzzi, O. Lugaresi, C. Locatelli, S. Rondinini, F. D'Acapito, E. Achilli, P. Ghigna, *Fixed energy X-ray absorption voltammetry*, Anal Chem. 85 (**2013**) 7009–7013.

[289] V. Briois, C. La Fontaine, S. Belin, L. Barthe, T. Moreno, V. Pinty, A. Carcy, R. Girardot, E. Fonda, *ROCK: the new Quick-EXAFS beamline at SOLEIL*, J Phys Conf Ser. 712 (**2016**) 012149.

[290] M. Fracchia, P. Ghigna, A. Vertova, S. Rondinini, A. Minguzzi, *Time-Resolved X-ray Absorption Spectroscopy in (Photo)Electrochemistry*, Surfaces. 1 (**2018**) 138–150.

[291] A. Shavorskiy, G. D'acunto, V. Boix De La Cruz, M. Scardamaglia, S. Zhu, R.H. Temperton, J. Schnadt, J. Knudsen, *Gas Pulse−X-Ray Probe Ambient Pressure Photoelectron Spectroscopy with Submillisecond Time Resolution*, Cite This: ACS Appl. Mater. Interfaces. 13 (**2021**) 47641.

[292] J. Melke, A. Schoekel, D. Gerteisen, D. Dixon, F. Ettingshausen, C. Cremers, C. Roth, D.E. Ramaker, *Electrooxidation of Ethanol on Pt. An in Situ and Time-Resolved XANES Study*, The Journal of Physical Chemistry C. 116 (**2012**) 2838–2849.

[293] R.G. Finke, M.W. Droege, P.J. Domaille, *Trivacant heteropolytungstate derivatives. 3. Rational syntheses, characterization, two-dimensional tungsten-183 NMR, and properties of tungstometallophosphates P2W18M4(H2O)2O6810- and P4W30M4(H2O)2O11216- (M = cobalt, copper, zinc)*, Inorg Chem. 26 (**1987**) 3886–3896.

[294] J.R. Galán-Mascarós, C.J. Gómez-Garcia, J.J. Borrás-Almenar, E. Coronado, *High nuclearity magnetic clusters: Magnetic properties of a nine cobalt cluster encapsulated in a polyoxometalate,* $[Co_9(OH)_3(H_2O)_6\ (HPO_4)_2(PW_9O_{343}]^{16-}$, Advanced Materials. 6 (**1994**) 221–223.

[295] T.J.R. Weakley, *The identification and x-ray structure of the diphosphatotris(nonatungstophosphato)-nonacobaltate(II) heteropolyanion*, J Chem Soc Chem Commun. (**1984**) 1406–1407.

[296] B. Ravel, M. Newville, *ATHENA, ARTEMIS, HEPHAESTUS: data analysis for X-ray absorption spectroscopy using IFEFFIT*, Urn:Issn:0909-0495. 12 (**2005**) 537–541.

[297] I.C. Man, H.Y. Su, F. Calle-Vallejo, H.A. Hansen, J.I. Martínez, N.G. Inoglu, J. Kitchin, T.F. Jaramillo, J.K. Nørskov, J. Rossmeisl, *Universality in Oxygen Evolution Electrocatalysis on Oxide Surfaces*, ChemCatChem. 3 (**2011**) 1159–1165.

[298] H. Wang, K.H.L. Zhang, J.P. Hofmann, V.A. de la Peña O'Shea, F.E. Oropeza, *The electronic structure of transition metal oxides for oxygen evolution reaction*, J Mater Chem A Mater. 9 (**2021**) 19465–19488.

[299] C. Yuan, H. Bin Wu, Y. Xie, X.W. Lou, *Mixed Transition-Metal Oxides: Design, Synthesis, and Energy-Related Applications*, Angewandte Chemie International Edition. 53 (**2014**) 1488–1504.

[300] W.T. Hong, M. Risch, K.A. Stoerzinger, A. Grimaud, J. Suntivich, Y. Shao-Horn, *Toward the rational design of non-precious transition metal oxides for oxygen electrocatalysis*, Energy Environ Sci. 8 (**2015**) 1404–1427.

[301] G. Kéranguéven, I.S. Filimonenkov, E.R. Savinova, *Investigation of the stability of the boron-doped diamond support for Co3O4-based oxygen evolution reaction catalysts synthesized through in situ autocombustion method*, Journal of Electroanalytical Chemistry. 916 (**2022**) 116367.

[302] Z. Liu, Z. Xiao, G. Luo, R. Chen, C.L. Dong, X. Chen, J. Cen, H. Yang, Y. Wang, D. Su, Y. Li, S. Wang, *Defects-Induced In-Plane Heterophase in Cobalt Oxide Nanosheets for Oxygen Evolution Reaction*, Small. 15 (**2019**) 1904903.

[303] W. Xu, F. Lyu, Y. Bai, A. Gao, J. Feng, Z. Cai, Y. Yin, *Porous cobalt oxide nanoplates enriched with oxygen vacancies for oxygen evolution reaction*, Nano Energy. 43 (**2018**) 110–116.

[304] G.A. Gebreslase, M.V. Martínez-Huerta, M.J. Lázaro, *Recent progress on bimetallic NiCo and CoFe based electrocatalysts for alkaline oxygen evolution reaction: A review*, Journal of Energy Chemistry. 67 (**2022**) 101–137.

[305] J. Suntivich, K.J. May, H.A. Gasteiger, J.B. Goodenough, Y. Shao-Horn, *A perovskite oxide optimized for oxygen evolution catalysis from molecular orbital principles*, Science (1979). 334 (**2011**) 1383–1385.

[306] S. Saddeler, G. Bendt, S. Salamon, F.T. Haase, J. Landers, J. Timoshenko, C. Rettenmaier, H.S. Jeon, A. Bergmann, H. Wende, B. Roldan Cuenya, S. Schulz, *Influence of the cobalt content in cobalt iron oxides on the electrocatalytic OER activity*, J Mater Chem A Mater. 9 (**2021**) 25381–25390.

[307] F. Dionigi, Z. Zeng, I. Sinev, T. Merzdorf, S. Deshpande, M.B. Lopez, S. Kunze, I. Zegkinoglou, H. Sarodnik, D. Fan, A. Bergmann, J. Drnec, J.F. de Araujo, M. Gliech, D. Teschner, J. Zhu, W.-X. Li, J. Greeley, B.R. Cuenya, P. Strasser, *In-situ structure and catalytic mechanism of NiFe and CoFe layered double hydroxides during oxygen evolution*, Nat Commun. 11 (**2020**) 2522.

[308] S. Anantharaj, S. Kundu, S. Noda, *"The Fe Effect": A review unveiling the critical roles of Fe in enhancing OER activity of Ni and Co based catalysts*, Nano Energy. 80 (**2021**).

[309] M. Li, Y. Gu, Y. Chang, X. Gu, J. Tian, X. Wu, L. Feng, *Iron doped cobalt fluoride derived from CoFe layered double hydroxide for efficient oxygen evolution reaction*, Chemical Engineering Journal. 425 (**2021**).

[310] L. Trotochaud, S.L. Young, J.K. Ranney, S.W. Boettcher, *Nickel–Iron Oxyhydroxide Oxygen-Evolution Electrocatalysts: The Role of Intentional and Incidental Iron Incorporation*, J Am Chem Soc. 136 (**2014**) 6744–6753.

[311] D.Y. Chung, S. Park, P.P. Lopes, V.R. Stamenkovic, Y.-E. Sung, N.M. Markovic, D. Strmcnik, *Electrokinetic Analysis of Poorly Conductive Electrocatalytic Materials*, ACS Catal. 10 (**2020**) 4990–4996.

[312] M.B. Stevens, C.D.M. Trang, L.J. Enman, J. Deng, S.W. Boettcher, *Reactive Fe-Sites in Ni/Fe (Oxy)hydroxide Are Responsible for Exceptional Oxygen Electrocatalysis Activity*, J Am Chem Soc. 139 (**2017**) 11361–11364.

[313] M.S. Burke, M.G. Kast, L. Trotochaud, A.M. Smith, S.W. Boettcher, *Cobalt–Iron (Oxy)hydroxide Oxygen Evolution Electrocatalysts: The Role of Structure and Composition on Activity, Stability, and Mechanism*, J Am Chem Soc. 137 (**2015**) 3638–3648.

[314] S. Hung, Y. Hsu, C. Chang, C. Hsu, N. Suen, T. Chan, H.M. Chen, *Unraveling Geometrical Site Confinement in Highly Efficient Iron-Doped Electrocatalysts toward Oxygen Evolution Reaction*, Adv Energy Mater. 8 (**2018**).

[315] J. Deng, M.R. Nellist, M.B. Stevens, C. Dette, Y. Wang, S.W. Boettcher, *Morphology Dynamics of Single-Layered Ni(OH)* $_2$ */NiOOH Nanosheets and Subsequent Fe Incorporation Studied by* in Situ *Electrochemical Atomic Force Microscopy*, Nano Lett. 17 (**2017**) 6922–6926.

[316] D. Friebel, M.W. Louie, M. Bajdich, K.E. Sanwald, Y. Cai, A.M. Wise, M.-J. Cheng, D. Sokaras, T.-C. Weng, R. Alonso-Mori, R.C. Davis, J.R. Bargar, J.K. Nørskov, A. Nilsson, A.T. Bell, *Identification of Highly Active Fe Sites in (Ni,Fe)OOH for Electrocatalytic Water Splitting*, J Am Chem Soc. 137 (**2015**) 1305–1313.

[317] G. Młynarek, M. Paszkiewicz, A. Radniecka, *The effect of ferric ions on the behaviour of a nickelous hydroxide electrode*, J Appl Electrochem. 14 (**1984**) 145–149.

[318] M. Görlin, J. Ferreira de Araújo, H. Schmies, D. Bernsmeier, S. Dresp, M. Gliech, Z. Jusys, P. Chernev, R. Kraehnert, H. Dau, P. Strasser, *Tracking Catalyst Redox States and Reaction Dynamics in Ni–Fe Oxyhydroxide Oxygen Evolution Reaction Electrocatalysts: The Role of Catalyst Support and Electrolyte pH*, J Am Chem Soc. 139 (**2017**) 2070–2082.

[319] M. Görlin, P. Chernev, J. Ferreira de Araújo, T. Reier, S. Dresp, B. Paul, R. Krähnert, H. Dau, P. Strasser, *Oxygen Evolution Reaction Dynamics, Faradaic Charge Efficiency, and the Active Metal Redox States of Ni–Fe Oxide Water Splitting Electrocatalysts*, J Am Chem Soc. 138 (**2016**) 5603–5614.

[320] J. Hwang, R.R. Rao, L. Giordano, Y. Katayama, Y. Yu, Y. Shao-Horn, *Perovskites in catalysis and electrocatalysis*, Science (1979). 358 (**2017**) 751–756.

[321] A. Badreldin, A.E. Abusrafa, A. Abdel-Wahab, *Oxygen-deficient perovskites for oxygen evolution reaction in alkaline media: a review*, Emergent Mater. 3 (**2020**) 567–590.

[322] I.S. Filimonenkov, S.Y. Istomin, B. Rotonnelli, J.J. Gallet, F. Bournel, E. V. Antipov, E.R. Savinova, G.A. Tsirlina, *Interfacial recharging behavior of mixed Co, Mn-based perovskite oxides*, Electrochim Acta. 398 (**2021**) 139257.

[323] S. Anantharaj, K. Karthick, S. Kundu, *Evolution of layered double hydroxides (LDH) as high performance water oxidation electrocatalysts: A review with insights on structure, activity and mechanism*, Mater Today Energy. 6 (**2017**) 1–26.

[324] L. Lv, Z. Yang, K. Chen, C. Wang, Y. Xiong, *2D Layered Double Hydroxides for Oxygen Evolution Reaction: From Fundamental Design to Application*, Adv Energy Mater. 9 (**2019**).

[325] H. Xu, J. Yuan, G. He, H. Chen, *Current and future trends for spinel-type electrocatalysts in electrocatalytic oxygen evolution reaction*, Coord Chem Rev. 475 (**2023**).

[326] Z. Liu, G. Wang, X. Zhu, Y. Wang, Y. Zou, S. Zang, S. Wang, *Optimal Geometrical Configuration of Cobalt Cations in Spinel Oxides to Promote Oxygen Evolution Reaction*, Angewandte Chemie - International Edition. 59 (**2020**) 4736–4742.

[327] H.Y. Wang, Y.Y. Hsu, R. Chen, T.S. Chan, H.M. Chen, B. Liu, *Ni3+-induced formation of active NiOOH on the spinel Ni-Co oxide surface for efficient oxygen evolution reaction*, Adv Energy Mater. 5 (**2015**).

[328] J.O. Olowoyo, R.J. Kriek, *Recent Progress on Bimetallic-Based Spinels as Electrocatalysts for the Oxygen Evolution Reaction*, Small. 18 (**2022**).

[329] P. Shukla, A. Chernatynskiy, J.C. Nino, S.B. Sinnott, S.R. Phillpot, *Effect of inversion on thermoelastic and thermal transport properties of MgAl2O4 spinel by atomistic simulation*, J Mater Sci. 46 (**2011**) 55–62.

[330] K.E. Sickafus, J.M. Wills, N.W. Grimes, Structure of Spinel, n.d.

[331] Z. Szotek, W.M. Temmerman, D. Ködderitzsch, A. Svane, L. Petit, H. Winter, *Electronic structures of normal and inverse spinel ferrites from first principles*, Phys Rev B Condens Matter Mater Phys. 74 (**2006**).

[332] K. Zhang, R. Zou, *Advanced Transition Metal-Based OER Electrocatalysts: Current Status, Opportunities, and Challenges*, Small. 17 (**2021**).

[333] M. Kim, J. Park, H. Ju, J.Y. Kim, H.S. Cho, C.H. Kim, B.H. Kim, S.W. Lee, *Understanding synergistic metal-oxide interactions of: In situ exsolved metal nanoparticles on a pyrochlore oxide support for enhanced water splitting*, Energy Environ Sci. 14 (**2021**) 3053–3063.

[334] L. Calvillo, F. Carraro, O. Vozniuk, V. Celorrio, L. Nodari, A.E. Russell, D. Debellis, D. Fermin, F. Cavani, S. Agnoli, G. Granozzi, *Insights into the durability of Co-Fe spinel oxygen evolution electrocatalysts: Via operando studies of the catalyst structure*, J Mater Chem A Mater. 6 (**2018**) 7034–7041.

[335] Q. Zhao, Z. Yan, C. Chen, J. Chen, *Spinels: Controlled Preparation, Oxygen Reduction/Evolution Reaction Application, and beyond*, Chem Rev. 117 (**2017**) 10121–10211.

[336] S.S. Wang, G.Y. Yang, *Recent Advances in Polyoxometalate-Catalyzed Reactions*, Chem Rev. 115 (**2015**) 4893–4962.

[337] F. Reikowski, F. Maroun, I. Pacheco, T. Wiegmann, P. Allongue, J. Stettner, O.M. Magnussen, *Operando Surface X-ray Diffraction Studies of Structurally Defined Co3O4 and CoOOH Thin Films during Oxygen Evolution*, ACS Catal. 9 (**2019**) 3811–3821.

[338] C.M. Welch, R.G. Compton, *The use of nanoparticles in electroanalysis: A review*, Anal Bioanal Chem. 384 (**2006**) 601–619.

[339] S.C. Chou, K.C. Tso, Y.C. Hsieh, B.Y. Sun, J.F. Lee, P.W. Wu, *Facile synthesis of Co3O4@CoO@Co gradient core@shell nanoparticles and their applications for oxygen evolution and reduction in alkaline electrolytes*, Materials. 13 (**2020**) 1–14.

[340] L. Zhou, B. Deng, Z. Jiang, Z.J. Jiang, *Shell thickness controlled core-shell Fe3O4@CoO nanocrystals as efficient bifunctional catalysts for the oxygen reduction and evolution reactions*, Chemical Communications. 55 (**2019**) 525–528.

[341] X. Liu, B.P. Pichon, C. Ulhaq, C. Lefevre, J.-M. Greneche, D. Begin, S. Begin-Colin, A Systematic Study of Exchange Coupling in Core-Shell Fe3-#O4@CoO Nanoparticles, **2015**.

[342] Z. Zhuang, W. Sheng, Y. Yan, *Synthesis of monodispere Au@Co3O4 core-shell nanocrystals and their enhanced catalytic activity for oxygen evolution reaction*, Advanced Materials. 26 (**2014**) 3950–3955.

[343] A.L. Strickler, M. Escudero-Escribano, T.F. Jaramillo, *Core-Shell Au@Metal-Oxide Nanoparticle Electrocatalysts for Enhanced Oxygen Evolution*, Nano Lett. 17 (**2017**) 6040–6046.

[344] Y. Lv, S. Duan, Y. Zhu, P. Yin, R. Wang, *Enhanced OER performances of Au@NiCo2S4 core-shell heterostructure*, Nanomaterials. 10 (**2020**).

[345] L. Royer, J. Guehl, M. Zilbermann, T. Dintzer, C. Leuvrey, B.P. Pichon, E. Savinova, A. Bonnefont, *Influence of the catalyst layer thickness on the determination of the OER activity of Fe3O4@CoFe2O4 core-shell nanoparticles*, Electrochim Acta. 446 (**2023**) 141981.

[346] A. Accogli, L. Bertoli, G. Panzeri, E. Gibertini, R. Pesce, G. Bussetti, L. Magagnin, *Electrochemical Characterization of Magnetite (Fe3O4) Nanoaggregates in Acidic and Alkaline Solutions*, ACS Omega. 6 (**2021**) 26880–26887.

[347] T. Burnus, Z. Hu, H.H. Hsieh, V.L.J. Joly, P.A. Joy, M.W. Haverkort, H. Wu, A. Tanaka, H.J. Lin, C.T. Chen, L.H. Tjeng, *Local electronic structure and magnetic properties of La Mn0.5 Co0.5 O3 studied by x-ray absorption and magnetic circular dichroism spectroscopy*, Phys Rev B Condens Matter Mater Phys. 77 (**2008**) 1–8.

[348] B. Beverskog, I. Puigdomenech, *Revised pourbaix diagrams for iron at 25–300 °C*, Corros Sci. 38 (**1996**) 2121–2135.

[349] T. Wiegmann, I. Pacheco, F. Reikowski, J. Stettner, C. Qiu, M. Bouvier, M. Bertram, F. Faisal, O. Brummel, J. Libuda, J. Drnec, P. Allongue, F. Maroun, O.M. Magnussen, *Operando Identification of the Reversible Skin Layer on Co3O4as a Three-Dimensional Reaction Zone for Oxygen Evolution*, ACS Catal. 12 (**2022**) 3256–3268.

[350] J.T. Mefford, A.R. Akbashev, M. Kang, C.L. Bentley, W.E. Gent, H.D. Deng, D.H. Alsem, Y.S. Yu, N.J. Salmon, D.A. Shapiro, P.R. Unwin, W.C. Chueh, *Correlative operando microscopy of oxygen evolution electrocatalysts*, Nature (London). 593 (**2021**) 67–73.

[351] Y. Peng, H. Hajiyani, R. Pentcheva, *Influence of fe and ni doping on the oer performance at the co3o4(001) surface: Insights from DFT+u calculations*, ACS Catal. 11 (**2021**) 5601–5613.

[352] H. Hajiyani, R. Pentcheva, *Surface Termination and Composition Control of Activity of the CoxNi1- xFe2O4(001) Surface for Water Oxidation: Insights from DFT+ U Calculations*, ACS Catal. 8 (**2018**) 11773–11782.

[353] G.S. Henderson, F.M.F. De Groot, B.J.A. Moulton, *X-ray absorption near-edge structure (XANES) spectroscopy*, Rev Mineral Geochem. 78 (**2014**) 75–138.

[354] K. Sartori, A. Musat, F. Choueikani, J.M. Grenèche, S. Hettler, P. Bencok, S. Begin-Colin, P. Steadman, R. Arenal, B.P. Pichon, *A Detailed Investigation of the Onion Structure of Exchanged Coupled Magnetic Fe3-δO4@CoFe2O4@Fe3-δO4Nanoparticles*, ACS Appl Mater Interfaces. 13 (**2021**) 16784–16800.

[355] A. Cimino, D. Gazzoli, M. Valigi, *XPS quantitative analysis and models of supported oxide catalysts*, J Electron Spectros Relat Phenomena. 104 (**1999**) 1–29.

[356] J.J. Velasco-Velez, V. Pfeifer, M. Hävecker, R.S. Weatherup, R. Arrigo, C. Chuang, E. Stotz, G. Weinberg, M. Salmeron, R. Schlögl, A. Knop-Gericke, *Photoelectron Spectroscopy at the Graphene–Liquid Interface Reveals the Electronic Structure of an Electrodeposited Cobalt/Graphene Electrocatalyst*, Angewandte Chemie International Edition. 54 (**2015**) 14554–14558.

[357] M.C.O. Monteiro, M.T.M. Koper, *Measuring local pH in electrochemistry*, Curr Opin Electrochem. 25 (**2021**) 100649.

Résumé détaillé en Français

Introduction et objectifs

Le mix énergétique mondial est largement basé sur les énergies fossiles. Or, celles-ci sont responsables du réchauffement climatique, du fait de la libération de gaz à effets de serre qui se produit lors de leur combustion. Afin de diminuer ces émissions, l'utilisation de sources d'énergies alternatives est nécessaire. Les énergies renouvelables telles que l'énergie solaire ou éolienne présentent l'inconvénient de l'intermittence de leur production, dépendant grandement des conditions météorologiques. Afin de palier à ce problème majeur, le développement de méthodes de transformation et de stockage de l'électricité produite est nécessaire. Parmi celles-ci, l'hydrogène produit à partir de l'électrolyse de l'eau est un vecteur d'énergie prometteur.

L'électrolyse de l'eau réalisée dans des cellules électrochimiques appelées « électrolyseurs » produit de l'hydrogène qui peut ensuite être retransformé en énergie électrique dans des cellules électrochimiques appelées « piles à combustible ». Il existe plusieurs technologies d'électrolyseurs, les cellules alcalines liquides,[1] les cellules à haute températures, aussi appelées électrolyseurs à oxydes solides,[2] et les technologies d'électrolyseurs à assemblages de membrane−électrode.[3–6] Comme la majorité des systèmes électrochimiques, les électrolyseurs fonctionnent par l'intermédiaire de deux électrodes, *i.e.* une cathode où la réduction de l'eau en dihydrogène a lieu (il s'agit de la réaction d'évolution de l'hydrogène, HER) ; une anode, où se produit l'oxydation de l'eau en dioxygène (réaction d'évolution de l'oxygène, OER – cette réaction est nécessaire pour produire les électrons consommés par l'HER). Un séparateur, soit liquide, soit membranaire, permet de conduire les ions (e.g., H^+ en milieu acide, OH^- en milieu alcalin) entre les deux électrodes. L'amélioration des électrolyseurs nécessite l'amélioration des performances des matériaux utilisés aux deux électrodes pour catalyser l'HER et l'OER. Ceci demande bonne caractérisation des matériaux qui composent les électrodes dans les conditions opérationnelles, pour comprendre leur comportement et les modifications qu'ils peuvent subir durant la catalyse des réactions électrochimiques.

L'étude de ces catalyseurs est traditionnellement réalisée via la corrélation des données électrochimiques récoltées lors de l'électrolyse et la comparaison des caractéristiques physico-chimiques de l'échantillon avant et après la mesure (*post-mortem*). Néanmoins les méthodes, dites « *ex-situ* », ne fournissent pas d'informations sur les transformations chimiques et les états transitoires qui peuvent exister lors de l'application d'un potentiel à l'électrode. Aussi, des méthodes de caractérisation durant la réaction (*operando*) ou dans des conditions simulant l'environnement auquel est soumis le catalyseur durant la réaction (*in situ*) sont de plus en plus couramment utilisés pour comprendre les systèmes catalytiques d'intérêt pour l'électrolyse.[7,8]

Parmi les différentes techniques d'analyses existantes, la spectroscopie (de manière générale) et plus particulièrement les spectroscopies d'absorption des rayons X (XAS, X-Ray Absorption Spectroscopy) et de photoélectron X (XPS, X-Ray Photoelectron spectroscopy) se démarquent du fait de leur propriétés non-destructives, quantitatives, de leur sensibilité aux éléments constituant l'échantillon ainsi qu'à leur degré d'oxydation. Ces informations sont cruciales pour suivre l'évolution de l'activité catalytique des matériaux, avant, pendant et après l'électrocatalyse et sont essentielles pour comprendre les mécanismes réactionnels. [8,9]

Dans ce manuscrit **l'objectif principal** est de montrer comment les spectroscopies XAS et XPS peuvent être utilisées dans des conditions *operando* afin d'obtenir des informations essentielles concernant les transformations que l'interface catalyseur-électrolyte (*i.e.,* le siège de la réaction électrochimique) peut subir durant la réaction. Elles permettent de suivre les modifications physico-chimiques subit par l'interface catalytique en conditions *operando*, et l'influence de ces changements sur la réactivité, afin d'obtenir une meilleure compréhension des réactions électrochimiques, ici dans le cas de l'OER. Pour cela, nous abordons trois systèmes différents, de complexité croissante.

Le **premier chapitre** commence par une introduction générale sur l'oxydation de l'eau par voie électrochimique. Elle est suivie par une description des fondamentaux théoriques des spectroscopies XPS et XAS avant de souligner leurs apports dans le cadre de la compréhension de l'OER présentés dans la littérature.

Dans le **second chapitre** nous nous intéressons à l'interface électrode−électrolyte simple, en absence de réaction électrochimique. Nous y présentons la méthode « Dip

and Pull » (D&P), qui permet d'analyser via XPS une interface modèle quasi bi-dimensionnelle, et ainsi d'effectuer des études expérimentales inédites sur le comportement de l'interface électrochimique (et, plus spécifiquement, de la double couche électrochimique) lorsqu'un potentiel est appliqué.

Dans le **troisième chapitre**, nous nous orientons vers un système plus complexe : la réaction d'oxydation de l'eau est maintenant présente, mais sur un catalyseur moléculaire modèle, un complexe de cobalt stabilisé par des polyoxométallates. Dans cette partie la spectroscopie XAS est utilisée dans des conditions *operando* afin d'étudier l'activité, et la stabilité du catalyseur: soit en conditions d'oxydation électrochimique, soit en conditions d'oxydation chimique.

Enfin, dans le **quatrième chapitre**, le catalyseur moléculaire est remplacé par un catalyseur plus proche de la réalité industrielle de l'électrolyse de l'eau : des nanoparticules cœur-coquille (C@S) à base d'oxides de fer et de cobalt à structure spinelle ($CoFe_2O_4$ et Fe_3O_4). Ici, la spectroscopie XAS nous permet de mettre en évidence l'influence de la morphologie de la nanoparticule sur son activité pour l'OER, et de corréler cette influence avec des changements du degré d'oxydation du Co induit par la structure C@S.

Résultats et discussion

La méthode «Dip and Pull» pour l'étude de la double couche électrochimique.

La double couche électrochimique désigne le phénomène de réorganisation des ions à l'interface électrode-électrolyte qui apparait lors de sa polarisation. Cette réorganisation résulte des interactions électrostatiques entre la charge électrique du métal composant l'électrode et des ions en solution, ce qui modifie localement leur concentration.[10]

Malgré les modèles analytiques,[11–15] les mesures expérimentales [16–18] et les modélisations via la dynamique moléculaire,[19–21] tentant de rendre compte de la structure de la double couche électrochimique, celle-ci est encore mal comprise,[22,23] et nécessite le développement de nouvelles méthodes *operando* afin de permettre un suivi expérimental de la réorganisation ionique à l'interface lorsque le potentiel est appliqué.

Dans cette optique, l'XPS, qui est une technique de spectroscopie quantitative, sensible à la surface et aux modifications locales induite par le potentiel électrique, est particulièrement adaptée. Plus spécifiquement, le montage «Dip and Pull» (D&P) représenté **Figure R.1.A**, permet d'étudier une interface modèle bi-dimensionnelle. La cellule spectro-électrochimique en question est un montage à trois électrodes dans lequel l'électrode de travail est successivement plongée puis retirée du bécher d'électrolyte directement au sein de la chambre d'analyse, laquelle est maintenue à une pression de l'ordre de 10 – 30 mbar. Cette immersion permet la formation d'un film électrolyte mince, aussi appelé ménisque, à la surface de l'électrode qui est ensuite analysé par XPS. Si le film d'électrolyte est suffisamment fin (< 30 nm) il permet l'analyse de l'électrolyte, de l'électrode et, ainsi, de l'interface, simultanément.

La position des pics de photoemission (*i.e.* énergie cinétique des photoélectrons) dépend de l'énergie du photon X ($h\nu$), de l'énergie de liaison de l'électron (BE) généralement référé par rapport au niveau de Fermi, et du potentiel électrique local (ϕ) suivant l'équation $\boldsymbol{h\nu = BE + KE + \phi}$. De ce fait, puisque la polarisation de l'interface électrode-électrolyte, et la formation de la double couche, modifie le potentiel électrique local, elle modifie également la position des pics XPS des éléments par

rapport à l'électrode de travail (cette dernière étant mise à la masse). Du fait du gradient de potentiel à travers de double couche électrochimique la position des pics dépends de leur distance par rapport à la surface de l'électrode. Le spectre XPS observé étant la somme des contributions des différentes couches d'électrolyte, il apparait alors *décalé* et *élargi* par rapport au spectre XPS obtenu en absence de gradient du potentiel entre l'électrode et l'électrolyte, qui se trouve à un potentiel de zéro charge (**figures R.1.B** et **C**). Il est donc théoriquement possible de déconvoluer le spectre XPS des ions en solution afin d'obtenir une estimation des modifications locales des concentrations de ces ions dans la double couche électrochimique en fonction de la polarisation de l'interface.

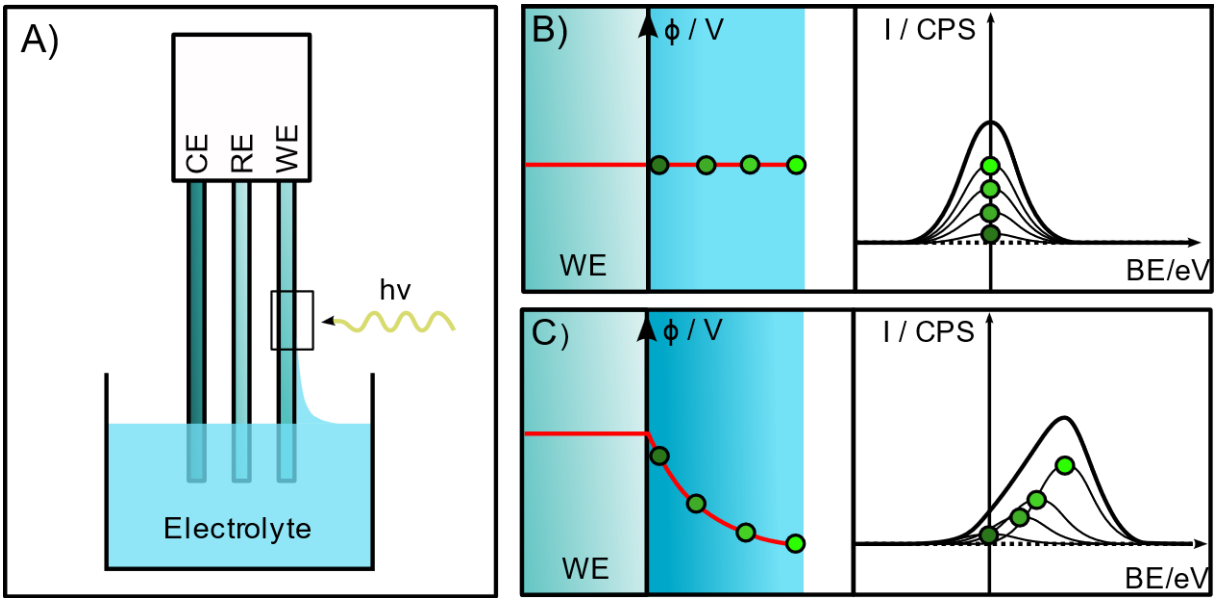

Figure R.1 : **A**) Montage « Dip and Pull » constitué d'un bécher d'électrolyte liquide dans lequel sont plongés trois électrodes : l'électrode de travail (WE), l'électrode de référence (RE) et la contre électrode (CE). L'électrode de travail est successivement plongée (Dip) puis retirée (Pull) de l'électrolyte afin de permettre l'analyse par spectroscopie photoélectronique X (XPS) de l'interface électrode-électrolyte au travers du film liquide résiduel à la surface de l'électrode. **B**) et **C**) illustrent les modifications du pic XPS d'un élément issu de l'électrolyte lorsque l'électrode est à un potentiel de zéro charge (**B**) ou pas (**C**).

Le suivi du décalage et de l'élargissement du pic XPS en fonction du potentiel appliqué à l'électrode de travail a été réalisé dans d'autres études [24,25] afin de déterminer le potentiel de zéro charge (PZC), correspondant à l'absence de gradient du potentiel à travers de double couche électrochimique lorsque l'élargissement du pic XPS est le plus faible. Néanmoins ces études ne fournissent pas d'informations supplémentaires

quant à la distribution exacte des ions dans la double couche. L'objectif du ***chapitre* 2** est donc l'obtention de la distribution des cations d'un électrolyte alcalin dans la double couche électrochimique via le suivi du spectre XPS en fonction du potentiel appliqué à l'électrode.

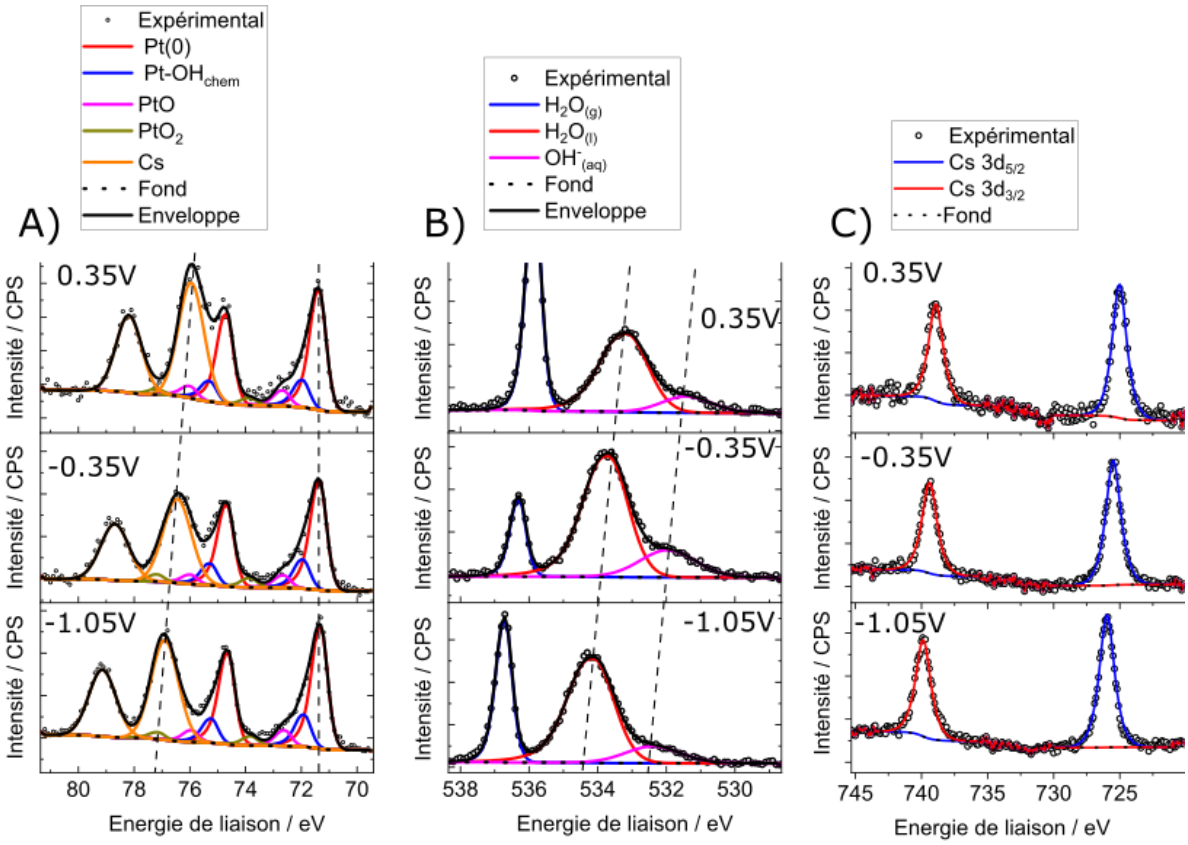

Figure R.2 : Spectres XPS de l'interface électrode–électrolyte (Pt / CsOH 1M) réalisés à 0,35 V, –0,35 V et –1,05 V *vs.* Ag/AgCl des régions **A**) Pt 4f / Cs 4d, **B**) O 1s et **C**) Cs 3d.

La spectroscopie XPS dans un montage D&P a été réalisé sur la ligne HIPPIE du synchrotron Max IV en Suède. Deux feuilles de platine ont été utilisées pour l'électrode de travail et la contre électrode. L'électrode de référence était une électrode Ag/AgCl, et l'électrolyte utilisé était une solution de CsOH 1M. Le choix de la concentration et du sel de l'électrolyte a été effectué afin de maximiser le signal XPS des cations lors de l'analyse, ainsi que pour se rapprocher des conditions opératoires communément observées lors de l'électrolyse de l'eau en milieu alcalin.

Les spectres XPS de l'interface électrode−électrolyte des régions Pt4f, Cs3d et O1s à −1,05 V, −0,35 V et +0,35 V *vs*. Ag/AgCl obtenus via ce montage sont présentés en **figure R.2**. La présence des pics associés aux platine (électrode) et aux espèces

$Cs^{+}_{(aq)}$, $OH^{-}_{(aq)}$, $H_2O_{(l)}$ (l'électrolyte) indiquent que l'analyse XPS considère bien l'interface électrode−électrolyte. Les pics associés à l'électrolyte se déplacent en fonction du potentiel (comme illustré **Figure R.1**) tandis que les pics associés à l'électrode restent à la même position, démontrant la bonne polarisation de l'interface. Nous avons utilisé le ratio entre les pics XPS Pt4f et Cs4d pour suivre en temps réel l'épaisseur du film mince d'électrolyte dans la région d'analyse, estimée à ~13 nm et s'assurer de sa stabilité.

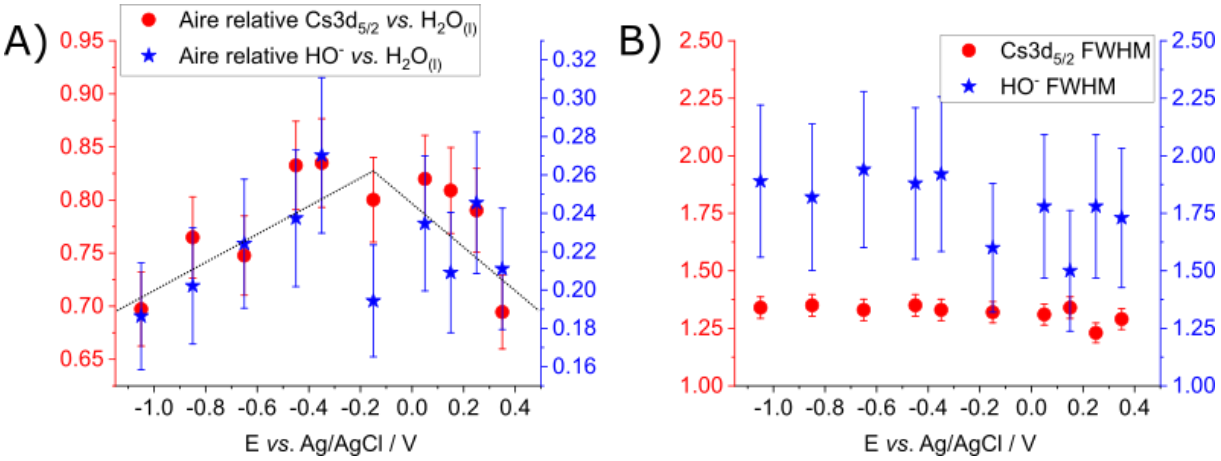

Figure R.3: A) Aires relatives des pics $Cs3d_{5/2}$ et O1s associé à OH^{-} comparés à celle du pics O1s associé à $H_2O_{(l)}$ à différents potentiels. **B)** Largeur à mi-hauteur (FWHM) des pics $Cs3d_{5/2}$ et O1s associé à OH^{-} en fonction du potentiel. Les incertitudes ont été estimées en prenant des positions extrêmes de modélisations des pics et du fond du spectre XPS.

Les différents spectres XPS de ces régions ont été analysés entre −1,05 V et +0,35 V *vs.* Ag/AgCl, après la vérification de la bonne polarisation de l'interface (décalage des pics XPS de l'électrolyte avec le potentiel) et de la bonne épaisseur d'électrolyte (ratio d'intensité des pics électrode-électrolyte). Les ratios des aires des composantes XPS des ions ($Cs3d_{5/2}$ et O1s associé à $OH^{-}_{(aq)}$) ont été suivis par rapport à la composante XPS du solvant ($H_2O_{(aq)}$) (voir **figure R.3.A**). Ces ratios sont donc directement proportionnels à la concentration de sel dans l'électrolyte au niveau de la région analysée. On observe ainsi une variation non-monotonique de la concentration, passant par un maximum aux alentours de −0,2 V. Cette variation peut s'expliquer majoritairement par les changements d'hydrophobicité de la surface lors de la variation du potentiel qui ont un impact direct sur le dynamisme de formation du film d'électrolyte et sa structure. Enfin l'élargissement des pics XPS associés au Cs3d et $HO^{-}_{(aq)}$ en fonction du potentiel est représenté **figure R.3.B**. Les changements mesurés ne sont pas significatifs, tandis que la théorie voudrait qu'on observe une évolution non-

monotonique, où le minimum de l'élargissement du pic correspondrait au PZC de l'interface.

Cette absence de variation, malgré la large gamme de potentiels balayée (ΔE = 1,4 V) s'explique par la concentration de l'électrolyte dans le ménisque. Celle-ci est déjà élevée dans la solution originelle (1M) et, dû à la faible pression dans la chambre d'analyse (15 mbar), s'est retrouvée concentrée encore d'avantage dans le ménisque dû aux effets d'évaporation. En effet l'analyse quantitative des composantes $HO^-_{(aq)}$ et $H_2O_{(aq)}$ du pics O1s montrent une concentration d'environ **10 M** dans la région d'analyse, soit 10 fois plus élevée que la concentration théorique attendue. Cette valeur correspond à la concentration thermodynamiquement associée à la pression de vapeur d'eau atteinte dans la chambre.[26]. Cette forte concentration a un effet négatif sur la possibilité d'observer des changements via XPS, puisque l'épaisseur de la double couche électrochimique est inversement proportionnelle à la concentration de l'électrolyte, et que plus l'épaisseur de la double couche est faible, plus l'élargissement des pics XPS associé à la réorganisation locale des ions sera faible. Ce phénomène a grandement limité notre capacité à analyser la réorganisation de la double couche électrochimique via XPS.

Néanmoins les concentrations élevées observées dans cette étude ne sont pas les seules limites qui peuvent être rencontrées dans l'utilisation du D&P. D'autres phénomènes tels que l'instabilité du ménisque ou son inhomogénéité peuvent impacter la qualité des mesures. Une méthode expérimentale et une analyse minutieuse des données est donc nécessaire pour éviter toute mauvaise interprétation des résultats.

Enfin il convient de souligner que, dans l'objectif d'étudier la double couche électrochimique via XPS, l'intensité du signal reste la principale limite. Certains paramètres tels que le choix du cation et de l'énergie des photons permettent d'augmenter respectivement l'intensité du signal (section efficace) et la sensibilité aux couches profonde du ménisque (et donc à l'interface). Cependant l'intensité globale du signal demeure trop faible dans les conditions de travail actuelles pour pouvoir étudier des systèmes où la concentration en ion est suffisamment diluée et l'épaisseur de la double couche suffisamment grande. Ceci empêche de fait l'analyse de la double couche même dans des conditions d'acquisitions idéales.

Etude *operando* de l'instabilité de complexes de cobalt substitués par des polyoxométallates

En nous éloignant de l'interface électrode−électrolyte d'un système modèle quasi bi-dimensionnel en absence d'une réaction électrocatalytique tel qu'étudié dans le second chapitre, nous introduisons dans le troisième chapitre un système plus complexe : un catalyseur moléculaire pour l'oxydation de l'eau, plus spécifiquement, un complexe de cobalt (II) stabilisé par des polyoxométallates (Co-POM).

Les complexes métalliques stabilisés par des polyoxométallates (M-POM) sont des espèces utilisées dans les différents domaines de la catalyse,[27–29] principalement grâce à leurs capacités d'oxydo-réduction.[30,31] Les espèces Co-POM, en particulier, catalysent la réaction d'oxydation de l'eau et présentent l'avantage d'être, dans le cadre de cette thèse, des espèces moléculaires modèles.[32,33] En effet, contrairement aux oxides métalliques classiquement utilisés pour l'OER, l'environnement chimique des sites catalytiques de ces complexes est bien défini et peut être utilisé pour l'étude fondamentale de cette réaction.[34–36]

Dans le **chapitre 3** nous nous intéressons aux Co_4-POM ($[Co_4(H_2O)_2(A\text{-}PW_9O_{34})_2]^{10-}$) et Co_9-POM ($[Co_9(H_2O)_6(OH)_3(HPO_4)_2(A\text{-}PW_9O_{34})_3]^{16-}$) et étudions leurs propriétés catalytiques pour l'oxydation de l'eau à l'aide des spectroscopies XAS et XPS dans des conditions *operando*.

Dans un premier temps le comportement électrochimique du Co_9-POM est étudié par voltampérométrie cyclique, dont les résultats sont reportés sur la **figure R.4**. On observe qu'entre 0,700 V et 1,650 V *vs.* l'électrode réversible à hydrogène (RHE, sauf mention du contraire, tous les potentiels de cette section seront *vs.* RHE), la voltampérométrie cyclique du système reste stable d'un cycle à l'autre, tandis que l'intensité dans le domaine anodique est plus grande pour le système avec catalyseur (traits plein) que le système sans catalyseur (en pointillé). Cette augmentation d'intensité peut être attribué à l'oxydation de l'eau et pourrait laisser penser que le Co_9-POM est stable et actif pour l'OER jusqu'à 1,650 V. En revanche, comme observé sur la **figure R.4.B**, une légère augmentation du potentiel maximal anodique jusqu'à 1,675 V a pour effet de changer drastiquement le profil de la voltampérométrie cyclique avec l'augmentation, cycle après cycle, du courant anodique mesuré à 1,650 V et l'apparition d'un pic cathodique, pouvant être associé à la transition Co(IV)/Co(III). Ces

deux observations peuvent être expliquées par la formation d'une couche de dégradation, constituée d'oxydes de cobalt et déposée à la surface d'une électrode de travail, déjà observée dans la littérature avec des sels de $Co(II)_{(aq)}$.[37] L'étude XPS et XAS *post-mortem* de la surface de l'électrode de travail après électrolyse a été réalisée et a effectivement montré la présence d'oxyde de cobalt aux degrés d'oxydations +II, et +III, tout en révélant une très faible teneur en tungstène (*i.e.,* des ratios différents de ceux observés dans le complexe moléculaire), ce qui confirme la dégradation du complexe et la formation d'une couche CoO_x à la surface de l'électrode de travail dans des conditions de l'OER.

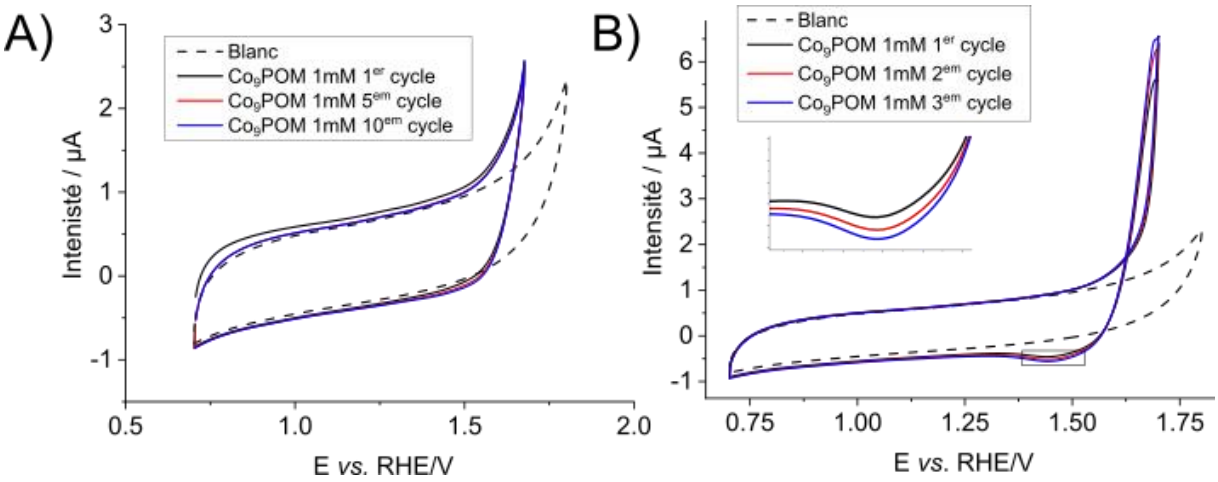

Figure R.4 : Voltampérométrie cyclique du Co_9-POM 1 mM dans un tampon phosphate de sodium à 0,72 M et pH 6. L'électrode de travail est constituée de carbone vitreux, la contre électrode est un fil de platine, et l'électrode de référence est une électrode de sulfate mercureux ($Hg|Hg_2SO_4$). La vitesse de balayage est de 20 mV/s. **A)** Avec une fenêtre de balayage entre 0,700 V et 1,650 V, et **B)** entre 0,700 V et 1,675 V *vs.* RHE.

Par la suite, afin d'explorer la présence d'un intermédiaire réactionnel ou la possible dégradation du catalyseur dans la gamme de potentiel de l'oxydation de l'eau par voie électrochimique, nous avons réalisé une série d'expériences XAS au niveau du seuil K du cobalt en conditions *operando*. Cette série d'expérience a été réalisée sur la ligne LUCIA du synchrotron Soleil en utilisant la cellule spectro-électrochimique liquide représentée sur la **figure R.5.A**.

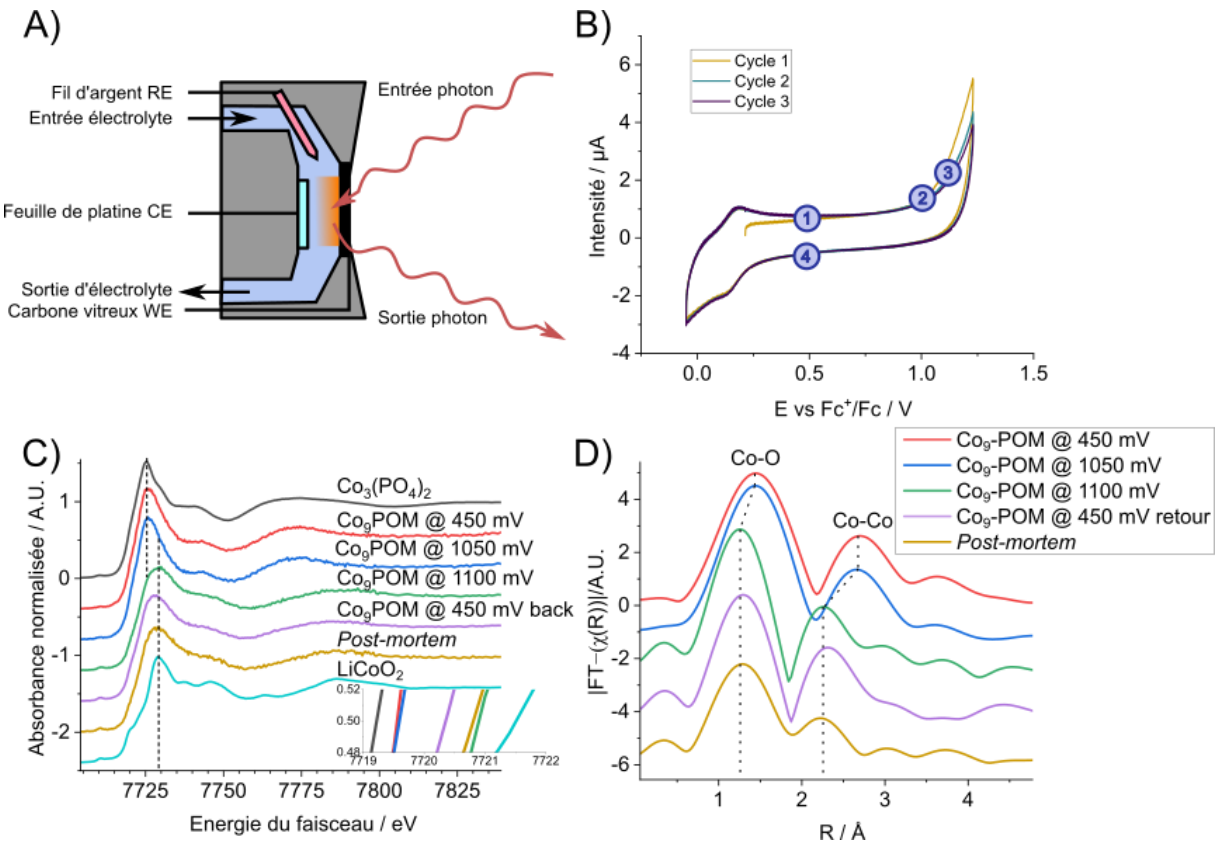

Figure R.5 : **A)** Représentation de la cellule spectro-électrochimique pour la XAS operando utilisée pour cette étude. L'électrolyte circule en flux continu via une pompe péristaltique en circuit fermé. Le corps de la cellule est en polypropylène et l'analyse s'effectue au travers de l'électrode de travail (carbone vitreux de 60 µm d'épaisseur). La contre électrode est une feuille de platine, et l'électrode de référence est un fil d'argent (*i.e.,* référence flottante). **B)** Voltampérométrie cyclique du système avant l'étude spectroscopique *operando*. Co_9-POM 1 mM dans un tampon de phosphate de sodium à 0,72 M, et à vitesse de balayage 20 mV/s. **C)** Spectres du Co au niveau du seuil K et **D)** FT-EXAFS des références $Co_3(PO_4)_2$ ($Co(II)_{Oh}$), $LiCoO_2$ ($Co(III)_{Oh}$), et du système Co_9-POM 1mM à différent potentiels. Les potentiels indiqués sont corrigés par rapport au couple Fc^+/Fc (~1,5 V *vs.* RHE).

Nous abordons dans un premier temps les résultats obtenus dans des conditions opératoires similaire aux expériences préliminaires présentées sur la **figure R.4,** avec 1 mM de Co_9-POM en solution. Les **figure R.5.C** et **D** montrent le spectre d'absorption du Co au niveau du seuil K et la transformée de Fourier de la partie EXAFS (Extended X-Ray Absorption Fine Structure) du signal respectivement. On y observe que du potentiel à circuit ouvert jusqu'à la limite de l'OER (de +0,450 à +1,05 V *vs*. Fc^+/Fc) le spectre du Co_9-POM en solution ne varie pas et correspond à celui de la référence Co(II) en environnement octaédrique. En revanche, l'application d'un potentiel

anodique au-dessus de +1,100 V *vs.* Fc^+/Fc montre une oxydation irréversible, avec le déplacement vers les hautes énergies du demi-saut, et un profil XANES qui s'approche du $LiCoO_2$ (cobalt (III) en environnement octaédrique). L'étude de la surface de l'électrode de travail en absence de Co_9-POM en solution (signal *post-mortem*) montre encore la présence de cobalt, prouvant la formation de la couche de dégradation CoO_x, sans que la présence d'un intermédiaire réactionnel du Co-POM ait été détectée. L'origine de cette dégradation pourrait être (i) chimique (avec le changement de pH local) ou (ii) due à une instabilité dans le cycle d'oxydoréduction (avec le changement de degré d'oxydation du cobalt de +II à +III).

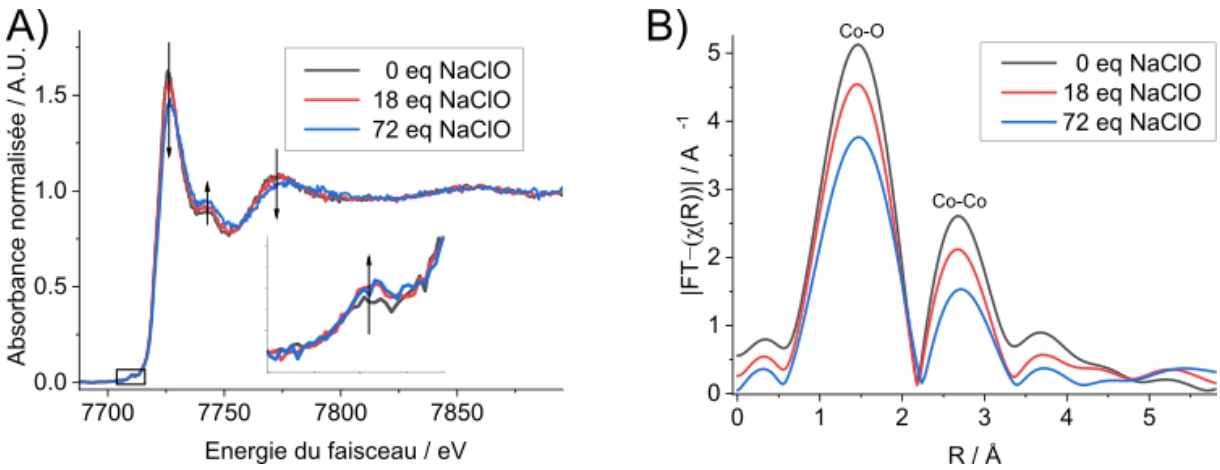

Figure R.6 : **A)** spectre d'absorption X du Co au niveau du seuil K et **B)** FT-EXAFS du Co_9-POM en solution à 1mM dans un tampon phosphate à 0,72 M pH 7, après l'ajout de 0; 18 et 72 mM de l'oxydant chimique NaClO, correspondant à 0; 2 et 8 équivalents d'oxydants par atome de cobalt.

Pour distinguer ces deux possibilités, dans un second temps, nous avons étudié le Co_9-POM en tant que catalyseur pour l'oxydation de l'eau par voie chimique par la mesure des spectres d'absorption X et des FT-EXAFS associés. Ici, l'objectif est de réaliser l'oxydation de l'eau dans le volume de la phase liquide (plutôt qu'à l'interface électrode-électrolyte) afin de limiter les modifications du pH local à l'interface de l'électrode/électrolyte qui pourraient être à l'origine de la dégradation du Co-POM. La solution de Co_9-POM est donc exposée à des quantités croissantes d'oxydant chimique (NaClO) afin d'étudier les possibles changements d'oxydation ou changements d'environnement chimique du cobalt par XAS. Une partie des résultats est présentée sur la **figure R.6**. Nous observons une absence de changement du degré d'oxydation du cobalt (absence de déplacement du demi-saut), et une

modification de l'environnement chimique de pair avec l'augmentation de la quantité d'oxydant ajouté en solution (mise en avant par une diminution des oscillations de l'EXAFS, tel que présenté sur la **figure R.6.A**, et la diminution de l'intensité des pics après la transformation de Fourier, voir **figure R.6.B**). Ces observations indiquent des changements irréversibles dans l'environnement chimique des atomes de Co suite à son oxydation qui interviennent dès les premiers ajouts d'oxydants, correspondant ici à 2 équivalents d'oxydants par atome de cobalt.

Dans ce chapitre nous démontrons finalement que le Co_9-POM ne peut pas être considéré comme un catalyseur modèle de la réaction d'oxydation de l'eau dû à sa rapide dégradation dans des conditions d'oxydation de l'eau par voie chimique ou électrochimique. Cette dégradation est provoquée à la fois par la modification du degré d'oxydation des atomes de cobalt lors du cycle d'oxydoréduction (lors de l'oxydation de l'eau par voie chimique ou électrochimique) et par les changements du pH local à l'interface électrode/électrolyte (lors de l'oxydation de l'eau par voie électrochimique). Cette conclusion a pu être réalisée grâce au suivi de l'environnement chimique du cobalt par absorption de rayon X dans différentes conditions d'oxydation.

Etude *operando* et *in-situ* de l'influence de l'épaisseur de la coquille de nanoparticules cœurs−coquilles sur l'activité de l'oxydation de l'eau par voie électrochimique

Dans le **chapitre 3**, nous concluons que le catalyseur réel de l'oxydation de l'eau par voie électrochimique était sans doute un produit de dégradation du CoPOM tel que l'oxyde de cobalt CoO_x, montrant ainsi que les oxydes de métaux de transitions sont de bons candidats pour cette réaction. Dans le **chapitre 4** nous proposons l'étude de l'OER par des catalyseurs hétérogènes à base d'oxydes de Co. Afin de faciliter l'analyse, nous nous focalisons sur des nanoparticules modèles, quasi mono-disperses et sphériques. Eu égard à sa nature prometteuse, un design « cœur-coquille » (C@S) a été utilisé, avec une coquille de $CoFe_2O_4$ et un cœur de Fe_3O_4.

Il a déjà été reporté dans la littérature que la combinaison de fer avec d'autres métaux de transitions tels que le cobalt ou le nickel pouvait avoir un effet bénéfique sur l'activité des catalyseurs pour l'OER (*vs.* l'équivalent sans fer), bien que l'origine de cette augmentation d'activité ne soit pas encore parfaitement comprise.[38] De plus la différence de composition entre le cœur et la coquille dans une nanoparticule C@S peut également avoir un effet synergique sur l'activité du système.[39–42] Nous nous proposons donc d'explorer ces différentes contributions en analysant plusieurs nanoparticules C@S avec des épaisseurs de coquilles différentes (d'environ 0,1 nm, 0,65 nm et 2 nm), comparées avec des nanoparticules sphériques de Fe_3O_4 et $CoFe_2O_4$ de même dimension (9 nm à 12 nm), en utilisant la spectroscopie d'absorption de rayons X.

Nous abordons le début de cette étude avec la comparaison de l'activité électrochimique de ces différents systèmes, représentée sur la **figure R.7**. Les matériaux Fe_3O_4 et $CoFe_2O_4$ ne sont pas, ou peu actifs pour l'OER (> 1,6 V *vs.* RHE), tandis que les nanoparticules C@S sont toutes actives pour l'OER. De plus, l'épaisseur de la coquille a un impact sur l'activité du matériau, avec une activité maximale pour une épaisseur de coquille de l'environ 0,65 nm. La morphologie C@S étant essentielle à l'activité du catalyseur pour l'OER, cela implique l'existence d'une synergie entre les matériaux de cœur et de coquille. Nous avons réalisé une première série d'expériences afin de comprendre l'origine de cette synergie.

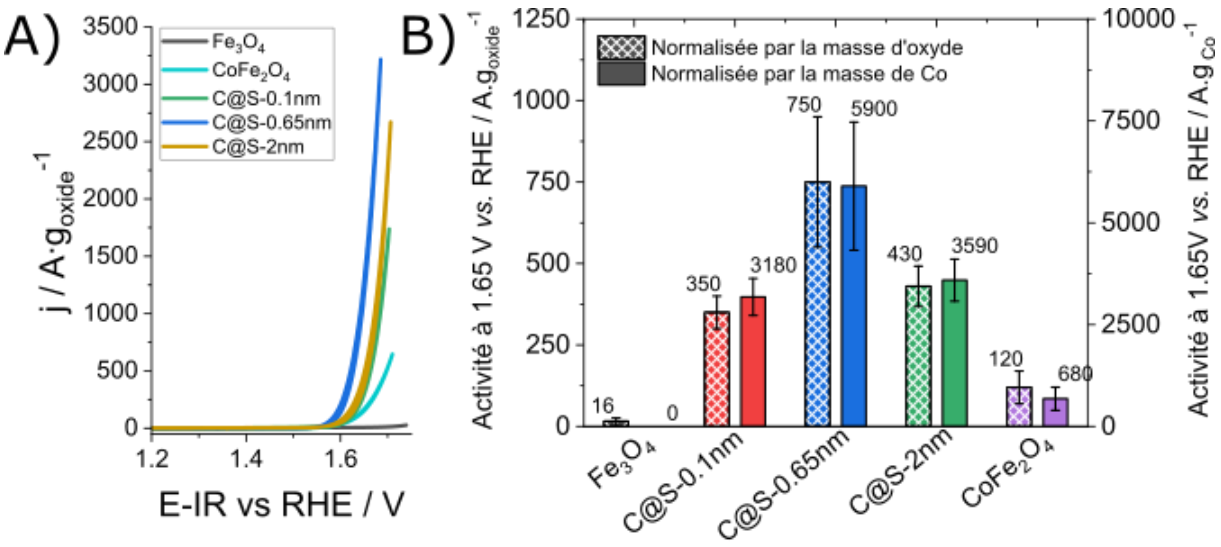

Figure R.7: **A)** Voltampérométrie cyclique (vitesse de balayage 10 mV/s dans NaOH 0.1 M) et **B)** activité à 1,65 V *vs.* RHE des nanoparticules Fe_3O_4, $CoFe_2O_4$, et des catalyseurs C@S avec des épaisseurs de coquilles de 0,1 nm, 0,65 nm et 2 nm.

Dans ce but, les spectres XAS du Co et du Fe au niveau de leur seuil L_3 ont été mesurés pour les nanoparticules C@S-0,65nm de 1,0 V à 1,6 V *vs.* RHE en conditions *operando* dans une cellule spectro-électrochimique à trois électrodes avec un électrolyte liquide à ISISS au synchrotron HZB en Allemagne. Les résultats, montrés sur la **figure R.8**, mettent en avant une absence d'oxydation du cobalt, tandis qu'une oxydation du fer est observée à partir de 1,4 V *vs.* RHE. L'absence sur les spectres XAS d'une oxydation du cobalt est assez surprenante puisque celle-ci est observée à partir de 1,1 V sur la voltampérométrie cyclique (**Figure R.8.C**, transition Co(II)→Co(III)). De même, l'oxydation Fe(II)→Fe(III) observée sur les spectres XAS est inattendue au vu de la composition de la coquille (la coquille de $CoFe_2O_4$ contenant du Fe(III) mais pas de Fe(II)). Ce changement d'oxydation du fer implique donc une oxydation du fer qui compose le cœur de la nanoparticule. Cette oxydation peut s'expliquer par l'oxydation successive du Co(II) à l'interface électrode−électrolyte en Co(III), puis d'un transfert d'électron entre le Co(III) nouvellement formé et le Fe(II) du cœur, conduisant à la stabilisation du Co(II) malgré les conditions oxydantes. Ceci pourrait être à l'origine de l'augmentation d'activité des systèmes C@S par rapport aux nanoparticules homogènes de $CoFe_2O_4$.

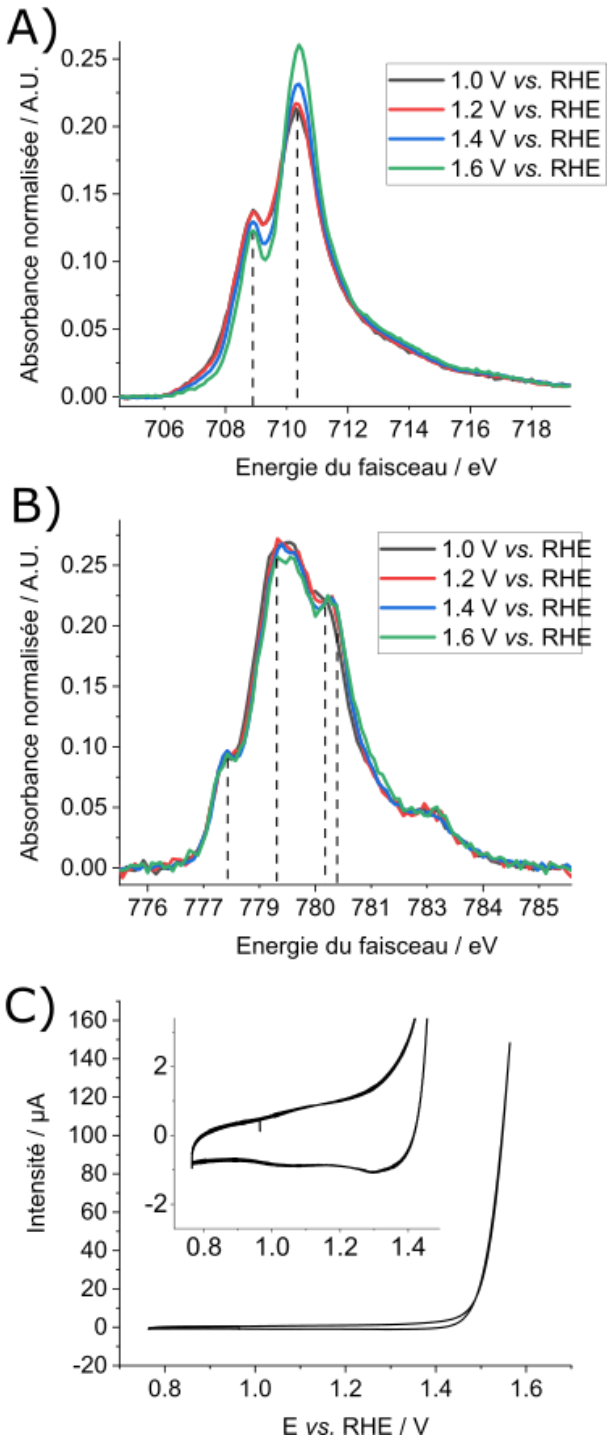

***Figure R.8** : **A)** spectres d'absorption X du Fe et **B)** Co au seuil L_3 des nanoparticules C@S-0,65nm mesurés dans l'intervalle de potentiel de 1,0 V à 1,6 V vs . RHE. **C)** Voltampérométrie cyclique du système spectro-électrochimique. Vitesse de balayage 20 mV/s. Les nanoparticules de C@S-0,65nm sont déposées sur une membrane échangeuse d'anion Fumatech et sont intégrées dans une cellule à trois électrodes avec NaOH 0,1M comme l'électrolyte liquide. Une bicouche de graphène fait office de collecteur de courant et sépare l'électrolyte liquide de la chambre d'analyse à vide.*

Afin d'étudier cette synergie plus en détails, nous nous sommes intéressés à l'influence de l'épaisseur de la coquille par XAS. Ces mesures ont été effectuées en conditions *in-situ*, afin de figer le système à un degré d'oxydation donné (*i.e.,* sans la réduction du catalyseur due à l'oxydation conjuguée de l'eau durant le cycle catalytique). Dans cette expérience, les nanoparticules $CoFe_2O_4$, Fe_3O_4, C@S-0,1nm et C@S-2nm ont été déposées sur une surface de silicium et exposées à un gaz oxydant (N_2O), les spectres XAS au seuil L_3 ont été mesurés et comparés. Les résultats correspondants sont montrés sur la **figure R.9**.

Nous observons que, contrairement à l'expérience *operando* dont les résultats sont montrés sur la **figure R.8**, en conditions *in-situ* (**figure R.9**) le Fe ne s'oxyde que très peu après exposition des nanoparticules à N_2O. Celle-ci n'est visible que via la légère

diminution d'intensité du pic à 707 eV, caractéristique du Fe(II). Les variations du spectre de Co au seuil L_3, en revanche, indiquent une oxydation du cobalt sur les nanoparticules $CoFe_2O_4$ et C@S-2nm, *i.e.* sur les C@S avec la coquille la plus épaisse ou sur le matériau homogène. L'échantillon C@S-0,1nm montre une oxydation beaucoup plus faible du Co(II) en Co(III) puisque le pic vers 779 eV, caractéristique du Co(III), n'augmente que très peu. Une stabilisation du cobalt à son degrés d'oxydation (+II) doit donc être lié à la faible épaisseur de la coquille de ces nanoparticules.

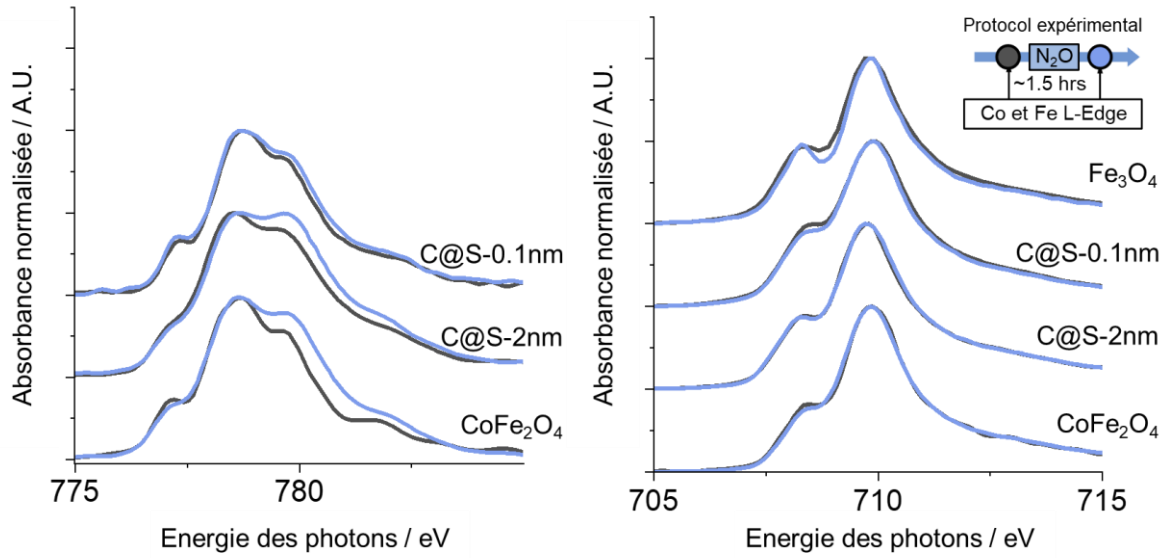

Figure R.9 : **A)** spectres d'absorption X du Fe et **B)** Co au seuil L_3 des nanoparticules Fe_3O_4, $CoFe_2O_4$, C@S-0,1nm et C@S-2nm avant (gris-vert) et après (bleu) leur exposition à 1 mBar de N_2O pendant 1h30.

Dans ce **quatrième chapitre** nous mettons en évidence comment l'utilisation du XAS en conditions *operando* et *in situ* permet d'étudier les changements du degré d'oxydation d'un électrocatalyseur. L'étude en conditions *in situ* (via l'exposition du catalyseur à des conditions oxydantes ***en l'absence réaction durant la mesure***, dû à l'absence de réactifs dans la chambre d'analyse) permet en particulier de mettre en avant l'influence de l'environnement chimique du site actif sur son état d'oxydation à l'équilibre. Nous avons montré ici que la présence de Fe(II) dans le cœur des nanoparticules stabilisait l'état bivalent du cobalt, stabilisation qui pourrait être à l'origine de l'activité supérieure de ces C@S pour l'OER *vs.* les nanostructures homogènes.

Conclusions et perspectives

Ce manuscrit présente différentes utilisations des spectroscopies XAS et XPS comme outils d'analyse de l'interface électrode-électrolyte d'un électrocatalyseur utilisé pour l'oxydation de l'eau. Nous montrons comment ces méthodes permettent de fournir des informations concernant la composition et l'état d'oxydation du matériau à sa surface pour aboutir à une meilleure compréhension du rôle du catalyseur. En particulier, nous illustrons comment l'analyse *operando* et *in-situ* combinés à ces techniques de spectroscopies permettent d'obtenir des informations sur les transformations chimiques transitoires qui ont lieu durant la réaction.

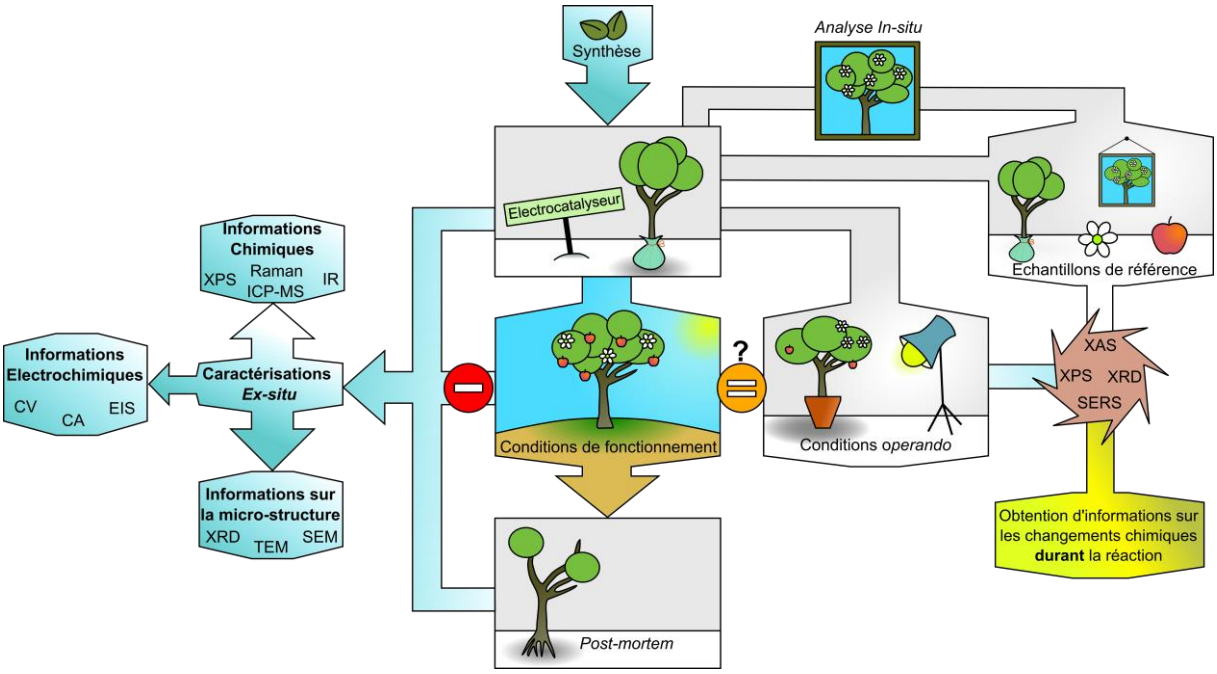

Figure R.10 : Feuille de route de la caractérisation d'un électrocatalyseur, illustrant la place des analyses *ex situ*, *in situ* et *operando* telles que définies dans ce manuscrit, dans le cycle de vie du catalyseur.

Bien que nous nous soyons concentrés sur les spectroscpies XAS et la XPS dans ce manuscrit, il est essentiel de rappeler que ces techniques ne se suffisent pas à elles seules. Réaliser une étude électrochimique complète permettant d'évaluer l'activité et la durabilité de l'échantillon, ainsi que des caractérisations *post-mortem* par des méthodes complémentaires de caractérisation (microscopie électronique, spectroscopie IR ou Raman, analyse thermogravimétrique, *etc.*) et un prérequis essentiel. Les techniques d'analyses dans les conditions *operando* par XAS et XPS apparaissent alors comme des outils permettant d'évaluer les changements

dynamiques ayant lieu durant la réaction, et qui ne pourraient pas être observés par d'autres moyens. Ces analyses *operando* nécessitent une préparation minutieuse en terme (i) de montage expérimental, (ii) d'acquisition de spectres de références, (iii) d'esprit critique en termes de compréhension du système et de l'analyse des résultats obtenus. En effet, comme illustré sur la **figure R.10**, les cellules spectro-électrochimiques doivent s'adapter aux besoins de l'analyse spectroscopique, et peuvent différer des conditions classiques d'utilisation du matériau catalytique. Une fois ce travail effectué, la comparaison des résultats *operando* obtenus avec des spectres de références (provenant d'échantillons commerciaux, synthétisés par l'utilisateur, du catalyseur avant réaction, *post-mortem* ou issu d'expériences *in situ* – exposition de l'échantillon à des conditions oxydantes sans réactifs, afin de « figer » le système dans un état d'oxydation), permet d'obtenir des informations sur les changements chimiques qui ont lieu durant la réaction.

Enfin, bien que le XAS et la XPS soient des méthodes de choix pour l'étude de systèmes électrochimiques, d'autres méthodes d'analyses peuvent être appliquées en conditions *operando* pour obtenir des informations complémentaires sur l'évolution des propriétés physico-chimiques de l'échantillon durant la mesure. Les techniques de diffusion des rayons X, ou les techniques dérivées de l'effet Raman, permettent de fournir des informations sur les changements cristallographiques et sur les interactions moléculaires à l'interface, par exemple. Ces informations ne peuvent pas être obtenues par XAS ou XPS. Une utilisation adaptée et raisonnée de ces méthodes *operando* est donc essentielle pour la bonne compréhension des systèmes électrocatalytiques.

Références

[1] J. Brauns, J. Schönebeck, M.R. Kraglund, D. Aili, J. Hnát, J. Žitka, W. Mues, J.O. Jensen, K. Bouzek, T. Turek, Evaluation of Diaphragms and Membranes as Separators for Alkaline Water Electrolysis, J Electrochem Soc. 168 (**2021**) 014510.

[2] A. Nechache, S. Hody, Alternative and innovative solid oxide electrolysis cell materials: A short review, Renewable and Sustainable Energy Reviews. 149 (**2021**) 111322.

[3] K. Ayers, The potential of proton exchange membrane–based electrolysis technology, Curr Opin Electrochem. 18 (**2019**) 9–15.

[4] Q. Feng, X. Yuan, G. Liu, B. Wei, Z. Zhang, H. Li, H. Wang, A review of proton exchange membrane water electrolysis on degradation mechanisms and mitigation strategies, J Power Sources. 366 (**2017**) 33–55.

[5] T.B. Ferriday, P.H. Middleton, Alkaline fuel cell technology - A review, Int J Hydrogen Energy. 46 (**2021**) 18489–18510.

[6] E.S. Davydova, S. Mukerjee, F. Jaouen, D.R. Dekel, Electrocatalysts for Hydrogen Oxidation Reaction in Alkaline Electrolytes, ACS Catal. 8 (**2018**) 6665–6690.

[7] Y. Yang, Y. Xiong, R. Zeng, X. Lu, M. Krumov, X. Huang, W. Xu, H. Wang, F.J. DiSalvo, Joel.D. Brock, D.A. Muller, H.D. Abruña, *Operando* Methods in Electrocatalysis, ACS Catal. 11 (**2021**) 1136–1178.

[8] R. Arrigo, In situ X-ray spectroscopic characterization techniques for electrocatalysis, Elsevier B.V, **2022**.

[9] B. Rotonnelli, M.-S.D. Fernandes, F. Bournel, J.-J. Gallet, B. Lassalle-Kaiser, In situ/operando X-ray absorption and photoelectron spectroscopies applied to water-splitting electrocatalysis, Curr Opin Electrochem. 40 (**2023**) 101314.

[10] A.J. Bard, L.R. Faulkner, Electrochemical Methods: Fundamentals and Applications, 2nd Edition, John Wiley & Sons, INC, **2001**.

[11] H.L.F. Von Helmoltz, , Ann. Physik. (**1853**) 211.

[12] G. Gouy, , Compt. Rend. 149 (**1910**).

[13] G. Gouy, , J. Phys. Radium. 9 (**1910**).

[14] D.L. Chapman, , Phil. Mag. 25 (**1913**).

[15] O. Stern, , Elektrochem. 30 (**1924**).

[16] R. Rizo, E. Sitta, E. Herrero, V. Climent, J.M. Feliu, Towards the understanding of the interfacial pH scale at Pt(111) electrodes, Electrochim Acta. 162 (**2015**) 138–145.

[17] Q. Deng, J. Weissmüller, Electrocapillary coupling during electrosorption, Langmuir. 30 (**2014**) 10522–10530.

[18] O.M. Magnussen, A. Groß, Toward an Atomic-Scale Understanding of Electrochemical Interface Structure and Dynamics, J Am Chem Soc. 141 (**2019**) 4777–4790.

[19] S. Levine, C.W. Outhwaite, L.B. Bhuiyan, Statistical mechanical theories of the electric double layer, J Electroanal Chem Interfacial Electrochem. 123 (**1981**) 105–119.

[20] E. Spohr, Molecular simulation of the electrochemical double layer, Electrochim Acta. 44 (**1999**) 1697–1705.

[21] A. Coretti, C. Bacon, R. Berthin, A. Serva, L. Scalfi, I. Chubak, K. Goloviznina, M. Haefele, A. Marin-Laflèche, B. Rotenberg, S. Bonella, M. Salanne, MetalWalls: Simulating electrochemical interfaces between polarizable electrolytes and metallic electrodes, Journal of Chemical Physics. 157 (**2022**).

[22] K. Doblhoff-Dier, M.T.M. Koper, Electric double layer of Pt(111): Known unknowns and unknown knowns, Curr Opin Electrochem. 39 (**2023**).

[23] W. Schmickler, Double layer theory, Journal of Solid State Electrochemistry. 24 (**2020**) 2175–2176.

[24] M. Favaro, B. Jeong, P.N. Ross, J. Yano, Z. Hussain, Z. Liu, E.J. Crumlin, Unravelling the electrochemical double layer by direct probing of the solid/liquid interface, Nat Commun. 7 (**2016**) 12695.

[25] M.F. Lichterman, M.H. Richter, B.S. Brunschwig, N.S. Lewis, H.J. Lewerenz, Operando X-ray photoelectron spectroscopic investigations of the electrochemical double layer at Ir/KOH(aq) interfaces, J Electron Spectros Relat Phenomena. 221 (**2017**) 99–105.

[26] J. Balej, Water vapour partial pressures and water activities in potassium and sodium hydroxide solutions over wide concentration and temperature ranges, Int J Hydrogen Energy. 10 (**1985**) 233–243.

[27] B. Keita, L. Nadjo, Polyoxometalate-based homogeneous catalysis of electrode reactions: Recent achievements, J Mol Catal A Chem. 262 (**2007**) 190–215.

[28] Z. Zeb, Y. Huang, L. Chen, W. Zhou, M. Liao, Y. Jiang, H. Li, L. Wang, L. Wang, H. Wang, T. Wei, D. Zang, Z. Fan, Y. Wei, Comprehensive overview of polyoxometalates for electrocatalytic hydrogen evolution reaction, Coord Chem Rev. 482 (**2023**) 215058.

[29] D. Gao, I. Trentin, L. Schwiedrzik, L. González, C. Streb, The reactivity and stability of polyoxometalate water oxidation electrocatalysts, Molecules. 25 (**2020**) 157.

[30] T. Ueda, Electrochemistry of Polyoxometalates: From Fundamental Aspects to Applications, ChemElectroChem. 5 (**2018**) 823–838.

[31] M.S. Balulla, J.A. Gamelas, H.M. Carapuça, A.M.V. Cavaleiro, W. Schlindwein, Electrochemical behaviour of first row transition metal substituted polyoxotungstates: A comparative study in acetonitrile, Eur J Inorg Chem. 4 (**2004**) 619–628.

[32] Q. Yin, J.M. Tan, C. Besson, Y. V Geletii, D.G. Musaev, A.E. Kuznetsov, Z. Luo, K.I. Hardcastle, C.L. Hill, A fast soluble carbon-free molecular water oxidation catalyst based on abundant metals, Science (1979). 328 (**2010**) 342–345.

[33] S. Goberna-Ferrón, L. Vigara, J. Soriano-López, J.R. Galán-Mascarós, Identification of a Nonanuclear {Co(II)9} Polyoxometalate Cluster as a Homogeneous Catalyst for Water Oxidation, Inorg Chem. 51 (**2012**) 11707–11715.

[34] P.P. Lopes, D.Y. Chung, X. Rui, H. Zheng, H. He, P.F.B.D. Martins, D. Strmcnik, V.R. Stamenkovic, P. Zapol, J.F. Mitchell, R.F. Klie, N.M. Markovic, Dynamically stable active sites from surface evolution of perovskite materials during the oxygen evolution reaction, J Am Chem Soc. 143 (**2021**) 2741–2750.

[35] F. Song, L. Bai, A. Moysiadou, S. Lee, C. Hu, L. Liardet, X. Hu, Transition Metal Oxides as Electrocatalysts for the Oxygen Evolution Reaction in Alkaline Solutions: An Application-Inspired Renaissance, J Am Chem Soc. 140 (**2018**) 7748–7759.

[36] J. Soriano-López, D.G. Musaev, C.L. Hill, J.R. Galán-Mascarós, J.J. Carbó, J.M. Poblet, Tetracobalt-polyoxometalate catalysts for water oxidation: Key mechanistic details, J Catal. 350 (**2017**) 56–63.

[37] M.W. Kanan, D.G. Nocera, In Situ Formation of an Oxygen-Evolving Catalyst in Neutral Water Containing Phosphate and Co^{2+}, Science (1979). 321 (**2008**) 1072–1075.

[38] S. Anantharaj, S. Kundu, S. Noda, “The Fe Effect”: A review unveiling the critical roles of Fe in enhancing OER activity of Ni and Co based catalysts, Nano Energy. 80 (**2021**).

[39] Z. Zhuang, W. Sheng, Y. Yan, Synthesis of monodispere Au@Co3O4 core-shell nanocrystals and their enhanced catalytic activity for oxygen evolution reaction, Advanced Materials. 26 (**2014**) 3950–3955.

[40] Y. Lv, S. Duan, Y. Zhu, P. Yin, R. Wang, Enhanced OER performances of Au@NiCo2S4 core-shell heterostructure, Nanomaterials. 10 (**2020**).

[41] A.L. Strickler, M. Escudero-Escribano, T.F. Jaramillo, Core-Shell Au@Metal-Oxide Nanoparticle Electrocatalysts for Enhanced Oxygen Evolution, Nano Lett. 17 (**2017**) 6040–6046.

[42] L. Royer, A. Bonnefont, T. Asset, B. Rotonnelli, J.J. Velasco-Vélez, S. Holdcroft, S. Hettler, R. Arenal, B. Pichon, E. Savinova, Cooperative Redox Transitions Drive Electrocatalysis of the Oxygen Evolution Reaction on Cobalt-Iron Core-Shell Nanoparticles, ACS Catal. 13 (**2023**) 280–286.

Benjamin Rotonnelli

Operando studies of the electrode/electrolyte interface using X-Ray absorption and X-Ray photoelectron spectroscopies

Résumé en français

Le développement de nouveaux catalyseurs pour la réaction de dégagement de l'oxygène (OER) est entravé par une compréhension limitée des phénomènes se produisant à l'interface électrode/électrolyte. Ces phénomènes - qu'ils soient liés au mécanisme réactionnel, au vieillissement du catalyseur, à sa dégradation, ou simplement à la polarisation de l'interface - dépendent du potentiel appliqué à l'électrode. Par conséquent, il est essentiel de pouvoir étudier le système électrochimique dans son état de fonctionnement, (*i.e operando*). Les techniques de spectroscopies−X telles que l'absorption des rayons-X (XAS) ou la photoélectronique-X (XPS) sont tout particulièrement indiquées pour l'étude de ces interfaces puisqu'elles sont sensibles au changement d'environnement chimique et au degré d'oxydation des éléments qui s'y situent. Dans ce manuscrit nous illustrons les avantages, les limites et les méthodes de ces techniques dans des conditions *operando* au travers de l'étude de 3 systèmes électrochimiques différents, plus ou moins proches d'une interface électrode/électrolyte modèle.

Mots clés : méthodes *in-situ* et *operando*; spectroscopie photoélectronique-X; spectroscopie d'absorption des rayons X; interface électrode/électrolyte; double couche électrochimique; 'Dip and Pull' (D&P); réaction de dégagement de l'oxygène (OER); complexe de cobalt stabilisés par des ligands polyoxométallates (Co-POM); nanoparticules cœur@coquille; méthode et analyse critique.

Résumé en anglais

The development of new electrocatalyst associated with the oxygen evolution reaction (OER) is limited by the comprehension we have about the different phenomena occurring at the electrode/electrolyte interface. Those phenomena, related to the reaction mechanism, the catalyst transformation during its operation, ageing, degradation or simply to the ionic rearrangement at the interface due to the electrode polarization, depend on the applied potential. Due to their dynamic nature, it is necessary to study the electrochemical system during the reaction conditions (*i.e. operando*). X-Ray based techniques such as X-Ray absorption (XAS) and X-Ray photoelectron spectroscopies (XPS) are particularly adapted to the study of those changes, as they are sensitive to the oxidation degree and the chemical environment changes of species at the interface. In this manuscript, we illustrate the advantages, the limitations and the experimental methodology associated to those spectroscopy techniques under *operando* conditions through the study of 3 different electrochemical systems, and how they allow to understand electrochemical interfaces of various complexities.

Keywords : *operando* and *in-situ methods;* X-ray photoelectron spectroscopy (XPS); X-ray absorption spectroscopy (XAS); electrode/electrolyte interface; electrochemical double layer; dip and pull setup (D&P); oxygen evolution reaction (OER); cobalt stabilised polyoxometalate (Co-POM); core@shell nanoparticles; method and critical analysis.